



HAL
open science

Millimeter and sub-millimeter satellite observations for ice cloud characterization : towards the ice cloud imager onboard MetOp-SG

Die Wang

► **To cite this version:**

Die Wang. Millimeter and sub-millimeter satellite observations for ice cloud characterization : towards the ice cloud imager onboard MetOp-SG. Physics [physics]. Université Pierre et Marie Curie - Paris VI, 2016. English. NNT : 2016PA066366 . tel-01480107

HAL Id: tel-01480107

<https://theses.hal.science/tel-01480107>

Submitted on 1 Mar 2017

HAL is a multi-disciplinary open access archive for the deposit and dissemination of scientific research documents, whether they are published or not. The documents may come from teaching and research institutions in France or abroad, or from public or private research centers.

L'archive ouverte pluridisciplinaire **HAL**, est destinée au dépôt et à la diffusion de documents scientifiques de niveau recherche, publiés ou non, émanant des établissements d'enseignement et de recherche français ou étrangers, des laboratoires publics ou privés.



LERMA



THÈSE

PRÉSENTÉE À

L'UNIVERSITÉ PIERRE ET MARIE CURIE

ÉCOLE DOCTORALE DES SCIENCES DE L'ENVIRONNEMENT D'ÎLE DE FRANCE

PRÉSENTÉE PAR

Die WANG

POUR OBTENIR LE GRADE DE DOCTEUR EN PHYSIQUE

MILLIMETER AND SUB-MILLIMETER SATELLITE OBSERVATIONS FOR
ICE CLOUD CHARACTERIZATION: TOWARDS THE ICE CLOUD IMAGER
ONBOARD METOP-SG

DIRECTRICE DE RECHERCHE : Catherine PRIGENT

CO-DIRECTEUR DE RECHERCHE : Carlos JIMENEZ

PRÉSENTÉE ET SOUTENUE LE 16 NOVEMBRE, 2016

DEVANT UN JURY COMPOSÉ DE :

Chantal CLAUD	LMD/Paris VI/CNRS	Présidente
Susanne CREWELL	Université de Cologne	Rapportrice
Jean-François MAHFOUF	Météo-France/CNRS	Rapporteur
Christophe ACCADIA	EUMETSAT	Examineur
Stefan BUHLER	Université de Hambourg	Examineur
Julien DELANOE	UVSQ/LATMOS	Examineur
Catherine PRIGENT	LERMA/CNRS	Directrice de thèse
Carlos JIMENEZ	LERMA/ESTELLUS	Co-Directeur de thèse

THÈSE COFINANCÉE PAR LE CNES ET AIRBUS

THÈSE PRÉPARÉE À L'OBSERVATOIRE DE PARIS, AU LERMA

致我的挚爱双亲...

RÉSUMÉ

Les observations météorologiques depuis les satellites dans le domaine des micro-ondes sont actuellement limitées à 190 GHz. La prochaine génération de satellites météorologiques opérationnels européens (EUMETSAT Polar System-Second Generation-EPS-SG), emportera un instrument, le Ice Cloud Imager (ICI), avec des fréquences sub-millimétriques jusqu'à 664 GHz, afin d'améliorer la caractérisation globale des nuages de glace. Pour préparer l'exploitation de ces nouvelles données, durant cette thèse, des travaux ont été effectués sur quatre axes complémentaires.

Des simulations réalistes de transfert radiatif ont été réalisées de 19 à 700 GHz, pour des scènes météorologiques réelles, couvrant une grande variabilité des nuages en Europe. L'objectif était double : premièrement mieux comprendre la sensibilité des ondes millimétriques et sub-millimétriques à la phase glacée des nuages, deuxièmement créer une base de données robuste pour développer une méthode d'inversion statistique des caractéristiques des nuages de glace. Un code de transfert radiatif atmosphérique (Atmospheric Radiative Transfer Simulator ARTS) a été couplé avec des profils atmosphériques simulés par un modèle méso-échelle de nuage (Weather Research and Forecasting WRF), pour douze scènes européennes aux moyennes latitudes. Les propriétés de diffusion des hydrométéores (glace, neige, graupel, pluie et eau dans le nuage) ont été soigneusement sélectionnées, en particulier pour la phase glace, et la compatibilité avec la microphysique de WRF a été testée: la Discrete-Dipole approximation (DDA) est adoptée pour calculer les propriétés diffusantes des particules de neige. Les simulations obtenues ont été systématiquement comparées avec des observations satellitaires coïncidentes d'imageurs et de sondes jusqu'à 200 GHz. L'accord entre les simulations et les observations montre la bonne qualité de la base de données, au moins jusqu'à 200 GHz.

Un algorithme d'inversion statistique à base de réseaux de neurones (NN) a ensuite été développé pour la détection et la quantification des paramètres des nuages de glace. Tout d'abord, la qualité statistique de la base de données développée avec WRF+ARTS et le contenu de l'information apporté par les températures de brillance simulées ont été étudiés grâce à une analyse en composantes principales et une étude des corrélations. La détection des nuages et l'inversion de leurs caractéristiques sont testées en prenant seulement les observations d'ICI, mais aussi en combinant les observations d'ICI et de MWI (MicroWave Imager) qui observe de 19 à 190 GHz, sur le même satellite que ICI. La classification donne des résultats très satisfaisants : la présence de phase glace dans le nuage est détectée avec un taux de succès de $\sim 90\%$ sur la terre et l'océan, seulement avec les canaux de ICI. Pour la quantification des hydrométéores, le contenu en glace des nuages n'est satisfaisante qu'au dessus de 0.05 kg/m^2 . L'erreur relative sur le contenu total de la phase glace (glace+neige+graupel, GNG) est inférieure à $\sim 40\%$ pour $0.1 \text{ kg/m}^2 < \text{GNG} < 0.5 \text{ kg/m}^2$ et au-dessous $\sim 20\%$ pour $\text{GNG} > 0.5 \text{ kg/m}^2$. L'ajout des canaux de MWI améliore la détection et la quantification de phase liquide des nuages, comme prévu. Pour l'estimation des profils des hydrométéores, l'algorithme d'inversion retrouve la forme général du profil nuageux, mais ne parviennent pas à détecter les détails.

Pour des environnements très froids et secs, la contribution de la surface au signal satellite peut être importante, même à des fréquences supérieures à 200 GHz. Un démonstrateur de ICI, ISMAR (International Sub Millimeter-wave Airborne Radiometer), a volé à bord de l'avion FAAM du UK, et a fourni des mesures jusqu'à 664 GHz. Les deux premières campagnes de cet instrument ont été soigneusement analysées, pour calculer l'émissivité de la surface à aux fréquences millimétriques. Deux nouvelles paramétrisations de l'émissivité des surfaces ont été développées au LERMA pour des fréquences jusqu'à 700 GHz : TELSEM² (Tool to Estimate Land Surface Emissivity from Microwave to sub-Millimeter waves) pour les continents et TESSEM² (Tool to Estimate Sea Surface Emissivity from Microwave to sub-Millimeter waves) pour l'océan. Les observations aéroportées d'ISMAR ont aidé à évaluer les deux modèles d'émissivité jusqu'à 325 GHz, sur l'océan, la glace de mer et la glace continentale.

ICI comporte deux canaux avec des mesures dans les deux polarisations orthogonales (à 243 et 664 GHz), pour offrir de nouvelles possibilités d'analyse des nuages. Des signaux de diffusion polarisée ont déjà été observés au dessus des nuages de glace, par des capteurs micro-ondes satellites entre 80 et 166 GHz. Dans cette thèse, les signaux polarisés ont été modélisés jusqu'à 874 GHz, pour les sphéroïdes orientés horizontalement. Les résultats obtenus pour des simulations sont en bon accord avec les observations d'ISMAR à 243 et 664 GHz. La polarisation fournit des informations supplémentaires sur les processus microphysiques liés à la phase glacée (la forme et l'orientation des particules). Cet effet de polarisation peut être important (plus de 10 K au-dessus des nuages de glace à certaines fréquences) et devrait être pris en compte dans les prochains algorithmes d'inversion des paramètres des nuages de glace.

Mots clés: Ice Cloud Imager (ICI), nuages de glace, télédétection, transfert radiatif, radiométrie micro-onde

ABSTRACT

The meteorological observations from satellites in the microwave domain are currently limited to 190 GHz. The next generation of European operational Meteorological Satellite (EUMETSAT Polar System-Second Generation-EPS-SG) will carry an instrument, the Ice Cloud Imager (ICI), with frequencies up to 664 GHz, to provide unprecedented measurements in the sub-millimetre spectral range, aiming to improve the characterization of ice clouds over the globe. To prepare this upcoming satellite-borne sub-millimeter imager, during this thesis, scientific efforts have been made on four complementary aspects.

Realistic radiative transfer simulations have been performed from 19 to 700 GHz, for real meteorological scenes, covering a large variability of clouds in Europe. The goal was two fold, first to better understand the sensitivity of the microwave to sub-millimeter waves to the cloud frozen phases, and second, to create a robust training database for a statistical cloud parameter retrieval. The Atmospheric Radiative Transfer Simulator (ARTS) is coupled with atmospheric profiles from the Weather Research and Forecasting (WRF) model, for twelve diverse European mid-latitude scenes. The single scattering properties of the hydrometeors (cloud ice, snow, graupel, rain, and cloud water) are carefully selected, especially for the frozen phases, and compatibility with the microphysics in WRF is tested: the Discrete-Dipole Approximation (DDA) is adopted for snow particles. The resulting simulations have been systematically compared with coincident satellite observations from imagers and sounders up to 200 GHz. The agreement between simulations and observations shows the good quality of the simulated training database, at least up to 200 GHz.

A statistical retrieval algorithm is then developed for the detection and quantification of the ice cloud parameters based on Neural Network (NN) methodologies. First, the statistical quality of the ARTS+WRF database, as well as the information content of the simulated brightness temperatures have been investigated, with Principal Component Analysis (PCA) and correlation analyses. Cloud detection and retrievals are performed using ICI channels only, but also using ICI plus the MicroWave Imager (MWI) observations that will be available from 19 to 190 GHz, on board the same platform as ICI. The classifier gives very satisfactory results in detecting the cloud frozen hydrometeors when using ICI-only channels, with an accuracy of $\sim 90\%$ in the cloud detection over land and ocean. For the cloud hydrometeor quantification, the retrieved cloud frozen phase contents are satisfactory with ICI-only channels for ice water path (IWP) above 0.05 kg/m^2 . The relative error for the retrieved integrated frozen water content (FWP) is below $\sim 40\%$ for $0.1 \text{ kg/m}^2 < \text{FWP} < 0.5 \text{ kg/m}^2$ and below $\sim 20\%$ for $\text{FWP} > 0.5 \text{ kg/m}^2$. Adding the MWI channels improves the detection and quantification essentially for the cloud liquid phases, as expected. For the hydrometeor profiles, the retrieval algorithm can capture the major vertical structures of the cloud profiles, but fail to detect the details.

Under very cold and dry environments, the surface contribution to the satellite signals can be significant, even at frequencies above 200 GHz. An aircraft demonstrator of ICI, the International Sub Millimeter-wave Airborne Radiometer (ISMAR), has been flown on board the FAAM UK aircraft, and provided measurements up to 664 GHz. The two first campaigns of this instrument have been carefully analyzed, to calculate the surface emissivity at millimeter frequencies. Two new emissivity parameterizations have been developed at LERMA for frequencies up to 700 GHz: the Tool to Estimate Land Surface Emissivity from Microwave to sub-Millimeter waves (TELSEM²) and the Tool to Estimate Sea Surface Emissivity from Microwave to sub-Millimeter waves (TESSEM²). The ISMAR airborne observations helped to evaluate the two emissivity models, up to 325 GHz, for ice-free ocean, sea ice, and continental ice.

ICI will have two window channel frequencies (243 and 664 GHz) with the capability of measuring both vertical and horizontal polarization signatures, providing new analysis possibilities. Polarized scattering signals over frozen clouds have already been observed by satellite microwave sensors up to 166 GHz. The scattering polarized signals were investigated here up to 874 GHz, by radiative transfer modeling for horizontally oriented spheroids. Good consistencies are revealed between the ISMAR observations and the simulations, at 243 and 664 GHz. The polarization signals provide additional information on the microphysics of the frozen phases (particle shape and orientation). This polarized effect can be significant (more than 10 K above some frozen clouds at some frequencies) and will have to be accounted for in the next retrievals of frozen cloud parameters.

Keywords: Ice Cloud Imager (ICI), ice clouds, remote sensing, radiative transfer, microwave radiometry

PUBLICATIONS

- V. S. Galligani, **D. Wang**, M. A. Imaz, P. Salio, C. Prigent, 2016: Analysis and validation of WRF microphysical schemes for deep moist convection over South-eastern South America (SESA) using radiative transfer simulations. (in preparation)
- **D. Wang**, C. Prigent, L. Kilic, S. Fox, C. Harlow, C. Jiménez, F. Aires, C. Grassotti, F. Karbou, 2016: *Surface emissivity at microwaves to millimeter waves over polar regions: parameterization and evaluation with aircraft experiments*. Journal of Atmospheric and Oceanic Technology (submitted)
- C. Prigent, F. Aires, **D. Wang**, S. Fox, and C. Harlow, 2016: *Sea surface emissivity parameterization from microwaves to millimeter waves*. Quarterly Journal of the Royal Meteorological Society, DOI:10.1002/qj.2953.
- **D. Wang**, C. Prigent, F. Aires, C. Jiménez, 2016: *Development of ice water path retrievals at millimeter and sub-millimeter wavelengths for the Ice Cloud Imager preparation*. IEEE Transactions on Geoscience and Remote Sensing, DOI:10.1109/ACCESS.2016.2625742.
- **D. Wang**, J. F. Miao, D.-L. Zhang, 2015: *Numerical Simulations of Local Circulation and Its Response to Land Cover Changes over the Yellow Mountains of China*. J. Meteor. Res., 29(4): 667-681.
- **D. Wang**, J. F. Miao, Z. M. Tan, 2013: *Impacts of topography and land cover change on thunderstorm over the Huangshan (Yellow Mountain) area of China*. Natural Hazards, 67(2): 675-699.
- Q. H. Xu, J. F. Miao, Y. K. Liu, L. P. Huang, **D. Wang**, 2013: *Response of sea and land breeze characteristics to urban heat island over the west coast of Bohai Bay*. Journal of the Meteorological Sciences, 33(4): 408-417.

ACKNOWLEDGMENT

Ce travail n'aurait jamais pu être réalisé sans le soutien total de ma directrice de thèse, C. Prigent. Je tiens à la remercier infiniment pour la confiance qu'elle m'a accordée tout au long de ma thèse. J'aimerais également lui dire à quel point j'adore son enthousiasme et sa passion pour le travail et la vie. En plus, son super pull jaune m'a sauvé du rhume plusieurs fois !

Mes plus vifs remerciements vont également à C. Jiménez pour son accueil chaleureux à chaque fois que j'ai sollicité son aide pour des questions scientifiques et informatiques. J'arrose ses plantes pour compenser, en fait !

Je tiens à remercier très chaudement les membres du jury (C. Claud, S. Crewell, J.-F. Mahfouf, C. Accadia, S. Buhler, J. Delanoë) d'avoir accepté de juger mes travaux. Dans 10 ans on ne se souviendra que de mon arrivée en taxi pour rattraper le RER en vrac au lieu de ma robe. Encore merci pour votre patience pour mon petit retard de début de soutenance !

Je remercie vivement le CNES et Airbus qui ont co-financé cette thèse.

Je voudrais remercier UK MetOffice pour le traitement des données ISMAR, ainsi que EUMETSAT pour leur soutien financier sur le projet sur l'émissivité de la surface.

Je souhaiterais aussi exprimer toute ma gratitude à F. Aires qui m'a aidé génialement à bien organiser et faire fonctionner 'mes neurones' ! Ses blagues et son Porto vont me manquer énormément.

Les mots ne sont pas suffisamment forts pour exprimer mes remerciements pour E. Defer qui m'a soutenu à tout moment pendant ces trois ans.

Je tiens à remercier chaudement V. S. Galligani avec qui j'ai partagé beaucoup de souffrance sur le code de transfert radiatif pendant ma thèse. Seulement ? (Non ! toute le reste de ma vie sans doute !).

Je souhaiterais aussi adresser ma gratitude à B. Albert et A. Coulais qui protègent toujours ma copine 'Antlia' et la rendent vivante et efficace !

Je remercie sincèrement V. Audon, V. Bigot, L. Girot, W. E. Khchai pour leur aide précieuse notamment pour les documents administratifs.

Je remercie ma belle J. Mathieu qui a contribué à améliorer mon français avec sa grande gentillesse et son infinie patience. Non, je ne parle pas de sa beauté naturelle ici !

Grand merci à F. Defrance qui m'a apporté tant : chant, danse, ... et même nourri de temps en temps. Son super fromage m'inspire beaucoup, miam !

Dois-je remercier A. Penkina avec qui j'ai passé de très bons moments en voyageant, en faisant du lèche vitrine, en buvant, en chantant ...

Je tiens à remercier mes meilleures amis (G.O., S.J., M.F., M.Y., T.N., ...) et mes chers collègues (G. Beaudin, E. Esteves, L. Kilic, V. Pellet, B. Pham, ...) de tout mon cœur pour avoir supporté mes blagues pas drôles, mon caractère de balance ...

感谢，在巴黎这场流动的盛宴里，遇见的人，经历的事。感谢，即使逆行，也仍自信，坚忍，永不言败的自己。我知道，巴黎的一切将伴随着我的一生，尤其是你。念挚爱双亲，天涯共此时。

Je ne pourrais jamais assez remercier mon gentil ours qui me donne du courage pour suivre mes rêves.

Contents

Abstract	iv
Publications	viii
Acknowledgment	x
Contents	xii
1 Introduction	1
1.1 Satellite remote sensing	3
1.2 The importance of ice cloud characterization	3
1.3 Observing ice clouds in the millimeter and sub-millimeter spectral range	4
1.4 Passive millimeter and submillimeter satellite instruments	6
1.5 Passive microwave to millimeter remote sensing to characterize the ice cloud	10
1.6 Thesis objectives	11
2 Realistic Radiative Transfer Simulations for Real Scenes in the Millimeter and Sub-millimeter Range	15
2.1 Real atmospheric scenarios	17
2.2 The cloud resolving model WRF	20
2.2.1 Description of the WRF model	20
2.2.2 WRF model configuration	22
2.2.3 Selection of microphysical scheme in WRF	23
2.3 Radiative transfer code	25
2.3.1 Description of ARTS	27
Description of the atmosphere	27
Sensor characteristics	29
Surface properties	29
Gas absorption	29
Scattering radiative transfer solvers	30
2.3.2 Particle scattering calculation	30
2.3.2.1 Particle dielectric property	30
Liquid water particles	31
Pure ice particles	31
Mixed-phase particles	32
2.3.2.2 The methods for calculating the particle scattering	34

	Spherical particles	34
	Non-spherical particles	35
	2.3.2.3 Compatibility of the particle characteristics simulated in the DDA databases with the WRF model	38
2.3.3	Surface emissivity	40
	2.3.3.1 Sea surface emissivity calculation	40
	2.3.3.2 Land surface emissivity calculation	42
3	A Statistical Retrieval of Cloud Parameters for the Millimeter Wave Ice Cloud Imager on board MetOp-SG	45
3.1	Evaluation of the simulation database below 200 GHz	49
3.2	Statistical analysis of the retrieval training database	52
3.3	Statistical retrieval of cloud hydrometeor contents	54
	3.3.1 Neural Networks technique	54
	3.3.1.1 Architecture and network function	55
	3.3.1.2 Training	57
	3.3.2 Cloud detection and classification	57
	3.3.2.1 A NN classifier	57
	3.3.2.2 Cloud classification results	58
	3.3.3 Cloud integrated content retrieval	59
	3.3.3.1 Retrieval algorithm	59
	3.3.3.2 Results	61
	3.3.4 Hydrometeor profile retrieval	65
	3.3.4.1 Retrieval approach based on a PCA representation	65
	3.3.4.2 Results	66
3.4	Conclusion	66
4	Microwave Surface Emissivity Calculations Using Airborne Measure- ments	69
4.1	Introduction	71
4.2	The instruments and the campaigns	73
	4.2.1 The instruments	73
	4.2.2 The campaigns	74
4.3	Evaluation of the ISMAR/MARSS observations	75
	4.3.1 Example of four flights	75
	4.3.2 Estimation of the ISMAR instrument noise	84
	4.3.3 Comparison of the observations and simulations, under clear sky assumptions	86
4.4	Emissivity estimation	93
	4.4.1 Methodology	93
	4.4.2 Estimation of the ice-free ocean surface emissivity	94
	4.4.2.1 Angular dependence of the emissivity	96
	4.4.2.2 Frequency dependence of the emissivity	99
	4.4.3 Estimation of the emissivity of the frozen surfaces	102
4.5	Conclusions	107
5	Simulations of the Microwave Polarized Scattering Signals over Frozen Clouds up to 874 GHz	111

5.1	Introduction	113
5.2	Radiative transfer simulations setup	115
5.3	Polarized scattering signatures of ice particles	116
5.4	Polarized scattering signatures of frozen particles	119
5.4.1	Dry snow	119
5.4.2	Wet snow	123
5.5	Conclusion	125
6	Conclusions and Perspectives	127
6.1	Conclusions	129
6.1.1	Realistic radiative transfer simulations of ICI observations	129
6.1.2	Development of a statistical retrieval algorithm for ICI	130
6.1.3	Surface emissivity estimation using airborne ISMAR observations	131
6.1.4	Analysis of the polarization signal with ICI	132
6.2	Perspectives	133
6.2.1	Efforts in radiative transfer understanding and modeling up to sub-millimeter frequencies	133
6.2.2	Developments in retrieval methodologies	134
6.2.3	The key role of the ISMAR aircraft observations	134
6.2.3.1	Analysis of the high frequency signals and evaluation of the radiative transfer simulations	135
6.2.3.2	Evaluation of the retrieval performance	136
A	Comparison of Passive Radiative Transfer Simulations for a Tropical Case	139
A.1	Introduction	141
A.2	Case description	141
A.2.1	Model configurations	142
A.2.2	Comparison between satellite observations and simulations	143
A.2.3	Discussion about the sensitivity of the microwave simulations to the hydrometeor characteristics	145
A.2.4	Conclusions	149
B	Paper A: Sea surface emissivity parameterization from microwaves to millimeter waves	151
C	Paper B: Surface emissivity at microwaves to millimeter waves over polar regions: parameterization and evaluation with aircraft experi- ments	169
D	Paper C: Development of ice water path retrievals at millimeter and sub-millimeter wavelengths for the Ice Cloud Imager preparation	223
	References	245

Chapter 1

Introduction

1.1 Satellite remote sensing

Satellite remote sensing, meaning the use of satellite-borne sensors to observe, measure, and record the electromagnetic radiation reflected or emitted by the Earth and its environment for subsequent analysis and extraction of information, has become a crucial tool to probe the Earth's atmosphere, and the land and ocean surfaces. As a unique opportunity for the continuous monitoring of the Earth system, the satellite observations have provided great advances in understanding the weather processes and climate system during the past decades. The global remote sensing systems combined with in situ measurements contribute to constrain the accuracy and reliability of the numerical prediction models for weather and climate applications, by feeding the models, and/or by evaluating the outputs.

The remote sensing applications are based on the variety of the electromagnetic waves that can interact with the Earth system. Therefore, understanding of the effects of the Earth's atmosphere and surface on the electromagnetic radiation traveling to the satellite is required. A frequency dependent absorption and scattering of the radiation is caused by the constituents of the atmosphere and the surface. The electromagnetic frequencies observed by the satellite instrument are carefully selected upon their ability to interact with the atmosphere and the surface. The instruments in the visible, infrared, or microwave domains provide a large range of diverse meteorological information. The observations from a variety of active and passive sensors are used. The passive sensors are designed to receive and measure the natural emissions produced by the Earth's atmosphere and surface, while the active instruments generate energy, transmit it and measure the signals that is back-scattered by the Earth system. Remote sensing is an indirect measurement, meaning that meteorological quantities are not measured directly, but by means of the electromagnetic radiation as an information carrier. The geophysical quantities of interest have to be reconstructed from the radiation measured by the satellites: this is called the retrieval or the inversion process.

1.2 The importance of ice cloud characterization

Clouds play a significant role in the Earth's weather and climate, due to their effects on the Earth's energy budget and on the Earth's hydrological cycle. Among the different types of clouds, ice clouds cover at least 20 % of the globe at any moment and up to 60-70 % in the tropical zone (Buehler et al., 2007b). The impact of ice clouds on the global Earth's energy budget is still unclear. They strongly influence the radiation budget of the atmosphere: they cool the atmosphere by reflecting the incoming solar radiation but also heat it by absorbing and re-emitting outgoing infrared radiation. Therefore, the net radiative effect of the ice clouds, according to both processes, is related to their macrophysical (e.g., ice content, horizontal extent, cloud altitude, cloud top temperature) and microphysical (e.g., ice particle shape, cloud optical thickness, and ice particle size) properties (Liou, 1986, Lohmann and Roeckner, 1995, Ramaswamy and

Ramanathan, 1989). These cloud parameters are considered as major tuning parameters to constrain the climate models in order to achieve a good agreement with the observations. However, so far, we lack measurements of these ice cloud parameters with sufficient accuracy and coverage in time and space. A good example is the Ice Water Path (IWP), defined as the integral of the ice water content through the depth of an ice cloud layer. There can be one order of magnitude difference between the IWP predicted by the major current global climate models (Eliasson et al., 2011, John and Soden, 2006, Waliser et al., 2011). Figure 1.1 compares the annually and zonally averaged IWP simulated by different coupled ocean-atmosphere models used in the 4th Assessment of the Intergovernmental Panel on Climate Change (IPCC AR5). The model simulations differ considerably, with larger discrepancies in the extratropical regions.

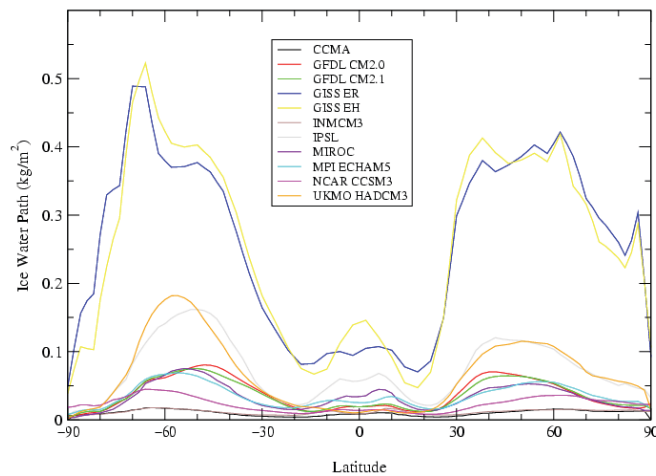


FIGURE 1.1: The climatology of zonal annual mean IWP from various climate models in the IPCC AR4 data archive. From John and Soden (2006).

The accuracy of the weather and climate models is related to the representation of the cloud microphysical processes (on cloud parameters, such as particle density, fallspeed, and particle size). The microphysical processes in the clouds are very complex in their spatial and temporal variability, controlling the formation, the growth, and the interactions of liquid droplets and frozen particles (Liou and Ou, 1989). In the cloud resolving models, the cloud microphysical processes interact with the macrophysics modules through the latent heating/cooling, the condensate loading, the surface mechanisms, and the radiative transfer processes, which are particularly challenging (Khain et al., 2015). They are parameterized differently in the various models, inducing large biases in model results.

1.3 Observing ice clouds in the millimeter and sub-millimeter spectral range

Ice clouds can be observed by remote sensing techniques operating at different wavelengths, from the microwave to the visible. Globally retrieved cloud parameters from

satellite observations can be used to constrain and validate the climate models. Figure 1.2 shows the vertical structure of a precipitating cloud and indicates schematically to which part of the cloud each type of instrument is sensitive (Waliser et al., 2009). The infrared and visible (IR+VIS in the Figure) radiometry techniques have been studied to quantify the ice cloud properties, especially for relatively thin cirrus clouds (Rossow and Schiffer, 1999), but they tend to saturate for moderate amounts of cloud ice and are sensitive to the uppermost layer of thick ice clouds (Buehler et al., 2012, Wu et al., 2008). Active visible instruments (lidar) can provide vertical information for rather thin clouds, but with a very limited spatial coverage. For instance, the Cloud-Aerosol Lidar with Orthogonal Polarization (CALIOP), a nadir-pointing dual-wavelength polarization lidar, can measure the vertical distribution profiles of clouds and aerosols, but with a footprint of 333 m (Winker et al., 2010). Microwaves (passive and active) are able to penetrate clouds and provide insight into the vertical profiles of most clouds, even well developed ones. The response of passive microwave observations to different cloud phases depends on the observation frequencies. At lower frequencies (below 60 GHz), the emission from the liquid cloud phase dominates, while scattering effects by the cloud ice phase become important at higher frequencies (Oguchi, 1983, Wu and Weinman, 1984). This scattering effect is responsible for the reduction of the upwelling thermal radiation, by which we can detect and quantify the ice phase in the clouds at a global scale. However, current passive microwave instruments on board satellites are limited in frequencies to 200 GHz, and cannot detect thin ice particles in the upper part of the clouds. Microwave active instruments (radar) give access to the ice cloud vertical structure, but with limited horizontal coverage (similar as lidar). For instance, the CloudSat radar (94 GHz) can measure the vertical profiles of cloud properties, but with a footprint of approximately 1.4 km (Stephens et al., 2002). Passive microwave retrievals can quantify the cloud parameters from thicker ice clouds than visible and infrared techniques, but they have difficulties characterizing the thin cirrus clouds. However, for the IWP estimations, large differences exist between the satellite measurements, as shown in Figure 1.3 (illustrating the ocean-only zonal averages of IWP from satellite datasets).

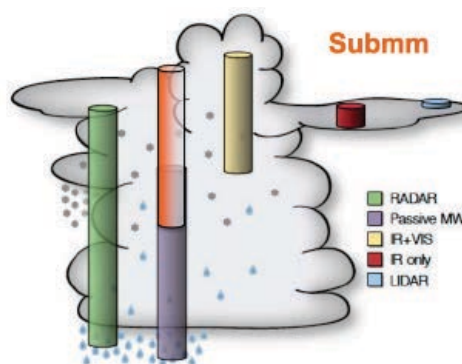


FIGURE 1.2: The columns indicate approximately where in the cloud profile the different measurement techniques are sensitive, from Eliasson et al. (2011).

Combining microwave and sub-millimeter measurements is a promising way to improve the capability of characterizing the ice cloud properties. Figure 1.4 shows the sensitivity of microwave to sub-millimeter radiation to the vertically integrated ice content and

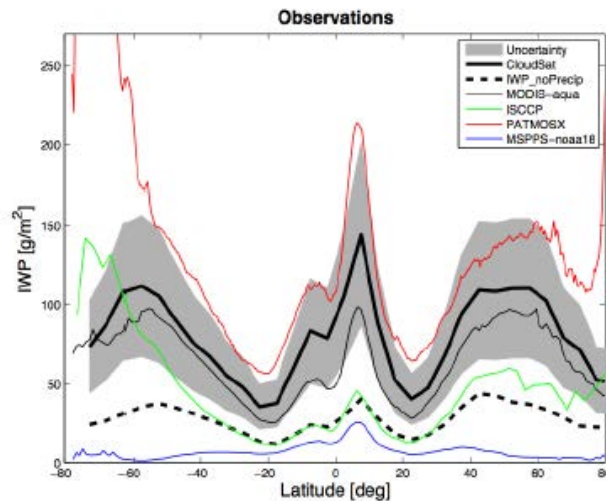


FIGURE 1.3: IWP ocean-only zonal averages of IWP from satellite datasets. The grey shaded area is the uncertainty interval. The results are for the period July 2006 to April 2008 (Eliasson et al., 2011). CloudSat represents CloudSat’s IWP 2B-CWC RO dataset and IWPnoPrecip represents CloudSats IWP product without profiles flagged to contain precipitation at the surface.

the ice particle size. The presence of the ice clouds reduces the upwelling brightness temperatures through the scattering effects, especially in the window channels between absorption lines. The brightness temperature depression increases with increasing ice water content and with increasing frequency. However, it saturates for high ice content at high frequencies. The microwave radiation is sensitive to the larger particles: with increasing frequencies in the millimeter, the sensitivity shifts to the smaller ice particles, making the detection and quantification of the cloud upper layers and cirrus possible. Combination of a large range of millimeter and sub-millimeter observations has been proposed to accurately retrieve the cloud microphysical and macrophysical properties (Evans et al., 2002, Jarret et al., 2007). This would complement the already existing infrared and microwave satellite observations for a better description of the cloud ice phase.

1.4 Passive millimeter and submillimeter satellite instruments

Satellite microwave atmospheric observations started with the Electrically Scanning Microwave Radiometer (ESMR) at 19.35 GHz onboard the Nimbus Series satellites in the early 1970’s. The Scanning Multichannel Microwave Radiometer (SMMR), also onboard the Nimbus satellites, followed, with two dual-polarized channels at 18 and 37 GHz. These instruments primarily focused on the precipitation retrieval over ocean, exploiting the strong contrast between the cold ocean background and the warm emission from the falling liquid particles below 50 GHz (e.g., Prabhakara et al., 1986, Wilheit et al., 1977).

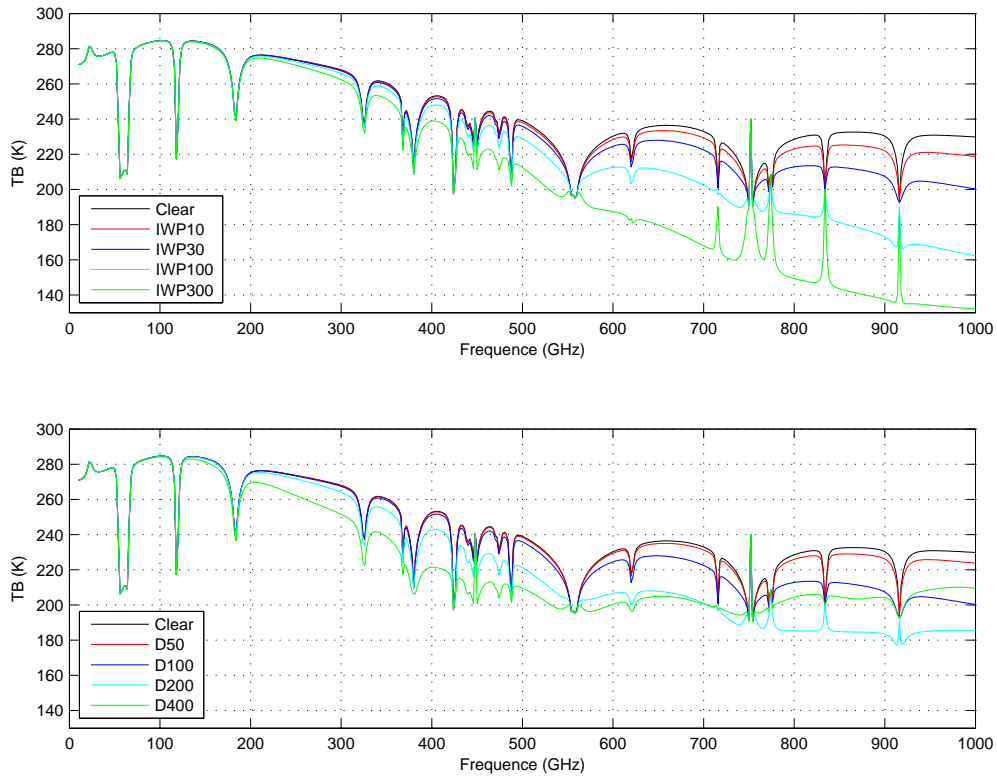


FIGURE 1.4: Top: Sensitivity of the microwave to sub-millimeter signals to the IWP (10, 30, 100, and 300 g/m^2) at nadir (the equivalent diameter is set to $100 \mu\text{m}$). Bottom: Sensitivity of the same signals to particle equivalent diameter (50, 100, 200, and $400 \mu\text{m}$) at nadir (the IWP is set to 30 g/m^2). The simulations have been done with the Atmospheric Radiative Transfer Simulator (ARTS), for tropical profiles from FASCOD. The cloud is set from 10 to 12 km.

Since 1987, microwave imagers and sounders provide observations up to 90 GHz in both V and H polarizations. Examples of three instruments are the Special Microwave Imager (SSM/I, [Colton and Poe, 1999](#)) series carried on board the Defense Meteorological Satellite Program (DMSP) satellites, the Tropical Rainfall Measuring Mission (TRMM) Microwave Imager (TMI, [Kummerow et al., 1998](#)), and the Advanced Microwave Scanning Radiometer for EOS (AMSR-E, [Kawanishi et al., 2003](#)). They are dedicated to the measurements of geophysical variables related to the Earth's climate and hydrology, including atmospheric water vapor, cloud liquid water, precipitation rate, cloud top temperature, surface winds, sea surface temperature, sea ice concentration, snow water equivalent, soil moisture, and surface emissivity.

Since 1991, the microwave satellite observations are available for meteorological applications over an expanded set of microwave frequencies up to 190 GHz. Frequencies higher than 80 GHz are used for the ice characterization because of the increasing scattering effect with increasing frequency. Examples of microwave imagers and sounders launched during the last decades are the Special Sensor Microwave/Temperature-2 (SSM/T-2), the Advanced Microwave Sounding Unit (AMSU), and the Microwave Humidity Sounder (MHS), the Special Sensor Microwave Imager/Sounder (SSMIS), the Sounder for Probing Vertical Profiles of Humidity (SAPHIR), the Microwave Analysis and Detection of

Rain and Atmospheric Structures (MADRAS), the Advanced Technology Microwave Sounder (ATMS), and the Global Precipitation Measurement (GPM) Microwave Imager (GMI). These instruments have allowed an improved characterization of different atmospheric clouds and surface parameters (e.g., Aires et al., 2012, Bernardo et al., 2013, Skofronick-Jackson et al., 2004, Wang et al., 2001).

During the past years, efforts have also been made to develop sub-millimeter radiometers devoted to the detection and quantification of ice clouds. Several airborne sub-millimeter radiometers have been built. They include: the Far-Infrared Sensor for Cirrus (FIRSC), an aircraft-based Fourier-transform spectrometer designed by the National Aeronautics and Space Administration (NASA) Langley Research Center that measures the radiance in the submillimeter spectral range from 300 to 3000 GHz (Vanek et al., 2001); the Millimeter-wave Imaging Radiometer (MIR), a cross-track imager owned by NASA Goddard Space Flight Center (GSFC), with 10 channels between 89 and 340 GHz (Racette et al., 1996); the Submillimeter-Wave Cloud Ice Radiometer (SWCIR), a cross-track scanning radiometer developed by the Jet Propulsion Laboratory to fly on the NASA DC-8, containing four receivers at 183, 325, 448, and 643 GHz (Evans et al., 2002); and the Compact Scanning Submillimeter Imaging Radiometer (CoSSIR), built by NASA/GSFC, operating with 12 channels from 183 to 874 GHz. Several sub-millimeter radiometers operating in a limb-scanning mode have also been launched in space for atmospheric chemistry (the Odin-SMR and the Earth Observing System Microwave Limb Sounder (EOS-MLS)), but the observation geometry results in relatively coarse horizontal spatial resolution. These measurements from space-based and airborne radiometers have been used to develop retrieval algorithms for ice cloud parameters (e.g., Deeter and Evans, 2000, Evans et al., 2005, Liu and Curry, 2000, Rydberg et al., 2009, Vivekanandan and Bringi, 1991, Wang et al., 2001, Weng and Grody, 2000, Wu et al., 2008). No down-looking sub-millimeter satellite radiometer has been flown yet.

The European Space Agency (ESA) and the European Organization for the Exploitation of Meteorological Satellites (EUMETSAT) have jointly planned to develop the next generation of European meteorological satellite (the Meteorological Operational Satellite-Second Generation (MetOp-SG), Kangas et al., 2012). The first conically scanning millimeter/sub-millimeter instrument, Ice Cloud Imager (ICI, see Figure 1.5), will observe from 180 to 664 GHz with a small antenna size, providing 16 km on-ground footprints, with a conical scanning mechanism (nearly constant incidence angle about 53°) (Alberti et al., 2012). It will fly on the platform MetOp-SG-B, to be launched in 2022. The same platform will also embark another MicroWave Imager (MWI) measuring at lower frequencies from 18 to 183 GHz. A MicroWave Sounder (MWS) will also be placed on the MetOp-SG suite at frequencies from 23 to 230 GHz,



FIGURE 1.5: The next generation of MetOp satellites. Ice Cloud Imager (ICI) will fly on this platform.

but on the platform MetOp-SG-A. The ICI and the MWI channel characteristics are presented in Table 1.1.

TABLE 1.1: Channel characteristics of the MWI and ICI radiometers, including their frequencies, BandWidth (BW), instrument noise (Net Δ T), polarization, and main spectral feature of each channel. From [Schlüssel et al. \(2016\)](#).

MWI					ICI				
Channels (GHz)	BW (GHz)	Net Δ T (K)	Polar.	Spectral feature	Channels (GHz)	BW (GHz)	Net Δ T (K)	Polar.	Spectral feature
18.7	0.2	0.7	V+H	Window	183.31 \pm 7.0	2 \times 2.0	0.7	V	H ₂ O
23.8	0.4	0.6	V+H	H ₂ O	183.31 \pm 3.4	2 \times 1.5	0.7	V	H ₂ O
31.4	0.2	0.8	V+H	Window	183.31 \pm 2.0	2 \times 1.5	0.7	V	H ₂ O
50.3	0.4	1.0	V+H	O ₂	243.2 \pm 2.5	2 \times 3.0	0.6	V+H	Window
52.61	0.4	1.0	V+H	O ₂	325.15 \pm 9.5	2 \times 3.0	1.1	V	H ₂ O
53.24	0.4	1.0	V+H	O ₂	325.15 \pm 3.5	2 \times 2.4	1.2	V	H ₂ O
53.75	0.4	1.0	V+H	O ₂	325.15 \pm 1.5	2 \times 1.6	1.4	V	H ₂ O
89.0	4.0	1.0	V+H	Window	448 \pm 7.2	2 \times 3.0	1.3	V	H ₂ O
118.7503 \pm 3.2	2 \times 0.5	1.2	V	O ₂	448 \pm 3.0	2 \times 2.0	1.5	V	H ₂ O
118.7503 \pm 2.1	2 \times 0.4	1.2	V	O ₂	448 \pm 1.4	2 \times 1.2	1.9	V	H ₂ O
118.7503 \pm 1.4	2 \times 0.4	1.2	V	O ₂	664 \pm 4.2	2 \times 5.0	1.5	V+H	Window
118.7503 \pm 1.2	2 \times 0.4	1.2	V	O ₂					
165.5 \pm 0.75	2 \times 1.35	1.1	V	Window					
183.31 \pm 7.0	2 \times 2.0	1.2	V	H ₂ O					
183.31 \pm 6.1	2 \times 1.5	1.1	V	H ₂ O					
183.31 \pm 4.9	2 \times 1.5	1.1	V	H ₂ O					
183.31 \pm 3.4	2 \times 1.5	1.1	V	H ₂ O					
183.31 \pm 2.0	2 \times 1.5	1.2	V	H ₂ O					

ICI will focus particularly on the remote sensing of ice clouds, and will be the first space instrument dedicated to the characterization of the ice clouds. It will measure cloud ice water path, ice particle size, and ice cloud altitude. It will help validate the cloud resolving models and the parameterization of the microphysical schemes in weather and climate models ([Cavan et al., 2011](#), [Sola et al., 2014](#)). An ICI demonstrator, the International SubMillimeter Airborne Radiometer (ISMAR), has been designed by the UK Met Office and operated on the Facility for Airborne Atmospheric Measurements (FAAM) BAe-146 aircraft to observe the brightness temperatures at frequencies from 118 to 664 GHz ([Fox, 2015](#), [Fox et al., 2014](#)). A further channel at 874 GHz will be added. ISMAR has been tested and operated in three aircraft field campaigns: the Sub-millimeter Trial in Cirrus and Clear Skies (STICCS-2) on November and December 2014, the Cold-air Outbreak and Sub-Millimeter Ice cloud Study (COSMICS) on March 2015 out of Prestwick, Scotland, and the very recent WINTeX-2016 campaign from Cranfield, UK. ISAMR has multiple scan directions, including downward and upward views. It can help develop ice cloud retrieval algorithms for ICI prior to launch, as well as evaluate gas absorption or surface emissivity models. It can also be used post-launch, for calibration/validation.

1.5 Passive microwave to millimeter remote sensing to characterize the ice cloud

The sensitivity of the microwave scattering signals to the microphysical characteristics in clouds have been analyzed using radiative transfer codes (e.g., the Atmospheric radiative transfer Simulator (ARTS, [Buehler et al., 2005](#), [Eriksson et al., 2011](#)), the Radiative Transfer for TOVS (RTTOV, [Hocking et al., 2014](#), [Matricardi et al., 2001](#)), and the Atmospheric Transmission at Microwaves (ATM, [Pardo et al., 2001](#))). There are two types of radiative transfer codes at microwave frequencies range: the physical (line-by-line), and fast models. The fast models (such as RTTOV) are normally used for operational purposes, by parameterizing the absorption coefficients to satisfy the needs of computational efficiency. Physical radiative transfer codes (e.g., ARTS and ATM) attempt to calculate the absorption coefficients with atmospheric profiles of gaseous for each absorption line to achieve the accuracy requirement, which are computationally expensive. The radiative transfer codes can be fed with atmospheric profiles from cloud resolving models, standard atmosphere data, and cloud radar. [Burns \(1997\)](#) used atmospheric fields from the University of Wisconsin Regional Atmospheric Modeling System for the hurricane Gilbert as inputs to the radiative transfer model developed by [Kummerow and Giglio \(1994\)](#). [Wiedner et al. \(2004\)](#) investigated TMI observations with ATM radiative transfer model coupled with Méso-NH cloud resolving model results. [Sreerekha et al. \(2008\)](#) simulated the brightness temperatures at AMSU-B channels with ARTS, taking the atmospheric components from the MetOffice Mesoscale model (UKMES) as inputs. [Geer and Baordo \(2014\)](#) studied a set of cases with RTTOV model fed by ECMWF 4D-Var assimilation system, in order to improve its performance to reproduce the scattering signals at frequencies up to 183 GHz. The sensitivity of the scattering signals to the snow properties has been also investigated using ARTS model coupled with the Méso-NH by [Galligani et al. \(2015\)](#). According to these studies, the ice cloud microphysical properties play a significant role in the simulated radiation, through their effect on the single scattering properties (SSPs).

Calculations of the scattering properties of the frozen hydrometeors require a detailed description of the ice cloud microphysical properties, such as particle size distribution, dielectric properties (related to the particle density), shape or orientation. To simplify the simulations, the SSPs of the snow and ice particles are generally calculated by the Mie theory under the assumption of spherical particles. For the small ice crystals with constant density (917 kg/m^3), this assumption is realistic at microwave frequencies, while for the snow and other frozen particles (e.g., graupels) it may not be appropriate. These frozen particles can have very complex shapes, varying with particle size ([Baran et al., 2011](#), [Heymsfield et al., 2002](#)). For a given particle mass, the scattering properties can vary significantly from a particle to the other, with changes in density, shape, and orientation (e.g., [Johnson et al., 2012](#), [Kim, 2006](#)). Spheroid particles and other simple shapes can be handled by the T-matrix code ([Mishchenko et al., 2002](#)). For more complex shapes, the Discrete Dipole Approximation (DDA) has been used recently ([Baum et al., 2005](#), [Hong et al., 2009](#), [Liu, 2008](#)).

Different methodologies have been developed for the retrieval of ice cloud parameters and snowfall, from existing observations below 200 GHz. [Liu and Curry \(1998\)](#) and [Deeter and Evans \(2000\)](#) retrieved the IWP using observations from airborne radiometers in the millimeter range at 89, 150, 183, and 220 GHz, while [Liu et al. \(1999\)](#) and [Zhao and Weng \(2002\)](#) developed IWP retrieval algorithms based on satellite observations from SSM/T2 and AMSU-B. A snowfall retrieval algorithm has also been developed using the AMSU-B measurements over land by [Skofronick-Jackson et al. \(2004\)](#), and evaluated with cases over the eastern United States. [Noh et al. \(2006\)](#) showed that the millimeter wavelength observations have the capacity to retrieve the integrated snow water content, but noted the difficulty in describing the ice cloud profile, due to the lack of sensitivity to the uppermost layers in the clouds.

The sub-millimeter wavelength measurements have the potential to derive the ice cloud information from upper tropospheric layers and to improve the retrieval performance of the ice cloud properties, especially for the ice cloud vertical structure. Some statistical methodologies have been developed to estimate the ice cloud quantities, for the exploitation of the sub-millimeter wave observations from satellites. [Jimenez et al. \(2007\)](#) retrieved the integrated cloud ice content, the cloud ice median mass equivalent sphere diameter, and the median cloud ice mass height, using two different training databases. The first database was derived from radiative transfer simulations applied to atmospheric profiles from the Atmospheric Radiation Measurements (ARM) program with the addition of randomly generated cloud quantities ([Evans et al., 2005](#)), while the second one combined profiles from Cloudnet radar data and European Centre for Medium range Weather Forecasting (ECMWF) analyses ([Rydberg et al., 2007](#)). This work illustrated the sensitivity of the ICI frequencies to the cloud parameters, with a theoretical accuracy of 20 %/17 % (median relative error) for IWP for a mid-latitude winter/tropical scenario. [Evans et al. \(2005\)](#) performed the retrievals of IWP and ice particle size with CoSSIR measurements from the Cirrus Regional Study of Tropical Anvils and Cirrus Layers Florida Area Cirrus Experiment (CRYSTAL-FACE) aircraft campaign, using a Bayesian Monte Carlo integration algorithm. [Defer et al. \(2008\)](#) developed a precipitation retrieval scheme to estimate the frozen particle content with Neural Networks (NNs), using a database of realistic atmospheric profiles derived from the Meso-NH cloud resolving model ([Chaboureau et al., 2008](#)) with simulated brightness temperatures at frequencies up to 424 GHz by radiative transfer model ([Meirolid-Mautner et al., 2007](#)). In addition, retrieval algorithms and databases based on the ISMAR airborne observations are being developed by several groups (e.g., Chalmers and Hamburg University) to estimate the IWP using NN and Monte Carlo algorithms. The relationships between frequencies are rather different depending on the assumptions in the simulated database, with direct consequences on the derived retrievals.

1.6 Thesis objectives

Better capturing and understanding the Earth energy budget and the Earth hydrological cycle requires accurate characterization and quantification of the ice cloud properties at a global scale. The detection and estimation of ice cloud properties (e.g., the amount of

ice contained in the cloud) from space with existing satellite observations at microwave frequencies (limited to 190 GHz for passive mode) are still a challenging task, with large discrepancies. The microwave cloud scattering signals observed from the satellites provide information of cloud ice phases, depending strongly on their microphysical properties (e.g., particle size, particle density, particle dielectric property, and particle shape). However, complex variability and lack of realistic parametrizations of the microphysical properties of cloud ice phases is a large difficulty in the quantification of ice clouds. This thesis seeks first to characterize the cloud ice properties using radiative transfer modeling, in order to improve the understanding of their interaction with the radiation in the microwave and sub-millimeter range. This is a critical step for the quantification of the ice cloud properties in preparation of the exploitation of the ICI instrument with millimeter and sub-millimeter channels, on board the MetOp-SG satellite.

In this thesis, the following objectives will be pursued:

- Our main objective is to develop a statistical retrieval algorithm to detect the ice clouds and to quantify the cloud IWP. To insure the quality of the retrieval, the statistical retrieval has to be trained on a realistic and statistically representative database of simulations. Our first priority will be to build a robust database of simulations for the future ICI observations. We will concentrate on mid-latitude Europe. Accurate radiative transfer simulations at ICI frequencies have to be performed, for realistic meteorological scenes. A Cloud Resolving Model can provide consistent and detailed atmospheric profiles for diverse situations. These profiles can then feed a radiative transfer simulator to obtain realistic simulations. There is first a need to improve our understanding of the interaction between the ice cloud microphysical properties and the radiative transfer in the millimeter and sub-millimeter range. A careful analysis of the scattering properties of the frozen particles in the microwave to millimeter range has to be conducted. The simulations will be performed for real situations, for possible comparisons with current satellite observations up to 200 GHz. Once a satisfactory simulation database is created, the retrieval algorithm will be developed. A two step algorithm will be tested: first the detection of the cloud structure, then the quantification of the IWP. Special care will be exercised in the quantification of the retrieval error, avoiding any over-optimistic error characterization.
- Airborne observations at ICI frequencies with ISMAR have been conducted. The second objective of this thesis will be to analyze available ISMAR observations, for surface emissivity considerations. An accurate description of the surface contribution to the satellite observations is necessary, even at the ICI high frequencies, in the case of very dry and cold atmospheres. Here, the ISMAR observations will be used to evaluate recently developed emissivity parameterizations over ocean, and polar regions.
- The last objective of this thesis is to extend the analysis to the polarized scattering signatures over clouds to the ICI frequencies. Observation and simulation studies have already been conducted at frequencies up to 160 GHz. Radiative transfer

simulations will be performed, and comparisons with ISMAR observations will be made up to 664 GHz qualitatively.

This thesis comprises six chapters: Chapter 2 presents the preparation of the radiative transfer simulations for real scenes in the millimeter and sub-millimeter range. In Chapter 3, the ice cloud statistical retrieval algorithm is developed and its performance is established. Chapter 4 presents the ISMAR observations, along with the evaluation of the emissivity models using the aircraft measurements. Chapter 5 focuses on the polarized scattering signals at millimeter and sub-millimeter waves over frozen clouds, based on radiative transfer modeling. Chapter 6 concludes this thesis by providing the scientific perspective on the work carried out.

Chapter 2

Realistic Radiative Transfer Simulations for Real Scenes in the Millimeter and Sub-millimeter Range

Our retrieval of cloud parameters from the passive microwave instruments on board the Meteorological Operational-Second Generation (MetOp-SG), namely the Ice Cloud Imager (ICI) and the MicroWave Imager (MWI), will rely on statistical inversion methods. This requires a training database that has to represent as well as possible the variability of the possible situations. Here, we will focus on the retrieval of cloud parameters in Europe, and the meteorological situations will be selected to cover the diversity of European weather conditions. The training dataset will be made of realistic radiative transfer simulations. This chapter presents the methodology and the tools to perform realistic radiation transfer simulations in the millimeter and sub-millimeter range for real meteorological scenes, to build up the training database. The Atmospheric Radiative Transfer Simulator (ARTS) will be used to simulate the brightness temperatures. ARTS will be fed by a detailed and realistic description of the atmospheric profiles and the cloud microphysical properties derived from a cloud resolving model (Weather Research and Forecasting, WRF) for a selection of diverse meteorological conditions. Calculation of the scattering properties of the cloud particles requires special attention, as the radiative transfer simulations are very sensitive to the scattering parameters. Two surface emissivity models, the Tool to Estimate Land Surface Emissivity from Microwave to sub-Millimeter waves (TELSEM²) and the Tool to Estimate Sea Surface Emissivity from Microwave to sub-Millimeter waves (TESSEM²), developed by the Laboratoire d'Etudes du Rayonnement et de la Matière en Astrophysique et Atmosphères (LERMA) will provide reasonable land and ocean surface emissivities. A schematic diagram presents the main necessary elements to prepare the retrieval database in this thesis (Figure 2.1).

2.1 Real atmospheric scenarios

Twelve diverse meteorological situations are collected to cover as well as possible the variability of cloud parameters, over Europe. These cases have been chosen by considering important atmospheric systems associated with the main weather regimes across Europe (e.g., the Azores High, the Icelandic Low, and the Siberian Anticyclone), and have been selected for their different locations in Europe, their different seasons, their different synoptic backgrounds (both ocean and land cases), and their contents of various precipitation types (convective, stratiform, and orographic precipitation). These twelve cases are presented below:

C1: July 2nd, 2007, Poland. A strong convective storm cell grew over the Sudety Mountains in Poland and expanded rapidly with wind speeds up to 90 km/h. The severe weather mainly took place in south-western and center Poland. Hail, lighting, and flash-flooding during this case caused severe damages in agriculture, forest, and electric facilities.

C2: March 1st, 2008, Central Europe. A severe extra-tropical cyclone named Emma was formed in the North Atlantic ocean, passing northern UK on February 29, and arrived in Central Europe (e.g., Austria, Germany, Poland, and the Czech Republic) on March 1st where winds reached up to 166 km/h (103 mph).

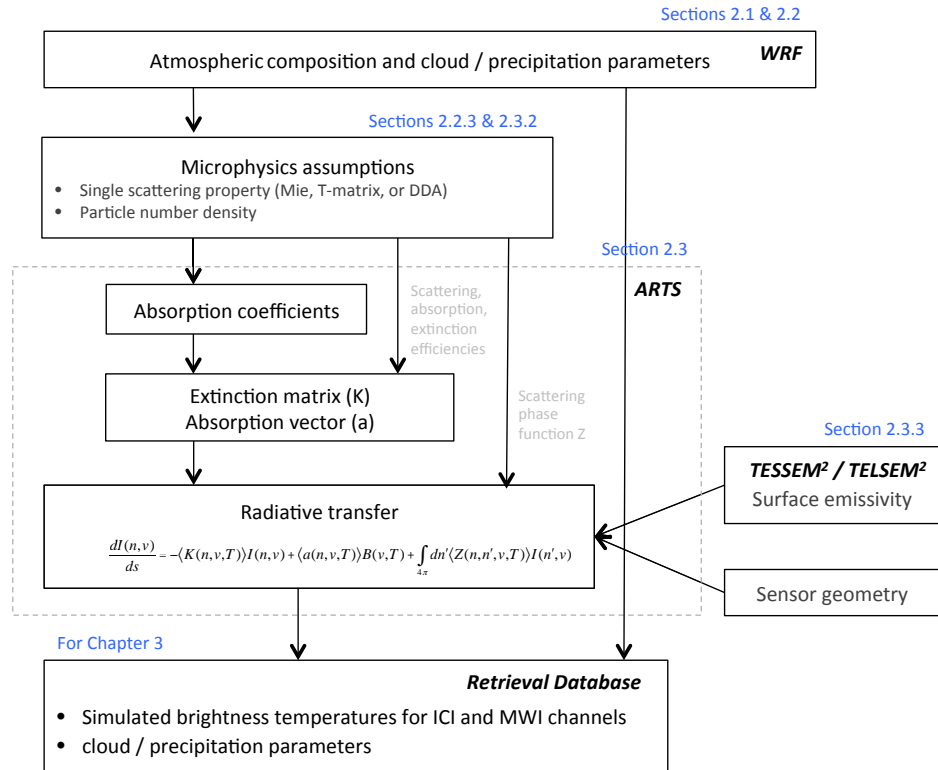


FIGURE 2.1: Schematic diagram showing the main necessary elements to prepare the retrieval database.

C3: May 20, 2008, Hungary. A rapid tornado thunderstorm (2 hours) developed over Hungary inducing severe precipitation, hail (2-5 cm), even flash floods in several regions. This storm was observed by Meteosat-9 IR10.8 image at 11:45 UTC and defined as a cold-ring shaped super-cell over Hungary and Serbia (Putsay et al., 2011). This thunderstorm was associated with a strong meso-cyclone, which indicated a probability of severe weather.

C4: December 8, 2010, France. Huge plunges in the jet-stream allowed cold waves to build over Europe for the past few weeks, laying the groundwork for winter storms with heavy snowfall. An exceptionally heavy afternoon snowstorm hit France. It was the biggest snowfall event in close to a quarter of a century. It forced Paris's Eiffel Tower and airports to shut down briefly. The snow fell heavily for several hours, reducing visibility to a quarter of a mile at times. According to the report of Météo-France, one weather station in Paris had ~ 11 cm of snow.

C5: August 18, 2011, Belgium. An extremely severe thunderstorm system developed over Belgium, with particularly strong downdraft. It initiated over France around 12:00 UTC as a shallow low, and then deepened and propagated over Belgium, Netherlands, and Germany.

C6: November 5, 2011, Mediterranean region. This was a rare Mediterranean tropical

cyclone that took place during November 4-6, 2011. It originated as a typical extratropical system in the Atlantic basin and slowly moved westwards crossing Spain and the Balearic Islands. When it arrived over the Mediterranean Sea, the cut-off lows and warmer surface made it strengthen and transform into a tropical-like storm. Then it continued to develop and reached France on November 8. A serious flooding with 600 mm rainfall during 72 hours occurred over the southwest part of Europe.

C7: June 28, 2012, UK. A series of thunderstorms occurred across the UK, induced by a double structured cold front over western and northern parts of the UK (Clark and Webb, 2013). Strong precipitation and flash flooding happened in several areas. Two tornadoes were observed in the Midlands. Exceptionally large hailstones were seen in Talgarth and Glasbury, leading to serious damages to transportation and cultivation.

C8: September 12, 2012, Italy. The Friuli Venezia Giulia case caused more than 100 mm of daily rainfall in this region (Manzato, 2012). The heavy rain and hail were associated with severe convective storms during two episodes. The first strong thunderstorm initiated and matured in the morning (from 8:00 to 10:00 UTC). The initial storm (near Vivaro) was triggered by an interaction between the moist southeasterly airflow and the Alps barriers. Then, several new convective systems started to form and develop in the following hours near the Adriatic coast. They were attributed to the convergence of the strong downdraft within the previous storm and westerly flow in the Veneto region. The second storm happened in the afternoon (from 15:00 to 19:00 UTC) along the North Adriatic coast.

C9: August 26, 2012, Italy. A cold front invaded western Europe on August 25, 2012, and passed the Alps region at night on August 26, 2012. It went on through Poland, Slovakia, Hungary, northern Italy, Slovenia, and western Balkan, inducing heatwave in the Mediterranean area. In addition, large hails and severe winds occurred in the Po valley and along the Adriatic coast of Italy. Two tornados were observed close to Ostia/Fiumicino and Porec.

C10: November 20, 2013, France. A remarkable snowfall was maintained for 24 hours by a depression fed by a flux from the Mediterranean at high altitudes with a wind draft from north in the lower layers. The orange alert was maintained for five departments since November 20 in the morning (Ain, Isere, Haute-Loire, Rhone, and Loire) and extended to twenty other regions. The southeastern France (Saint-Etienne) was under a thick layer of snow (30 to 40 cm), blocking traffic and hampering transportation in the surrounding region.

C11: January 19, 2013, Portugal. An extreme windstorm (Gong) influenced the Portuguese coasts on January 19, 2013, with a central lowest pressure of 968 hPa and wind gusts of 140 km/h. This windstorm developed explosively between the Azores and the Iberian Peninsula, with the help of a southerly movement of a polar jet-stream. This storm brought heavy rain in Portugal, causing the destruction of national forests and farms.

C12: October 27, 2013, UK. The St. Jude storm (Cyclone Christian), a severe European windstorm, formed in the western Atlantic on October 26, 2013, and strengthened under

a strong jet-stream with incoming tropical airflow. The center low rapidly developed and intensified as it crossed the North Sea. During this storm, the wind speed was up to 194.4 *km/h* on October 28 and the lowest pressure was 967.6 *hPa*.

2.2 The cloud resolving model WRF

The cloud resolving model WRF is used in this thesis to generate and provide realistic atmospheric states for the radiative transfer simulations. The WRF outputs of interest include the mixing ratio profiles of six water species (water vapor, cloud water, rain, cloud ice, snow, and graupel), the temperature and the pressure profiles, the surface altitude, the surface temperature, and the wind speed at 10 *m*. In addition, some key hydrometeor microphysical properties, such as particle size distribution (PSD) and particle density, are given by the WRF microphysical schemes.

2.2.1 Description of the WRF model

The WRF model is a new generation mesoscale numerical weather prediction system and data assimilation system, designed for both atmospheric research and operational forecasting needs. The WRF includes two distinct dynamical solvers, referred to as the Nonhydrostatic Mesoscale Model (NMM) and the Advanced Research WRF (ARW). The ARW core, an experimental and advanced research version, is developed and maintained by the National Center for Atmospheric Research's (NCAR) Mesoscale Microscale Meteorology (MMM) Laboratory. The NMM core is mainly designed for forecasting operations, developed by the National Centers for Environmental Prediction (NCEP). The WRF model was designed to be a flexible, state-of-the-art, and portable code for generating atmospheric simulations efficiently in different computing environments (e.g., massively-parallel supercomputers and laptops). The WRF model is capable of simulating the cases under both real and idealized conditions, with a large range of scales from meters to thousands of kilometers. It is suitable for use in idealized simulations, physical parameterization research, real-time data assimilation research, real-time forecasting, hurricane research, downscaling climate simulations, and coupling with other models.

The ARW dynamical core is used in this thesis. It resolves the fully compressible and non-hydrostatic dynamical Euler equations. A terrain-following vertical coordinate is used, with vertical grid stretching permitted and a constant top pressure. The nestings are available in three options: one-way interactive, two-way interactive, and moving nests. In one way nested runs, the information exchanges between the parent and the inner nests are strictly down-scale, and the inner nests do not feedback to the parent nest. Note that the microphysics variables are only used for initial conditions but not for boundary conditions in one way. In two way nested runs, all the nests run simultaneously and communicate with each other. The nest feedback impacts the solution in the parent grid domain. The moving nests are designed primarily for the hurricane tracking

simulations. Four map projections, including Lambert conformal, Mercator, Polar stereographic, and latitude-longitude (for global domain) are supported. The model state variables are staggered using an Arakawa C-grid. The WRF model provides numerous physics options, and the available choices depend on the WRF version. The major physics features and modules include the microphysical processes, the cumulus parameterizations, the surface physics, the planetary boundary layer, and the atmospheric radiation.

The WRF modeling system contains four major steps (described in Figure 2.2): WRF Preprocessing System (WPS), WRF Data Assimilation System (WRF-DA), ARW solver, and Post-processing. The first step, WPS, is responsible for defining simulation domains; interpolating time-invariant terrestrial data (e.g., terrain, land use, and soil types) on defined domains; extracting (from GRIdded Binary (GRIB) formatted) and horizontally interpolating time-varying meteorological fields (e.g., wind field, temperature, humidity, and surface pressure) on WRF model grids. The meteorological data, can be derived from several available sources (e.g., NCEP Final Analysis (GFS-FNL) (2.5° and 1°, 12 and 6 hourly) and NCEP GDAS Final Analysis (0.25°, 6 hourly)). The second step, WRF-DA, is optional and is used to assimilate observations (e.g., satellite and radar measurements) to interpolated domains from WPS to update the initial conditions when running WRF. The third step (ARW Solver) is composed of several initialization programs for idealized and realistic cases, and the numerical integration programs. In the Post-processing step, a number of tools can be used to visualize and analyze the WRF outputs, in Network Common Data Form (NetCDF) format, for example, the NCAR Graphics Command Language (NCL) and ARWpost (creating Grid Analysis and Display System (GrADS) output files). More information can be found in the WRF User's Guide.

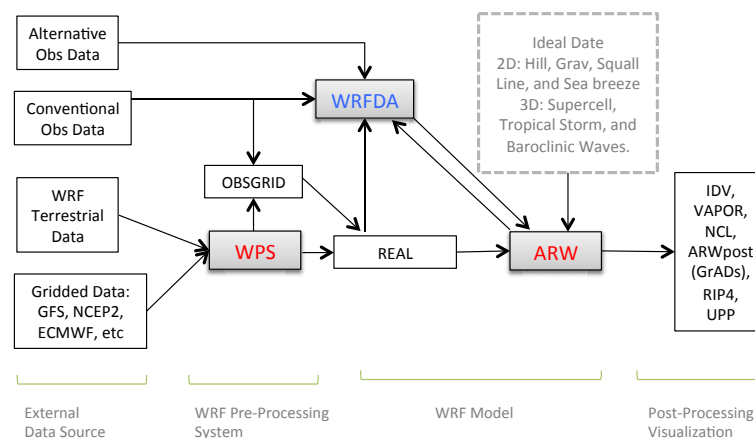


FIGURE 2.2: WRF modeling system flow chart (adapted from WRF User's Guide). IDV: Integrated Data Viewer, VAPOR: Visualization and Analysis Platform for Ocean, Atmosphere, and Solar Researchers, RIP4: Read/Interpolate/Plot, and UPP: NCEP Unified Post Processor.

2.2.2 WRF model configuration

In this thesis, the WRF (Skamarock et al., 2008) version 3.5.1 modeling system (released in April 2013) with the ARW dynamic core is used to provide realistic atmospheric and hydrometeor profiles and microphysical cloud parameters. The initial and lateral boundary conditions in WRF are obtained from NCEP FNL data every six hours on 1-degree by 1-degree grids. Two two-way interactive domains were designed for all the simulations, with 9 and 27 km horizontal grid spacing in the inner and outer domains (shown in Figure 2.3), respectively. The atmospheric fields in the inner domain with its 9 km resolution are compatible with the ICI horizontal resolution (16 km) and are used as inputs to the radiative transfer simulations. The Lambert conformal projection has been used here, since we concentrate on midlatitude cases (30° and 60° have been specified as true latitudes). 104 vertical levels are defined for the two domains from the surface to 50 hPa, with 20 levels within the lowest 2 km to better capture the characteristics of the planetary boundary layer. All the simulations were included by Noah 4-layer land surface model (Chen and Dudhia, 2001), Monin-Obukhov surface scheme (Janjic, 2002), Yonsei University (YSU) planetary boundary layer scheme (Hong et al., 2006b), Rapid Radiative Transfer Model (RRTM) longwave radiative simulation (Mlawer et al., 1997), Dudhia shortwave radiative simulation (Dudhia, 1989), and Kain-Fritsch cumulus scheme (Kain, 2004). These physics options are chosen based on the experience I gained with some mid-latitude case simulations (Wang et al., 2013, 2015).

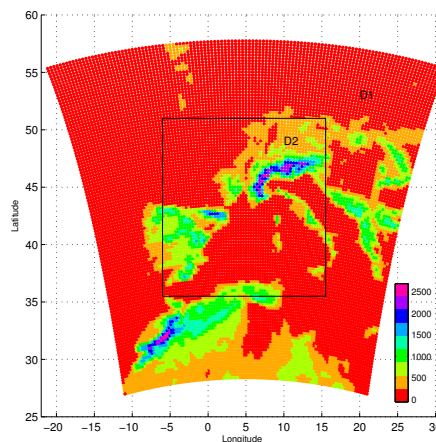


FIGURE 2.3: Terrain height (m) and WRF domain configuration for case 4 over France on December 08, 2010 at 17:00 UTC. Grid increment for Domain 1 (colored), 2 (rectangle) is, respectively, 27 km and 9 km.

The WRF configurations for the 12 selected cases are detailed in Table 2.1. The geographic location for each case is indicated as the center of the two domains. A 48-h forecast was run for each case, with spin-up time beyond 16 hours. In order to easily evaluate the radiative transfer simulation with the satellite observations in Chapter 3, the forecast fields from WRF around the Special Sensor Microwave Imager/Sounder (SSMIS) over-pass times will be analyzed and used as inputs in the radiative transfer simulations. The SSMIS observations have similar frequencies as MWI and ICI below 200 GHz, with the same geometry. This is the reason why these measurements will be used to evaluate the radiative transfer simulations performed here. Figure 2.4 presents

the rainfall rates and sea surface pressures predicted by the WRF model for the 12 cases around the SSMIS over-pass times. The exact SSMIS over-pass times for all the cases are indicated in Table 2.1. The synoptic situations of these events show a large variability including extra-tropical cyclones (e.g., cases 2 and 12), tropical-like cyclones (e.g., case 6), cold fronts (e.g., case 9), and mesoscale convective systems (e.g., case 8), with various precipitation ranges (larger in cases 6, 7, and 11, smaller in cases 4 and 5).

TABLE 2.1: The WRF model configurations and the SSMIS over-pass times for all the 12 cases. The coordinated Universal Time (UTC) is used here.

Case	C1		C2		C3		C4	
Domains	D1	D2	D1	D2	D1	D2	D1	D2
Start time	07/02/07 00:00		03/01/08 00:00		05/19/08 12:00		12/07/10 12:00	
End time	07/04/07 00:00		03/03/08 00:00		05/21/08 12:00		12/09/10 12:00	
Grid points	100×100	142×142	90×90	121×121	100×100	106×88	100×100	124×124
Center	51°N, 15°E		45°N, 23°E		44°N, 18°E		50°N, 4°E	
OBS time	07/02/07 18:13		03/01/08 17:21		05/20/08 04:52		12/08/10 16:43	
Case	C5		C6		C7		C8	
Domains	D1	D2	D1	D2	D1	D2	D1	D2
Start time	08/18/11 00:00		11/05/11 00:00		06/28/12 00:00		09/12/12 00:00	
End time	08/20/11 00:00		11/07/11 00:00		06/30/12 00:00		09/14/12 00:00	
Grid points	100×100	100×100	120×120	169×169	110×110	172×172	100×100	112×112
Center	52°N, 6°E		43°N, 5°E		55°N, 5°W		45°N, 23°E	
OBS time	08/18/11 17:00		11/05/11 17:01		06/28/12 17:15		09/12/12 16:07	
Case	C9		C10		C11		C12	
Domains	D1	D2	D1	D2	D1	D2	D1	D2
Start time	08/26/12 00:00		11/20/13 00:00		01/18/13 00:00		10/26/13 00:00	
End time	08/28/12 00:00		11/22/13 00:00		01/20/13 00:00		10/28/13 00:00	
Grid points	120×90	160×148	100×100	112×112	100×100	136×136	100×100	106×106
Center	45°N, 15°E		50°N, 2.5°E		42°N, 6°W		54°N, 5°W	
OBS time	08/26/12 16:22		11/20/13 17:05		01/19/13 07:19		10/26/13 17:28	

2.2.3 Selection of microphysical scheme in WRF

The microphysical processes in the clouds control the formation, the growth, and the interactions of liquid droplets and frozen particles (Liou and Ou, 1989). Furthermore, cloud microphysical processes interact with the macrophysics modules in the cloud model through the latent heating/cooling, the condensate loading, the surface mechanisms, and the radiative transfer processes, all very challenging to parameterize (Khain et al., 2015, Rajeevan et al., 2010). Generally, two different approaches can be used to simulate the cloud microphysical processes in the cloud models: the explicit bin-resolving method and the bulk method. The bin-resolving approach calculates explicitly the PSD, which is computationally very expensive. The bulk method predicts few moments of the PSD, which can meet the requirements of mesoscale and climate models in their computational efficiency (Khain et al., 2015).

A number of bulk microphysical schemes are available in WRF V3.5.1 to parameterize the cloud microphysical processes, including the single- and the double-moment approaches. The single-moment microphysical schemes predict the mixing ratio of each hydrometeor (Dudhia, 1989, Kessler, 1969, Lin et al., 1983, Rutledge and Hobbs, 1983), while the double-moment schemes also provide the number concentrations for some hydrometeor species (Lim and Hong, 2010, Morrison et al., 2005, Thompson et al., 2008).

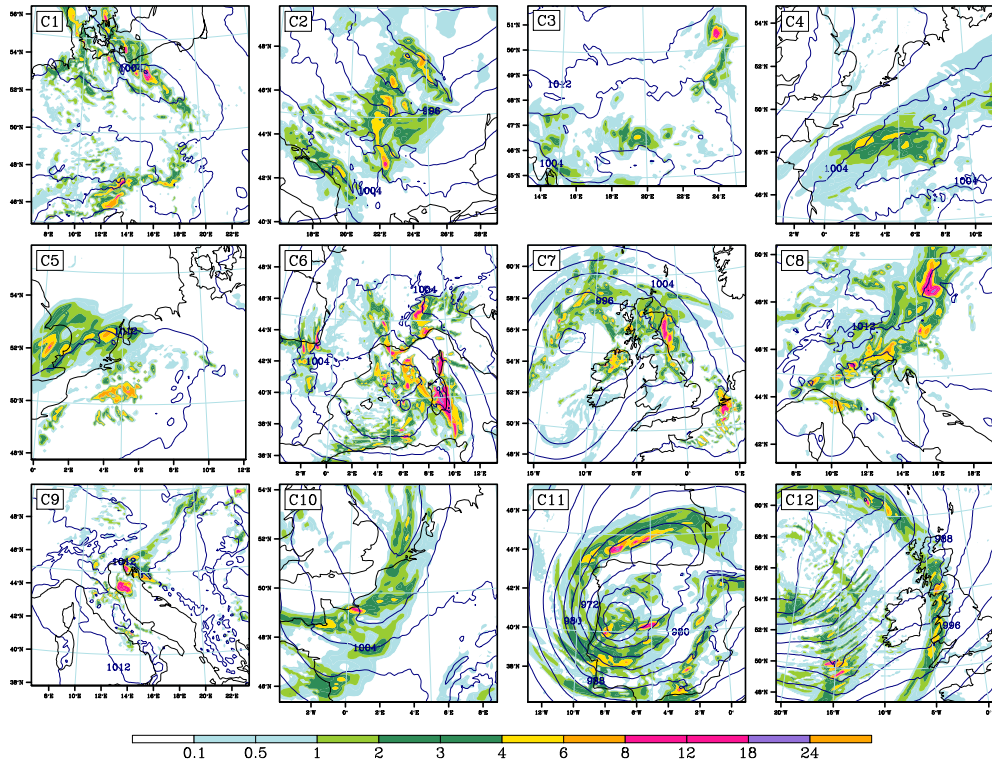


FIGURE 2.4: The surface rainfall rate (mm/h , colored) and the surface pressure (hPa , contour) for all the 12 cases around the SSMIS over-pass times in Table 2.1. The WRF outputs are given at closest full hours.

In many single- and double-moment schemes, the gamma particle size distribution is assumed:

$$N(D) = n_o D^\mu e^{-\lambda D} \quad (2.1)$$

where D is the equivalent spherical diameter (m), $N(D)$ is the number concentration (m^{-3}) of a specified hydrometeor, n_o is the intercept parameter (m^{-4}), μ is the dispersion, and λ is the shape parameter (m^{-1}). According to Marshall and Palmer (1948) and Gunn and Marshall (1958), the PSD can be simplified as an exponential distribution (given in Equation 2.2) in certain cases (e.g., for precipitating particles), by setting $\mu = 0$.

$$N(D) = n_o e^{-\lambda D} \quad (2.2)$$

The parameterizations for various microphysical schemes in WRF are specified in Table 2.2, which should a wide variety. In addition, various hydrometeor species may be predicted by using different microphysical schemes. For example, the WRF Single-Moment 6-Class Microphysics Scheme (WSM6, Hong et al., 2006a), the WRF Double-Moment 6-Class Microphysics Schemes (WDM6, Lim and Hong, 2010), and the Thompson (Thompson et al., 2008) scheme predict five types of hydrometeors, including cloud ice, snow,

rain, graupel, and cloud water, while the Milbrandt-Yau (Milbrandt and Yau, 2005) scheme can predict six hydrometeor species (hail is added). Therefore, the choice of microphysical scheme can significantly influence the predicted hydrometeor species, their contents, and their spatial distributions. As shown in Figure 2.5, the vertically integrated contents and the locations of five hydrometeors, including cloud ice, snow, rain, graupel, and cloud water, as outputs from the WRF model with different microphysical schemes are considerably different.

Generally, information about key parameters controlling the scattering properties namely the particle sizes, their densities, or their shapes, are still largely simplified in all microphysical schemes. For example, the snow density is fixed to a constant value (e.g., 100 kg/m^3) in some schemes (e.g., Hong et al., 2004, Lin et al., 1983, Morrison et al., 2009, Tao and Simpson, 1993). In cloud microphysical processes, a mass-diameter relationship is often assumed to distribute the total mass among hydrometeors of varying diameter. The mass of snow can be expressed as:

$$m(D) = aD^b \quad (2.3)$$

where a is the coefficient, and b is the exponent. Therefore, for a constant snow density (ρ), $a = (\pi/6)\rho$ and $b = 3$, even if a and b largely depend on the air temperature, the crystal structure, and the degree of rimming as indicated by Locatelli and Hobbs (1974). The interpretation of the WRF outputs with regard to the necessary parameters to feed the radiative transfer simulations is not always straightforward, and as a consequence, the choice of microphysical scheme in WRF remains challenging.

In this thesis, the WRF WSM6 (Hong and Lim, 2006) microphysical scheme has been selected after several tests: it provides robust results and runs fast enough. This scheme has been developed primarily by Lin et al. (1983) and Rutledge and Hobbs (1983). It includes a temperature dependent intercept parameter for snow, the autoconversion of cloud water to rain, and the inclusion of sedimentation of ice particles (Hong et al., 2004, Hong and Lim, 2006). The assumptions on the PSD and particle densities are described in Figure 2.6. It predicts the mixing ratios of five hydrometeors (cloud ice, snow, graupel, rain, and cloud water). The major characteristics of each hydrometeor type (e.g., PSD and density) are indicated in Table 2.2.

2.3 Radiative transfer code

Radiative transfer models are used to simulate satellite radiances for given atmospheric situations and observing conditions (i.e., frequency, polarization, and geometry). Radiative transfer models can be classified into physical (line-by-line) and fast models. Physical models calculate the absorption coefficients in details, summing up all the contributions from the different gaseous components and hydrometeors. In the fast models, such as the Radiative Transfer for TIROS Operational Vertical Sounder (RTTOV), the absorption coefficients have been parameterized as a function of atmospheric state and

TABLE 2.2: The particle size distributions (PSDs) N , the intercept parameters n_0 , the slope parameters λ , and the densities ρ of predicted hydrometeors in the WRF WSM6 (WRF Single-Moment 6-Class Microphysics Scheme, [Hong et al., 2006a](#)), WDM6 (WRF Double-Moment 6-Class Microphysics Schemes, [Lim and Hong, 2010](#)), Milbrandt ([Milbrandt and Yau, 2005](#)), Thompson ([Thompson et al., 2008](#)), and Morrison ([Morrison et al., 2005, 2009](#)) microphysical schemes. T is the air temperature in K; T_0 is the temperature of the triple point of water in K; D is the equivalent spherical diameter in m ; ρ_a is the air density in kg/m^3 ; q is the hydrometeor mixing ratio in kg/kg ; M_2 and M_3 are predicted 2nd and 3rd moments.

Scheme	Hydro	N (m^{-3})	n_0 (m^{-4})	λ (m^{-1})	ρ (kg/m^3)
WSM6	Rain	$n_0 e^{-\lambda D}$	8×10^6	$(\pi \rho n_0 / \rho_a q)^{1/4}$	1000
	Snow	$n_0 e^{-\lambda D}$	$2 \times 10^6 e^{0.12(T-T_0)}$	$(\pi \rho n_0 / 6 \rho_a q)^{1/4}$	100
	Cloud water	1×10^8			1000
	Cloud ice	$5.38 \times 10^7 (2.08 \times 10^{22} D^8)^{0.75}$			916
	Graupel	$n_0 e^{-\lambda D}$	4×10^6	$(\pi \rho n_0 / \rho_a q)^{1/4}$	500
WDM6	Rain	$\lambda^2 n D e^{-\lambda D}$	8×10^6	$(\pi \rho \Gamma(5) n / 6 \Gamma(2) \rho_a q)^{1/3}$	1000
	Snow	$n_0 e^{-\lambda D}$	$2 \times 10^6 e^{0.12(T-T_0)}$	$(\pi \rho n_0 / 6 \rho_a q)^{1/4}$	100
	Cloud water	$3 \lambda^3 n D^2 e^{(-\lambda D)^3}$		$(\pi \rho \Gamma(2) n / 6 \Gamma(1) \rho_a q)^{1/3}$	1000
	Cloud ice	$5.38 \times 10^7 (2.08 \times 10^{22} D^8)^{0.75}$			916
	Graupel	$n_0 e^{-\lambda D}$	4×10^6	$(\pi \rho n_0 / \rho_a q)^{1/4}$	500
Milbrandt	Rain	$n_0 e^{-\lambda D}$	$n \lambda^2 / \Gamma(2)$	$(\pi \rho \Gamma(4) n / 6 \Gamma(1) q)^{1/3}$	1000
	Snow	$n_0 e^{-\lambda D}$	$n \lambda^2 / \Gamma(2)$	$(\pi \rho \Gamma(4) n / 6 \Gamma(1) q)^{1/3}$	100
	Cloud water	$3 \lambda^6 n D^5 e^{(-\lambda D)^3}$	$n \lambda^2 / \Gamma(2)$	$(\pi \rho \Gamma(5) n / 6 \Gamma(2) q)^{1/3}$	1000
	Cloud ice	$n_0 e^{-\lambda D}$	$n \lambda^2 / \Gamma(2)$	$(440 \Gamma(4) n / \Gamma(1) q)^{1/3}$	500
	Graupel	$n_0 e^{-\lambda D}$	$n \lambda^2 / \Gamma(2)$	$(\pi \rho \Gamma(4) n / 6 \Gamma(1) q)^{1/3}$	400
	Hail	$n_0 e^{-\lambda D}$	$n \lambda^2 / \Gamma(2)$	$(\pi \rho \Gamma(4) n / 6 \Gamma(1) q)^{1/3}$	900
Thompson	Rain	$n_0 e^{-\lambda D}$	$(9 \times 10^9 - 2 \times 10^6) \tanh((10^{-4} - q) \times 4 \times 10^4) / 2 + (9 \times 10^9 - 2 \times 10^6) / 2$		1000
	Snow	$M_2^4 / M_3^3 (490.6 e^{-20.78 M_2 D / M_3} + 17.46 e^{(-3.29 M_2 D / M_3)(M_2 D / M_3)})$			
	Cloud water				1000
	Cloud ice	$n_0 e^{-\lambda D}$			890
	Graupel	$n_0 e^{-\lambda D}$	$\max(10^4, \min(200/q, 5 \times 10^6))$		400
Morrison	Rain	$n_0 e^{-\lambda D}$	$n \lambda / \Gamma(1)$	$(\pi \rho \Gamma(4) n / 6 \Gamma(1) q)^{1/3}$	1000
	Snow	$n_0 e^{-\lambda D}$	$n \lambda / \Gamma(1)$	$(\pi \rho \Gamma(4) n / 6 \Gamma(1) q)^{1/3}$	100
	Cloud water	$n_0 D^\mu e^{-\lambda D}$	$n \lambda^{\mu+1} / \Gamma(\mu+1)$	$(\pi \rho \Gamma(\mu+4) n / 6 \Gamma(\mu+1) q)^{1/3}$	1000
	Cloud ice	$n_0 e^{-\lambda D}$	$n \lambda / \Gamma(1)$	$(\pi \rho \Gamma(4) n / 6 \Gamma(1) q)^{1/3}$	1000
	Graupel	$n_0 e^{-\lambda D}$	$n \lambda / \Gamma(1)$	$(\pi \rho \Gamma(4) n / 6 \Gamma(1) q)^{1/3}$	400

observing conditions. The physical models are more computationally expensive than fast models. Fast models are used in Numerical Prediction Centers where large amount

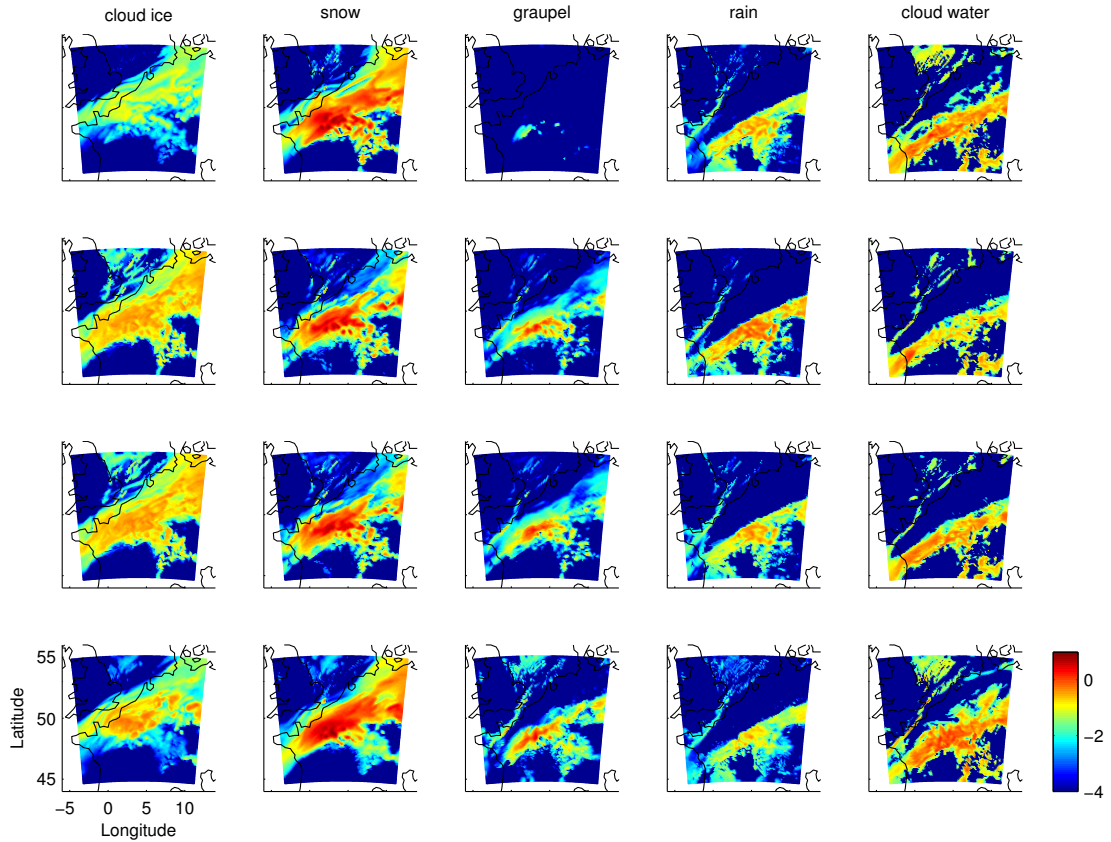


FIGURE 2.5: Vertically integrated contents of cloud ice, snow, graupel, rain, and cloud water as simulated by WRF with four different microphysical schemes (Morrison scheme in first row, WDM6 in second row, WSM6 in third row, and Milbrandt–Yau fourth row), for case 4 over France on December 08, 2010 at 17:00 UTC. The colorbar shows in the log₁₀ of the vertically integrated content in kg/m^2 .

of satellite radiances have to be simulated in their data assimilation systems. For new instruments and for research purposes, line-by-line models such as ARTS (Buehler et al., 2005, Eriksson et al., 2011) are chosen.

2.3.1 Description of ARTS

ARTS version 2.2 (Eriksson et al., 2011), a very flexible tool and line-by-line model, can be used to solve the radiative transfer equation with different atmospheric conditions and sensor configurations for full Stokes vector. As a freely available software program, ARTS concentrates on simulating full 3D atmospheric thermal radiation for both microwave and infrared spectral ranges (Buehler et al., 2006, John et al., 2006) in any planetary atmosphere. It was used initially for analyzing the ground-based and the satellite-based sensors in the millimeter and sub-millimeter spectral ranges (Buehler et al., 2007a, John and Buehler, 2004, 2005).

Description of the atmosphere In ARTS, the atmosphere can be described in 1D, 2D, and 3D, which stands for different complexities in radiative transfer simulations.

quantities (e.g., temperature and water vapor) only vary as a function of pressure. Correspondingly, the radial coordinate is used to deal with the atmospheric profiles. The 2D atmosphere is mostly defined inside the orbit plane, and the atmospheric components follow linear variations in both pressure levels and latitude grids. More generally and realistically, the atmosphere is constructed in 3D as in the real nature (Figure 2.7). For this situation, spherical coordinates are adopted, including radius, latitude, and longitude grids. The ranges of latitude and longitude are from -90° to 90° and from 0° to 180° , respectively. Note that the atmospheric quantities vary following the equal pressure levels in ARTS.

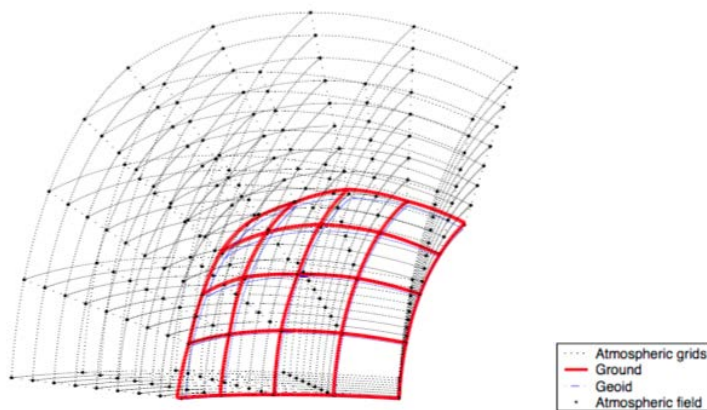


FIGURE 2.7: Schematic of a 3D atmosphere in ARTS. Radii and fields are here defined to vary linearly along the latitude and longitude grid points. This means that the radius of a pressure level has a bi-linear variation inside the area limited by two latitude and longitude grid values, while the atmospheric fields have a tri-linear variation inside the grid cells (from ARTS User's Guide).

Sensor characteristics In ARTS, the observation geometry is very flexible: ARTS can take into account and incorporate different observation geometries (including scanning feature) and sensor characteristics efficiently. It can handle different measurements, such as ground-based, down looking, limb sounding, and balloon/aircraft measurements. In the code, both the observed locations and the viewing directions have to be specified. The former is expressed by the geometrical altitude, latitude, and longitude. The latter is described by zenith and azimuth angles. Notice that only for 3D cases, we have to set up both zenith and azimuth angles, because the azimuth angle does not exist in 1D and 2D atmospheres.

Surface properties In ARTS, the surface is described by the lowest boundary of the indicated atmosphere in the simulations, and is defined by the geometrical altitude. As default, the surface is considered as a sphere in all the dimensions. However in the 2D and 3D assumptions, the surface can be arbitrary shaped under a complete reference ellipsoid.

Gas absorption ARTS can provide the absorption matrix at each point for the next step in the radiative transfer simulation. There are two available options in ARTS for

the absorption coefficient calculation: making an explicit line-by-line calculation or using predefined complete absorption models (e.g., [Liebe and Layton, 1987](#), [Rosenkranz, 1998a,b](#)). The line-by-line calculation means that the gas absorption has to be calculated at each point along the propagation path, resulting in a more accurate but computationally expensive computing process ([Sreerekha et al., 2002](#)).

Scattering radiative transfer solvers ARTS handles scattering atmospheres with two modules: the Discrete Ordinate Iterative (DOIT, [Emde et al., 2004](#)) method, and the reverse Monte Carlo (MC, [Davis et al., 2005](#)) method, with a full and efficient account of polarization effects. The DOIT algorithm is strongly recommended in the 1D particle scattering calculation. To save computation resources, the scattering radiative transfer calculations are confined only to the region of the atmosphere of interest for the scattering mechanisms (called the 'cloudbox' in ARTS). All the hydrometeors should be contained in this region. This method is presented in detail in ARTS User's Guide and [Emde et al. \(2004\)](#). This method is used in this thesis in Chapter 5. For the polarized radiative transfer simulations for 3D scenarios, ARTS-MC algorithm appears to be the best approach and it calculates the scattering efficiently. The computational effort concentrates on the calculation of the Stokes vector at the indicated location in the indicated direction. For further information, please refer to the ARTS User's Guide and to [Davis et al. \(2007\)](#). In the calculations in Chapters 2, 3, and Appendix A, ARTS-MC method is adopted, with complex 3D geometry. Until recently, ARTS was mostly used for the simulation of pristine small ice crystals that characterize cirrus clouds.

2.3.2 Particle scattering calculation

The scattering properties of the hydrometeors depend on:

- their dielectric properties that depend in turn on their phases (liquid or frozen), on their densities, and on their temperatures;
- their size distributions;
- their shapes;
- their orientations.

All this information is clearly not available from the cloud resolving models, and assumptions will have to be made to calculate the single scattering properties (SSPs) of the hydrometeors.

2.3.2.1 Particle dielectric property

The dielectric properties strongly affect the SSPs. They directly depend upon the molecular structure of the medium. The relative refractive index m is the square root of the complex dielectric permittivity ε :

$$m = \sqrt{\varepsilon} = \sqrt{\varepsilon' - i\varepsilon''} \quad (2.4)$$

The real part of the complex dielectric permittivity ε' is associated with the characteristics of the electric field polarization and anomalous dispersion, while the imaginary part ε'' links to the absorption of the electromagnetic waves.

According to Snell's Law (Equation 2.5), when microwaves move from one medium to another, they change direction. Therefore, the relative refractive index effects on the propagation of microwaves between two media, and can be expressed as $m = m_1/m_0$, where m_1 is the complex refractive index and m_0 is the surrounding medium index. Generally, in the Earth atmosphere, $m_0 = 1$. So m is regarded as the complex refractive index m_1 .

$$m_1 \sin \theta_1 = m_2 \sin \theta_2 \quad (2.5)$$

where m_1 and m_2 are the refractive indices of two media, and θ_1 and θ_2 are the corresponding angles of incidence and refraction.

Liquid water particles The refractive index for liquid water in the microwave has been well studied. It changes as a function of temperature and frequency. In this thesis, the complex dielectric properties of liquid water are calculated with the parameterization from Liebe et al. (1991). It provides the dielectric constants of liquid water between 100 GHz and 30 THz at atmospheric temperatures. In Figure 2.8, the frequency dependencies of the real and imaginary parts of the complex dielectric property of water are shown. The dielectric property of pure water decreases with increasing frequency, and then stabilizes in the millimeter range.

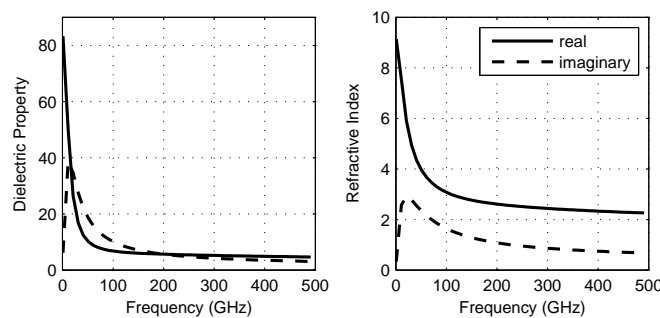


FIGURE 2.8: The real and imaginary parts of the dielectric property (left) and the refractive index (right) of pure liquid water from Liebe et al. (1991) at 10°C as a function of frequency.

Pure ice particles For the pure ice particles, the Matzler (2006) model is generally suggested to calculate their dielectric properties at temperatures between 20.0 and 273.15 K for the frequency range between 0.01 and 3000 GHz (Eriksson et al., 2015). Figure 2.9 presents the refractive indices of ice as a function of frequency at 0°C, -10°C,

and -20°C , respectively. The real part of the refractive index remains fairly constant over the microwave range, while the imaginary part of the refractive index increases with frequency. The imaginary part of the refractive index of ice is smaller than for liquid water. Therefore ice is more transparent at microwave frequencies, with lower dielectric loss.

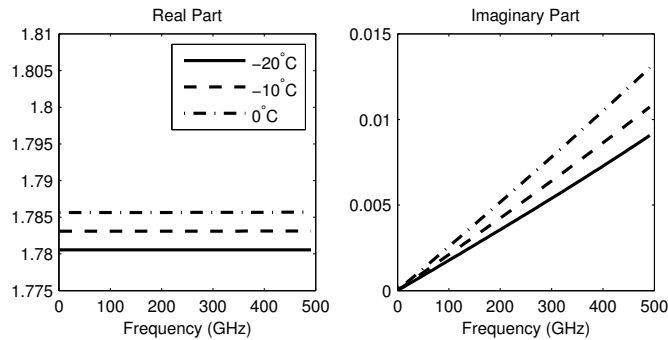


FIGURE 2.9: The real and imaginary parts of the refractive indices of pure ice from Matzler (2006) at 0°C , -10°C , and -20°C as a function of frequency.

Mixed-phase particles Compared to pure ice and liquid water, the dielectric property of the mixed-phase hydrometeor is not well understood and still needs to be further studied. The uncertainties in the dielectric property calculations for the mixed-phase hydrometeor highly impact the SSP calculation. The mixed-phase hydrometeors, including snow, graupel, and hail, are generally assumed as mixtures of different components (e.g., ice-air or ice-air-water). Here, dry snow is composed of an air core with ice inclusions, as described by (Gherboudj et al., 2010), while particles with water embedded in dry snow are defined as wet snow (Battaglia et al., 2003, Fabry and Szyrmer, 1999). The mixed-phase hydrometeors can be represented by a single effective medium, and their effective dielectric properties, determined strongly by the density, can be described by mixing rules (e.g., Bruggeman, 1935, Debye, 1929, Garnett, 1906, Sihvola, 2000). There are many different mixing rules, but the selection of one is not obvious, leading to uncertainties in radiative transfer simulations (Liao and Meneghini, 2005). Among these different mixing rules, the Maxwell-Garnett formula (Garnett, 1906), with respect to the roles of the background matrix and the inclusions, has been commonly suggested (e.g., Battaglia et al., 2003, Olson et al., 2001a,b) and is used in this thesis.

The Maxwell-Garnett formula can be expressed as:

$$\varepsilon_{eff} = \varepsilon_e + 3f\varepsilon_e(\varepsilon_i - \varepsilon_e)/(\varepsilon_i + 2\varepsilon_e - f(\varepsilon_i - \varepsilon_e)) \quad (2.6)$$

where ε_e and ε_i are the dielectric permittivities of surrounding and inclusion. $f = nV$ is the dimensionless volume fraction of the inclusions in the mixed-phase particle. V is the volume of spherical inclusions and n is the number density. To calculate the dielectric property of the mixed hydrometeor, the dimensionless volume fraction f is expressed as a function of the densities of its components, with different variations in the definition of its inclusions and matrix (Bohren and Battan, 1982, Klaassen, 1988). For the dry snow, the volume fraction f can be defined as $f = \rho_s/\rho_i$, where ρ_s is dry snow density

and ρ_i is the pure ice density. For the wet snow, the volume fraction f can be given as

$$f = \frac{\rho_s \rho_w - \rho_m \rho_w}{\rho_s \rho_m - \rho_m \rho_w} \quad (2.7)$$

where ρ_m and ρ_w are the densities of wet snow and water, respectively. As mentioned above, snow particles can be defined as a 2-component (dry snow, consisting of air and ice) or 3-component mixture (wet snow, consisting of air, ice, and water). For the wet snow, the Maxwell-Garnett formula should be applied twice, for air and ice first and then for dry snow and liquid water. Figure 2.10 presents the dielectric properties of two types of dry snowflakes (air core surrounded by ice and ice core surrounded by air) calculated with the Maxwell-Garnett formula at 0°C at 157, 344, and 664 GHz. The snowflake density is from Mitchell et al. (1990) (specified in Table 2.4). The real parts are related to the particle density (independent on frequency), while the imaginary parts are a function of temperature, frequency, and density. Note that the differences in imaginary parts of the dielectric properties at different frequencies are larger for smaller and denser particles than for larger and lighter particles. In addition, the results can be very different when we change the order of the inclusion and the background. The dry snowflakes with air core surrounded by ice have stronger dielectric properties. Therefore, the snow density is a key parameter to control its dielectric property, with the dielectric property of snow being a weighted average of the dielectric properties of its components.

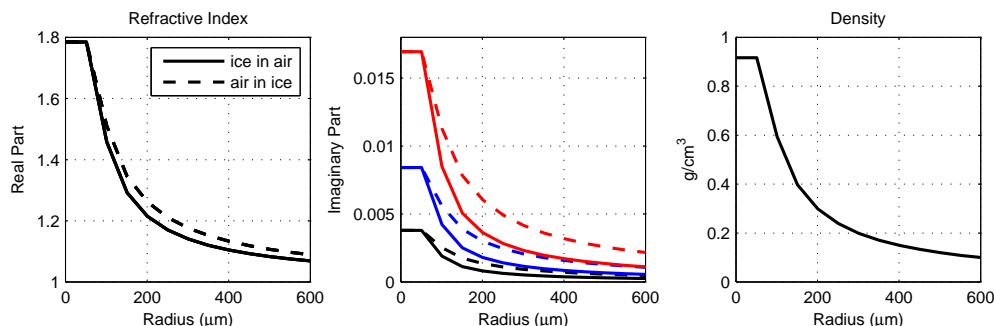


FIGURE 2.10: The real and imaginary parts of the refractive indices of dry snowflake calculated by the Maxwell-Garnett formula at 0°C at 157 GHz (black), 344 GHz (blue), and 664 GHz (red) as a function of particle size. The snowflake density is from Mitchell et al. (1990) ($\rho = 0.012D_s^{-1}$, in cgs units). The snowflake is defined as a mixture of two components (i.e., ice and air) in two different ways (i.e., air core surrounded by ice and ice core surrounded by air). The refractive index of pure ice is calculated with Matzler (2006).

Many experiments and studies investigate the snowflake density (e.g., Locatelli and Hobbs, 1974, Magono and Nakamura, 1965, Mitchell et al., 1990), and the results show that the snowflake density varies considerably depending on the crystal habit, decreasing with increasing particle size (as shown in Figure 2.11). Even if some snow parameterizations have a stronger physical justification than others, difficulty still exists in the determination of the most appropriate one, due to the lack of reliable long term data to evaluate the model results. Magono and Nakamura (1965) found that the density of dry snow is roughly proportional to D^{-1} , while the density of the wet snow is roughly proportional to $D^{-1.5}$. In addition, the inner part of the snowflake is probably denser

than its outer part, making it reasonable to consider the snow particle with a continuous varying density from a density close to pure ice in the inner part to a density close to the air in the outer part.

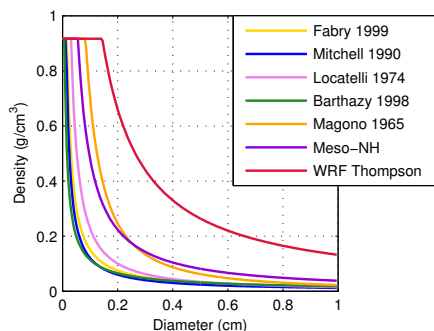


FIGURE 2.11: Different snow densities from different literatures (shown in Table 2.4). The snow densities from two cloud resolving models (WRF with Thompson microphysical scheme and Méso-NH) are also presented as comparison.

TABLE 2.4: Density parameterizations of snow from the literatures and two cloud resolving models (in cgs units), D is the real diameter of the snowflake.

Parameterization	Reference
$\rho = 0.015D^{-1}$	Fabry and Szyrmer (1999)
$\rho = 0.012D^{-1}$	Mitchell et al. (1990)
$\rho = 0.015D^{-1.18}$	Locatelli and Hobbs (1974)
$\rho = 0.018D^{-0.8}$	Barthazy (1998)
$\rho = 0.022D^{-1.5}$	Magono and Nakamura (1965)
$\rho = 0.038D^{-1.1}$	Méso-NH (Pinty and Jabouille, 1998)
$\rho = 0.132D^{-1}$	WRF Thompson (Thompson et al., 2008)

2.3.2.2 The methods for calculating the particle scattering

Spherical particles For coated or concentrically layered spheres, the Lorenz-Mie theory or Lorenz-Mie-Debye theory with fast numerical computations, is employed to describe exactly and analytically the interaction between the electromagnetic radiation and the particles. This theory, named after its developer Gustav Mie, is an analytical solution of Maxwell's equations for the electromagnetic radiation scattering in terms of infinite series. The Mie code provides the absorption, scattering, and extinction cross sections, for a given frequency, particle size, and dielectric property. Here the absorption/scattering cross section, in unit of area, is quantity describing how much incident radiation is absorbed from/scattered to all directions by the particles. The extinction cross section represents the total losses of energy from the incident beam due to both absorption and scattering, which is defined as the sum of the absorption and scattering cross sections. In this thesis, the SSPs of the hydrometeors will be calculated using the Mie theory for spherical particles except for snow, for the reason that the Mie calculation has shown limitations (Galligani et al., 2015, Kulie et al., 2010) with the difficulty to account for the 'soft' nature of the particles (Liu, 2004). For liquid particles (cloud water and rain), and for frozen particles such as cloud ice and graupel, these assumptions have proved realistic (Kulie et al., 2010, Meiold-Mautner et al., 2007).

Non-spherical particles The T-matrix method has been developed by [Mishchenko et al. \(2002\)](#), to efficiently calculate the SSPs for spheroids, cylinders, and horizontally aligned particles. It requires particle dielectric property, maximum particle diameter (D_{max}), particle shape, aspect ratio (the ratio of the largest diameter over the smallest diameter), and frequency as inputs. Figure 2.12 gives the scattering (C_{sca} , in m^2), absorption (C_{abs}), and extinction (C_{ext}) cross sections from the T-matrix code for pure ice particles (aspect ratio = 1.6) at seven different frequencies as a function of mass-equivalent particle radius r_e . Here the C_{sca} or C_{abs} can be interpreted as the effective area of a particle presented to the incident beam, leading to some of the beam being absorbed from or scattered into other directions. The C_{ext} is defined as the amount of electromagnetic energy which becomes extincted over the incoming electromagnetic flux intensity ([Knoll, 2010](#)), caused by both scattering and absorption of the electromagnetic energy, therefore:

$$C_{ext} = C_{sca} + C_{abs} \quad (2.8)$$

For ice particles of a given radius, scattering increases with increasing frequency (and decreasing wavelength). The scattering efficiency depends upon the ratio between the particle size and the wavelength. For liquid particles, absorption contributes largely to the extinction (with high absorption cross section, not shown here).

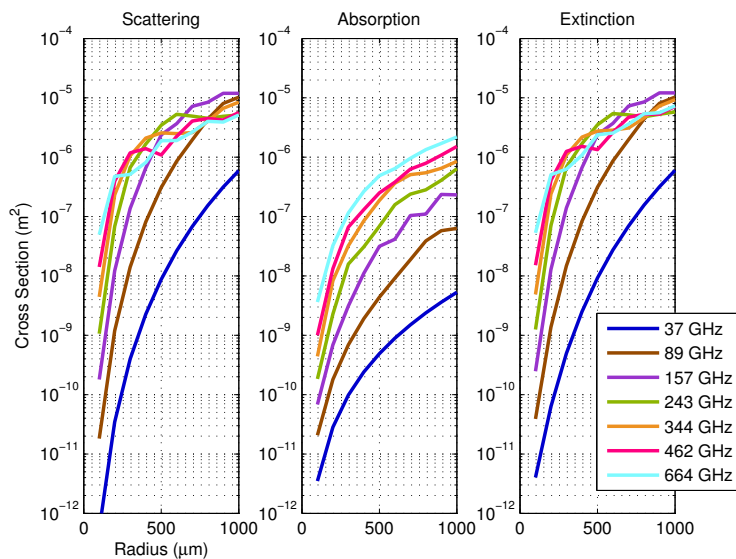


FIGURE 2.12: The absorption, scattering, and extinction cross sections for spheroid ice particles (aspect ratio = 1.6) at frequencies from 37 to 664 GHz calculated by the T-matrix code as a function of mass-equivalent particle radius.

For particles of arbitrary shapes and complex geometries, a more complex model, the Discrete Dipole Approximation (DDA), has been widely investigated to calculate the SSPs of frozen particles (e.g., [Evans and Stephens, 1995](#), [Hong, 2007](#), [Kim, 2006](#), [Okamoto, 2002](#)). The basic idea of the DDA was introduced by [DeVoe \(1964, 1965\)](#) for the study of scattering properties of molecular aggregates. Then [Draine and Flatau \(1994\)](#) developed the DDA model for the calculation of the frozen particle SSPs. In the DDA

model, a particle can be represented by an array of dipoles in a cubic lattice with an adequately small inter-dipole spacing with respect to the incident wavelength, in order to obtain the desired accuracy. However, the DDA calculations are very time consuming and expensive computationally, especially for large particles. Several pre-computed DDA databases for frozen particles of different shapes are available (e.g., [Hong et al., 2009](#), [Liu, 2008](#), [Nowell et al., 2013](#)), which can be incorporated directly into the radiative transfer models (e.g., ARTS and RTTOV). The main characteristics of these three databases are summarized in Table 2.5.

TABLE 2.5: The frozen particle habits, D_{max} , range of equal-mass sphere radius, the coefficient a , the exponent b of the Liu, Hong, and Nowell DDA databases (SI units). L is the particle length and d is the hexagonal diameter (distance between opposite vertices).

Database	Particle habits	D_{max} (μm)	Radius (μm)	a	b
Liu	Long column ($L/d = 4$)	121-4835	25-1000	37.09	3
	Short column ($L/d = 2$)	83-3304	25-1000	116.12	3
	Block column ($L/d = 1$)	66-2632	25-1000	229.66	3
	Thick plate ($L/d = 0.2$)	81-3246	25-1000	122.66	3
	Thin plate ($L/d = 0.05$)	127-5059	25-1000	32.36	3
	3-bullet rosette	50-10000	19-1086	0.32	2.37
	4-bullet rosette	50-10000	19-984	0.06	2.12
	5-bullet rosette	50-10000	21-1058	0.07	2.12
	6-bullet rosette	50-10000	21-1123	0.09	2.13
	Sector snowflakes	50-10000	25-672	0.002	1.58
Dendrite snowflakes	75-12454	33-838	0.01	1.9	
Hong	Hexagonal solid column	2-2000	0.74-283.39	0.03	2
	Hollow column	2-2000	0.85-310.88	0.02	2
	Hexagonal plate	2-2000	0.90-897.65	0.75	2.47
	6-branch bullet rosette	2-2000	0.84-307.98	0.18	2.34
	Aggregate	2-2000	1.07-344.21	65.45	3
	Droxtal	2-2000	0.51-514.72	347.31	3
Nowell	200 μm 6-bullet rosette	200-8864	65-1219		
	400 μm 6-bullet rosette	200-10701	65-1327		
	200 and 400 μm 6-bullet rosettes	200-12584	65-1124		

We firstly introduce the Liu database ([Liu, 2008](#)), in which the SSPs have been computed for eleven ice particle types, including columns, plates, rosettes, and snowflakes, at 22 frequencies from 3 to 340 GHz. All frozen particles are assumed to be randomly oriented. The ice refractive indices are taken from [Matzler \(2006\)](#) at five temperatures from 233.15 to 273.15 K. In addition, two types of snowflakes, sector-like and dendrite, are defined in the Liu database. The difference between the two types of snowflakes is that the ice volume is concentrated on six main branches in the sector-like snowflakes, while it spreads more uniformly in the basal plane in the dendrite snowflakes, leading to a much lower density (as shown in Figure 2.14). Liu database contains the absorption cross section C_{abs} , the scattering cross section C_{sca} , the backscattering cross section C_{bac} , the asymmetry parameter g , and the phase function $P(\cos(\theta))$, where θ is the scattering angle (the angle between incident and observing directions). C_{bac} describes the scattered energy in the opposite direction of the incident radiation; $P(\cos(\theta))$ is defined to describe the angular distribution of the scattered energy, and is given in 37 equally spaced directions between 0° and 180° ; g represents the degree of symmetry of

the scattered energy distributed with respect to the plane dividing forward and backward hemispheres.

The other DDA database, Hong database (Hong et al., 2009), has been generated to provide the SSPs (i.e., the extinction efficiency Q_{ext} , the absorption efficiency Q_{abs} , the single-scattering albedo, the asymmetry parameter g , and the scattering phase matrix P) for six non-spherical frozen habits (hexagonal solid column, hollow column, hexagonal plate, 6-branch bullet rosette, aggregate, and droxtal) ranging from 2 to 2000 μm in D_{max} at 21 frequencies from 89 to 874 GHz. The ice refractive index is taken from Warren (1984) at a temperature of 243.15 K. Here, Q_{ext}/Q_{abs} is defined as the ratio of a particle's extinction/absorption cross section (C_{ext}/C_{abs}) to the geometrical cross section of the equal-mass spherical particle and is expressed as:

$$Q_{ext} = \frac{4C_{ext}}{\pi D_e^2} \quad (2.9)$$

$$Q_{abs} = \frac{4C_{abs}}{\pi D_e^2} \quad (2.10)$$

where D_e is the mass equivalent diameter. The particles are randomly oriented in this database, and the scattering phase matrix P contains six independent matrix elements ($P_{11}, P_{12}, P_{22}, P_{33}, P_{34}, P_{44}$). The detailed definitions of these six habits can be found in Hong et al. (2009).

Based on the work of Liu (2008), a new snowflake aggregation model has been developed to calculate the SSPs for aggregate snowflakes by Nowell et al. (2013), with D_{max} between 200 and 800 μm . The bullet rosettes have been used as the basis for the aggregate flakes, considering their common presence in the upper level of clouds, especially in cirrus clouds (Arnott et al., 1994, Field and Heymsfield, 2003, Heymsfield and Iaquinta, 2000, Heymsfield et al., 2002). The average numbers of bullets in the rosettes are 5.8 ± 0.6 (about 6), so 6-bullet rosettes have been used to generate the aggregate flakes here. The DDA calculation has been performed for ten frequencies from 10.65 to 183.31 GHz. The ice refractive index is derived from Matzler (2006) at a temperature of 263.15 K. This database will not be considered in the following comparisons and analysis, because the phase function that is essential in the radiative transfer simulations is not included.

Figure 2.13 presents the absorption efficiency Q_{abs} , the scattering efficiency Q_{sca} , and the asymmetry parameter g for some particles in the three DDA databases at 94 GHz, as a function of the particle size parameter x . The size parameter x , a dimensionless quantity which can be used to identify the scattering regimes, is defined as:

$$x = 2\pi r/\lambda \quad (2.11)$$

where r is the particle radius and λ is the wavelength. Only long columns, thick plates, 6-bullet rosette, sector snowflakes, and dendrite snowflakes in the Liu database are shown and discussed here. For comparison, the SSPs calculated with the Mie code assuming either an equal-mass solid sphere and two low-density spheroids (referred to

as soft spheroids, with volume fractions (f) of 0.82 and 0.35) are also presented. The ice refractive index is derived from Matzler (2006). The differences on Q_{abs} , Q_{sca} , and g between different databases increase with size parameter, which is related to various particle shapes. For $x < 0.5$, there is a good agreement between the particle types, while for $x > 1$, different types of particles show quite different behaviors. The Hong database has systematically a larger Q_{abs} than the Liu database, which is expected as a result of the higher imaginary part of the refractive index in Warren (1984) (for Hong) compared to Matzler (2006) (for Liu) below 400 GHz (Eriksson et al., 2015). There are considerable spreads in the g for $x > 0.5$. However, the variation in Q_{sca} for $x < 1$ is not evident, which can be explained by the fact that the Q_{sca} depends on the integrated P in all the directions, which is less sensitive to the particle shape.

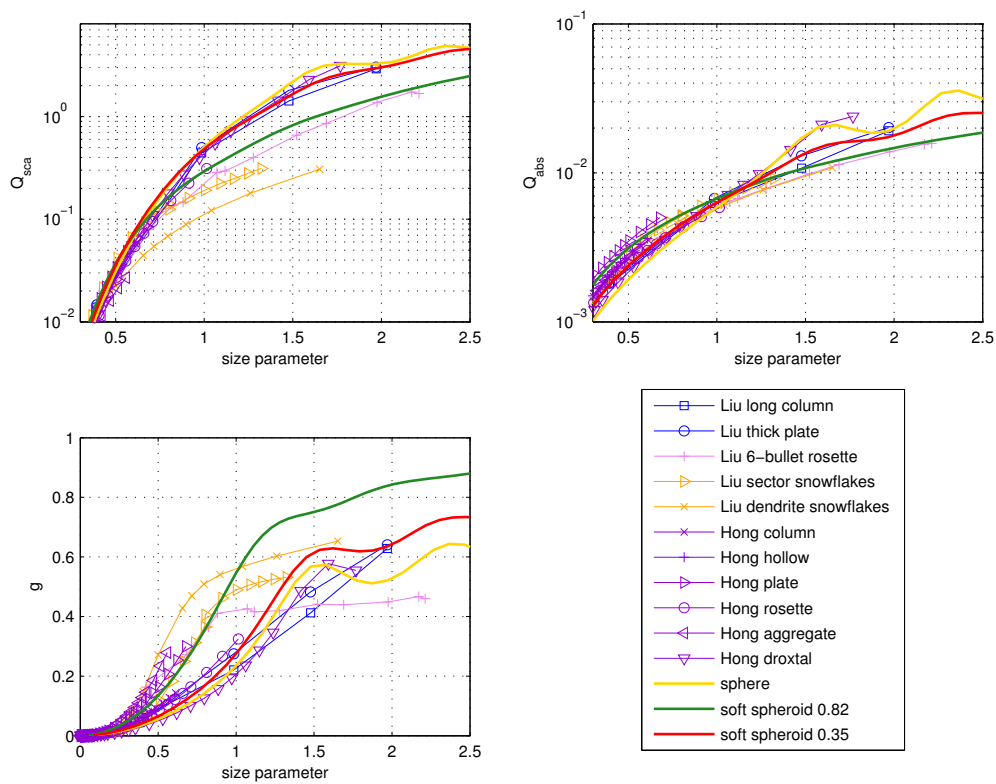


FIGURE 2.13: The absorption efficiency Q_{abs} , the scattering efficiency Q_{sca} , and the asymmetry parameter g for some particles in the three DDA databases at 94 GHz, as a function of the particle size parameter x . For comparison, the SSPs of an equal-mass solid sphere and two low-density spheroids (referred to as a soft spheroids, with volume fractions of 0.82 and 0.35) are also shown.

2.3.2.3 Compatibility of the particle characteristics simulated in the DDA databases with the WRF model

Uncertainties in the description of the physical properties of the frozen particles (e.g., particle size, density, and shape) can lead to large uncertainties in the simulated brightness temperatures, and consequently large discrepancies with the satellite observations. Therefore, the idea is to use more realistic snow SSPs, instead of the ones calculated by the Mie code or the T-matrix method. Are the DDA hypotheses compatible with the

cloud resolving model parameterization? Here, we test the compatibility of the hypotheses adopted in the DDA calculations and in the cloud resolving model. Comparisons of snow particle densities and particle sizes from the DDA databases and the WRF WSM6 scheme are performed, on account of their key roles in the SSP calculations.

Density is a key parameter that directly controls the dielectric properties and thus the scattering properties of the frozen particles. The snow particle densities in the WSM6 scheme and in the DDA databases are compared in Figure 2.14, as a function of the particle maximum diameter (D_{max}). According to the mass-diameter relationship (Equation 2.3) for frozen particles, parameters a and b control the particle mass, hence control the relationships between the D_{max} and the particle density. The snow density in Figure 2.14 shows a considerable variability depending on the particle type. For several particle habits (e.g., Hong column, Hong rosette, Liu bullet rosettes, Liu sector snowflakes, and Liu dendrite snowflakes), they have size-dependent densities (the density decreases with the particle size). However, for the other particle habits (e.g., Hong aggregate, Liu block column, and Liu thick plate), the density keeps constant when particle size changes. The density of Hong aggregates is closer to the one given in the WRF WSM6 scheme, providing more consistency with the cloud resolving model outputs.

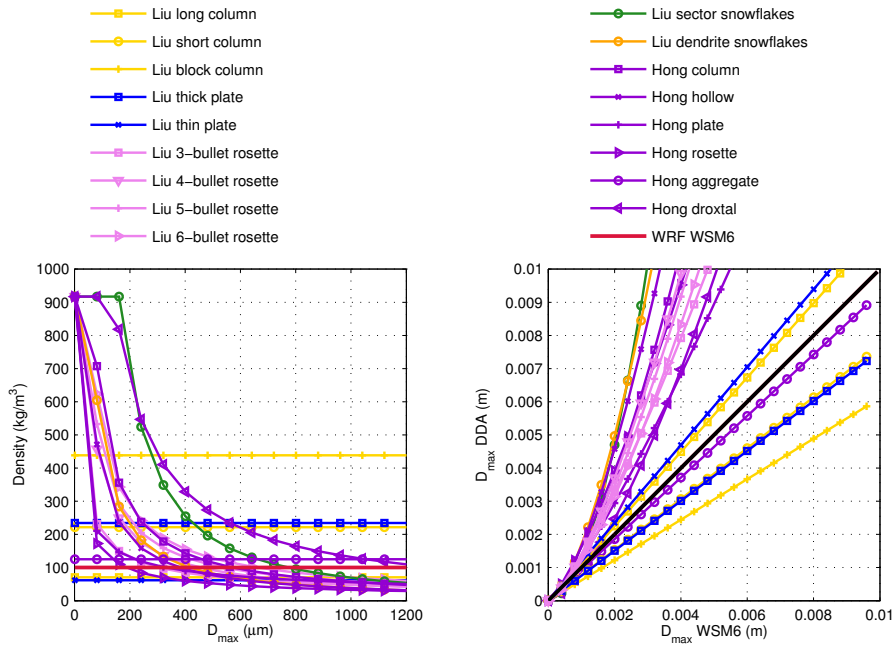


FIGURE 2.14: Left: Particle densities derived from Liu and Hong DDA databases and WRF WSM6 scheme as a function of particle D_{max} . Right: Comparison between the particle D_{max} from DDA databases and the one from WRF WSM6 scheme under the same particle mass.

To further investigate the consistency between the WRF WSM6 scheme and the DDA databases, the relationships between the D_{max} in different databases are also presented in Figure 2.14. It reveals that the D_{max} of the Hong aggregate matches better the one from the WRF WSM6 scheme. This database has already been selected by Eriksson et al. (2015) for its better performances as compared to other DDA databases and also has

the advantage of providing SSPs at frequency range from 89 to 874 GHz. At lower MWI frequencies, the SSPs for snow are calculated with the Mie theory under the assumption of spheres, with the scattering becoming negligible in this frequency range.

2.3.3 Surface emissivity

Satellite observations from microwave radiometers can be affected by the surface contribution at frequencies where the atmospheric opacity is limited (i.e., at low frequencies and in window channels). With increasing frequencies, the atmosphere becomes gradually more opaque due to the increase in the continuum absorption from some species. However, under dry and cold atmospheric conditions (in polar and sub-polar regions), the higher frequencies are still sensitive to the surface (Wang et al., 2016). Therefore, it is important to accurately represent the surface emissivity for the quantification of the contribution of the surface emission in the microwave region, even at high frequencies. To simulate accurately the radiative transfer processes for the real scenes, an accurate representation of the surface properties is necessary. ARTS can only handle surface emissivities for three types of surfaces, including blackbody surfaces, specular surfaces, and Lambertian surfaces (an ideal scattering rough surface). In this thesis, two surface emissivity models (TELSEM² and TESSEM²) are used to provide realistic surface emissivities to ARTS up to 664 GHz over land and sea, separately.

2.3.3.1 Sea surface emissivity calculation

Over open water, the emissivity varies with surface wind speed and direction, sea surface properties, and salinity. Assuming a flat specular ocean surface, the emissivity can be calculated from the Fresnel equation (Born and Wolf, 1980) for different incidence angles and orthogonal polarizations. As the surface wind speed increases, wave development increases, and the sea surface becomes rough. Two-scale surface roughness effects (the large-scale and the small-scale) should be considered. The large-scale waves can be handled by geometric optics approach, and the small-scale roughness related to ripples should be added. In addition, above a certain wind speed, foam emissivity cannot be neglected. Microwave sea emissivity modeling has advanced significantly over the last decades (English, 2006). A number of emissivity models have been developed for both scientific research and for operational codes (Boukabara et al., 2002, English and Hewison, 1998, Guissard et al., 1992, Prigent and Abba, 1990, Stogryn, 1967, Wentz, 1983, Wilheit, 1979), however they only can calculate the surface emissivity for frequencies up to 200 GHz.

During this thesis, TESSEM² (Prigent et al., 2016) has been developed by LERMA and is used to calculate the sea surface emissivities up to 700 GHz, with the required inputs. TESSEM² is a parameterization of the sea surface emissivity from 10 to 700 GHz for a large range of surface and observation conditions. It is based on the Fast Microwave Emissivity Model (FASTEM, Liu et al., 2011) at low frequencies up to 200 GHz where FASTEM has been thoroughly evaluated. It follows a physical emissivity model developed by LERMA (Prigent and Abba, 1990) where FASTEM is not valid. Figure 2.15

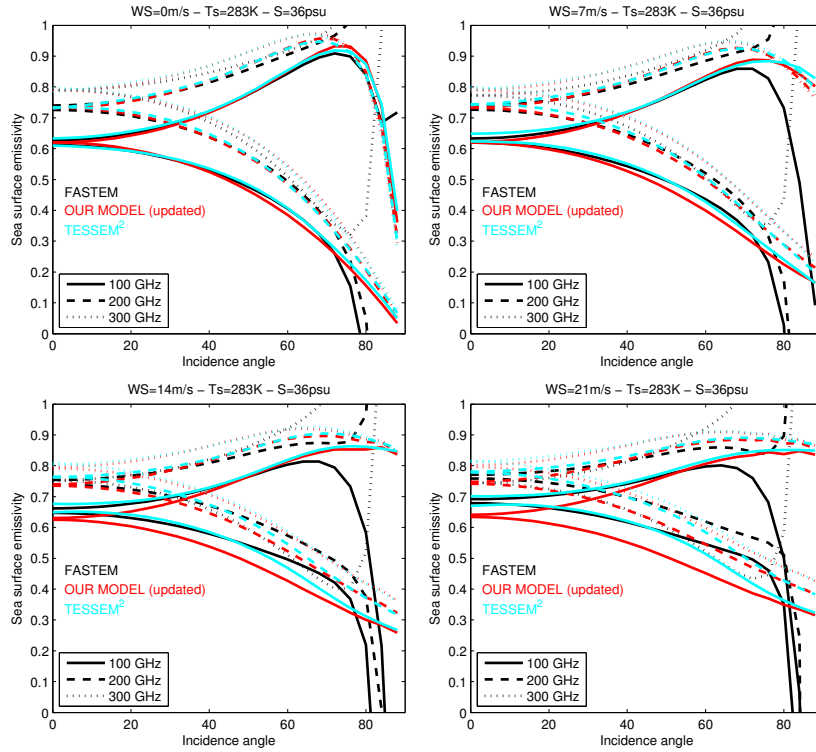


FIGURE 2.15: The emissivity angular dependence, as derived from the new parameterization TESSEM² (cyan). For comparison, the emissivity from FASTER (black) and from our physical model (with the FASTER updates in red). Results are presented for four wind speeds and for three frequencies (100, 200, and 300 GHz).

shows the comparisons of FASTER, LERMA model, and TESSEM², at 100, 200, and 300 GHz, for 4 different wind speeds (0, 7, 14, and 21 *m/s*), at 283 K, and a salinity at 36 *psu*. Figure 2.16 shows the frequency dependence of these models, for three incidence angles (0°, 25°, and 50°).

Unrealistic emissivities are calculated with FASTER for large angles ($> 50^\circ$) and higher frequencies (> 200 GHz). LERMA updated model provides realistic angle dependence, compared with the Fresnel calculation, while it provides a smooth increase of the emissivities after 200 GHz, consistent with the theory that the frequency dependence of the dielectric properties of sea water predicts a smooth increase of the emissivities with frequency. The new emissivity parameterization fits the two models in their validity ranges, with a root mean square (rms) error of 0.007 in emissivity for both polarizations. The angular and frequency dependences are consistent with the expected models over their validity ranges, and provide smooth transitions between the 180-300 GHz domain in frequency, and between the 55°-75° domains in incidence angle, for both polarizations.

TESSEM² has been evaluated by the ISMAR and MARSS observations from the Sub-millimetre Trial In Cirrus and Clear Skies (STICCS-2) and the Cold-air Outbreak and Sub-Millimeter Ice Cloud Study (COSMICS) campaigns up to 325 GHz in Chapter 4. It is a fast parameterization and it is written in Fortran 90. It can easily be implemented in community radiative transfer codes, such as RTTOV, Community Radiative Transfer

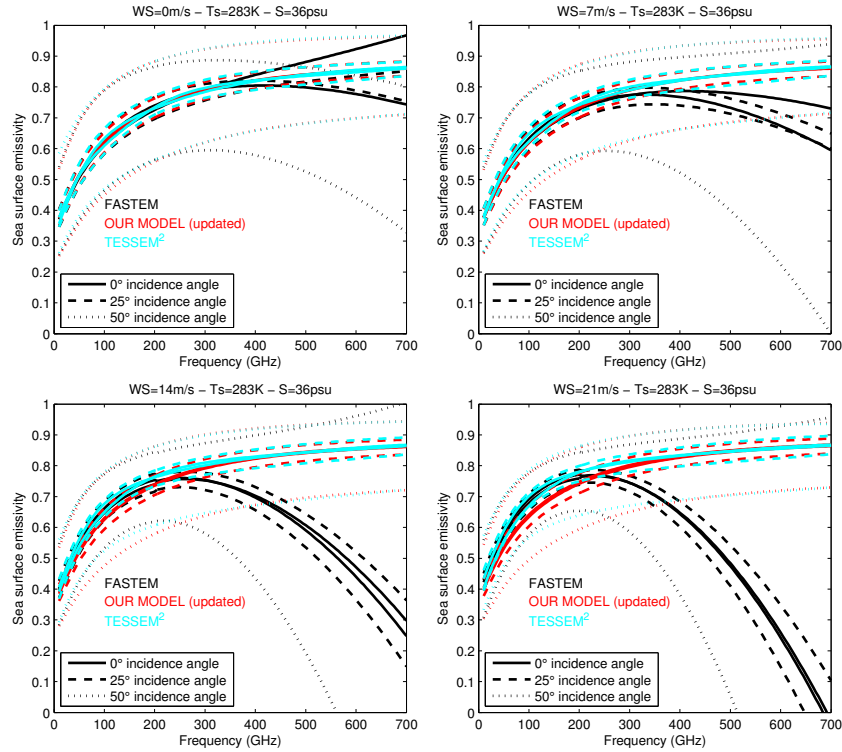


FIGURE 2.16: Same as Figure 2.15 but for the frequency dependence, for three incidence angles (0° , 25° , and 50°).

Model (CRTM), and ARTS. Its inputs are: the frequency (GHz), the incidence angle ($^\circ$), the wind speed at 10 m (m/s), the surface temperature (K), and the salinity (psu). The surface emissivities are calculated for the two orthogonal polarizations. In addition, the Jacobians can be estimated analytically, with respect to the environmental variables (wind speed, surface temperature, and salinity) for the forth coming assimilation. The code is available to the community upon request.

TESSEM² has been incorporated into ARTS simulations to provide realistic sea surface emissivity in this thesis. Figure 2.17 presents the sea surface emissivities calculated by TESSEM² at 31.4, 89, 165.5, and 243 GHz for case 7 over the UK on June 28, 2012 (presented in Section 2.1) on the WRF grids and for an incidence angle of 53° at two both V and H polarizations. The inputs for TESSEM² are from WRF simulations. A higher variability can be found on the emissivity at horizontal polarization, with increasing emissivities in the region with high wind speeds caused by the storm. The vertically polarized emissivities are always higher than the horizontally polarized ones, as expected.

2.3.3.2 Land surface emissivity calculation

In this thesis, realistic microwave land surface emissivities are derived from TELSEM² (Wang et al., 2016). TELSEM² is an updated version of TELSEM (Tool to Estimate the Land Surface Emissivity in the Microwaves, Aires et al., 2011). It has been developed to

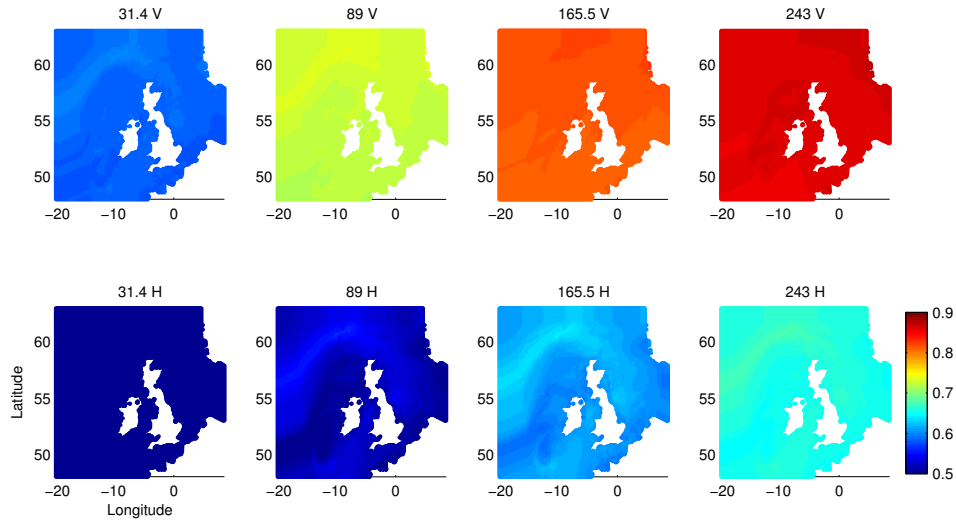


FIGURE 2.17: The sea surface emissivities calculated by TELSEM^2 at 31.4, 89, 165.5, and 243 GHz at both V and H polarizations at an incidence angle of 53° , for case 7 over UK at 17:00 on June 28, 2012.

provide the land surface emissivities up to 700 GHz, including continental snow/ice and sea ice emissivities, in the framework of the preparation for the ICI on board MetOp-SG. It relies upon satellite-derived emissivities up to 200 GHz, and it is anchored to the Special Sensor Microwave/Imager (SSM/I) TELSEM monthly climatology dataset over 15 years (from 1993 to 2007) from 19 to 85 GHz. For comparison purposes and to help characterize the frequency dependence at higher frequencies, emissivities from Météo-France and the National Oceanic and Atmospheric Administration (NOAA) at frequencies up to 190 GHz were also used, calculated from the SSMIS and the Advanced Microwave Sounding Unit-B (AMSU-B) observations. The original spatial resolution for TELSEM^2 is $0.25^\circ \times 0.25^\circ$. TELSEM^2 has been evaluated with the observations of the ISMAR and the MARSS between 89 and 325 GHz, who operated on board the Facility for Airborne Atmospheric Measurement (FAAM) aircraft during the COSMICS campaign over Greenland (Wang et al., 2016). The evaluation of the TELSEM^2 model will be presented in Chapter 4. TELSEM^2 is coded in Fortran and has been already coupled to RTTOV. In addition, it is available to the community, with its updated database. The inputs of the code are the frequency, the incidence angle, the latitude, the longitude, and the month. It outputs the emissivity for both orthogonal polarizations, along with the error covariance matrix.

TELSEM^2 is incorporated into ARTS simulations to provide realistic land surface emissivity up to 700 GHz in this thesis. Figure 2.18 presents the land surface emissivities derived from TELSEM^2 at 31.4, 89, 165.5, and 243 GHz for case 7 on the WRF grids at 53° for both V and H polarizations. The land emissivity shows more spatial variability (especially in the coastal and snow covered regions over southern Norway) than over the ocean (in Figure 2.17). The estimations are expected to be challenging over snow covered areas with high variability in space and in time. The surface emissivity for the snow over southern Norway lightly decreases with frequency, with the H polarized component being significantly lower and more variable than the V polarized component.

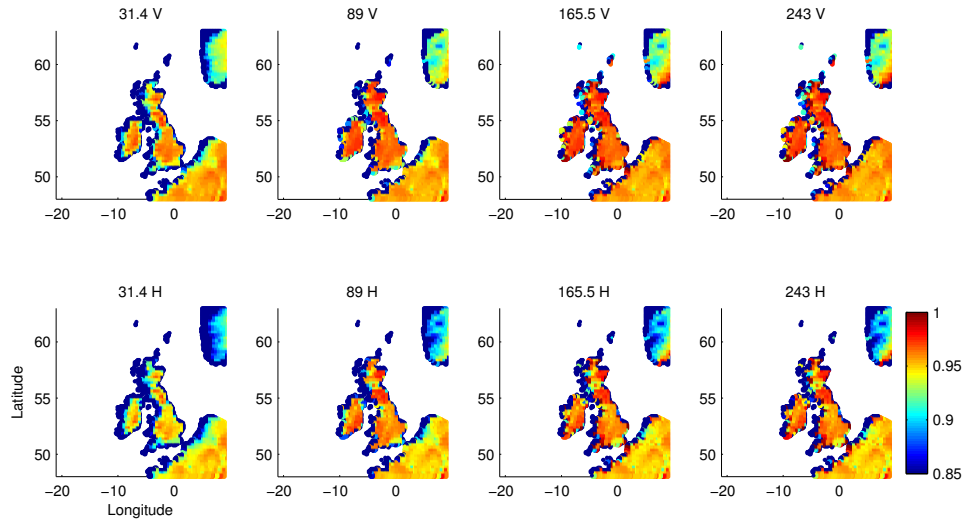


FIGURE 2.18: The land surface emissivities calculated by TESSEM² at 31.4, 89, 165.5, and 243 GHz at both V and H polarizations for 53°, for case 7 over UK at 17:00 UTC on June 28, 2012.

With the help of the relevant tools presented in this chapter, the WRF+ARTS simulations have been performed at SSMIS, MWI, and ICI channels for the selected twelve cases, for the preparation of the cloud parameters retrieval. The simulated brightness temperatures at SSMIS channels will be systematically compared to collocated observations below 200 GHz in the first part of Chapter 3 to gain the confidence for our models and hypotheses. Then the statistical methods will be developed to detect and quantify the ice cloud parameters with the simulated brightness temperatures at ICI or MWI+ICI channels in the second part of Chapter 3.

Chapter 3

A Statistical Retrieval of Cloud Parameters for the Millimeter Wave Ice Cloud Imager on board MetOp-SG

In this chapter, our objective is to design a statistical retrieval algorithm to extract primarily the ice cloud parameters, based on an extensive database of simulations provided by realistic atmospheric scenarios over Europe. Our analysis involves first the Ice Cloud Imager (ICI) instrument, but the methodology is also applied to the combination of the ICI and the MicroWave Imager (MWI) instruments (see Chapter 1 for their descriptions) to evaluate their synergy. The steps to build the retrieval database have been presented in Chapter 2, along with the relevant tools.

First, as described in Section 2.1, twelve diverse meteorological situations are collected to cover as well as possible the variability of the different cloud scenarios in Europe, in terms of cloud parameters, for the development of statistical retrievals of cloud parameters in this chapter. These cases have been selected by considering the important atmospheric features associated with main weather systems across Europe in different seasons, over various surfaces (e.g., ocean and land surfaces), with different precipitation types. Then, the Weather Research and Forecasting (WRF) model, is used to provide the atmospheric profiles, clear and cloudy (see Section 2.2). This ensures physical consistency among the different parameters of the atmospheres. The synoptic situations of these events simulated by WRF are shown in Figure 2.4, displaying a large meteorological variability. The histograms of the vertically integrated hydrometeor contents (i.e., ice water path (IWP), snow water path (SWP), rain water path (RWP), graupel water path (GWP), and cloud water path (CWP)) are given in Figure 3.1. The different scenes show very different distributions of cloud hydrometeor contents, especially for the SWP, which has a large dynamical range (maximum values of SWP between 1.5 and 4.5 kg/m^2). In addition, to investigate the vertical distribution of each hydrometeor, the domain-averaged hydrometeor profiles are illustrated in Figure 3.2, showing large variability for the different cloud scenarios.

Second, radiative transfer simulations are performed on the resulting atmospheric profiles, using the Atmospheric Radiative Transfer Simulator (ARTS) along with carefully selected scattering optical properties of the hydrometeors (see Section 2.3). Coupling the cloud model and the radiative transfer simulator requires specific care to maintain consistency between the cloud particles generated by the cloud resolving model and their scattering properties. The assumptions on the microphysical properties in the cloud resolving model and the calculation of the single scattering properties have already been discussed in Section 2.3.2.

Third, in this chapter in Section 3.1, the simulations are systematically compared to collocated Special Sensor Microwave Imager Sounder (SSMIS) satellite observations below 200 GHz. The real SSMIS over-pass times have been checked for all the 12 cases and specified in Table 2.1. The retrieval training database is analyzed statistically in Section 3.2.

Last, statistical retrieval schemes are developed to detect and retrieve cloud hydrometeor contents (both frozen and liquid phases), based on Neural Network (NN) methodologies (Section 3.3). The retrieval processing is shown in Figure 3.3. The first step consists in the detection of clouds (hydrometeors), followed by the quantification of each hydrometeor (integrated quantity and atmospheric profile). A Principal Component Analysis

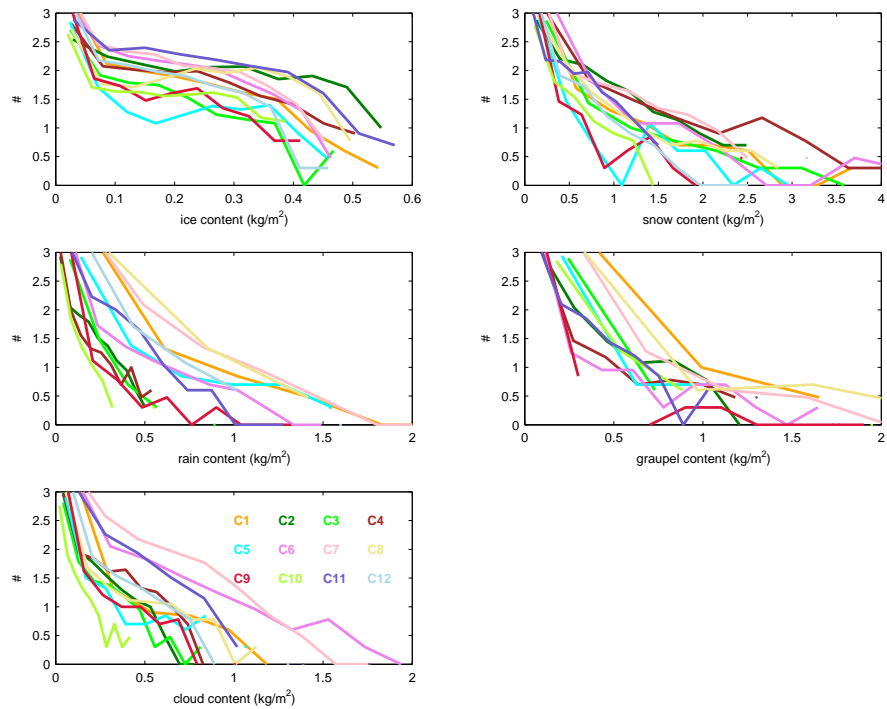


FIGURE 3.1: Histograms of ice water path (IWP), snow water path (SWP), rain water path (RWP), graupel water path (GWP), and cloud water path (CWP) from WRF model for 12 cases around SSMIS over-pass times. The y-axis is in \log_{10} .

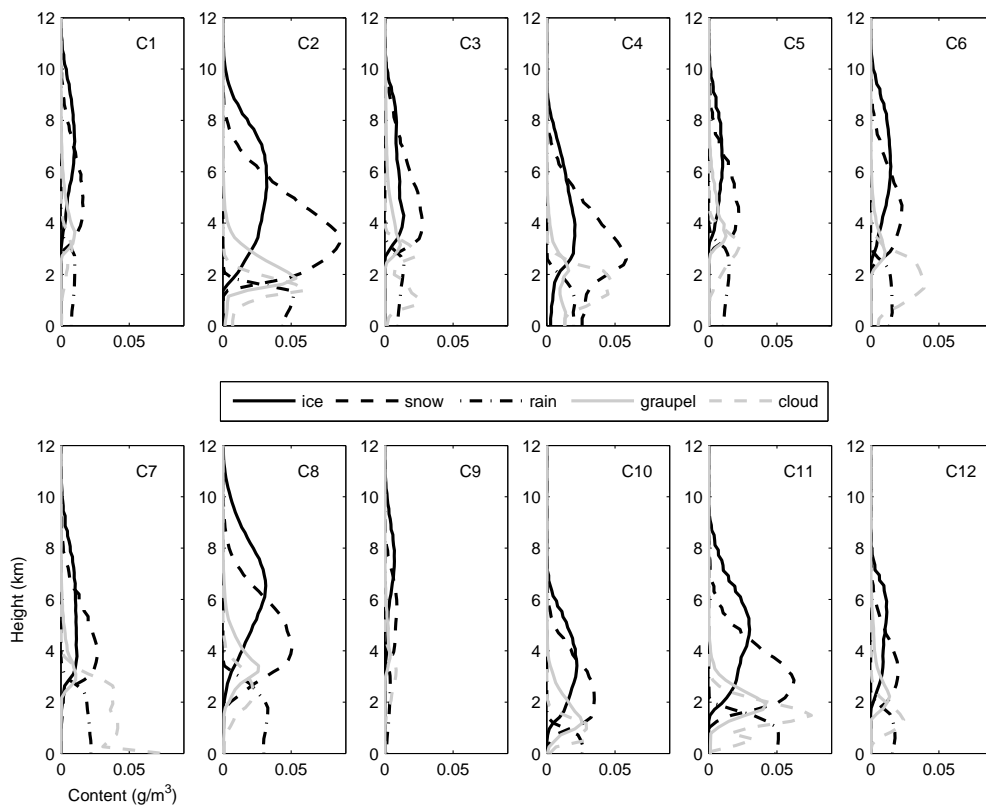


FIGURE 3.2: The domain-averaged hydrometeor profiles of cloud ice, snow, rain, cloud water, and graupel for 12 cases around SSMIS over-pass times.

(PCA) technique is used for the hydrometeor profile retrieval to reduce the number of retrieval parameters. These two statistical inversions are trained using the realistic database generated in Chapter 2.

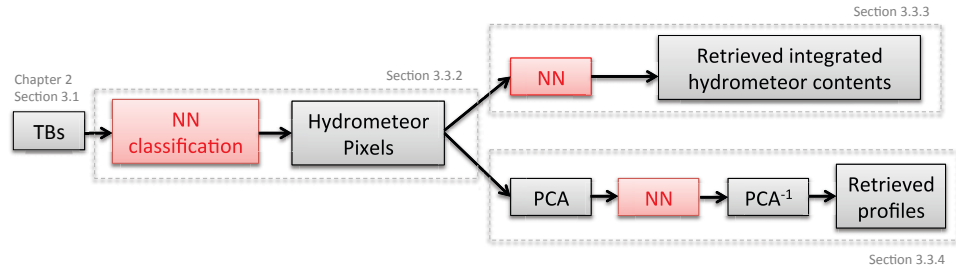


FIGURE 3.3: Retrieval processing for the cloud detection and quantification.

3.1 Evaluation of the simulation database below 200 GHz

The WRF+ARTS simulations described above represent real meteorological cases and have been selected to correspond to SSMIS over-pass. The simulations are thus evaluated by comparing with the SSMIS observations for the frequencies from 89 to 183 GHz. Figure 3.4 shows the observed and simulated brightness temperatures at 6 SSMIS channels, for two meteorological situations (cases 7 and 11). At all frequencies, the spatial structures of the observations are fairly well reproduced by the coupled WRF+ARTS simulations. At 89 GHz horizontal polarization, the emission from the cloud liquid phase is clearly observable over the cold oceanic background (the emissivity over ocean is significantly lower than over land). At this frequency, the good agreement between the simulations and the observations suggests that the liquid cloud characteristics have been correctly modeled by WRF and that TELSEM² and TESSEM² (introduced in Section 2.3.3) generate realistic surface emissivities. At 150 GHz, the observed brightness temperature depressions related to the scattering effect of the cloud frozen particles are also well reproduced by the simulations, implying that the parameterization of cloud frozen quantities from WRF is realistic (see Section 2.2.3), as well as the selected scattering assumptions (see Section 2.3.2). In the three channels located in the water vapor absorption line at 183.3 GHz (183.3 ± 1 , ± 3 , and ± 7 GHz), the water vapor absorption tends to mask the cloud emission and scattering as well as the surface contribution, with the extent of the masking depending on the spectral distance from the center of the absorption line: the agreement between the simulations and the observations confirms the quality of the WRF simulations and their efficient coupling with ARTS. Similar conclusions can be drawn from other cases (not shown). However, note that the cloud and precipitation structures can be slightly misplaced by the cloud model compared to the observations, as already mentioned by several authors (e.g., Bauer et al., 2011, Wattrelot et al., 2014). For case 11 for instance, the WRF simulates the extratropical cyclone over the North Atlantic closer to the Portugal, compared to the satellite observations.

For a systematic comparison of the simulations and observations, minimizing the effect of the observed mislocations, the histograms of the observed and modeled brightness

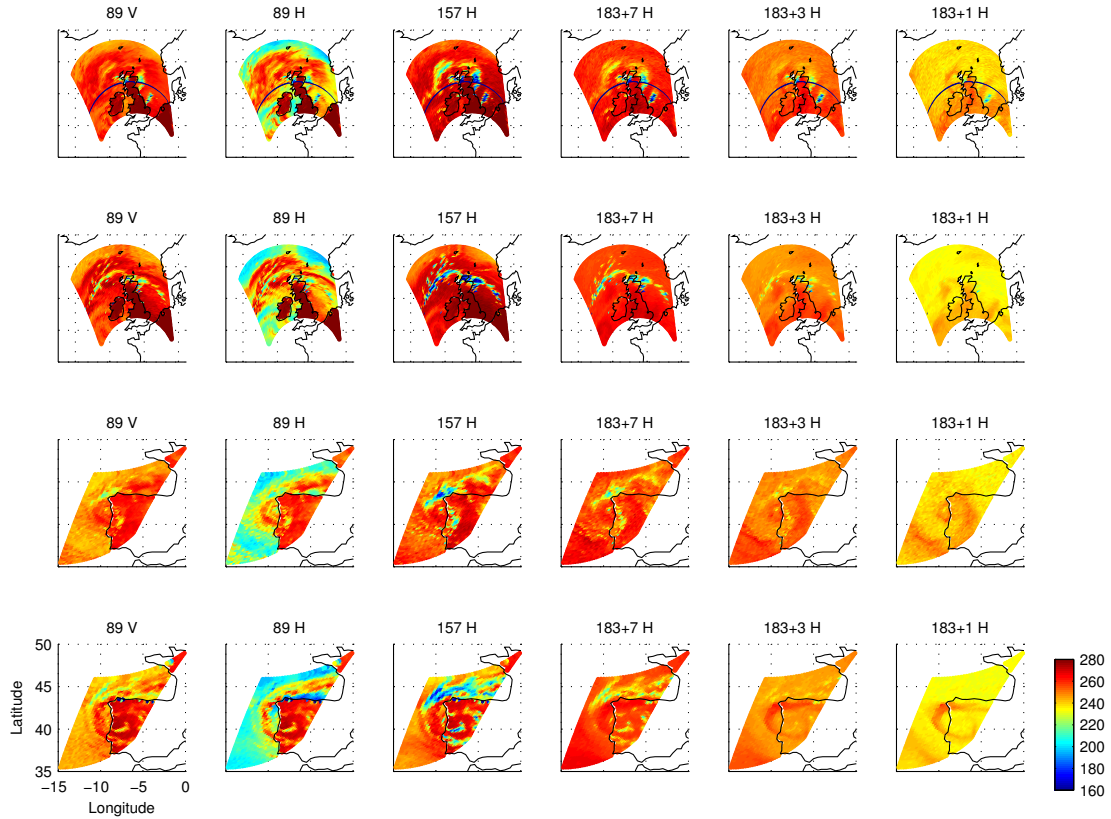


FIGURE 3.4: Observed (first and third rows) and simulated (second and fourth rows) brightness temperatures (K) at six SSMIS channels for case 7 (2 top rows) over UK at 17:00 UTC on June 28, 2012, and case 11 (2 bottom rows) over Portugal at 07:00 UTC on 19 January, 2013.

temperatures are compared, for some SSMIS frequencies and for the pixels in all the 12 scenes (Figure 3.5). The coastal pixels have been excluded to avoid the large differences in brightness temperatures related to the high variability of the surface emissivity around the coast in addition to the difference in resolution between the surface emissivity estimation and the satellite footprints. At 89, 157, and 183 ± 7 GHz, the simulations produce lower brightness temperatures than observations. This can be due to an overestimation of the cloud frozen phases in WRF simulations (see Figure 3.1), to deficiencies in the SSPs of the frozen particles, or to a combination of these two effects. Overall, the WRF+ARTS model reproduces rather well the brightness temperature distributions for all the investigated channels at frequencies lower than 190 GHz. It gives us confidence in the possibility to simulate realistic brightness temperatures at higher frequencies up to 664 GHz.

Figure 3.6 shows the simulated brightness temperatures at all ICI and MWI channels for case 11. At low frequencies, strong contrasts are observed between ocean and land, with an increasing effect of the cloud structures over ocean as the frequency increases. In the window channels at 89 GHz and above, the presence of frozen particle is characterized by the scattering that increases with frequency. Above 325 GHz, the atmospheric opacity above the clouds tends to mask the scattering signals, at least for this case. In addition, channels around 50 and 118 GHz O_2 absorption lines are sensitive to the O_2 emission

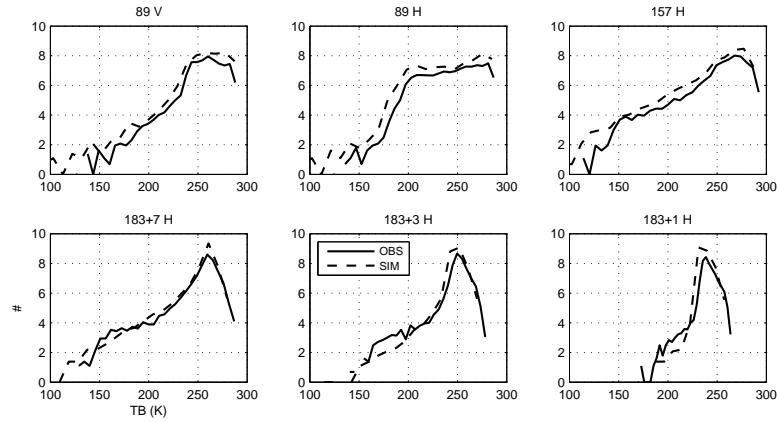


FIGURE 3.5: Histograms of observed and simulated brightness temperatures at six SSMIS channels for all the 12 cases at SSMIS over-pass times. The pixels on the coast are removed. The y-axis is in log10.

which can be used to derive the atmospheric temperature profiles (e.g., Karbou and Prigent, 2005a, Rosenkranz, 2001, Stahli et al., 2013), while channels around the 183 GHz water vapor absorption line are sensitive to the water vapor composition and are used to retrieve atmospheric water vapor (e.g., Brogniez et al., 2011, Selbach et al., 2003).

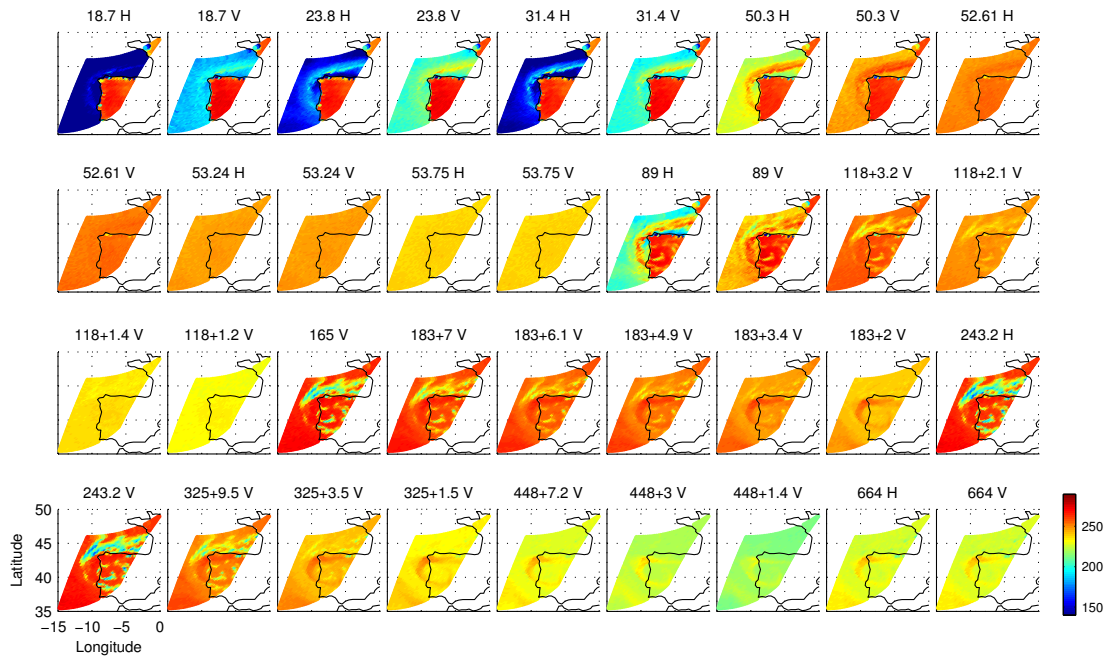


FIGURE 3.6: Simulated brightness temperatures (K) at MWI and ICI channels for case 11 over Portugal at 07:00 UTC on 19 January, 2013

3.2 Statistical analysis of the retrieval training database

Our retrieval database contains (1) the geophysical variables describing the 12 cases of Section 2.1 (surface and atmospheric variables, especially the vertically integrated contents and the vertical profiles of six hydrometeors), and (2) the corresponding simulated brightness temperatures at ICI and MWI channels. This retrieval dataset contains 57 % pixels over land and 43 % pixels over ocean. A question could arise: Are these cases enough for the training of a statistical retrieval? The 12 cases could be disjointed or describing only a part of the possible hydrometeor cases. In order to verify this aspect, leave-one-out generalization tests have been performed to ensure that these 12 cases sample well the complex space of hydrometeor profiles. The quality of a statistical retrieval database is essential for either a Bayesian (Kummerow et al., 2015) or a NN (Defer et al., 2008) retrieval scheme. As a consequence, it is important to first analyze the quality of this database.

First, a preliminary information content analysis is performed in order to measure the degrees of freedom in the hydrometeor variables to retrieve and the information actually carried out by the satellite observations (i.e., ICI or MWI channels). PCA is a statistical procedure that uses an orthogonal linear projection to transform correlated original vectors into a new uncorrelated coordinate system. PCA aims at explaining as much variance as possible in the first components, so it is a good technique to analyze the variability of a database, in particular by estimating the number of degrees of freedom.

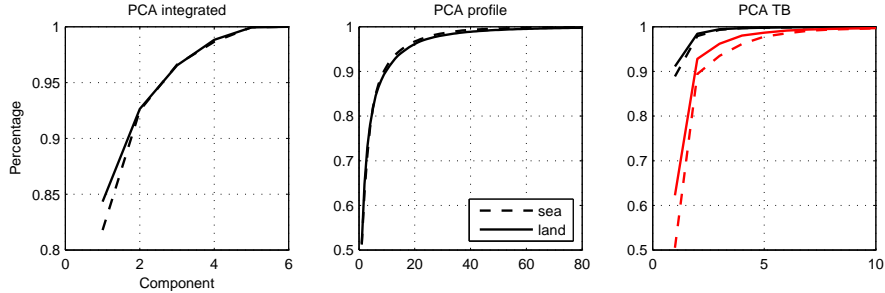


FIGURE 3.7: Percentage of total variance in PCA for vertically integrated hydrometeor contents (left), the hydrometeor profiles (middle), and the simulated brightness temperatures (right) for ICI-only (black) and ICI+MWI (red) channels over sea and land.

Figure 3.7 represents the variance explained by the first PCA components for the hydrometeor information (integrated quantities and atmospheric profiles) and on the microwave brightness temperatures. Results show that the six integrated hydrometeor contents (resp. $104 \times 6 = 624$ variables of the hydrometeor profiles) from WRF can be explained by 4 (resp. 36) components that represent more than 99 % of the variance. Results are similar for land and ocean surfaces. These results mean that in order to retrieve the hydrometeor variables with 1 % precision, at least 4 independent pieces of information would be required for the integrated quantities and 36 for the profiles. Strong correlation has been shown in Figure 3.8 between frozen particles. However, only 4 pieces of information can be derived from the 13 ICI channels (again for 99 % variance). This means that there are strong correlations between the ICI channels, as

shown in Figure 3.9. This number increases to 7 pieces of information when using the 39 ICI+MWI channels. These results stress out the difficulty of retrieving the integrated hydrometeor information with only ICI channels, and the hydrometeor profiles even when adding the MWI channels.

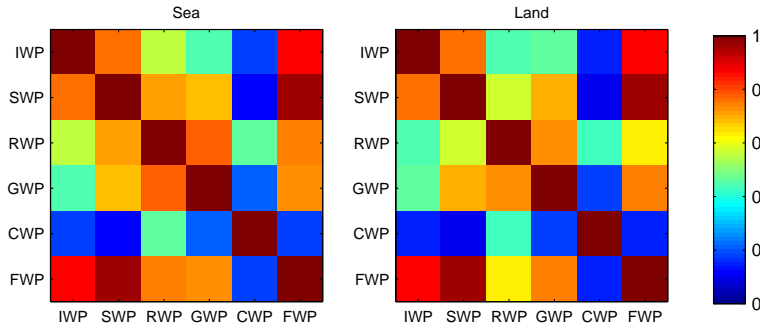
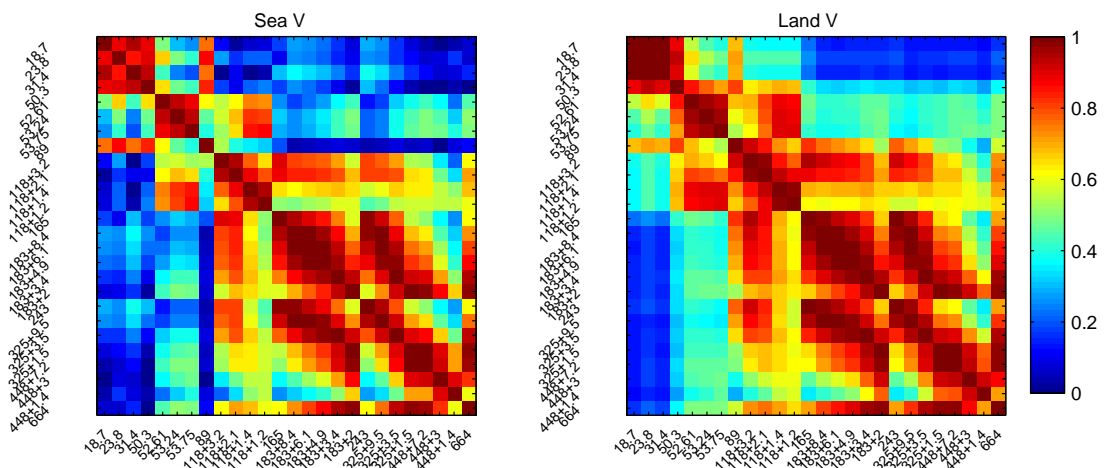


FIGURE 3.8: Correlation coefficients (absolute values) of the integrated hydrometeor contents (frozen water path (FWP=IWP+SWP+GWP), ice water path (IWP), snow water path (SWP), rain water path (RWP), graupel water path (GWP), and cloud water path (CWP)) over sea and land.



for the cloud water (< 0.2 for all the channels). Therefore, Figure 3.10 shows the potential of ICI channels for frozen particle retrieval but also the difficulty for the liquid particle retrieval. However, ICI information can be complemented with MWI observations. The correlation between the MWI brightness temperatures and the integrated hydrometeors contents (also see Figure 3.10) has been calculated as well. Lower frequencies are typically the more sensitive channels to the integrated cloud liquid properties, especially over sea with a correlation of 0.72/0.74 at 31.4 GHz for cloud water/rain, which shows well the complementarity of both instruments.

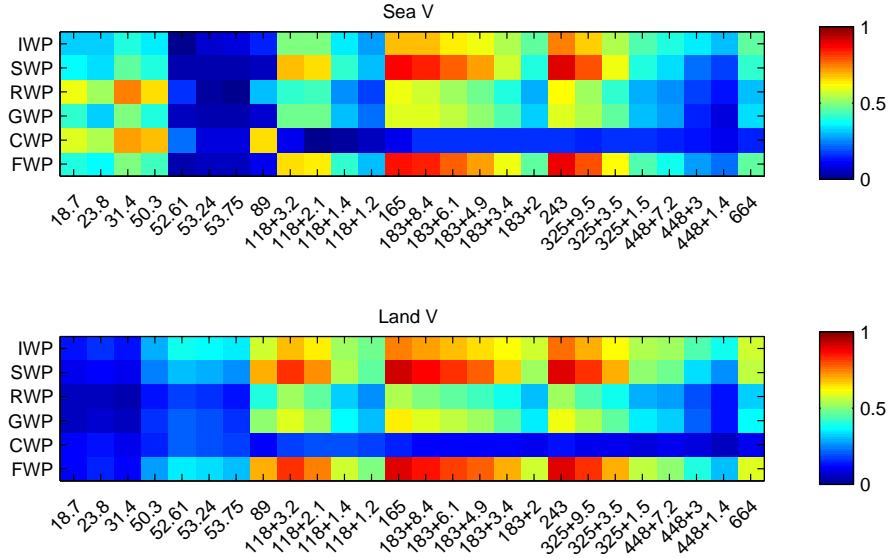


FIGURE 3.10: Correlation coefficients between the integrated hydrometeor contents and the simulated brightness temperatures for MWI and ICI channels over sea and land, for vertical polarization.

3.3 Statistical retrieval of cloud hydrometeor contents

In this Section, a statistical retrieval scheme is developed to retrieve cloud hydrometeor contents (both frozen and liquid phases). A first step consists in the detection of clouds, and the second one in the quantification of each hydrometeor (integrated quantity and atmospheric profile), as illustrated in Figure 3.3. These two statistical setups are trained using the realistic database presented in Chapter 2. Retrievals have been performed systematically using ICI-only or ICI+MWI channels.

3.3.1 Neural Networks technique

NNs have been used for the statistical retrievals. The artificial NN, inspired by biological neural networks (human brain), can be used to estimate or approximate complex and unknown functions depending on a large numbers of inputs. The human brain consists of a multitude of neurons interconnected by synapses, allowing the neurons to exchange

information with each other. The concept of the artificial NN is to imitate the biological NN processes mathematically, by designing a network of computing nodes to solve complex problems. This section will briefly explain the theory of the NN.

3.3.1.1 Architecture and network function

In a NN, the computing nodes are arranged in a number of layers (see Figure 3.11). The specific layout for every layer, the computing nodes and their connections are considered as the NN architecture, which is crucial and essential in the functioning of the NN system. The NN architecture should be defined first. In the first step, the input and output layers are specified by giving the same number of neurons as the (input and output) variables in the problem needed to be solved. The second step consists in defining how many layers should be used as hidden layers (between the input and output layers). The third step is to decide what should be the number of neurons in each hidden layer, which depends on the complexity of the problem to be performed. Generally, the NN architecture is designed to be a trade-off between a NN sufficiently complex to correctly approximate the mapping between the input spaces, and a NN simple enough in order to avoid the problem of over-fitting and over-parameterization (losing the ability to generalize to new situations). The last step is to decide the type of connection between the neurons in the different layers. In principle, there are many types of NN, which organize the neurons in different layers and allow the inputs for the NN to propagate in different ways. In this chapter, we use multilayer feed-forward networks. In a multilayer feed-forward network, each layer, consisting of nodes, receives their inputs from nodes in a layer directly below and sends their outputs to nodes in a layer directly above.

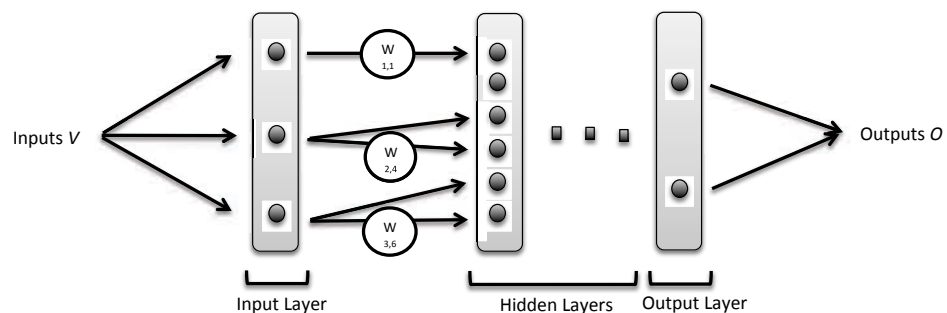


FIGURE 3.11: Schematic of a neural network architecture. Depicted is a feed-forward network with three input variables, 2 output variables and at least one hidden layer with seven neurons. The parameters w denote the synaptic weights assigned to the neuron connections.

In a NN, for a neuron having m inputs (v_1, \dots, v_m) , the weighted sum of all the inputs s can be given as

$$s = \sum_{i=1}^m (w_i \times v_i) + w_b \times b \quad (3.1)$$

where b is the bias, w_1, \dots, w_m are the weighting matrix, and w_b is the weight of the bias. This sum is transformed with a transfer function, so the total output of a neuron o can be expressed as

$$o = f(s) = f\left(\sum_{i=1}^m (w_i \times v_i) + w_b \times b\right) \quad (3.2)$$

where f is the transfer function. Figure 3.12 illustrates this process.

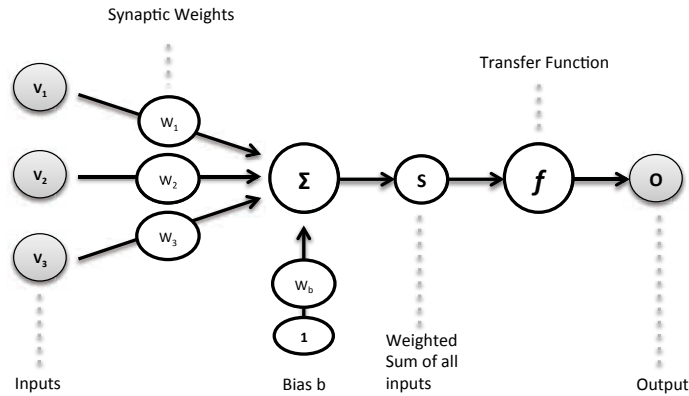


FIGURE 3.12: Schematic representation of a neuron, showing the neuron inputs v , the bias b , the connection weights w , the summer, the weighted sum of all inputs s , the transfer function f and the neuron output o .

There are different types of transfer functions, including the linear, the hard-limit, the logarithmic sigmoid, and the tangent sigmoid functions. Different transfer functions are chosen for different layers, which is subject to the example the NN is used for. In general, the linear function is used on the output layer of a NN, for the reason that it transforms the inputs to the outputs in an unlimited range. The hard limit function is generally used to group the inputs into discrete classes, by projecting the inputs onto the value -1 (below a certain threshold) or 1 (above this threshold). The logarithmic sigmoid function is typically set to the hidden layers of feed-forward networks, due to that it gives continuous outputs between 0 and 1. The tangent sigmoid function is also usually used in function approximations in the hidden layers of a NN, by projecting the input data onto a continuous values between -1 and 1.

The weighted sum of inputs will be computed and the transfer function will be given for each neuron, which is performed in parallel for all the neurons in one layer. Considering that there are n neurons in one layer with m inputs, the output from this layer can be given as (in matrix notation)

$$\mathbf{o} = f(\mathbf{W}\mathbf{v} + \mathbf{b}) \quad (3.3)$$

The same process is repeated for all neurons in the different layers. Supposing that we have a NN of two layers with weight matrices \mathbf{W}_1 and \mathbf{W}_2 , bias vectors \mathbf{b}_1 and \mathbf{b}_2 and transfer functions f_1 and f_2 , separately, the outputs \mathbf{O} of this NN can be expressed as

$$\mathbf{O} = f_2(\mathbf{W}_2\mathbf{o}_1 + \mathbf{b}_2) = f_2(\mathbf{W}_2(f_1(\mathbf{W}_1\mathbf{V} + \mathbf{b}_1)) + \mathbf{b}_2) \quad (3.4)$$

where \mathbf{V} is the transfer function.

3.3.1.2 Training

The weight and biases of the NN are fixed during the training process. After the training step, the NN is expected to learn the underlying relationships linking the inputs to the outputs. A training database is needed in this step, including a sample of input data with the corresponding desired output data. The training database should be sufficiently large to detect and find the major statistical relationships between the inputs and outputs in the NN.

3.3.2 Cloud detection and classification

The cloud detection (i.e., presence of cloud or not) and classification (i.e., specification of the cloud type) has two main applications. First, it is an interesting way to measure the information content of the satellite observations and study the sensitivity of each channel to the several types of hydrometeors (frozen and liquid). Second, it is a necessary preliminary step before the actual cloud retrieval that intends to quantify the hydrometeor quantities.

Over ocean, cloud liquid water contents are routinely estimated from the cloud emissions measured between 19 and 85 GHz by imagers such as the Special Sensor Microwave Imager (SSM/I) or the Advanced Microwave Scanning Radiometer (AMSR) (Alishouse et al., 1990, Ferraro et al., 1996, Greenwald, 2002, ODell et al., 2008). Over land, the problem is more complicated. The land surface emissivity is usually close to unity, making atmospheric features difficult to identify against such a background because of the limited contrast. In addition, the land surface emissivity is variable in space and time and difficult to model. However, efforts have been made to estimate cloud liquid water over land, using *a priori* information on the surface properties (Aires et al., 2001). From observations above 80 GHz, cloud ice information has been extracted, from both imagers such as SSM/I and water vapor sounders such as AMSU-B (Greenwald, 2002, Hong et al., 2005, Weng and Liu, 2003).

3.3.2.1 A NN classifier

The NN is a nonlinear statistical model (Bishop, 1996). It can be used as a regression tool to estimate quantities, but it can also be used as a classifier, see for instance Aires et al. (2011) for a cloud classification. A standard feed-forward NN is used for each hydrometeor, in order to classify what type of cloud is present. The NNs have 13 or 39 inputs corresponding to the ICI or ICI+MWI channels, 10 neurons in the hidden layer and one output neuron. The NNs are trained with binary data (0 for no cloud,

1 for cloud pixel), but the NN outputs are continuous values between 0 and 1 and this output represents the *a posteriori* probability for the pixel to be cloudy (Richard and Lippmann, 1991). Once trained, the NNs will provide from the satellite observations only and for each pixel, a probability of being cloudy. A threshold on this probability will be needed to decide if the pixel is cloudy or not.

The training of the NNs uses the database containing the simulated (WRF+ARTS) brightness temperatures for ICI-only and ICI+MWI channels, for the twelve mid-latitude scenarios in Europe. The cloud flag for each hydrometeor is identified according to a $> 0.01 \text{ kg/m}^2$ threshold on each hydrometeor column mass. A classification has also been defined for the total hydrometeor and total frozen hydrometeor (ice+snow+graupel) contents using the same threshold. The database is used to construct the learning (to train the NNs) and the testing (to test the NNs ability to classify) datasets.

The NNs are trained using a standard back-propagation algorithm (Rumelhart et al., 1986). A leave-one-out approach is used to minimize or prevent the over-fitting problem where NNs perform well on the training dataset, but are unable to work on new atmospheric situations. Each time, 11 out of the 12 cases are used for the training, and the remaining case is used to test the NN. This is performed 12 times, to obtain 12 testing cases. The results presented in the following section will be the synthesis of these 12 testing cases. Using a different approach would conduct to arbitrary obtain generalization results very dependent on the choice of the testing dataset (often with too optimistic results). The leave-one-out approach provides more confidence on the robustness of the results.

3.3.2.2 Cloud classification results

Figure 3.13 presents the histogram of the NN *a posteriori* probability of being cloudy, for each hydrometeor, over land and sea separately, for the 12 cases, from both ICI-only and ICI+MWI information. The solid (resp. dashed) line represents the probability distribution of the non-hydrometeor (resp. hydrometeor) pixels. Ideally, the solid line would be a Dirac distribution over zero, and the dashed line would be a Dirac distribution over one. The wider the intersection of distribution, the more ambiguous the classification becomes. It can be noticed that this is not the case, and some distributions are more ambiguous for some hydrometeors (e.g., rain). Therefore, different thresholds for the classification need to be used for different hydrometeors. Threshold values of 0.4, 0.5, 0.4, 0.2, 0.3, and 0.5 have been chosen for total frozen, cloud ice, snow, graupel, rain, and cloud water hydrometeors, respectively. Resulting classification accuracies are satisfactory: 85.0 (88.9) %, 89.3 (84.6) %, 94.7 (83.3) %, 91.3 (90.4) %, 85.0 (71.5) %, and 89.9 (35.8) %, over land, for the non-hydrometeor pixels (resp. the hydrometeor pixels). These rates are similar over the sea since the surface contribution is very limited at frequencies higher than 183 GHz (ICI channels) due to larger atmospheric opacity. The classification has also been performed for each hydrometeor when using ICI+MWI channels, the resulting accuracy for each hydrometeor has been specified in red. As expected, adding lower frequencies improves the detection of cloud liquid phases, with an increase of the classification accuracies of 10.0 % over land and 15.6 % over sea for the

rainy pixels, and 18.7 % and 62.0 % for the cloud water pixels. For the frozen particles, the classifier gives very similar results when using ICI-only or ICI+MWI channels, which suggests that the MWI channels do not provide more information on the detection of the frozen particles than ICI.

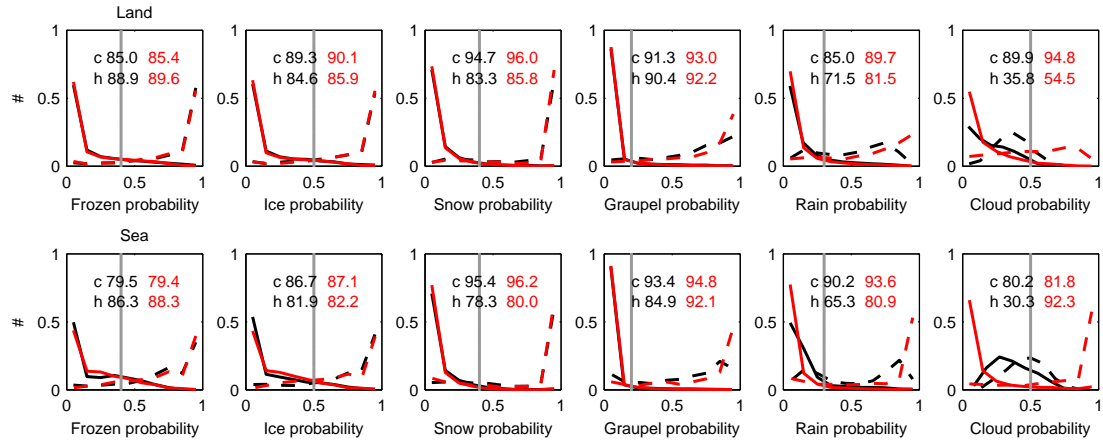


FIGURE 3.13: Histogram of probability for each integrated hydrometeor content retrieved by a NN classification with ICI-only (black) and ICI+MWI (red) channels over sea and land. The classification accuracies for the non-hydrometeor (c) and hydrometeor pixels (h) are shown. The threshold value for each hydrometeor is shown in grey line.

Figure 3.14 shows the spatial patterns of the vertically integrated contents, the *a posteriori* cloud probabilities estimated by the NN classifier with ICI+MWI channels, the retrieved flags, and the initial flags, for all the six hydrometeors and the total hydrometeors, for case 11. The estimated spatial structure of each hydrometeor pixel by the NN classifier is globally similar to the initial one, which suggested that our classification has a good performance in detecting the location of each hydrometeor and total cloud, as well as a good assessment of the classification uncertainties. However, we have difficulty in getting good spatial patterns of liquid phases from the NN classifier when using ICI-only channels, leading to a bad detection of spatial distribution of total hydrometeor content (in Figure 3.15), due to a lack of lower frequencies.

3.3.3 Cloud integrated content retrieval

3.3.3.1 Retrieval algorithm

The relationships between the brightness temperatures at different frequencies and the hydrometeor column masses are complex, multivariate in nature, and non-linear. A multilayer feedforward NN retrieval algorithm is again chosen to model these complex physical links. The number of inputs are the same (13 channels for ICI-only and 39 channels for the ICI+MWI channels), 10 neurons in the hidden layer, and 6 neurons are used to code the FWP (IWP+SWP+GWP), IWP, SWP, RWP, GWP, and CWP retrieved vertically integrated quantities.

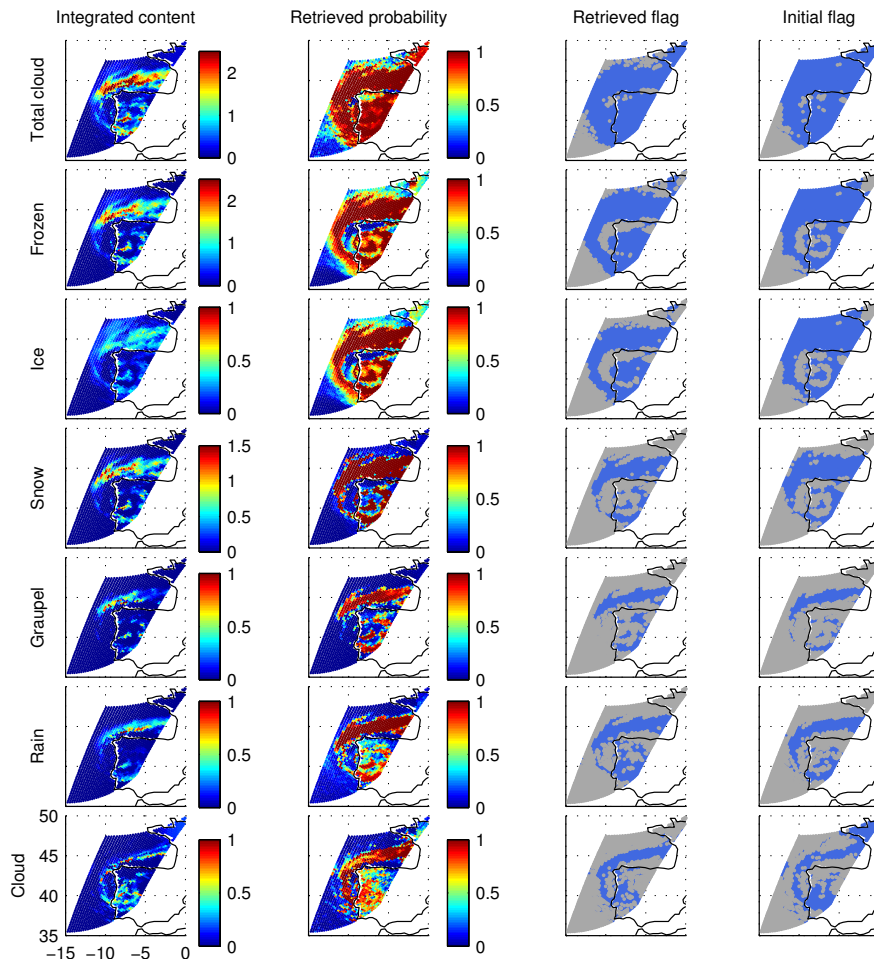


FIGURE 3.14: The spatial patterns of six integrated contents (kg/m^2), the probabilities estimated by the NN classifier with ICI and MWI channels, the retrieved flags (cloudy pixels are in blue, clearsky pixels are in grey), and the initial flags for six hydrometeors and the total hydrometeors for case 11 over Portugal at 07:00 UTC on 19 January, 2013.

The training and testing datasets are the same ones used in Section 3.3.2 for the cloud detection and classification, except that this time the variables to be retrieved are not binary (presence or not of the cloud) but continuous (i.e., the cloud integrated content quantities). The dataset contains only pixels classified as cloudy by our detection/classification process. However, to reduce the classification uncertainty impact on the hydrometeor content retrieval, instead of using a total cloud classification, we use the individual hydrometeor classification that has good accuracy in terms of spatial structures (see Figure 3.14). This can help avoid ambiguity of the cloud liquid phase detection when using only ICI channels (see Figure 3.15). Again, the leave-one-out process (11 cases for training and one case for testing, repeated 12 times) was used to train and test the NNs, ensuring that no over-training was artificially increasing confidence on the retrievals.

In addition, the leave-one-out scheme ensures that the 12 cases sample well the space of possible hydrometeor profile states because no significant difference in generalization tests is measured on the 12 trials. This means that besides being chosen to be diverse,

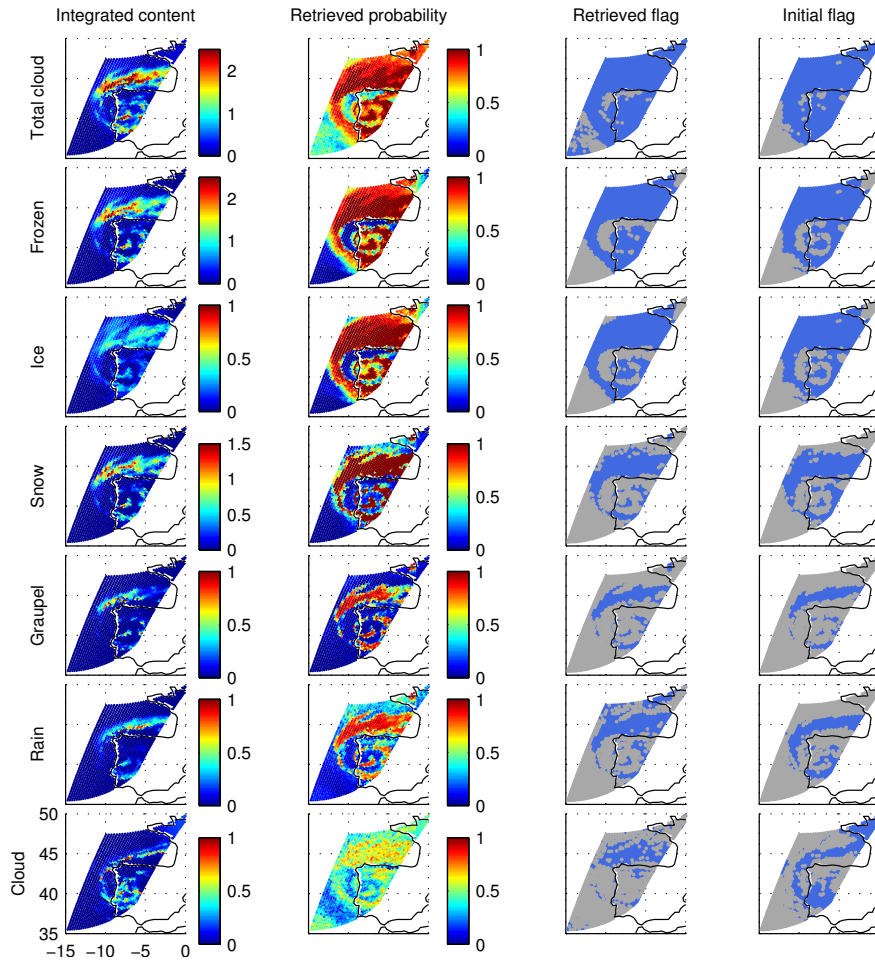


FIGURE 3.15: Same as Figure 3.14, but with ICI-only channels.

there is no extreme departure of one case compared to the remaining 11 cases, or the statistical NN retrieval is able to interpolate between the cases. This gives confidence in the dataset built in Chapter 2.

To determine the ability of the retrieval algorithm to accurately quantify the hydrometeor quantities, the differences between the retrieved and initial values are measured in terms of both the absolute and relative averaged errors, over several bins in the hydrometeor range. Indeed, the relative error (resp. absolute error) is generally more relevant for evaluating the retrieval performances for the larger (resp. smaller) hydrometeor contents.

3.3.3.2 Results

Figure 3.16 shows the scatter plots of the retrieved column mass of the six hydrometeors versus the initial ones, over land and sea, for ICI-only and ICI+MWI channels. No instrument noise is considered so far. Each color represents one of the 12 cases (each one is the testing dataset in the leave-one-out approach), which is the same as in Figure 3.1. When considering only ICI channels, the retrieved cloud liquid phases (RWP and CWP)

saturate at their lower values, slightly underestimating the higher liquid phase contents, and overestimating the lower ones. This implies that the increasing opacity at higher frequencies and near the water vapor absorption lines masks the signal from lower liquid clouds to a large extent. In contrast, the agreement between the retrieved and initial cloud frozen phase contents is very good, in particular for the SWP, due to the strong scattering signals at higher frequencies by frozen particles. Note that the slight saturation regime appears also in the IWP retrieval over both land and sea, leading to a retrieved IWP between 0 and 0.4 kg/m^2 .

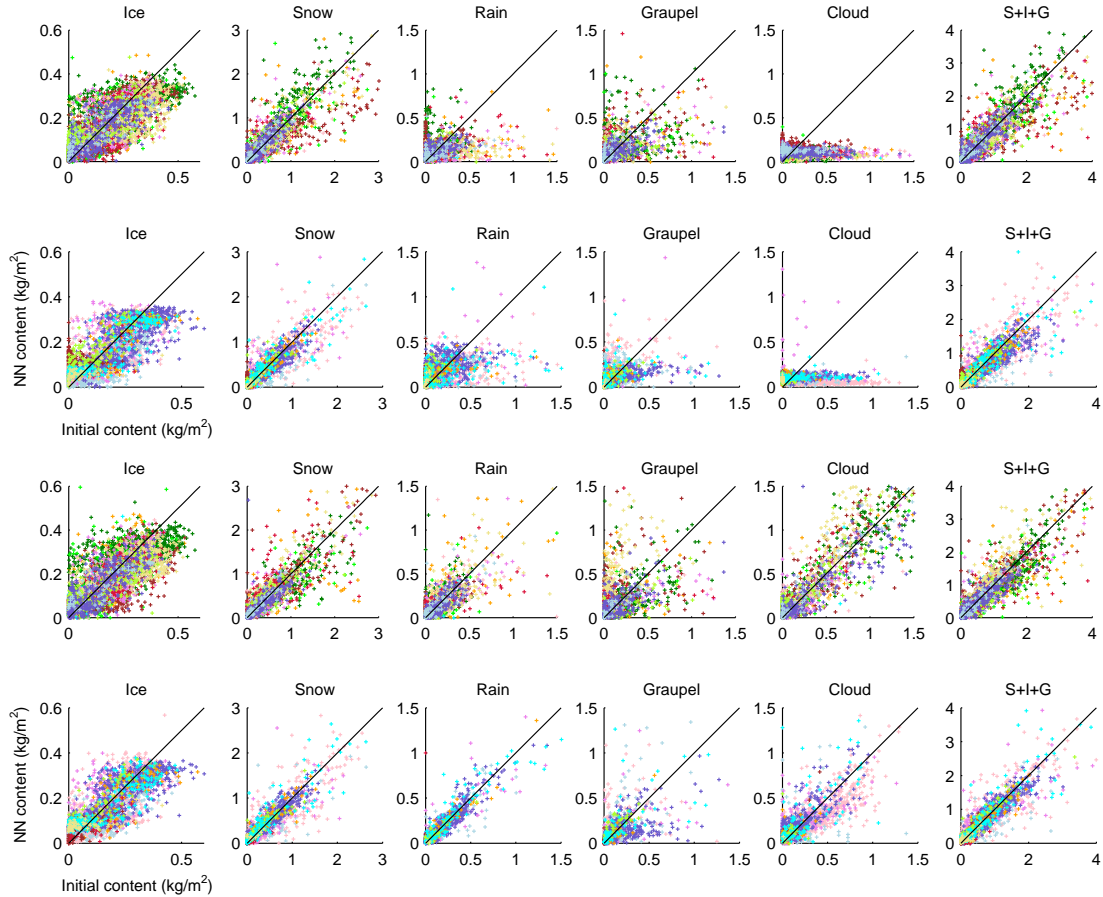


FIGURE 3.16: Scatter plots of vertically integrated contents of ice, snow, rain, graupel, cloud water, and frozen particles from the WRF outputs and the NN method with ICI-only channels (2 top rows) and ICI+MWI channels (2 bottom rows) over land (first and third rows) and sea (second and fourth rows). Each color represent the results for one case when it is regarded as the testing case, which keeps the same as in Figure 3.1.

When adding the MWI channels, the retrieval performances are improved for all the vertically integrated hydrometeor contents, but most significantly for the cloud liquid phases, as expected. It illustrates well how low frequency microwave channels can penetrate clouds and rain to some extent, allowing the retrieval of the cloud liquid contents in a vertical column. Therefore, combining ICI and MWI instruments, by covering the frequency range from 18.7 to 664 GHz, allows overcoming the limitations of lower frequencies (i.e., not sensitive to the smaller frozen particles at higher altitudes) and of higher frequencies (i.e., lack of capacity to extract the information from lower altitudes).

Over sea, the retrieval algorithm reproduces better the integrated hydrometeor contents, specially for the cloud liquid phases when using ICI+MWI channels. This is due to the fact that the emission from cloud liquid phases is contaminated by the emission from land surface, and is relatively important over the cold sea surface, at surface-sensitive microwave channels. As a consequence, these channels have a larger impact over sea than over land, as discussed by Kummerow et al. (1996), Marecal and Mahfouf (2001).

The ICI+MWI retrieved and initial hydrometeor content patterns are shown in Figure 3.17 for case 11. The spatial distributions of all the hydrometeors are well retrieved, such as the convective parts (the northern part of the eyewall and surrounding the eye of the cyclone). However, the higher initial IWP concentrated on the north of the eye is missing in retrieval results, whereas they are presented by the intermediate values due to the saturation regime. Surprisingly, there is no evident discontinuity on the retrieved RWP and CWP over land/sea, even this is generally observed in rainfall retrievals (McCollum and Ferraro, 2003, Yuter et al., 2006). This land/sea discontinuity however appears when only ICI channels are used in the CWP retrieval. This is due to the difficulty in distinguishing the emitted signals from cloud liquid particles from warmer land surface, losing the direct link between the brightness temperatures and the CWP.

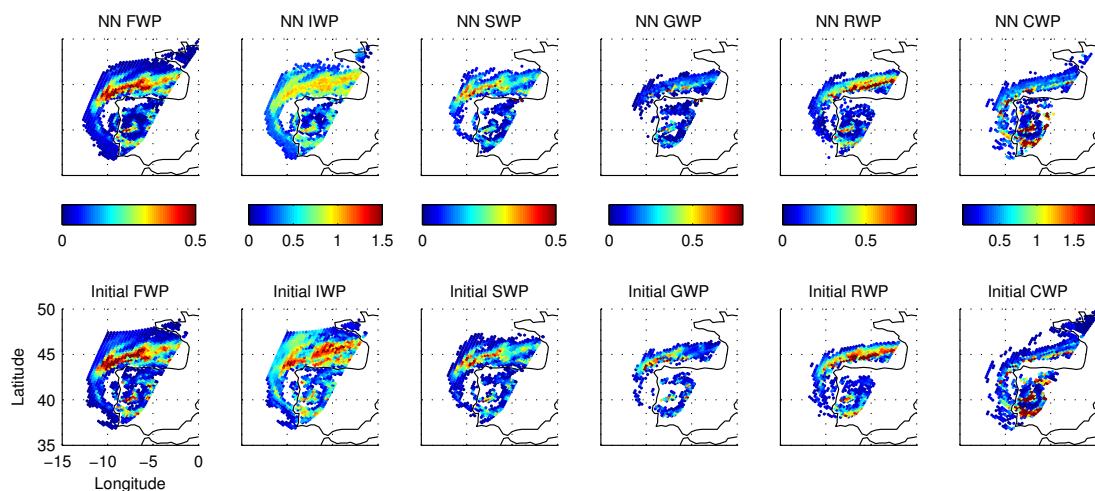


FIGURE 3.17: The patterns of retrieved and initial IWP, SWP, RWP, GWP, CWP, and FWP for case 11 over Portugal at 07:00 UTC on 19 January, 2013..

Figure 3.18 shows the average absolute and relative retrieval errors, per bin of 0.01, 0.04, 0.04, 0.04, 0.02, and 0.06 kg/m^2 for, respectively, the six hydrometeors contents (IWP, SWP, RWP, GWP, CWP, and FWP), over land and sea, with ICI-only and ICI+MWI channels. The limited information from higher frequencies (ICI-only) induces large absolute and relative retrieval errors in RWP, CWP, and GWP (situated at relative lower altitudes), notably for larger contents. Therefore, the following discussion will focus on the retrieval results with ICI+MWI channels. As expected, in the light hydrometeor content ranges, the relative errors are higher, even exceed 100 % for very small contents. The relative retrieval errors for IWP, SWP, RWP, GWP, CWP, and FWP drop and remain nearly below 20 %, 20 %, 20 %, 40 %, 30 %, and 20 % for 0.25, 0.5, 0.25, 0.2, 0.2, and 0.5 kg/m^2 and above, respectively. They increase again and start

to fluctuate for larger hydrometeor contents, due to the rarity of these cases in our retrieval database. The absolute errors increase with hydrometeor contents, except for the IWP. The absolute errors are larger than 0.04 kg/m^2 for the IWP less than 0.05 kg/m^2 , showing the difficulty in lower IWP retrieval. This high uncertainty associated with the low IWP is due to the sensitivity of brightness temperatures to other variables such as snow and graupel particle presences. Note that both absolute and relative errors for the IWP retrieval are very similar in two channel-configurations, demonstrating that the ICI channels can provide enough information for the IWP retrieval.

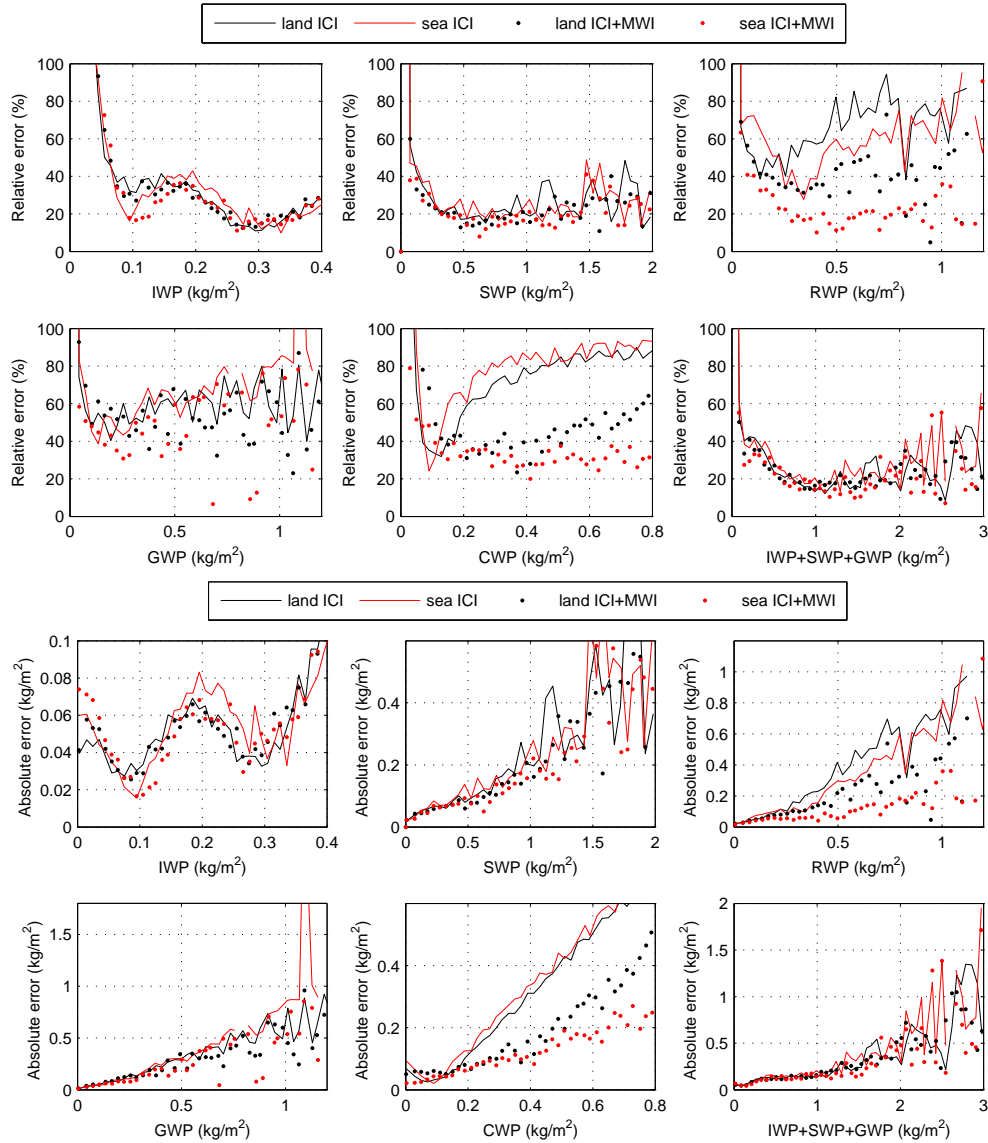


FIGURE 3.18: Retrieval relative (2 top rows) and absolute (2 bottom rows) errors per bin of 0.01, 0.04, 0.04, 0.04, 0.02, and 0.06 kg/m^2 for IWP, SWP, RWP, GWP, CWP, and FWP, separately, with ICI-only and ICI+MWI channels over sea and land.

In addition, the impact of the realistic instrumental noises on the accuracy of the retrieval algorithm was investigated. The instrumental noise goes from 0.6 K to 1.2 K for the MWI channels and from 0.6 K to 1.9 K for the ICI channels (see Table 1.1 in Chapter 1). The noise values at all the channels were added to the simulated brightness temperatures

but their impact on retrieval results was negligible (see Figure 3.19). This indicates that the uncertainty introduced by the instrumental noise is negligible compared to the other sources of uncertainties such as, for instance, the low-information content of some channels for some hydrometeors, or the ambiguity of the signal in one channel.

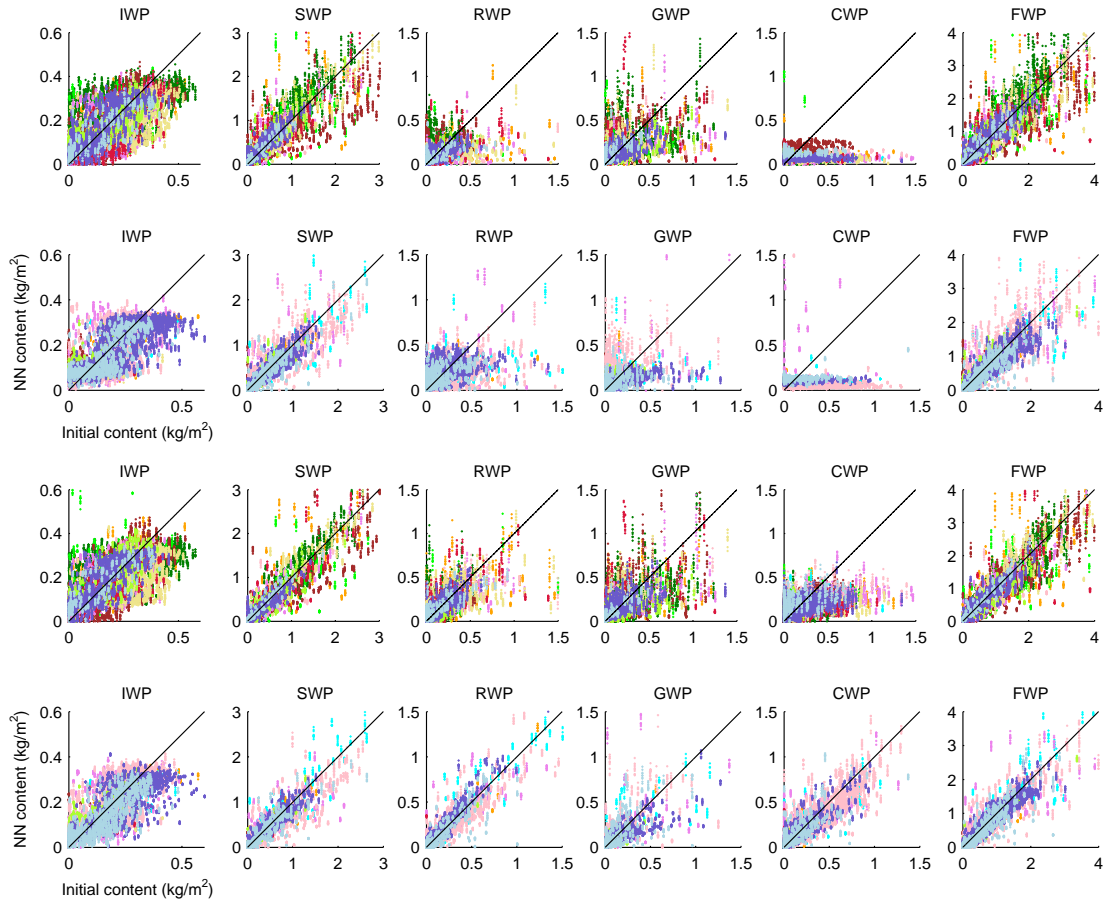


FIGURE 3.19: Same as in Figure 3.16, but with instrumental noises.

3.3.4 Hydrometeor profile retrieval

3.3.4.1 Retrieval approach based on a PCA representation

In order to represent the IWC, SWC, RWC, GWC, CWC, and FWC vertical profiles, 6×10^4 variables are needed. It would be unrealistic to retrieve independently these 624 variables from the small number of microwave channels (and even lower number of independent pieces of information in the observations, see Section 3.2). Therefore, a PCA technique was used to reduce the size of the outputs in the retrieval algorithm, by using the strong dependencies (correlations) that exist between the vertical layers in the profiles, and among the hydrometeor types. In order to represent 99 % of the 6 hydrometeor profiles variance, 35 components are necessary over sea and 42 components over land. Note that the PCA has been performed over all the hydrometeor profiles at once. A NN model is then used to retrieve from, the microwave channels, these 35 or

42 components that are then reversed into the original coordinate to obtain the hydrometeor profiles. It should be noted that only 4 (resp. 6) pieces of information were present in the ICI-only (resp. ICI+MWI) channel-configuration (Section 3.2) so obviously, only the dominant part of the profile variability can be retrieved, not the details (e.g., vertical inversions in the profiles or subtle altitude-localization in the atmospheric column).

3.3.4.2 Results

Figure 3.20 shows the initial and retrieved IWC, SWC, RWC, GWC, CWC, and FWC profiles from the ICI+MWI channels (with no instrumental noises), for case 11, along the transect between 8°W and 9°W. The vertical structures of the cloud systems, especially the convective cores, are well reproduced, with the similar amount and location of the frozen particles that the WRF predicted ones. For the IWC profile retrieval, the results imply that the retrieved IWCs are much larger (up to 0.15 kg/m^3) than the initial ones (up to 0.08 kg/m^3). This overestimation might be because the NN retrieval gets confused between the contribution to the brightness temperatures of the ice and other frozen particles. For the liquid particle profile retrievals, the NN underestimates their contents, with limited vertical structures compared to the initial ones. Overall, the retrieval algorithm can capture the principal structure of frozen phase profiles. Considering the number of pieces of information required to fully represent the hydrometeor profiles, and the information content of the satellite observations, the retrieval of the six hydrometeor profiles remains a true challenge. Our retrieval gives one profile solution (i.e., the simplest and most regular profiles) among all the possible ambiguous ones. This is the only possible strategy, unless an independent source of information is added (e.g., a physical model in a variational assimilation context).

3.4 Conclusion

In this chapter, a statistical retrieval algorithm of cloud parameters has been developed based on the simulated brightness temperatures for ICI and MWI channels, at frequencies from 19 to 664 GHz, for the preparation of the next generation of European operational meteorological satellite. The retrieval database is derived from ARTS radiative transfer simulations fed by a detailed and realistic description of the atmospheric profiles from WRF cloud resolving model, for twelve European mid-latitude scenarios. Successful evaluation by comparison with the SSMIS observations up to 190 GHz gives us confidence in these WRF+ARTS simulations. Our retrieval database contains the geophysical variables of interest describing the 12 cases and the corresponding simulated brightness temperatures at ICI and MWI channels.

First, the statistical quality of the database, as well as the information content of the simulated brightness temperatures have been investigated, with PCA and correlation analyses. 4 (36) independent pieces of information can describe 99 % of the variability of the vertically integrated content (of the profiles). However, only 4 (6) pieces of

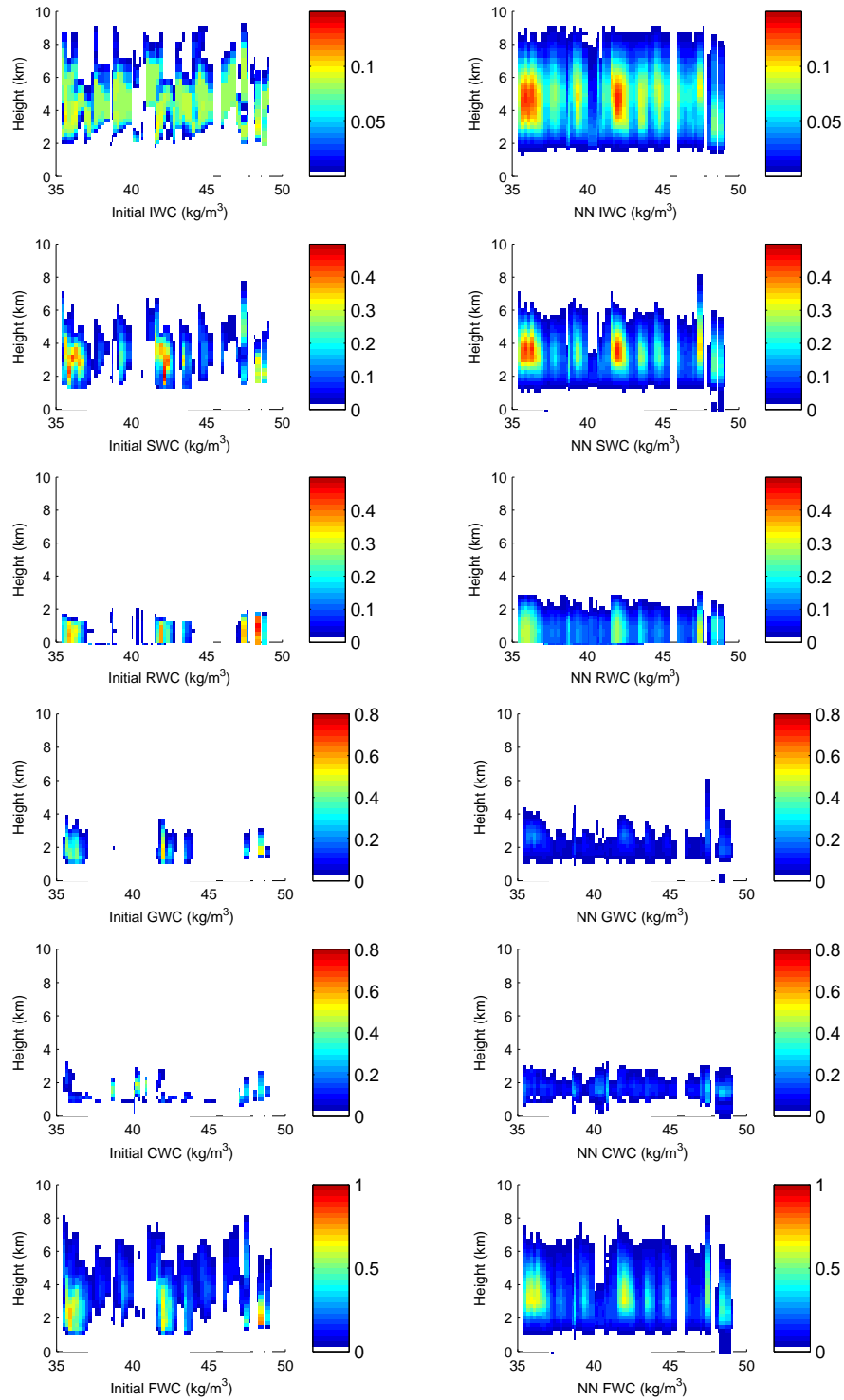


FIGURE 3.20: Initial (left) and retrieved (right) IWC, SWC, RWC, GWC, CWC, and FWC profiles from the ICI+MWI channels for case 11, along the transect between 8°W and 9°W .

information can be derived from 13 ICI (39 ICI+MWI) channels (for again 99 % variance), which shows the difficulty of integrated hydrometeor content retrievals with only ICI channels and the hydrometeor profile retrievals, even with ICI+MWI channels. In

addition, according to the correlation analysis, the ICI channels have stronger correlations with cloud frozen phases than with the liquid phases (especially with the cloud ice particles for frequencies above 448 ± 7.2 GHz), indicating their potential for the frozen particle retrieval. The MWI channels at lower frequencies are therefore added to the retrieval to improve the quantification of liquid particle phase.

A NN classifier and a NN retrieval algorithm are developed to detect and quantify each cloud hydrometeor quantity, trained in the WFR+ARTS database, for ICI-only and for ICI+MWI channels. The classifier gives very satisfactory accuracy in detecting the cloud frozen hydrometeors when using ICI-only channels, with an accuracy of ~ 90 % of the cloud detection over land and ocean. For the cloud hydrometeor quantification, the retrieved cloud frozen phase contents is satisfactory with ICI-only channels for IWP above 0.05 kg/m^2 . The absolute error is larger than 0.04 kg/m^2 for IWP less than 0.05 kg/m^2 , showing the difficulty in lower IWP retrieval. The relative error for the retrieved integrated frozen water content (FWP) is below ~ 40 % for $0.1 \text{ kg/m}^2 < \text{FWP} < 0.5 \text{ kg/m}^2$ and below ~ 20 % for $\text{FWP} > 0.5 \text{ kg/m}^2$. Adding the MWI channels improves the detection and quantification essentially for the cloud liquid phase, as expected. The retrieval results are better over sea than over land, however, there is no evident discontinuity between them. For the hydrometeor profiles, the retrieval algorithm can capture the major vertical structures of the cloud profile, but fails to detect the fine scale structures.

Chapter 4

Microwave Surface Emissivity Calculations Using Airborne Measurements

4.1 Introduction

The next generation of (EUMETSAT) Polar System-Second Generation (EPS-SG) will carry an instrument, the ICI, with frequencies up to 664 GHz (see Chapter 1 for its channels and other characteristics). It will expand the current capabilities for the characterization of the cloud frozen phase, but this is challenging as the radiative transfer models have not been fully developed and evaluated yet up to these frequencies. More specifically, no effort has been made yet toward the estimation of the surface emissivity at frequencies above 200 GHz. Under a large range of atmospheric conditions, satellite observations above 200 GHz will not be sensitive to the surface contribution, due to the increased atmospheric opacity with frequencies. However, for dry atmosphere, a portion of the signal received by the satellite can come from the surface (see Figure 4.1 that presents the total atmospheric transmission at nadir, as calculated by ARTS, for five standard atmospheres from the Fast Atmospheric Signature Code (FASCOD)). Under dry and cold conditions, a reliable estimate of the surface emissivity is necessary to account for the surface contribution and perform an accurate retrieval of the atmospheric properties. High atmospheric transmissions at high frequencies occur primarily around the poles and at mid-latitude during winter, even up to 480 GHz.

Over open ocean, the emissivity varies primarily with the surface wind speed, and models have been developed to estimate the emissivity as a function of surface wind speed and direction, sea surface temperature, and salinity. Several models exist for the calculation of the ocean emissivity. The FAST microwave Emissivity Model (FASTEM) (English and Hewison, 1998, Liu et al., 2011) is currently used in major Numerical Weather Prediction centers up to 200 GHz and provides realistic estimates of the sea surface emissivities. It is based on a full physical emissivity model. For computational efficiency, the full model has been parameterized for current observations up to 200 GHz and up to 65° incidence angle. FASTEM has undergone several updates, from FASTEM-1 to FASTEM-6. The changes from one version to the other, are documented in Bormann et al. (2004). The parameterization is optimized for frequencies below 200 GHz. It has been calibrated and validated in the operational framework. Another emissivity model, based on similar principles has been developed by Prigent and Abba (1990). It is a geometric optic model, with the sea surface described as a set of flat surfaces with a bi-directional slope distribution, derived from photographic observations of the sun glitter on the sea. The initial version of this physical model has been updated using the FASTEM model for the dielectric properties of sea water, for the foam cover, and for the foam emissivity.

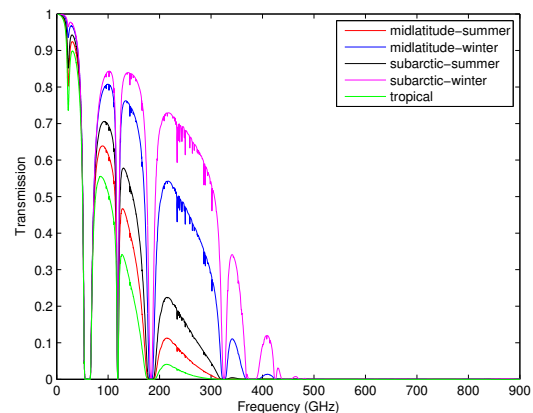


FIGURE 4.1: Total transmission of the atmosphere at nadir, as calculated with ARTS, for five standard atmospheres from FASCOD.

Based on these two models, an emissivity parameterization (the Tool to Estimate the Sea Surface Emissivity at Microwaves and Millimeter waves, TESSEM², Prigent et al., 2016) was developed at LERMA and has already been presented in Chapter 2. It mimics FASTEM up to 200 GHz and transitions smoothly to our physical model for higher frequencies.

For the frozen surfaces, physical modeling (e.g., numerical modeling, theoretical modeling) of the emissivity of snow and ice at microwave frequencies is particularly complex, given the large variety of the snow and ice signatures in this frequency range. The interaction between the radiation and snow/ice involves both volume and surface scattering, and the mechanisms are very variable in space and time. A variety of models exists (see Matzler (2006) for a review). Four major models are available to the community: the Community Radiative Transfer Model (CRTM) from NOAA (Weng et al., 2001), the single-layer model from Helsinki University of Technology (HUT) (Pulliainen and Grandeil, 1999), the Microwave Emission Model of Layered Snowpack (MEMLS) from University of Bern (Wiesmann and Matzler, 1999), (adapted by Tonboe (2010) for sea ice), and the Dense Media Radiative Transfer (DMRT) snow models (Picard et al., 2013, Tsang et al., 2007). However, the need in these models for a detailed description of the snow and ice parameters (e.g., the snow grain size distribution, the stratification of the snow medium, and the quantification of the brine inclusion in sea ice) makes it very difficult to provide realistic estimates at continental scales where such information is clearly not available. Even if a perfect model existed, the lack of reliable input parameters would jeopardize its robustness. Modeling results above 100 GHz can be very misleading as the complexity of the interaction of the radiation and the surface might not be taken into account at high frequencies. Some efforts to validate the MEMLS model have been conducted, with airborne measurements between 89 and 190 GHz (Harlow, 2011, Harlow and Essery, 2012). However, even under controlled environments, the emissivity modeling is very challenging.

Microwave emissivities have also been calculated directly from satellite observations, removing the atmospheric contribution (gas and clouds) and the modulation by the land surface temperature. This technique has been applied to conical imagers such as SSM/I, TMI, the Advanced Microwave Scanning Radiometer-E (AMSR-E) (e.g., Moncet et al., 2011, Prigent et al., 2006, 2005, 1997) but also to cross-track sounders such as AMSU (e.g., Karbou et al., 2005, Karbou and Prigent, 2005b, Prigent et al., 2005). These estimates capture well the spatial and temporal variabilities of the emissivities. An analysis of the spectral, angular, and polarization dependences of these satellite-derived emissivities was conducted (Prigent et al., 2008), and led to the development of the Tool to Estimate Land Surface Emissivities at Microwave frequencies (TELSEM). TELSEM provides a parameterization of the emissivity for all observing conditions and for all continental surfaces, given the surface location and month in the year, for frequencies from 19 to 90 GHz. It is anchored to a robust climatology of 19 to 85 GHz emissivities, calculated from 15 years of SSM/I observations (Prigent et al., 2006). Compared to model calculations (e.g., CRTM), TELSEM provides emissivity estimates that agree better with satellite observations up to 90 GHz, especially over polar regions (Bernardo et al., 2013, Prigent et al., 2015).

Most satellite-derived emissivity studies focused so far on the frequency range up to 100 GHz, where the atmospheric transmission is significant. Between 100 and 200 GHz, the need for reasonable estimates of the emissivity at AMSU/the Microwave Humidity Sounder (MHS)/the Special Sensor Microwave Imager/Sounder (SSMIS)/the Advanced Technology Microwave Sounder (ATMS) window channels around 160 GHz has triggered some efforts (e.g., at Météo-France (Karbou et al., 2014), at NOAA, and at UK Met Office), but they have not been consolidated yet. The snow and ice emissivities have been estimated from aircraft observations at AMSU frequencies up to 190 GHz, onboard the UK FAAM aircrafts (Harlow, 2009, 2011, Hewison and English, 1999, Hewison et al., 2002). These studies confirmed the large variability of the snow, ice, and sea ice emissivities as a function of ice and snow types.

A pragmatic approach to parameterize (the Tool to Estimate Land Surface Emissivity from Microwave to sub-Millimeter waves, TELSEM², Wang et al., 2016) the snow and ice emissivities up to 700 GHz has been implemented at LERMA (details in Chapter 2). It makes extensive use of the existing satellite-derived emissivities to provide realistic estimates along with reasonable spatial and temporal variabilities.

This chapter focuses on the evaluation of the TESSEM² and TELSEM², using the ISMAR and MARSS measurements. The ISMAR is the demonstrator for ICI and provides as unique opportunity to document the surface emissivity in the 200-700 GHz range. It has been designed to operate at the ICI frequencies (Fox et al., 2014). It flew on the FAAM BAe-146 aircraft during two campaigns (presented in Section 4.2). The other instrument, MARSS, was operated onboard the same aircraft, at frequencies from 89 to 183 GHz. The observations of ISMAR and MARSS are examined and evaluated (in Section 4.3) to investigate their quality and stability. Then the surface emissivity parameterizations are partly evaluated by comparison with emissivity estimation from the ISMAR and MARSS observations in Section 4.4. Section 4.5 concludes this chapter.

4.2 The instruments and the campaigns

4.2.1 The instruments

ISMAR has been jointly funded by the UK Met Office and ESA (see Figure 4.2). It has been designed and built by a consortium of Rutherford Appleton Laboratory (RAL), Radiometer Physics GmbH (RPG), and Systems Engineering and Assessment (SEA) (Charlton et al., 2009, Fox, 2015). It is an along-track scanning radiometer, and it operates with multiple channels at millimeter and sub-millimeter wavelengths: five channels in the oxygen line at 118.75 GHz, three channels in the 325.15 and the 448 GHz water vapor lines, and two window channels at 243.2 and 664 GHz. The two window channels have two orthogonal polarizations which rotate with scan angle, giving both V and H polarizations in the +50° downward view. It is the same for the other channels, but only V polarization is given in the +50° downward view (Fox, 2015). The instrument is calibrated against two blackbody targets, one at ambient temperature, the other one

heated. The instrument viewing angles are between $+55^\circ$ and -10° downward and between $+10^\circ$ and -40° upward. Each scan takes ~ 4 s. A typical scan pattern will start at the forward (heated) calibration target and step through the nadir views, the aft (unheated) calibration target, and finally the zenith views. The integration time for each angle is around 100 ms, as well as for each calibration load.

MARSS is an along-track scanning passive radiometer as well. It observes in five channels, including two window channels (89 and 157 GHz) and three channels near the water vapor line (183 GHz). These channels correspond to channels 16 to 20 on AMSU (Saunders et al., 1995). MARSS was first operated on the UK Met Office Research Flight C-130 Hercules aircraft, and then moved to the FAAM BAe-146 aircraft (indicated in Figure 4.2). These are also close to channels that will be available on the Microwave Imaging Radiometer (MWI). The radiometer consists of an external pod containing the scanning mechanism and the calibration targets, and a part in the fuselage with the front end receiver. Each scan takes 3 s, with 18 scene views (9 upward and 9 downward at each 10° from -40° to $+40^\circ$) and 2 views to the blackbody targets. A single linear polarization is measured in each channel, and the polarization rotates with scan angle. For more details, see Guillou et al. (1996), Hewison (2006).



FIGURE 4.2: The positions of ISMAR and MARSS on board the FAAM BAe-146 research aircraft.

The channels specifications for both instruments are listed in Table 4.1.

4.2.2 The campaigns

ISMAR and MARSS operated onboard the FAAM BAe-146 research aircraft at altitudes from 50 to 35000 ft, in three scientific campaigns. Note that the last one is very recent and has not been analyzed yet, but some information can be found in Chapter 6. The first, the Sub-millimeter Trial in Cirrus and Clear Skies (STICCS-2) operated out of Prestwick (Scotland, UK) between November 26, 2014 and December 15, 2014, and concentrated on measurements in clear-sky and thin cirrus cases. The second, the Cold-air Outbreak and Sub-Millimeter Ice cloud Study (COSMICS) took place during the period March 4-25, 2015, also from Prestwick, with flights up to Greenland. I participated in flight ‘B878’ in the STICCS-2 ISMAR campaign. Table 4.2 provides information on the different flights during these two campaigns (a total of 15 flights).

In addition to the ISMAR and MARSS instruments, a large number of instruments flew in the aircraft during these campaigns: infrared and visible spectrometers, a mini-lidar, cloud imaging probes, cloud droplet probes, an aerosol sampler, and dropsondes. The in situ vertical temperature, humidity, and wind speed profiles below the aircraft can

TABLE 4.1: Channel characteristics of the ISMAR and MARSS instruments, including their frequencies, BandWidth (BW), instrument noise (measured Net Δ T on liquid nitrogen cooled target over 60 seconds, from Fox et al., 2016), polarization, Field-Of-View (FOV) angle (full-width at half-maximum), and main spectral features. The polarizations indicated here are the polarizations in the +50° downward view for all the channels. The MWI (MicroWave Imager) is an instrument on board the MetOp-SG as ICI.

Instrument (GHz)	Channels (GHz)	Freq. Off. (GHz)	BW (GHz)	Net Δ T (K)	Polar.	FOV (deg)	Spectral feature
MARSS (MWI)	89	± 1.1	0.65	0.42	Mixed	12.0	Window
$5 \times$ ISMAR (MWI)	5×118.75	± 1.1	0.4	0.4	$5 \times V$	$5 \times <3.8$	$5 \times O_2$
		± 1.5	0.4	0.4			
		± 2.1	0.8	0.3			
		± 3.0	1.0	0.3			
		± 5.0	2.0	0.3			
MARSS (MWI)	157.0	± 2.6	2.6	0.69	H	11.0	Window
$3 \times$ MARSS (ICI)	3×183.31	± 1.0	0.45	0.64	$3 \times H$	3×6.2	$3 \times H_2O$
		± 3.0	1.0	0.44			
		± 7.0	2.0	0.35			
$2 \times$ ISMAR (ICI)	2×243.2	± 2.5	3.0	0.3	V	$2 \times <3.6$	$2 \times$ Window
				0.4	H		
$3 \times$ ISMAR (ICI)	3×325.15	± 1.5	1.6	1.6	$3 \times V$	$3 \times <3.6$	$3 \times H_2O$
		± 3.5	2.4	0.7			
		± 9.5	3.0	1.1			
$3 \times$ ISMAR (ICI)	3×448.0	± 1.4	1.2	1.1	$3 \times V$	$3 \times <3.6$	$3 \times H_2O$
		± 3.0	2.0	1.6			
		± 7.2	3.0	2.8			
$2 \times$ ISMAR (ICI)	2×664.0	± 4.2	5.0	3.3	V	$2 \times <3.8$	$2 \times$ Window
				1.3	H		

be measured by the dropsondes, with possible shifts between the air masses sounded by the dropsondes and the ones observed by the microwave instruments.

4.3 Evaluation of the ISMAR/MARSS observations

4.3.1 Example of four flights

All flights have been examined and evaluated, but for illustration purposes, four of them (i.e., B875, B893, B896, and B898) will be detailed here. They correspond to flights of interest for emissivity calculation, two for the ice-free ocean emissivity, the other two for sea ice and continental ice emissivities, with low level altitude transects and limited cloudiness.

Flights B893 (from the COSMICS campaign) and B875 (from the STICCS-2 campaign) are of special interest for the ice-free ocean emissivity calculations. Flight B893 took off the east coast of Scotland on March 10, 2015, under clear sky condition. Figure 4.3 shows the flight path, with the aircraft altitude in color (also shown on the right as a function of observation time). A number of low-level runs were performed at 100, 500, and 1000 *ft* above the surface around 16:00. The closest atmospheric profiles in time and space are extracted from the European Reanalysis Interim (ERA Interim). The

corresponding surface skin temperature, the 10-m wind speed, the total integrated Water Vapor Content (WVC), and the cloud fraction are plotted in Figure 4.4. The conditions are rather cold and dry (~ 280 K for the sea surface temperature and ~ 7 kg/m² for WVC). Four dropsondes were released during that flight, from high altitudes (about 33000 ft) (their releases are indicated by squares in Figure 4.3 on the left).

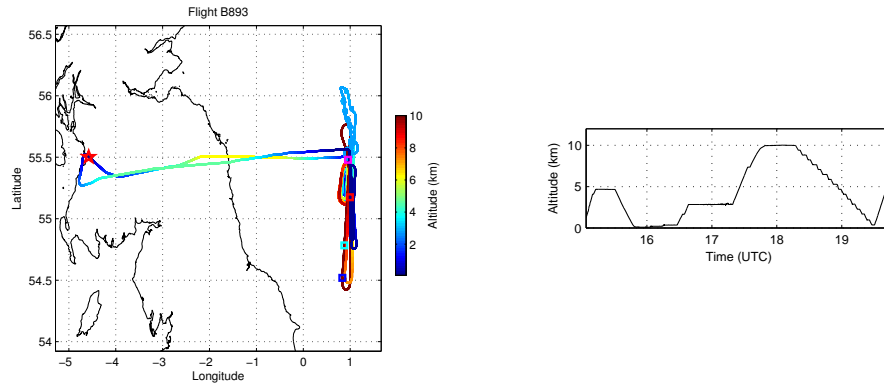


FIGURE 4.3: Left: The flight track of B893 with the flight altitude in color. The red star is the place for take off, and the four squares in blue, light blue, red, and purple show the launching points of the first, second, third, and fourth dropsondes, respectively. Right: The flight altitude as a function of time.

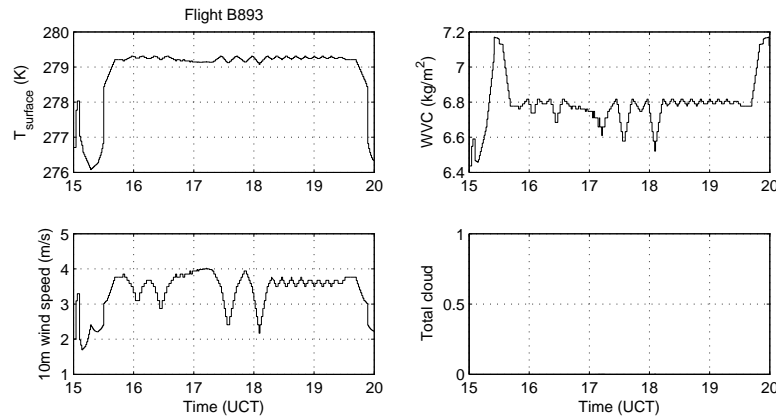


FIGURE 4.4: The surface skin temperature, the integrated water vapor content, the 10-m wind speed, and the fraction of total cloud against the observation time during flight B893 from ERA Interim data.

Figures 4.5 and 4.6 present the measured brightness temperatures for all channels, for the up-looking views at zenith and for the down-looking views at nadir, respectively. Around 17:00, the plane orbited at angles between 20° and 60° at 9000 ft, inducing related changes in most channels (except the most opaque and saturated ones), for both zenith and nadir views. Otherwise, the brightness temperatures appear stable, with the expected flight altitude dependence. The frequency dependences from a channel to the other are also in agreement with the expectation. Limited spikes appear, related to a few short periods of instrument instabilities. The 664 GHz channels are much noisier than the other ones, especially in the vertical polarization. In addition, the polarization difference at this frequency is not negligible even for the up-looking views where no polarization difference is expected.

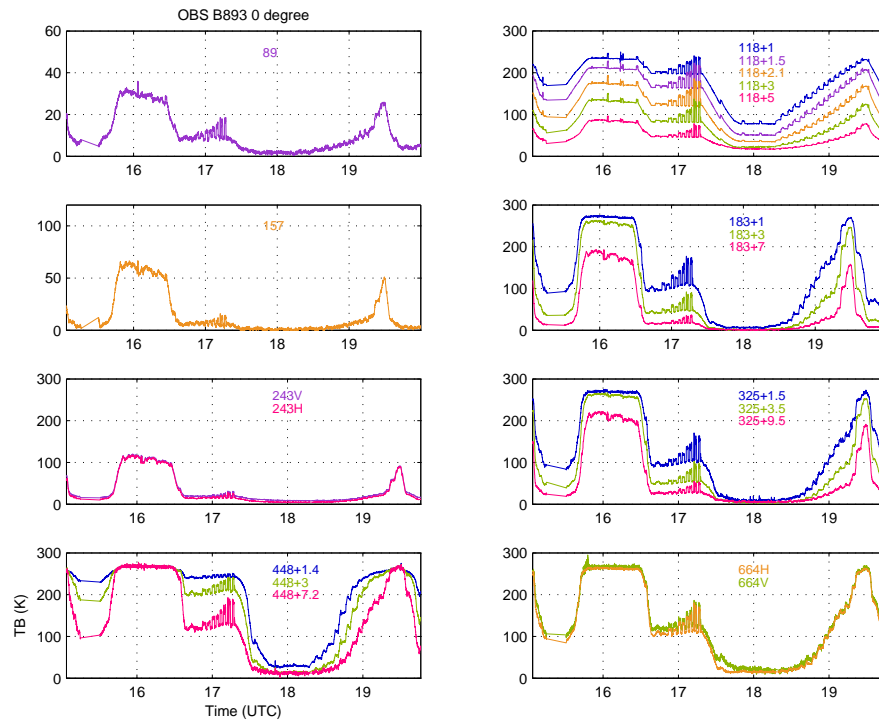


FIGURE 4.5: The MARSS and ISMAR observations as a function of observation time for flight B893 at zenith.

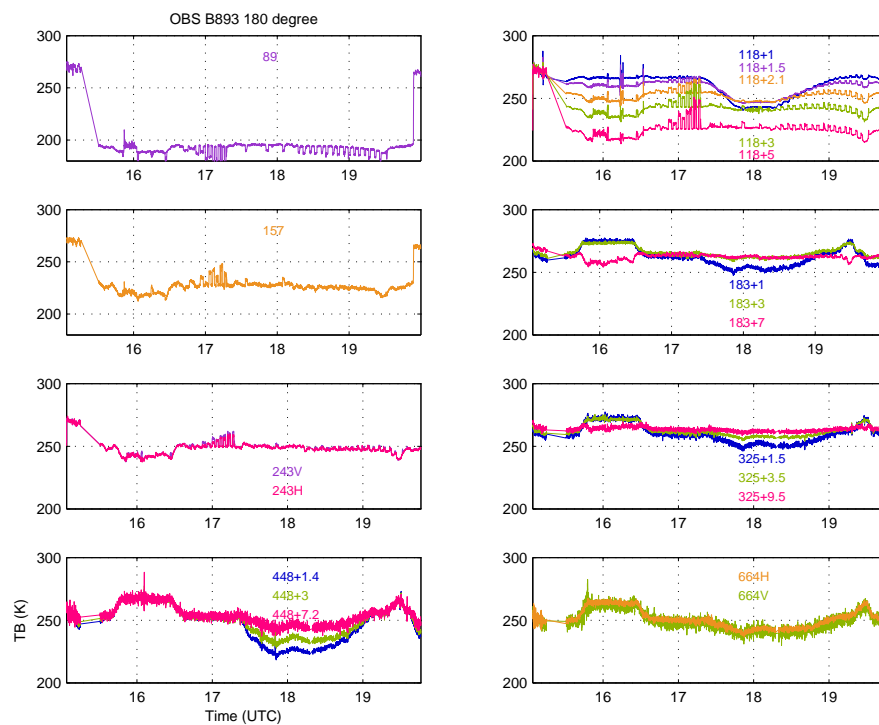


FIGURE 4.6: Same as Figure 4.5, but at nadir.

Flight B875 was operated under clear sky conditions as well on November 28, 2014 in

Northwest of Scotland. Like flight B893, observations are mostly performed over the sea (shown in Figure 4.7). Low-level observations were conducted around 15:00. During this flight, the water vapor content (shown in Figure 4.8) is $\sim 11\text{--}12 \text{ kg/m}^2$, a bit higher than the one during flight B893 (in Figure 4.4).

Figures 4.9 and 4.10 show the observed brightness temperatures for all channels of the MARSS and ISMAR for this flight, for the up-looking views at zenith and for the down-looking views at nadir, respectively. The 243 GHz V channel was noisy. Occasional spikes are found for the 325.15 ± 1.5 and 448 ± 1.4 GHz channels. The 664 GHz H channel is less stable, and some noisy brightness temperatures are observed from 16:02 to 16:21, 16:36 to 16:57, and 17:13 to the end of the flight. Four dropsondes, marked in Figure 4.7, were released at 30000-34000 *ft*.

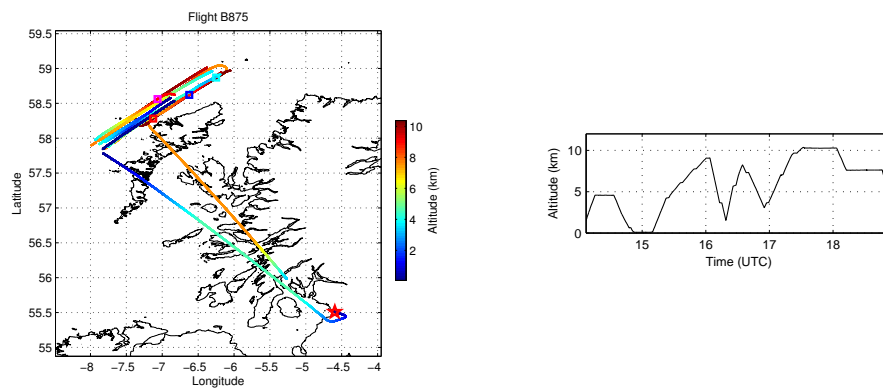


FIGURE 4.7: Left: The flight track of B875 with the flight altitude in color. The red star is the place for taking off and the four squares in blue, light blue, red, and purple show the launching points of the first, second, third, and fourth dropsondes, respectively. Right: The flight altitude as a function of time.

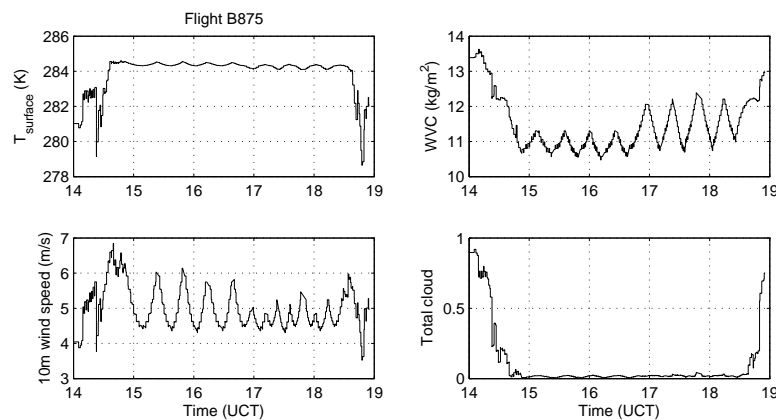


FIGURE 4.8: The surface skin temperature, the integrated water vapor content, the 10-m wind speed, and the fraction of total cloud against the observation time during flight B875.

TABLE 4.2: Flight characteristics during the two campaigns.

Flight	Date	Location	Comments
<hr/>			
STICCS	2014		
B875	Nov. 28 (5h)	North-west of Scotland (sea)	Clear sky condition. Several low-level runs for emissivity retrieval.
B878	Dec. 02 (5h)	East coast of Scotland (sea) and east of England (land)	One part under clear sky over the sea off the east coast of Scotland at different altitudes, the other part, thin cirrus conditions over land on the eastern of England.
B879	Dec. 03 (3h)	West of Prestwick (sea)	Stratocumulus cloud conditions with clear air above and above clouds.
B884	Dec. 14 (5h)	North-east of Edinburgh (sea)	Cloud conditions (cirrus, cumulus, and stratocumulus). First part for wind probe calibration maneuvers, and the second part for cirrus cloud study.
<hr/>			
COSMICS	2015		
B889	Mar. 05 (2.6h)	Northwest of Prestwick (sea)	ISMAR measurements aborted during this flight.
B891	Mar. 08 (1.7h)	East of Edinburgh (sea)	Test of ISMAR and analysis of the cirrus clouds. ISMAR operated normally on the ground and initially in flight, failure during climb at around FL160.
B892	Mar. 09 (2.7h)	West coast of Scotland (sea)	ISMAR test in clear air above stratocumulus clouds.
B893	Mar. 10 (5.3h)	East coast of Scotland (sea)	Low-level runs under clear sky conditions for surface emissivity study.
B894	Mar. 11 (4.6h)	Northeast of Aberdeen (sea)	Intent to measure cirrus off north-east Scotland. Aborted due to aircraft science power failure.
B895	Mar. 13 (3.7h)	North of Scotland (sea)	Cirrus study.
B896	Mar. 17 (5.1h)	Over Greenland	Measurement over Greenland, with some clouds observed during the flight.
B897	Mar. 18 (3.5h)	East coast of Iceland	Flight over a precipitating frontal system. Three transects across the system. Cloud varied from thin and broken cirrus clouds to full-depth precipitating clouds. Measurements mostly above the cloud tops.
B898	Mar. 19 (4.5h)	Over Greenland	Clear sky condition mainly, with some occasional cirrus. Some low level observations over the ice cap.
B900	Mar. 21 (2h)	Along west Scottish coastline	Measurement of cirrus from Prestwick to Iceland. Aircraft science power failed at the beginning of the science section, and redirection toward Keflavik. Observations over land along west Scottish coastline.
B901	Mar. 22 (2.5h)	West of Reykjavik	Not designed for ISMAR. Measurements above and below supercooled liquid stratocumulus clouds.

Flights B896 and B898, from the COSMICS campaign, are of special interest for emissivity calculations over snow and ice: they provide level runs suitable for surface emissivity calculation, under dry and cold conditions. They took place over Greenland on March 17, 2015 and on March 19, 2015, respectively. Figure 4.11 indicates the two flight patterns and the flight altitudes. The two flights started from Iceland and aimed at the Greenland summit, with B898 east of B896. Low-level runs for flight B896 were designed from the Greenland plateau down to the coast over the sea ice after 16:00. The high-level runs were in the vicinity of the summit in conjunction with satellite over-pass. The atmospheric background during these flights are presented in Figure 4.12. The Greenland

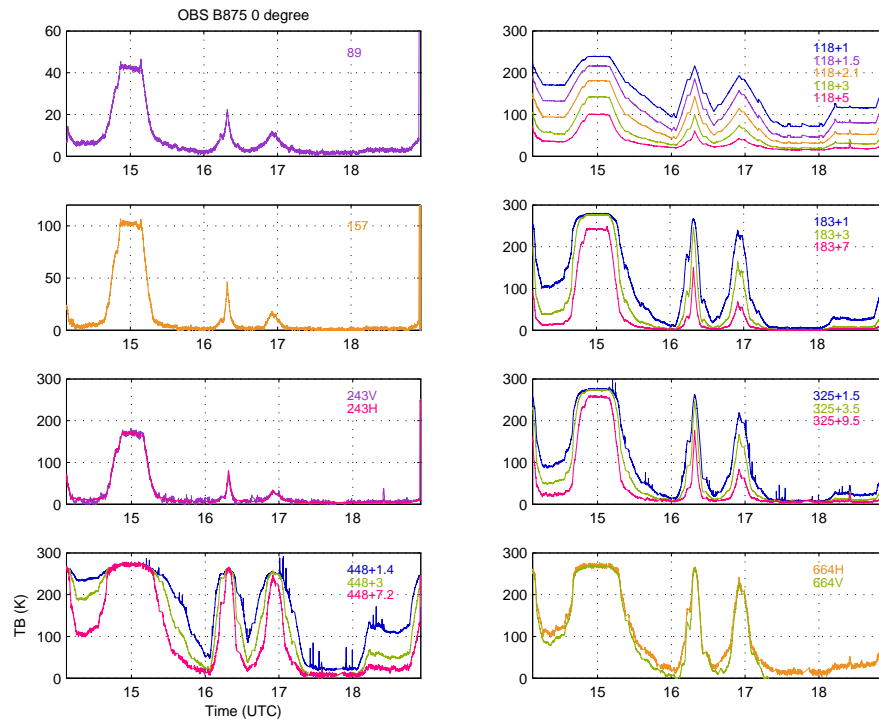


FIGURE 4.9: The MARSS and ISMAR observations as a function of observation time for flight B875 at zenith.

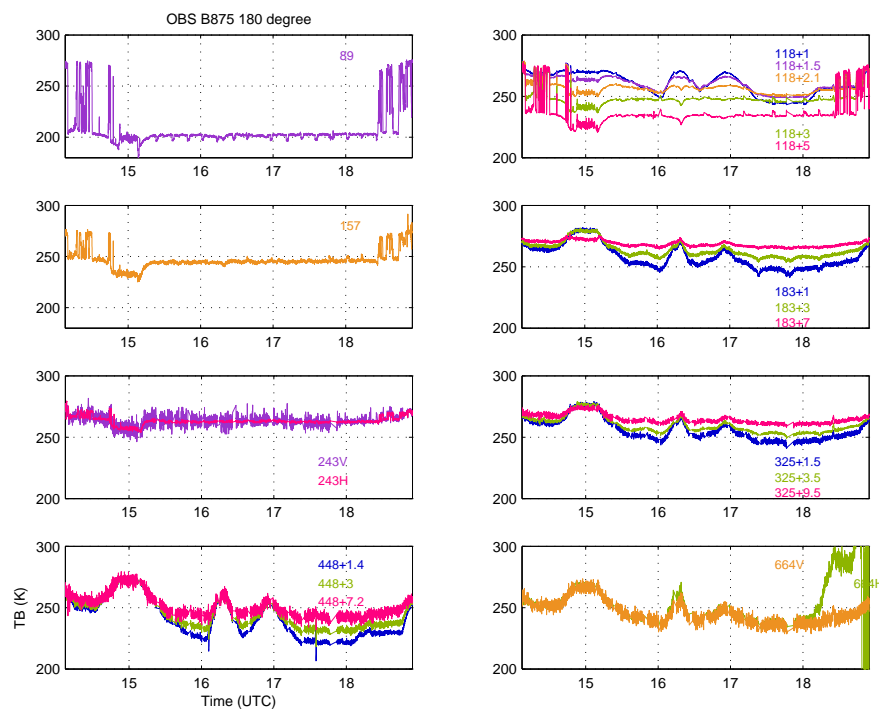


FIGURE 4.10: Same as Figure 4.9, but at nadir.

surface temperature is around 230 K, and the WVC is less than 1 kg/m^2 .

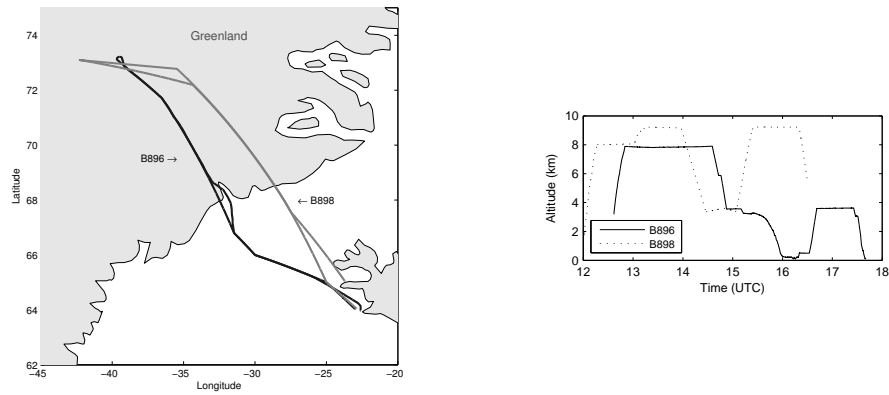


FIGURE 4.11: Left: The flight tracks of flights B896 and B898. Right: The flight altitudes as a function of time for these two flights.

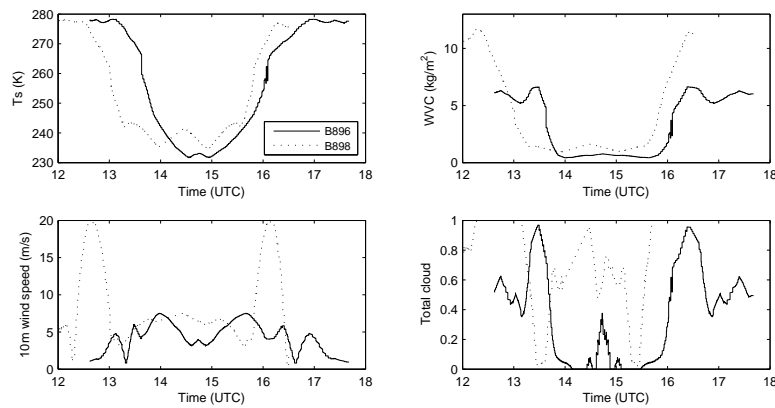


FIGURE 4.12: The surface skin temperatures, the integrated water vapor contents, the 10-m wind speeds, and the fractions of total clouds against the observation time during flights B896 and B898.

Figures 4.13/4.15 and 4.14/4.16 present the observed brightness temperatures at zenith and nadir respectively for flight B896/B896. From Iceland to Greenland, these two flights overpassed sea ice on their way toward the Greenland summit, and then flew back to Iceland (Figures 4.11). During flight B896, the temperature separation between the two calibration targets were below 50 K from 14:00 to 16:36, but data still appear stable. The 448 ± 1.4 GHz voltage saturated around 15:00, and was very close to saturation shortly after 16:00. For the down-looking views, a rather large spatial variability is noticed up to $\sim 14:00$. This corresponds to the over flying of coastal regions with large spatial variability (sea ice, fjord, and mountainous areas). After 14:00, the aircraft overflies the Greenland plateau and the brightness temperatures are smoother, especially at window frequencies. Some clouds were present during these flights (Figures 4.12), with some expected effects, especially at high frequencies. Note that, according to the lidar measurements, provided by UK Met Office, ERA-Interim was overestimating cloud cover, which were clear over the summit plateau. For flight B896, there was no cloud presence below the aircraft between 13:48 ($\sim 68.5^\circ\text{N}$) and 16:12 (close to the coast). For flight B898, there was high cloud below the aircraft up until about 13:24 (69.5°N), after which it was clear until 15:24 (70°N). The 664 GHz channels are much noisier than the

other ones, as in previous discussions. The polarization difference at this frequency is still not negligible.

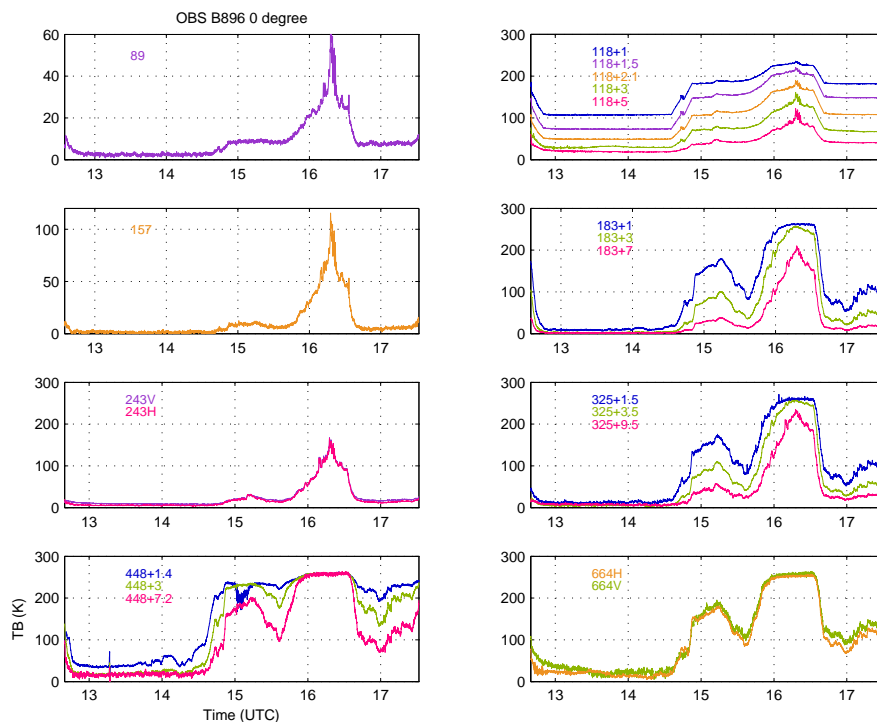


FIGURE 4.13: The MARSS and ISMAR observations as a function of observation time for flight B896 at zenith.

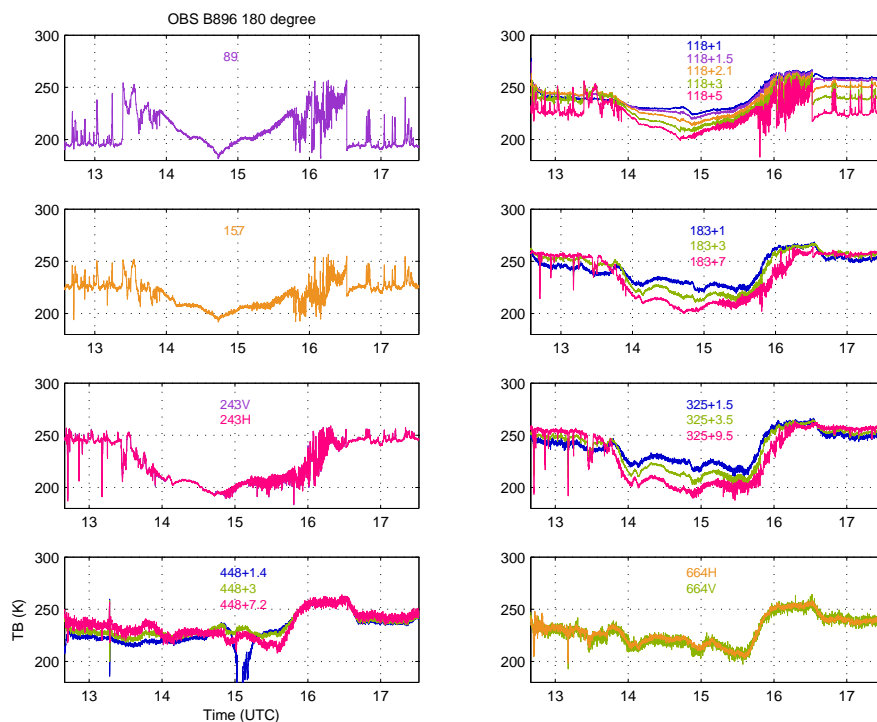


FIGURE 4.14: Same as Flight 4.13, but at nadir.

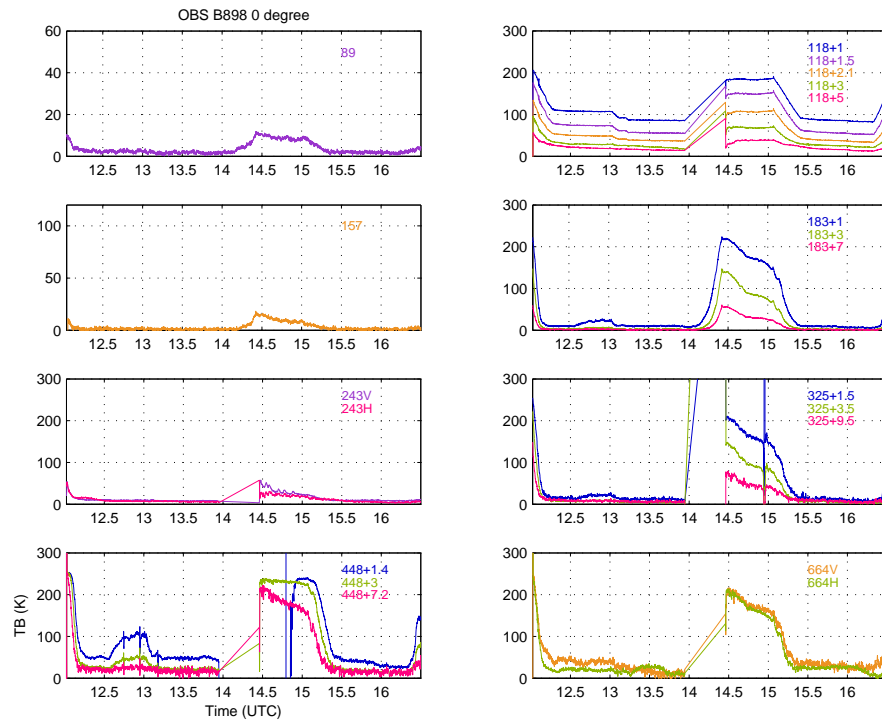


FIGURE 4.15: The MARSS and ISMAR observations as a function of observation time for flight B898 at zenith.

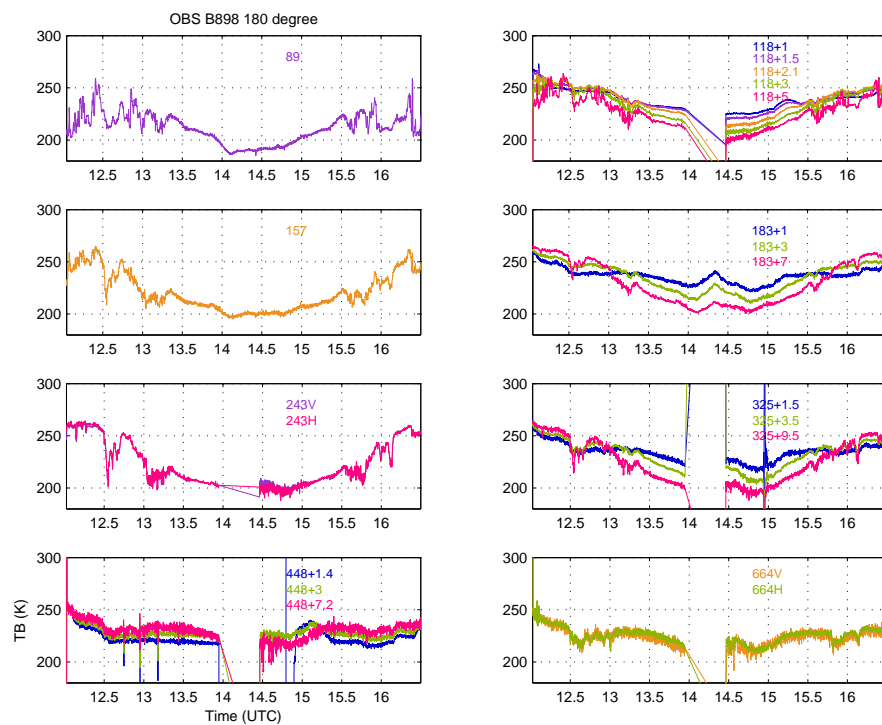


FIGURE 4.16: Same as Figure 4.15, but at nadir.

4.3.2 Estimation of the ISMAR instrument noise

Three versions of the ISMAR TB observations were provided by the UK Met Office. The version differences correspond to different ways of handling the calibration (calculation of the gain and offset, as well as averaging or not of the temperature measurements across the calibration loads). The first version of the data ('firstlook') involved a smoothing of the calibration factors (gain and offset) over 30 s. The second version (r004) did not involve any time averaging, but the temperature measurements across the loads were spatially averaged (contrarily to the first version where only the central thermistor was used). The last version of the data (r006) adopted a smoothing of the calibration factors over 60 s along with a temperature averaging at the load surfaces (S. Fox, personal communication). The three versions of the data are compared. The standard deviations (stds) of the brightness temperatures for all channels are calculated over 30 s for all the flights, separately for the upwelling and downwelling views at zenith and nadir (other integration times have been tested, with limited changes). This std includes the instrument random noise ($\text{Ne}\Delta T$) as well as the signal natural variability over the 30 s related to changes in observing conditions (plane attitudes and atmosphere/surface heterogeneity). The results for flight B893 are presented in Figures 4.17, 4.18, and 4.19. The corresponding MARSS noises are also shown, although they do not change from a version to the other. The changes in ISMAR data between versions are limited between the version without any smoothing of the calibration and the two others, except in the regions where low brightness temperatures were measured (such as around 18:00, see Figures 4.5 and 4.6). Version 'r006' of the data is suggested by S. Fox and used throughout this thesis, as this may reduce some of the measurement biases due to the better estimations of the calibration target temperatures.

The evaluation of the instrument noise by estimating the stds of the brightness temperatures calculated over 30 s is systematically performed for all the flights, using version 'r006' of the data. Figure 4.20 presents the results (zenith and nadir) for the flight B893 for each channel, as a function of the flight altitude. It shows that the window channels (89, 157, and 243 GHz) are much more stable for the up-looking views than for the down-looking views above a certain altitude. This is expected as for the upward views in transparent channels, the signal will not be contaminated much by the atmosphere, whereas for the downward views, it includes the surface variability as well as the contribution from the water vapor in the lower layers. The channels that are affected significantly by the atmospheres are more stable for the downward views than for the upward views: for the downward views, the signal is close to saturation and the variability of the atmospheric and observing conditions do not impact the signal much. As a consequence, for the transparent channels, the stds of the upward views around the mean values at high altitudes should be close to the instrument random noise whereas for the other channels the downward views at high altitudes should be representative of the instrument noise. The 664 GHz channels have significantly different behaviors for the V and H polarizations, with the vertical polarization much noisier than the horizontal one, confirming the previous remarks about the questionable quality of the 664 GHz vertical polarization channel. Table 4.3 compares our estimate of the instrument random noises averaged over all flights with the instrument noise specifications. For most

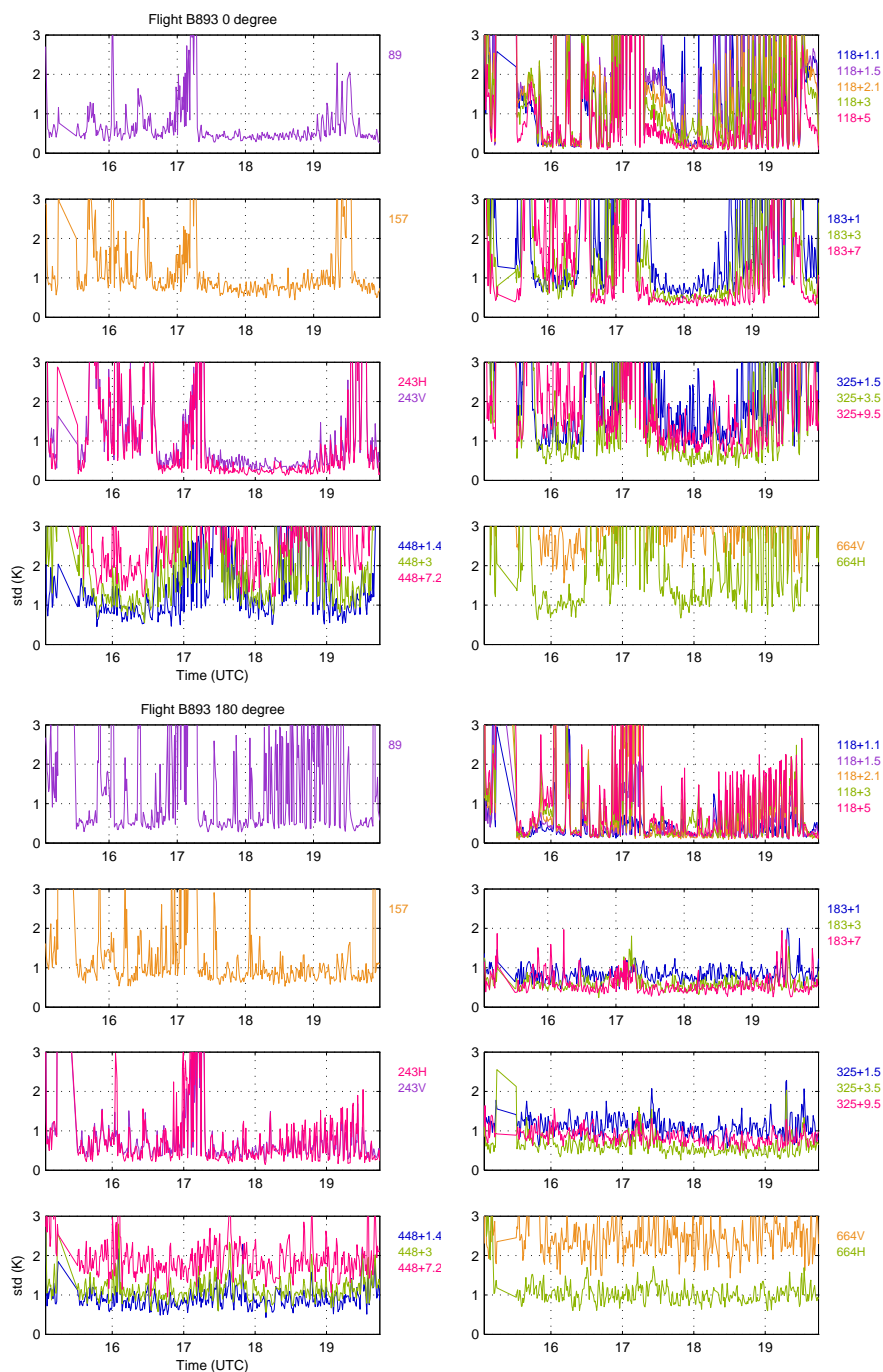


FIGURE 4.17: For flight B893, evaluation of the instrument noise for the first version 'firstlook' of the data for both zenith and nadir views, as a function of time.

channels, the noise evaluation from the aircraft observations is close to the specification. The 243 GHz V, and 448 ± 7 GHz are noticeable exceptions. Note that the intent here is to provide a preliminary assessment of the instrument quality, to show that the observations were usable at least for the emissivity calculation rather than to characterize the instrument. The detailed analysis of the instrument noise has been done carefully by Fox et al. (2016).

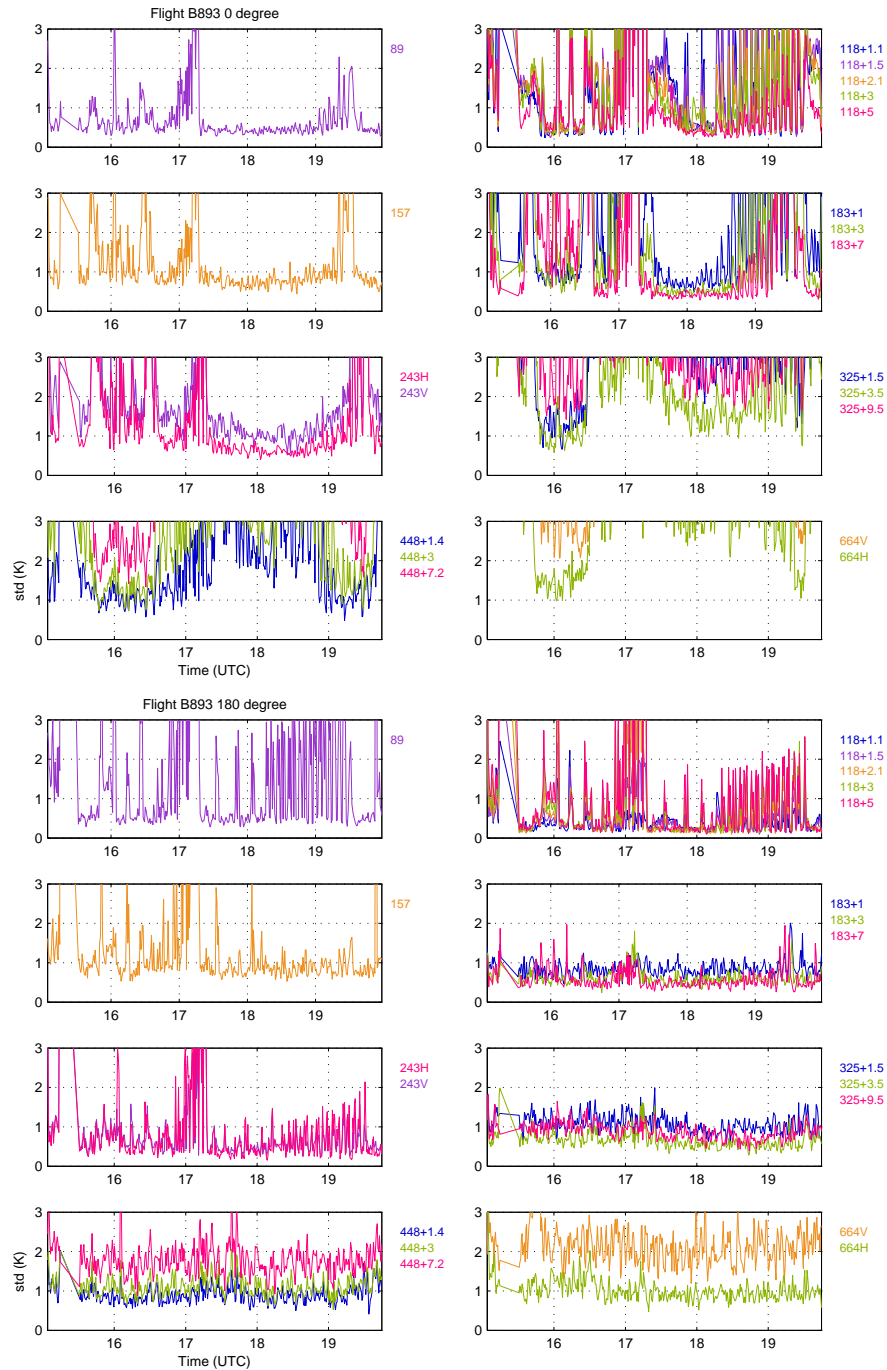


FIGURE 4.18: Same as Figure 4.17, but for the second version 'r004'.

4.3.3 Comparison of the observations and simulations, under clear sky assumptions

The radiometric measurements are now evaluated, by comparing the upward views with radiative transfer simulations, under clear sky assumptions. The downward views could be contaminated by the surface contribution and will not be considered here for this evaluation step. ARTS is adopted to simulate the atmospheric radiative transfer, see Chapter 2 for an introduction to this radiative transfer model. We selected the [Rosenkranz](#)

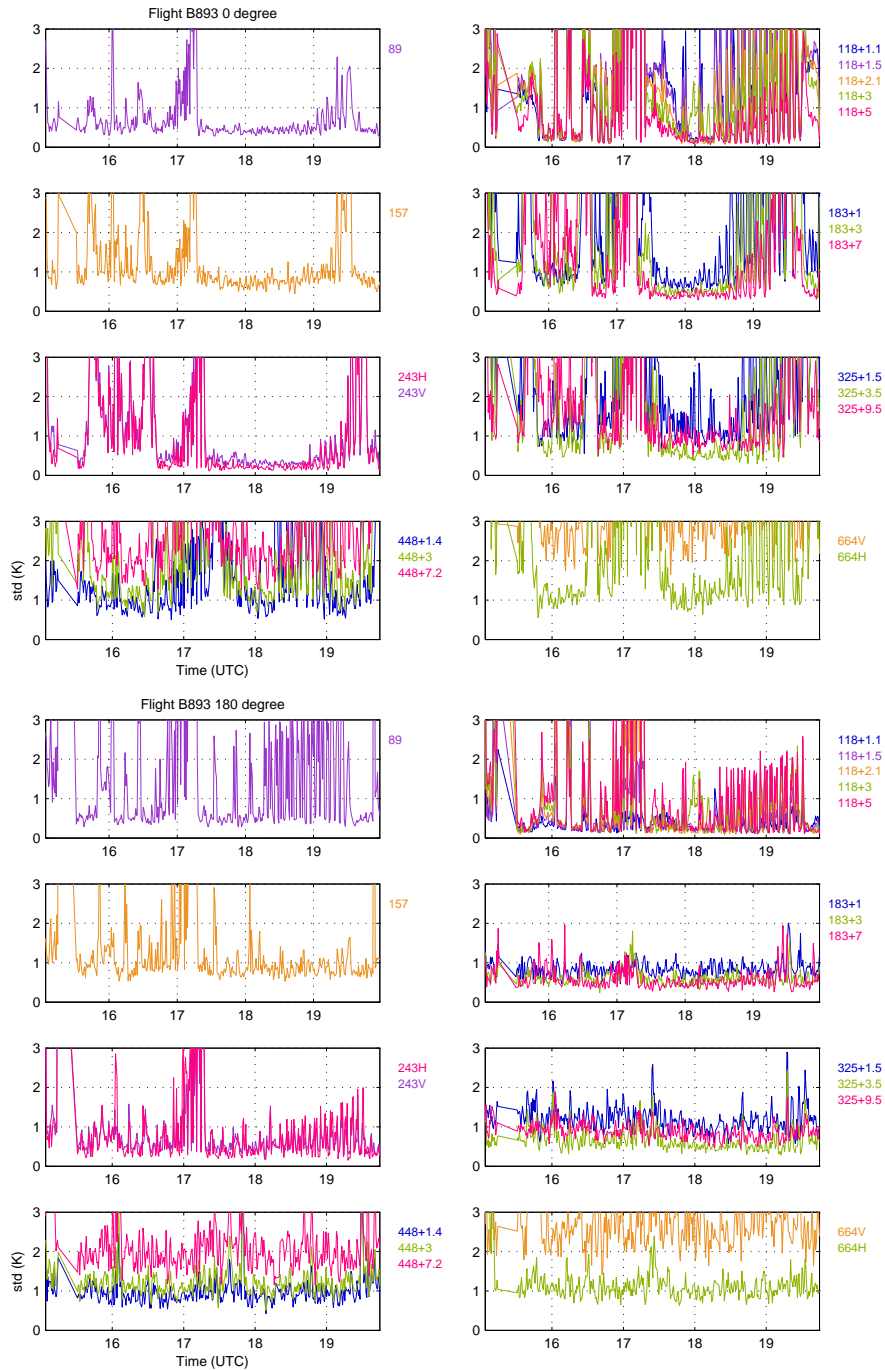


FIGURE 4.19: Same as Figure 4.17, but for the third version 'r006'.

(1998a,b) absorption models for water vapor, oxygen, and nitrogen. The atmospheric profile information is extracted from ERA-Interim profiles ($0.125^\circ \times 0.125^\circ$ horizontal spatial resolution on 60 model lays). The pitch, roll, and orientation angles of the aircraft are taken into consideration in the simulations. Clear sky condition is assumed for all the simulations.

Figures 4.21 and 4.22 show the brightness temperature differences (simulations-observations) for all ISMAR and MARSS channels as a function of time, for flights B893 and B875.

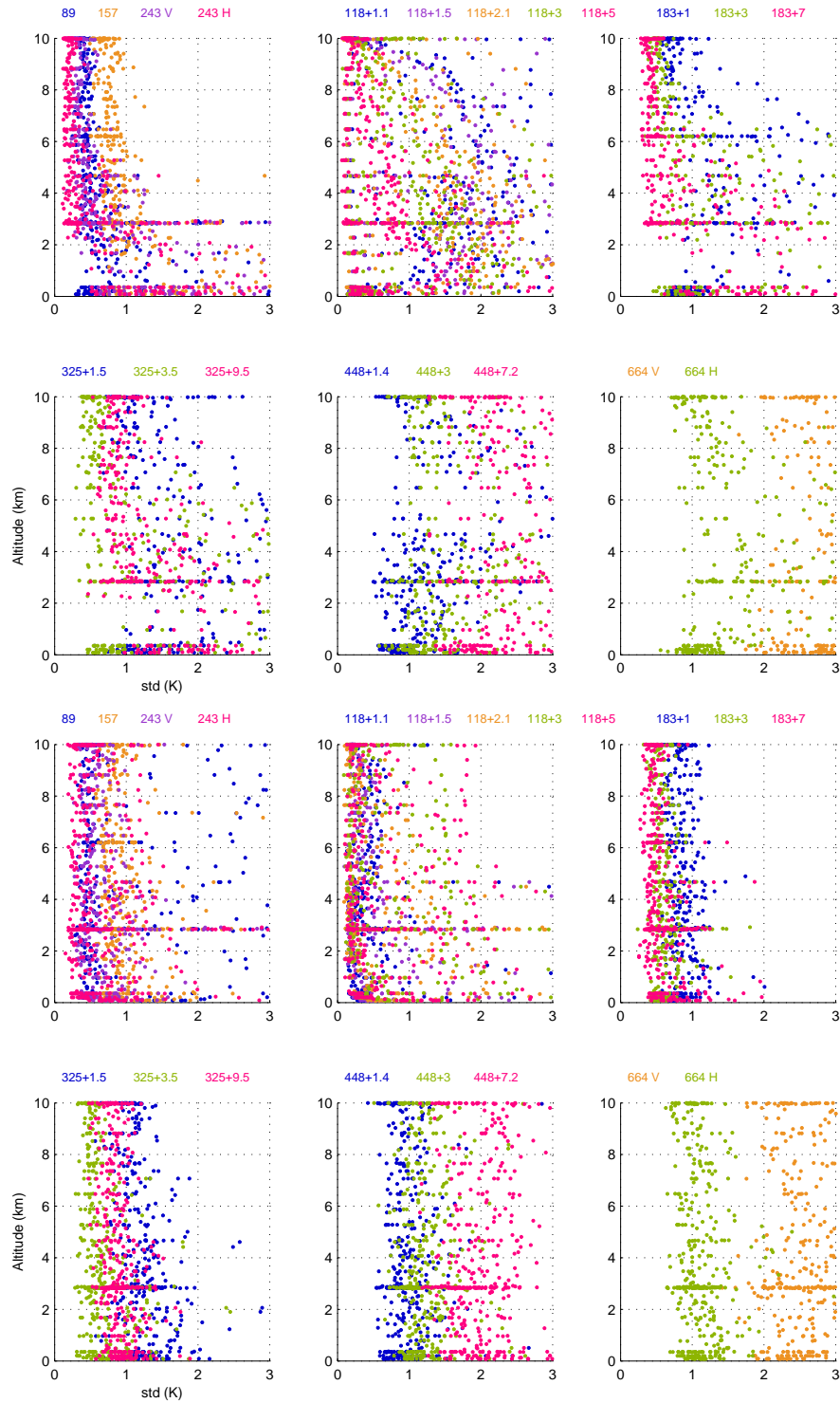


FIGURE 4.20: Estimation of the instrument random noise ($N_e\Delta T$), for flight B893, for both nadir (top) and zenith (bottom) views, as a function of the altitude, for the third version 'r006'.

The simulations agree well with the observations at window channels at 89 and 157 GHz. At 243 GHz, the simulations underestimate the observations, especially for the V polarization. There is a significant difference between the V and H polarizations, that is not expected especially under clear sky condition. It has already been noticed that

TABLE 4.3: Summary of the observed brightness temperature stds (K) for ISMAR and MARSS channels over all the flights. The stds indicated in bold are the median values for the high level runs. The instrument noise (measured $\text{Net}\Delta T$ on liquid nitrogen cooled target over 60 seconds, from Fox et al., 2016) for each channel is also given.

Freq. (GHz)	Tb std zenith (K)	Tb std nadir (K)	$\text{Net}\Delta T$ (K)
89	0.4	1.4	0.42
118.7503±1.1	0.4	0.2	0.4
118.7503±1.5	0.3	0.3	0.4
118.7503±2.1	0.3	0.3	0.3
118.7503±3.0	0.3	0.6	0.3
118.7503±5.0	0.2	1.1	0.3
157	0.8	1.2	0.69
183.248±0.75	1.0	0.8	0.64
183.248±2.5	0.6	0.6	0.44
183.248±6	0.4	0.5	0.35
243.2 V	1.0	1.2	0.3
243.2 H	0.3	0.7	0.4
325.15±1.5	1.5	1.1	1.6
325.15±3.5	0.7	0.6	0.7
325.15±9.5	1.2	1.0	1.1
448±1.4	1.7	0.9	1.1
448±3.0	1.8	1.2	1.6
448±7.2	2.7	2.0	2.8
664 V	3.4	2.6	3.3
664 H	1.6	1.1	1.3

the 243 GHz V channel is noisier than expected (in Section 4.3.1). At the 118 GHz channels in the oxygen absorption band, the discrepancy between model and simulation increases when moving away from the line center. This has also been observed for the other flights and by the other groups. These differences are thought to be caused by detector non-linearity, but they should not significantly affect the emissivity retrievals as they are most pronounced at high altitude where the downwelling brightness temperature at the surface is dominated by emission from the atmosphere between the aircraft and the surface. During flight B893, at 183, 325, 448, and 664 GHz, differences are rather large when the aircraft flies in the middle troposphere. This behavior is emphasized in Figure 4.23 that presents the brightness temperature differences as a function of altitude. Large differences appear between 2000 and 6000 *m* at these frequencies. The mean biases at these middle observation levels reach 61.4 K at 448±7.8 GHz with a root-mean-square deviation (RMSE) of 61.8 K. These channels are all very sensitive to water vapor, and the ERA-Interim water vapor profile might not capture all the atmospheric variability of the water vapor in that case. In water vapor absorption centers at 183±1 and 325.15±1.5 GHz, much larger brightness temperature biases of 55.5 K and 51.0 K appear, while less (13.9 K and 10.5 K) at the edge of the water vapor lines (183±6 and 325.15±9.5 GHz). For the flight B875 (shown in Figure 4.24), the simulated brightness temperatures are higher than the observed ones between 3000 and 4000 *m* from 183 to 664 GHz, which could be induced by an overestimated water vapor content. On the contrary, the lower simulated brightness temperatures around 2000 *m* could be attributed to the underestimated water vapor contents. Note that neither of these discrepancies will affect the retrieval of emissivity during low-level flight since the observed downwelling brightness temperatures will be used in the emissivity calculations.

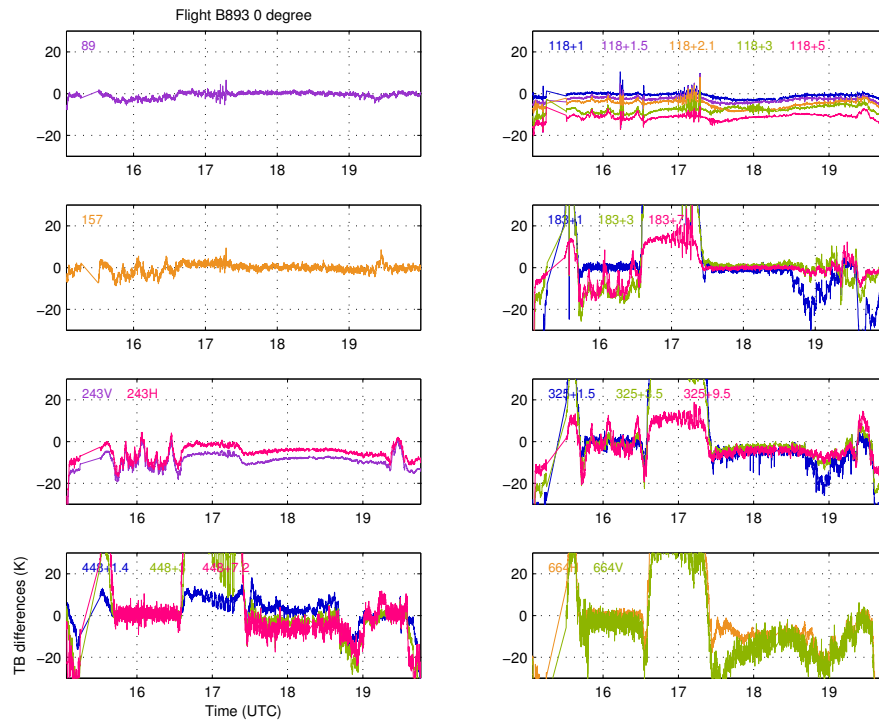


FIGURE 4.21: Time series of brightness temperature differences (simulations - observations) during the flight B893 for the zenith up-looking views, at all the MARSS and ISMAR channels.

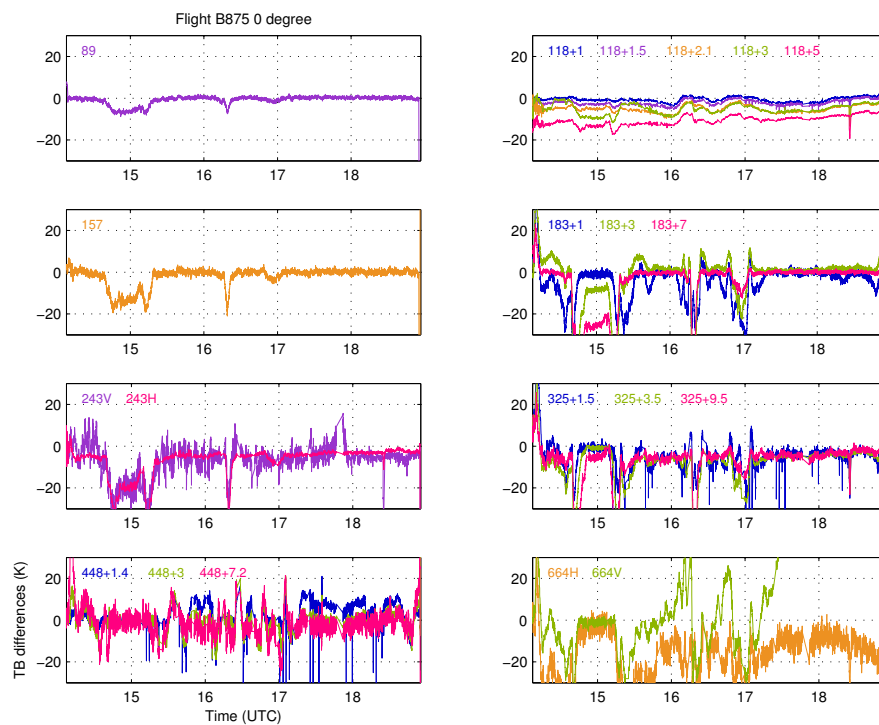


FIGURE 4.22: Same as Figure 4.21, but for flight B875.

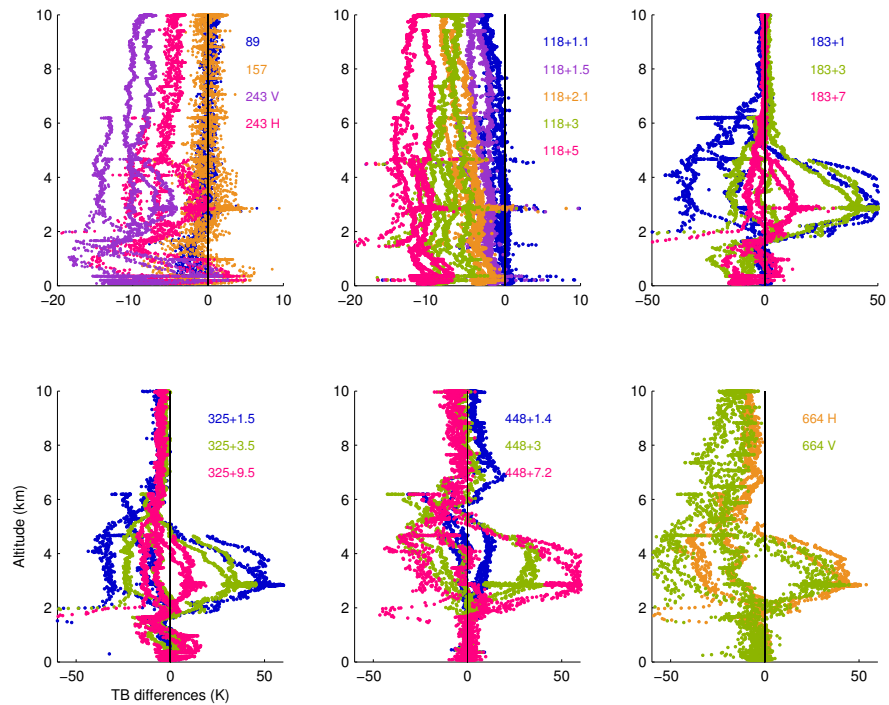


FIGURE 4.23: Brightness temperature differences (simulations – observations) against the aircraft altitudes during the flight B893 at all the MARSS and ISMAR channels.

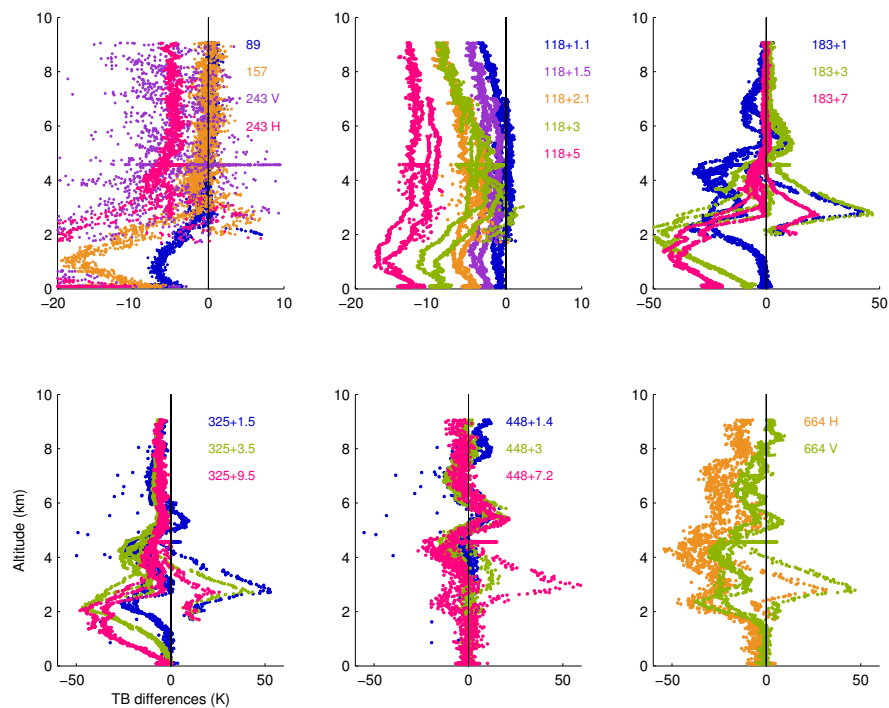


FIGURE 4.24: Same as Figure 4.23, but for flight B875.

To evaluate the accuracy of the atmospheric profiles, comparisons between the ERA-Interim profiles and the measurements of the dropsondes are performed. During the flight B893/B875, four dropsondes were released from high altitudes (above 30000 *ft*) at 17:54/16:03, 17:57/17:37, 18:06/17:41, and 18:09/17:52, respectively. Descending

through the atmosphere, the dropsondes measure the atmospheric profiles, (i.e., temperature, water vapor, pressure, and wind speed profiles). The dropsondes are followed by GPS receivers that transmit meteorological information back to the onboard receiving systems. Figure 4.25 shows the water vapor profiles from the dropsondes and ERA-Interim during flights B893 and B875. The atmospheric profiles derived from the dropsondes present fine vertical structures of the atmosphere with more than 1200 layers below 10000 *m*. During flight B893, they capture dry layers around 3000 *m*, 4500 *m*, and 5500 *m* that are missed by the ERA-Interim analyses. It is clear that ERA-Interim profiles contain more water vapor, especially in the middle troposphere, between 2000 and 6000 *m*. The water vapor volume mixing ratio in the ERA-Interim data is more than twice larger than the dropsonde measurement in these layers. Note that the aircraft orbited at angles between 20° and 60° at 9000 *ft* around 17:00, inducing that the profiles used in the simulations were not sampling exactly the same atmosphere as the observations. This can also result in disagreement between the observations and radiative transfer simulations. During flight B875, ERA-Interim water vapor profiles are underestimated between 1000 to 3000 *m*, inducing the negative biases of simulated brightness temperatures. The trend is opposite for the layers between 3000 and 4000 *m*.

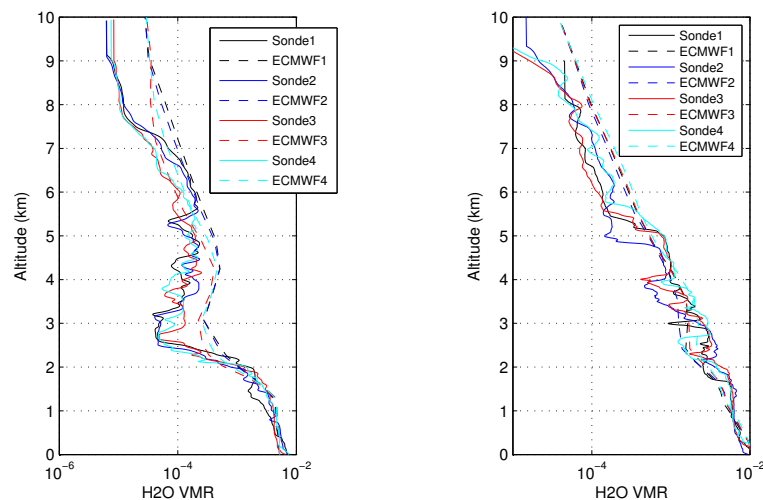


FIGURE 4.25: The water vapor volume mixing ratio profiles from the four dropsondes released at 17:54/16:03, 17:57/17:37, 18:06/17:41, and 18:09/17:52, respectively, and the ERA-Interim profiles at 18:00 during the flight B893 (left)/B875 (right).

The comparisons between the observations and simulations have also been done for flights B896 and B898 for up-looking cases (zenith). Only the comparison for flight B896 is shown here in Figure 4.26. The up-looking simulated and observed brightness temperatures are in rather good agreement, although there are some discrepancies. During this flight, between 16:12 and 16:30, the aircraft is close to the surface, the differences are likely due to cloud presence above the aircraft which is not included in the simulations. This effect is less pronounced in channels close to the center of the absorption lines and at much higher frequencies (448 and 664 GHz) where the atmosphere is opaque and radiates at a similar temperature than the clouds. Between 15:00 and 15:24, the differences are greatest in channels sensitive to water vapor absorption and are thought to be caused by errors in the ERA-Interim water vapor profile used in the simulations.

At 243 GHz, the observations are warmer than the simulations, particularly at high altitudes, and there is some difference between the two polarizations which is not expected under clear sky conditions. A similar effect is seen in the oxygen absorption band at 118 GHz where the difference between model and simulation increases when moving away from the line center.

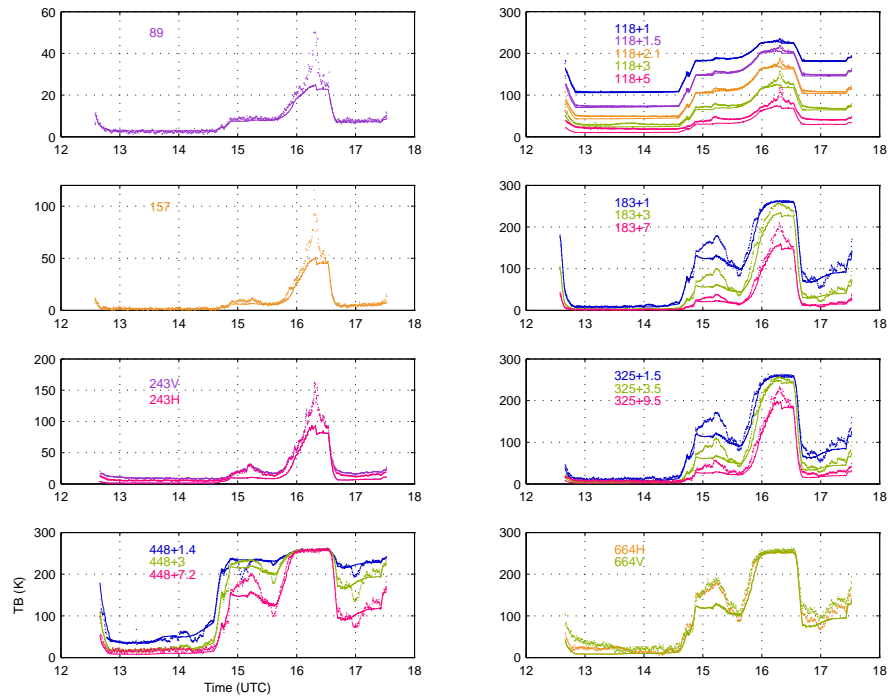


FIGURE 4.26: The ISMAR and MARSS upward observations for all channels as a function of the observation time for flight B896 at zenith (dotted lines). The simulations by ARTS are also presented (solid lines).

In conclusion, except for transitory periods where at least one channel does not function properly, the radiometers have rather low noise, close to the specifications. Some problems have been noted at 243 and 664 GHz, in terms of polarization differences, and the 664 GHz vertical polarization channel is significantly noisier than the expectation. However, most collected data are of sufficient quality to initiate an estimation of the emissivity directly from the observations.

4.4 Emissivity estimation

4.4.1 Methodology

The surface emissivity will be directly estimated from the aircraft observations, avoiding the errors related to the contribution of the radiative transfer simulations. Under clear sky conditions, assuming specular reflection, the radiative transfer equation can be

written as:

$$T_{bp} = T_s \times \varepsilon_p \times e^{-\tau(0,H)/\mu} + (1 - \varepsilon_p) \int_0^H T(z)\alpha(z)e^{-\tau(0,z)/\mu} dz + \int_0^H T(z)\alpha(z)e^{-\tau(z,H)/\mu} dz \quad (4.1)$$

where T_{bp} is the observed brightness temperature by the ISMAR radiometer for polarization p ; T_s is the surface skin temperature; ε_p is the surface emissivity for polarization p ; τ is the atmospheric opacity; μ is the $\cos(\theta)$, where θ is the incidence angle; H is the aircraft height; $T(z)$ is the atmospheric temperature at altitude z ; $\alpha(z)$ is the atmospheric absorption coefficient at altitude z ;

On the right side of Equation 4.1, the three terms stand for the surface emission, the downwelling atmospheric emission after the reflection by the surface, and the upwelling atmospheric emission, respectively. The surface emissivity can be deduced:

$$\varepsilon_p = \frac{T_{bp} - T_u - T_d \times e^{-\tau(0,H)/\mu}}{e^{-\tau(0,H)/\mu} \times (T_s - T_d)} \quad (4.2)$$

In the case of the aircraft observations, T_{bp} is the upward brightness temperature measured by ISMAR or MARSS. The downwelling brightness temperature T_d is calculated at the surface using a combination of the up-looking aircraft observations down to the aircraft altitude and simulations based on ERA-Interim database below the aircraft. The upwelling brightness temperature T_u and the upwelling atmospheric emission τ are estimated with ARTS, using the ERA-Interim database. The surface temperature T_s is taken from the ERA-Interim database (the Operational Sea Surface Temperature and Sea Ice Analysis (OSTIA) analysis could also be used). For flight B896, T_s has been estimated from some aircraft instrumentation by C. Harlow at the UK Met Office: the emissivity calculations have been tested with these different T_s .

4.4.2 Estimation of the ice-free ocean surface emissivity

The sea surface emissivities can be calculated with the method introduced above for all the ISMAR and MARSS channels, for the low level transects. However, for the very low level flight (100 *ft*), some aircraft reflections have been suspected when looking at nadir (S. Fox, UK Met Office). We checked this effect during flight B893. Figure 4.27 zooms on the low level runs during that flight (the four top rows the observations at nadir (0°), the four bottom rows the observations at 40°). When flying at the lowest altitude (100 *ft*) over the ocean, the nadir views for the window channels (89 GHz, 118±5 GHz, and 157 GHz) are significantly higher than during the runs at 500 and 1000 *ft*. This higher brightness temperatures observed at nadir at 100 *ft* cannot be explained in terms of atmospheric or surface variability. This effect decreases with increasing incidence angle, and is not observable for large angles (see the measurements at 40° incidence angle in the four lower panels in Figure 4.27). It is attributed to the reflection of the aircraft at the surface, with the aircraft having warmer brightness temperatures than the atmosphere at these window channels. As a consequence, when estimating the emissivity close to nadir, care will have to be exercised for the very low altitudes.

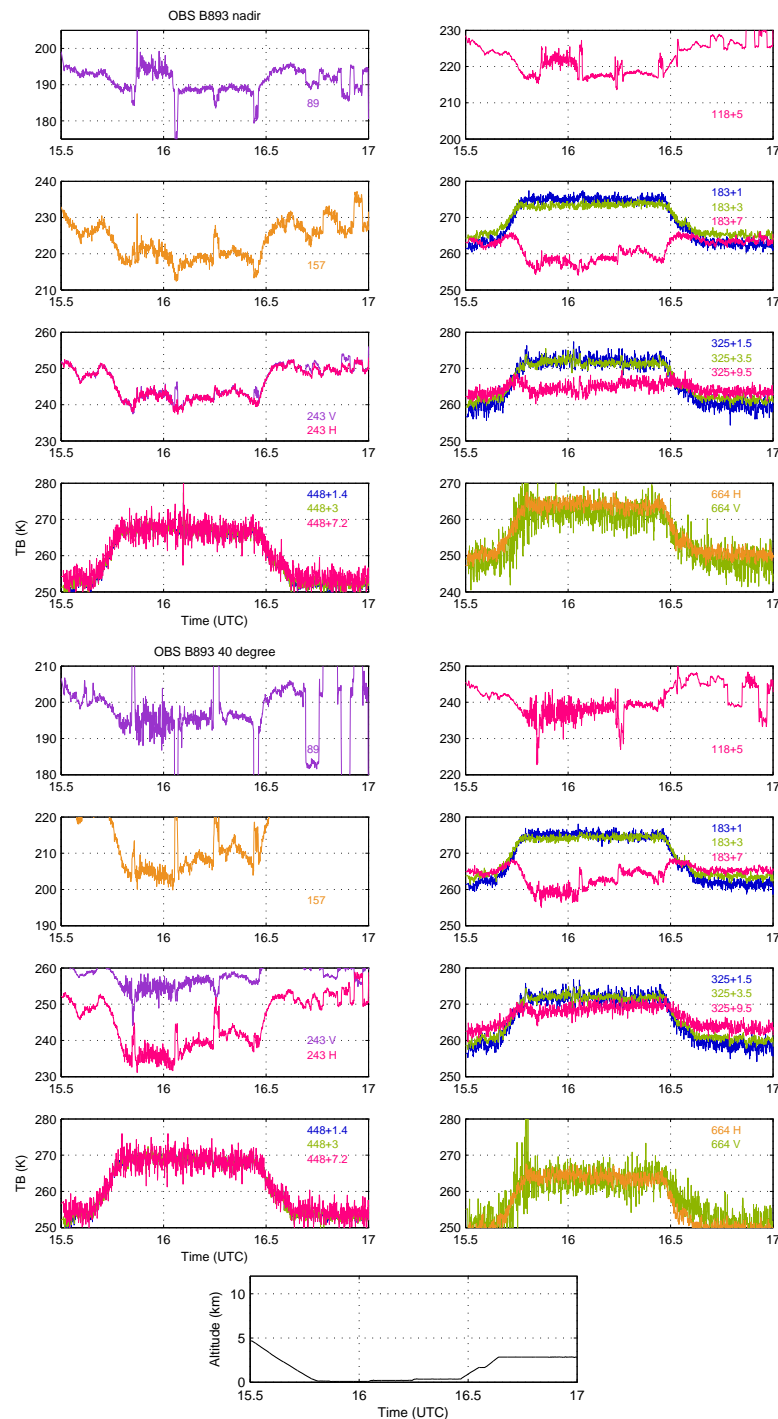


FIGURE 4.27: Zoom on ISMAR and MARSS observations for the low level runs during flight B893, at nadir (0° top four panels) and at 40° (bottom four panels). The flight altitude is also indicated.

The aircraft emissivity estimates over ice-free ocean will be compared with sea surface emissivity model calculations. Three comparisons will be conducted: with FASTEM, with the LERMA geometric optic model, and with TESSEM² (presented in Chapter 2). The input parameters for the models are derived from ERA-Interim (wind speed and

sea surface temperature). The salinity is fixed to 36 psu.

The polarization measured by ISMAR or MARSS rotates with scan angle. The detailed polarization scheme observed by ISMAR and MARSS are described in Fox (2015). For MARSS at 89 GHz, the polarization is intermediate at large scan angles and it is close to vertical polarization at nadir. At 157 and 183 GHz, the polarizations rotate from horizontal in the extreme forward scan direction to vertical in the extreme backward scan direction. For ISMAR, the polarization rotation is similar than for the 157 and 183 GHz MARSS channels. The horizontal or vertical polarization is detected in the most forward downward view when the aircraft wings are leveled. In other configurations they will detect mixed polarizations. For the comparison with the estimated emissivity from the observation, the modeled surface emissivity e_m can be expressed as:

$$e_m = \cos(\theta_p)^2 e_h + \sin(\theta_p)^2 e_v \quad (4.3)$$

where θ_p is the actual polarization angle which is converted and calculated by the actual scan angle, following the information provided by the UK Met Office along with the brightness temperatures; e_h and e_v are the surface emissivities in horizontal and vertical polarizations.

The emissivities have been estimated for different flights when flying at low altitudes over ocean. For the opaque channels, due to the very limited contrast between the surface and the downwelling atmospheric contribution (T_s close to T_d in Equation 4.2), the estimates are very noisy in these channels. As a consequence, the results will be presented here for the following channels: 89, 118.75 ± 5 , 157, 183.31 ± 6 , 243.2 V and H, and 325.15 ± 9.5 GHz.

Figure 4.28 shows the emissivity estimation from the ISMAR and MARSS observations, during the low level runs at 100 *ft* for the flight B893, around 16:00, at 20° incidence angle. The wind speed is stable during this transect, as well as the sea surface temperature (see Figure 4.29). The retrieved emissivities are more stable at window frequencies such as 89 and 157 GHz than at 183 or 325 GHz. For a given frequency, the horizontal polarization is lower than the vertical one, as expected, and there is a general increase of the emissivity with frequency for a given polarization, except at 325 GHz.

4.4.2.1 Angular dependence of the emissivity

Figure 4.30 analyzes the angular dependence of the mean retrieved and simulated sea surface emissivities at each frequency for the lower level transect at 100 *ft* during flight B893. The indicated angles are not the exact angles of observation, but are very close to them, within a few degrees (maximum 3° difference): the scanning scheme combined to the aircraft altitude provides actual incidence angle that are not fixed in time. Note that for the ISMAR frequencies, the emissivities are not calculated close to 50° , as the downwelling radiation is not measured in that direction. As expected, the three sea surface emissivity models provide very similar results below 200 GHz, with TESSEM²

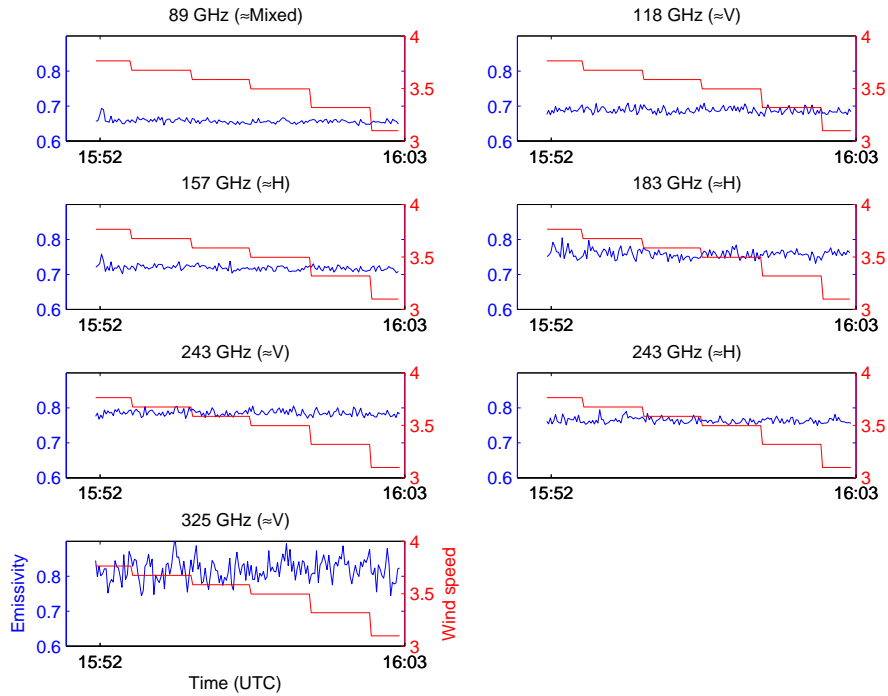


FIGURE 4.28: Emissivity estimation from ISMAR and MARSS observations during flight B893, at 89, 118.75 ± 5 , 157, 183.31 ± 6 , 243.2, and 325.15 ± 9.5 GHz, at 20° incidence angle. The surface wind speed from ERA interim is also shown. There is an indication of the polarization status in the title of each plot.

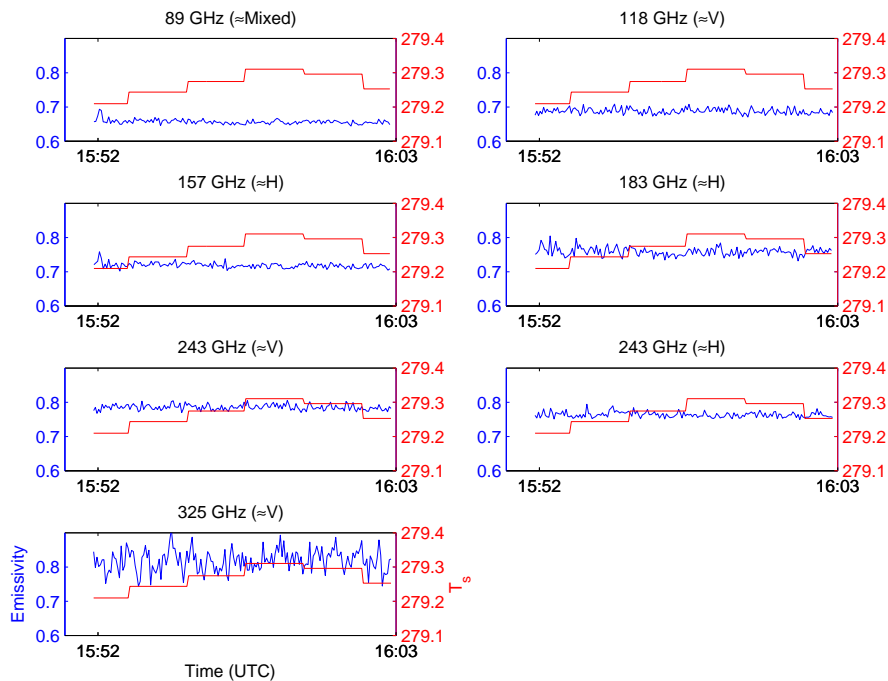


FIGURE 4.29: Same as Figure 4.28, but with surface temperature from ERA interim data.

closer to LERMA model above 200 GHz. The simulations and aircraft estimations agree rather well for more transparent channels, for all polarizations. At 183 and 325 GHz, the

agreement is not very good. This is likely due to the strong opacity of these channels, and the related lack of contrast between T_s and T_d at these frequencies that are strongly affected by the water vapor. For the other frequencies, the emissivities increase smoothly with increasing angle for the vertical polarization, while they decrease for the horizontal polarization. The retrieved emissivities are noisier at larger incidence angles, especially close to water vapor lines. The difference between simulated and retrieved emissivities increases for large incidence angles. For instance, at 118 GHz, the outer channel of the oxygen absorption band, the std of the aircraft emissivity estimate reaches 0.04 close to 40° , much more than at nadir (less than 0.01).

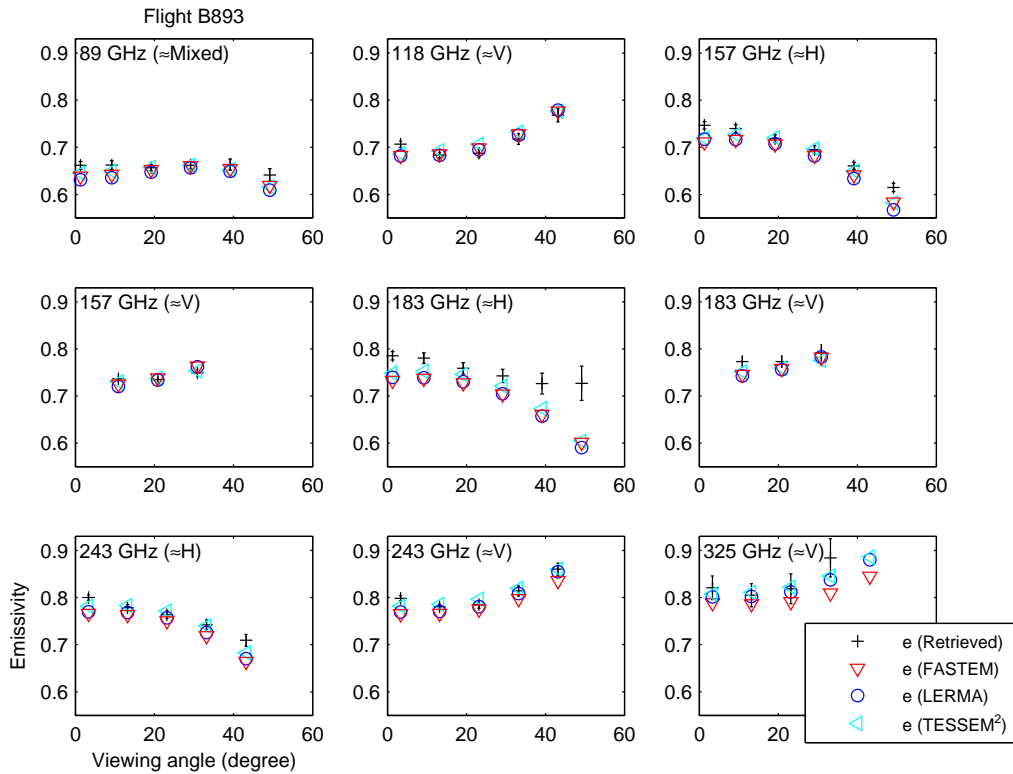
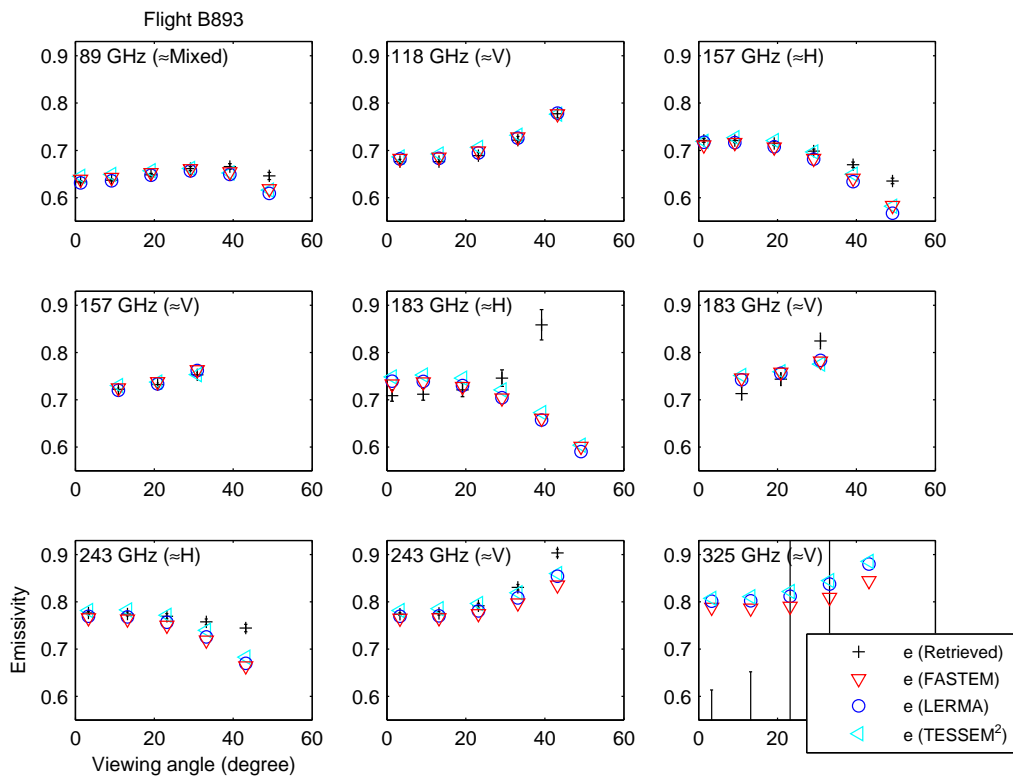


FIGURE 4.30: The angular dependence of the mean retrieved emissivities estimated from ISMAR and MARSS observations during the low level runs for flight B893, at 89, 118.75 ± 5 , 157, 183.31 ± 6 , 243.2, and 325.15 ± 9.5 GHz, for the 100 ft level run. The simulated emissivities by FASTEM, LERMA emissivity model, and TESSEM² are also presented. The std is indicated for each mean retrieved emissivity (error bar).

Close to nadir, an overestimation of the aircraft emissivities is noted, with respect to the simulations (at 89, 118, and 157 GHz). This is likely related to the aircraft shadow effect (discussed in Section 4.4.2). To confirm this hypothesis, the emissivities are calculated from the aircraft run at 500 ft. Figure 4.31 (the same as Figure 4.30, but at 500 ft) shows that the observed behaviors close to nadir agree now very well with the simulations. However, at large angles and in water vapor sensitive channels (183 and 325 GHz), the agreement tends to degrade.

The sensitivity of the emissivity estimates to the geophysical parameters has been tested, for both the TESSEM² model and aircraft estimates (not shown). For the aircraft

FIGURE 4.31: Same as Figure 4.30 but for the 500 *ft* level run.

estimates, the only ancillary parameters in Equation 4.2 is T_s , the ocean surface skin temperature. The surface emissivities were calculated using the ECMWF T_s , but also using lower T_s (-2 °C) and higher T_s ($+2$ °C) values. For the TESSEM² model, the sensitivity to both surface temperature (± 2 °C) and wind speed (± 3 *m/s*) changes is tested. The sensitivities of the model to these two parameters are rather limited, at least around these T_s and wind speed values (more sensitivity is expected at higher wind speeds). The aircraft retrieval is more sensitive to T_s . However, from this experiment under the considered environment, changes in T_s or in wind speed would not improve the model and observation agreement.

A similar analysis is also provided for flight B875 for the low level run at 100 *ft* (Figure 4.32). During that transect, the surface temperature is close to 284 K, the wind speed is around 5 *m/s*, and the integrated water vapor content is ~ 11 *kg/m*². Due to the moister atmospheric conditions compared to flight B893, the retrieved emissivities present a larger variability at 183 and 325 GHz. At nadir, the overestimation of the aircraft retrievals as compared to the model results at the lower frequencies are related to the aircraft shadowing effect, as previously discussed.

4.4.2.2 Frequency dependence of the emissivity

Figures 4.33 and 4.34 present the frequency dependence of the mean retrieved sea emissivities at different angles from nadir to 50° along with their stds for the low level

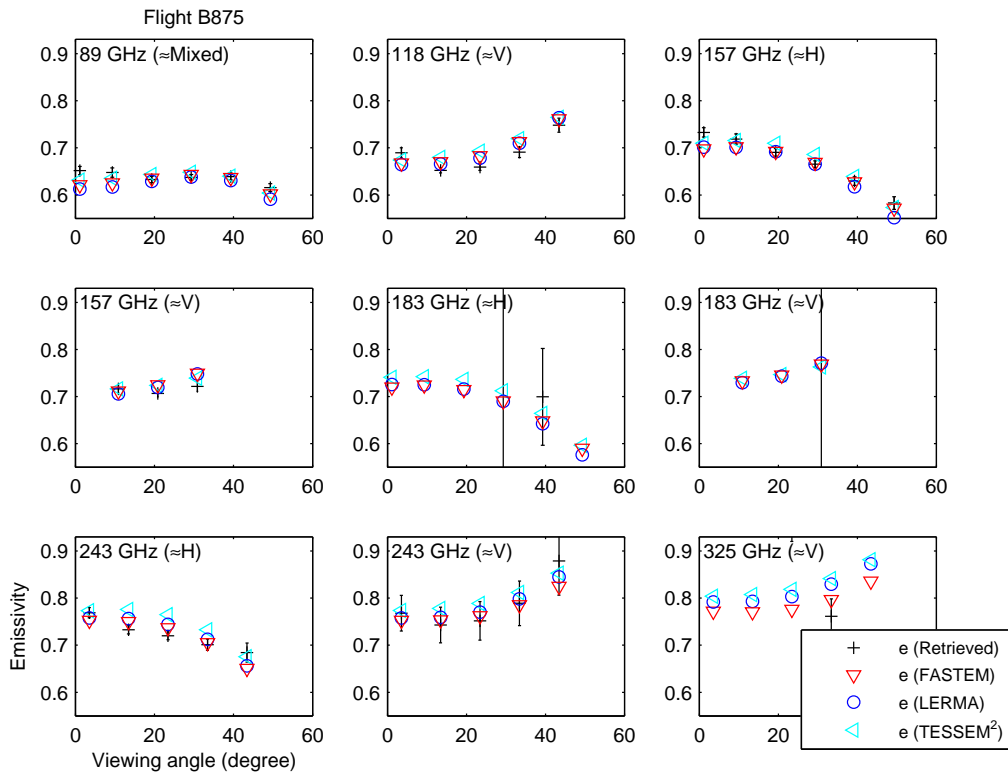


FIGURE 4.32: Same as Figure 4.30, for flight B875.

transects during flights B893 and B875. The simulated surface emissivities by the models are also plotted. At 89, 157, and 243 GHz window channels, the agreement between the retrieved and simulated emissivities is much better than at sounding channels. As already discussed, the aircraft estimations are overestimated close to nadir (100 *ft* altitude flight). The model results are very close to the aircraft estimates, for more observing conditions, up to 243 GHz. The emissivities at 325 GHz are poorly retrieved at larger angles ($\geq 30^\circ$). The estimations for flight B875 are worse than for flight B893.

To further evaluate the TESSEM² performance, the estimated ocean emissivities by TESSEM² for flights B893 and B875 are used in the radiative transfer simulations. The results are compared with the observed brightness temperatures by ISMAR for the downlooking cases at different incidence angles (0°, 20°, and 40°) (the brightness temperature differences are shown in Figure 4.35). At nadir, the flight shadow effect obviously influences the simulations at 100 *ft* for both flights, with mean differences of -7.8 K, -5.6 K, -5.6 K, and -1.0 K for 118, 243 V, 243 H, and 325 GHz, respectively (for flight B875, when the TESSEM² results are used). The consistency increases at larger angles (without shadow effect), with mean differences below -1.7 K for all the channels at 20° and 40°. Note that this is not the case for the 243 GHz H channel at 40° (mean difference is up to -4.12 K), which may be associated with the parameterization in TESSEM². The simulations are also done using the results from FASTEM as comparison. The brightness temperature differences are larger than using the TESSEM² emissivities in all presented situations, especially at 243 GHz (~ 3 K more). The std

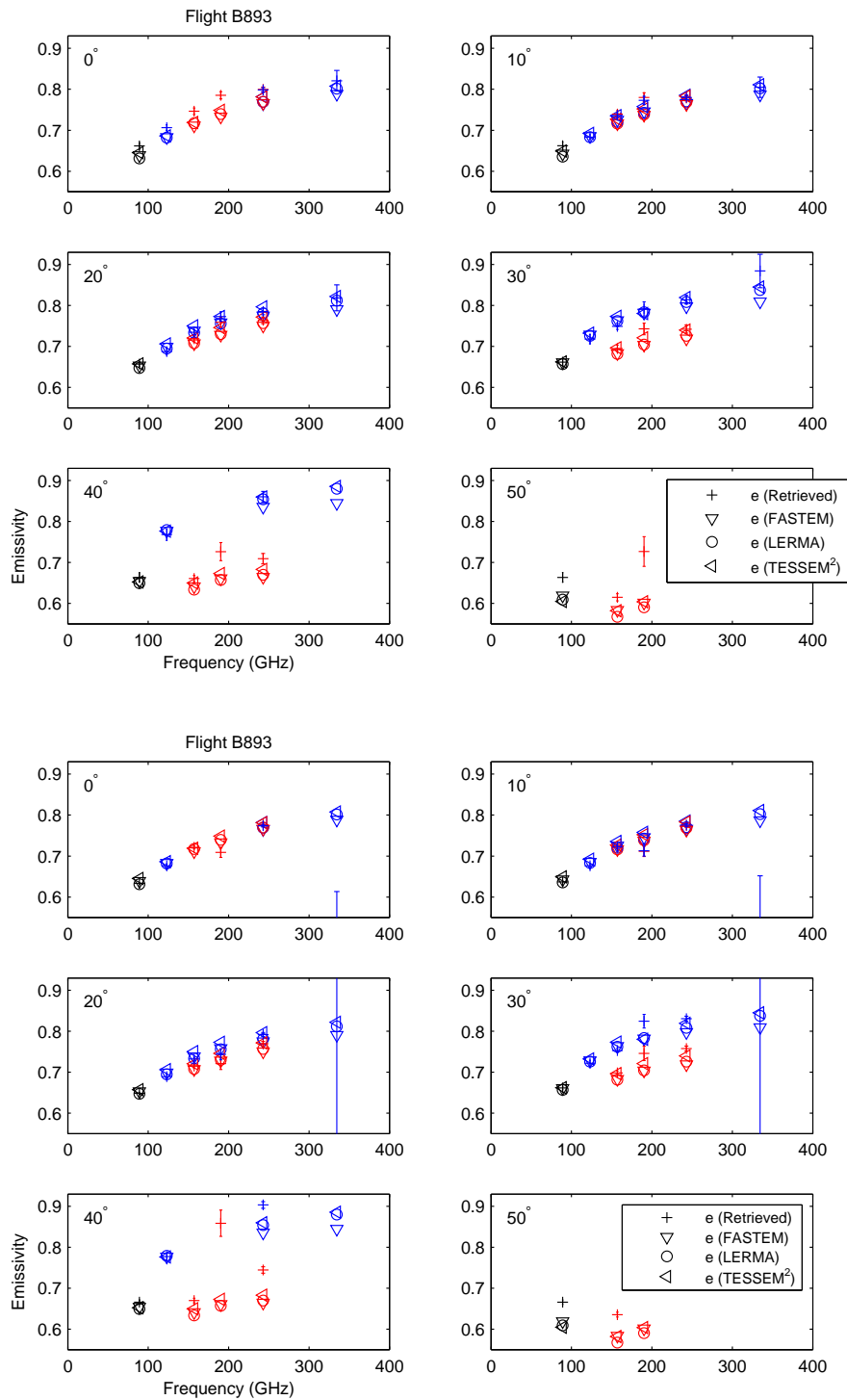


FIGURE 4.33: The frequency dependence of the mean retrieved emissivities estimated from ISMAR and MARSS observations during flight B893, at 89, 118.75 ± 5 , 157, 183.31 ± 6 , 243.2, and 325.15 ± 9.5 GHz, for different angles. The blue symbols present the emissivities close to V polarization, the red ones close to H polarization, and the black ones close to mixed polarization. The simulated emissivities by FASTEM, by the LERMA model, and by TESSEM² are also presented. The std is indicated for each mean retrieved emissivity (error bar).

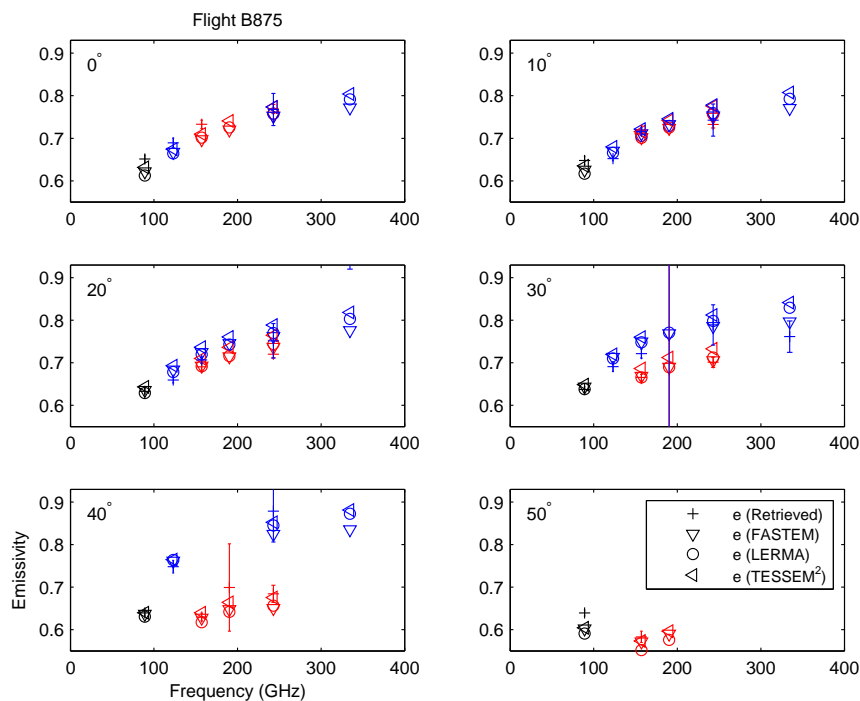


FIGURE 4.34: Same as Figure 4.33, but for flight B875.

depends strongly on the quality of the observations, and does not have evident change using one emissivity model and the other. It is clear to see that the 243 GHz V channel is noisy during flight B875 as mentioned in Section 4.2.

4.4.3 Estimation of the emissivity of the frozen surfaces

Flights B896 and B898 were dedicated to the exploration of the cold environments, with long runs over Greenland (presented in Section 4.3.1). Following the same methodology as described in Section 4.4.1, the surface emissivities are calculated over sea-ice and continental ice during these flights. The atmosphere is very dry, and its contribution is expected to be limited, even at high flying altitude and at high frequencies.

The TELSEM² estimates are systematically compared to the aircraft-derived emissivities (see Chapter 2 for the TELSEM² description). The only inputs to TELSEM² are the latitude and longitude of the point, the month of observation, and the observing conditions (frequency, incidence angle, and polarization). Figure 4.36 presents the TELSEM² emissivities in the region for frequencies up to 325 GHz, at 40° for both sea and continental ices, along with the flight patterns for B896 and B898. The TELSEM² emissivity shows a significant spatial variability, especially close to the coast both over sea and continental ices. This is to be confronted by the aircraft observations, keeping in mind that the spatial resolution of TELSEM² is very poor compared to the aircraft footprint. In these areas of marginal sea ice on March and in coastal region with significant topography, the comparison is expected to be challenging.

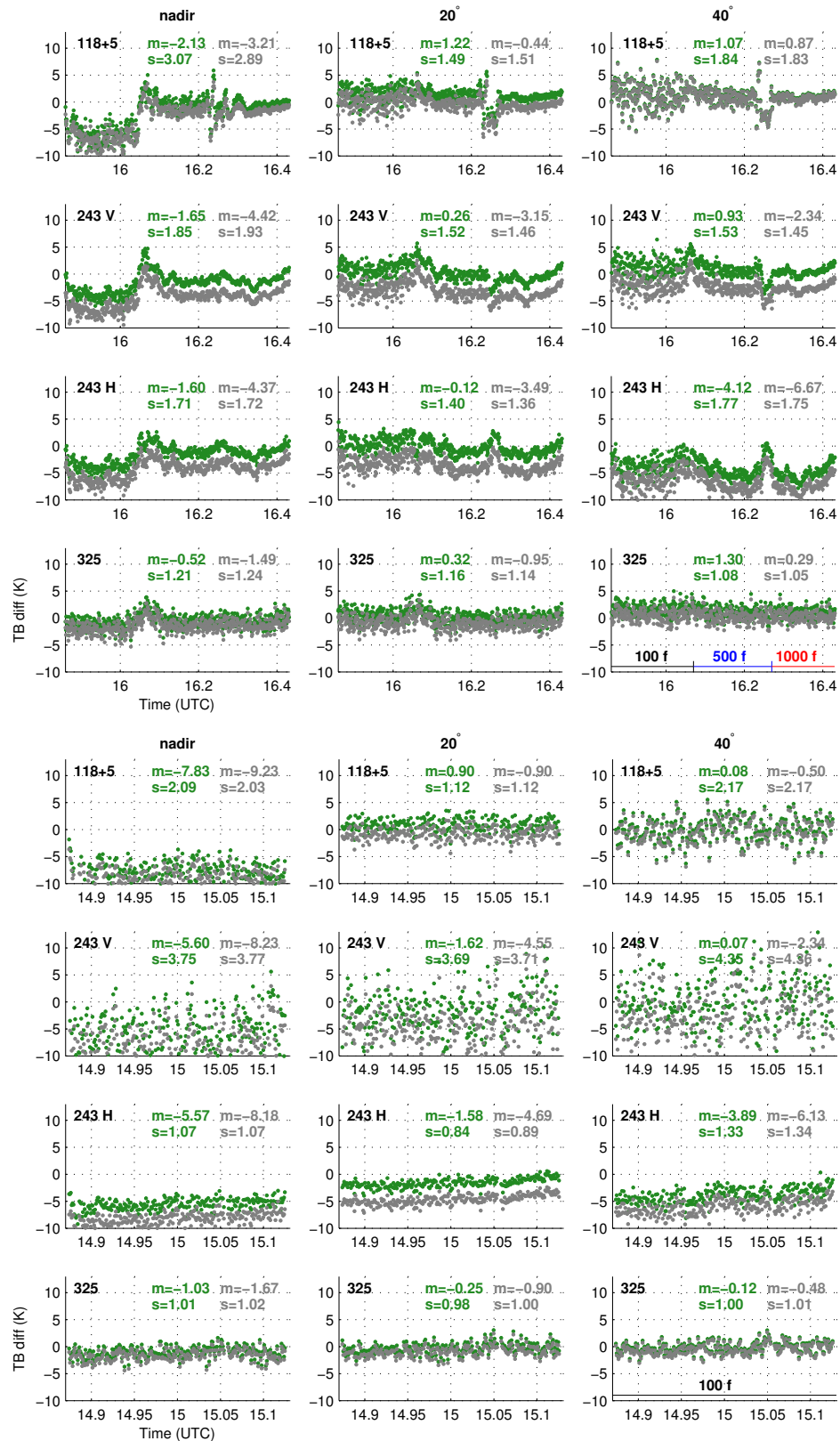


FIGURE 4.35: The brightness temperature differences between the observations (by ISMAR) and simulations (with the emissivities from TESSEM² (green) and FASTEM (grey)), for flights B893 and B875, at different incidence angles (0°, 20°, and 40°).

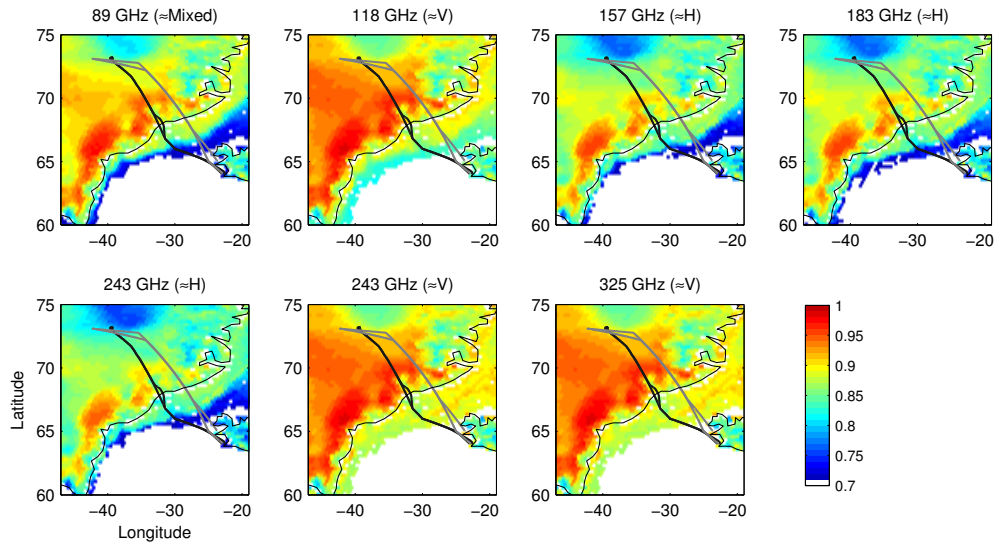


FIGURE 4.36: B896 and B898 flight patterns, superposed on the TELSEM² emissivities estimated for ISMAR and MARSS frequencies up to 325 GHz, at 40° incidence angle, for both sea and continental ices.

Figure 4.37 shows the aircraft-retrieved emissivities at 0°, as a function of latitude for the window channels (89, 157, and 243 GHz) and the channels farthest from the absorption line centers (118±5, 183±7, and 325±9.5 GHz). The top (resp. bottom) rows present the emissivities calculated on the way to (resp. from) Greenland. Sea ice is present from 67°N to 68°N in latitude; the rest of the transect is over continental ice. The TELSEM² emissivities are also presented for comparison, for the same frequencies, incidence angles, and polarizations. Over sea ice (from 67°N to 68°N), the aircraft retrieved emissivities show a very large variability. On the way to Greenland, it is likely due to the natural spatial variability of the sea ice that is expected to be high, but on the way back from Greenland, the poor temperature separation between the calibration targets is suspected, inducing an increased noise in the retrievals during this section of the flight. At 325 GHz, the estimates between 67°N and 68.5°N are very noisy, especially on the way back from Greenland: this is due to the lack of sensitivity to the emissivity in this region (as shown in Figure 4.38). Figure 4.38 shows the downward-looking brightness temperatures simulated for flight B896 with two assumed surface emissivities: 0.5 and 0.9, to further investigate the channel sensitivity to the surface. At 448 GHz and above, it is evident that there is no sensitivity to the emissivity, both on the way to and from Greenland: the two simulations of the down-looking brightness temperatures are identical, despite the large difference in emissivity. As a consequence, it is not possible to estimate the emissivity from these observations at 448 GHz and above.

Over continental ice, from 69°N to 73°N, the agreement between the TELSEM² and the aircraft estimates is very good at 89 GHz, but degrades at higher frequencies. Beyond 71°N, the differences between the aircraft retrievals and TELSEM² may be induced by two reasons. The first reason maybe related to the errors in ERA-Interim water vapor profile. The second one maybe related to our hypothesis made in TELSEM², assuming that the surface emissivity is constant at frequencies higher than 90 GHz. Beyond 71°N, the region is associated to class 5, according to TELSEM² types. The

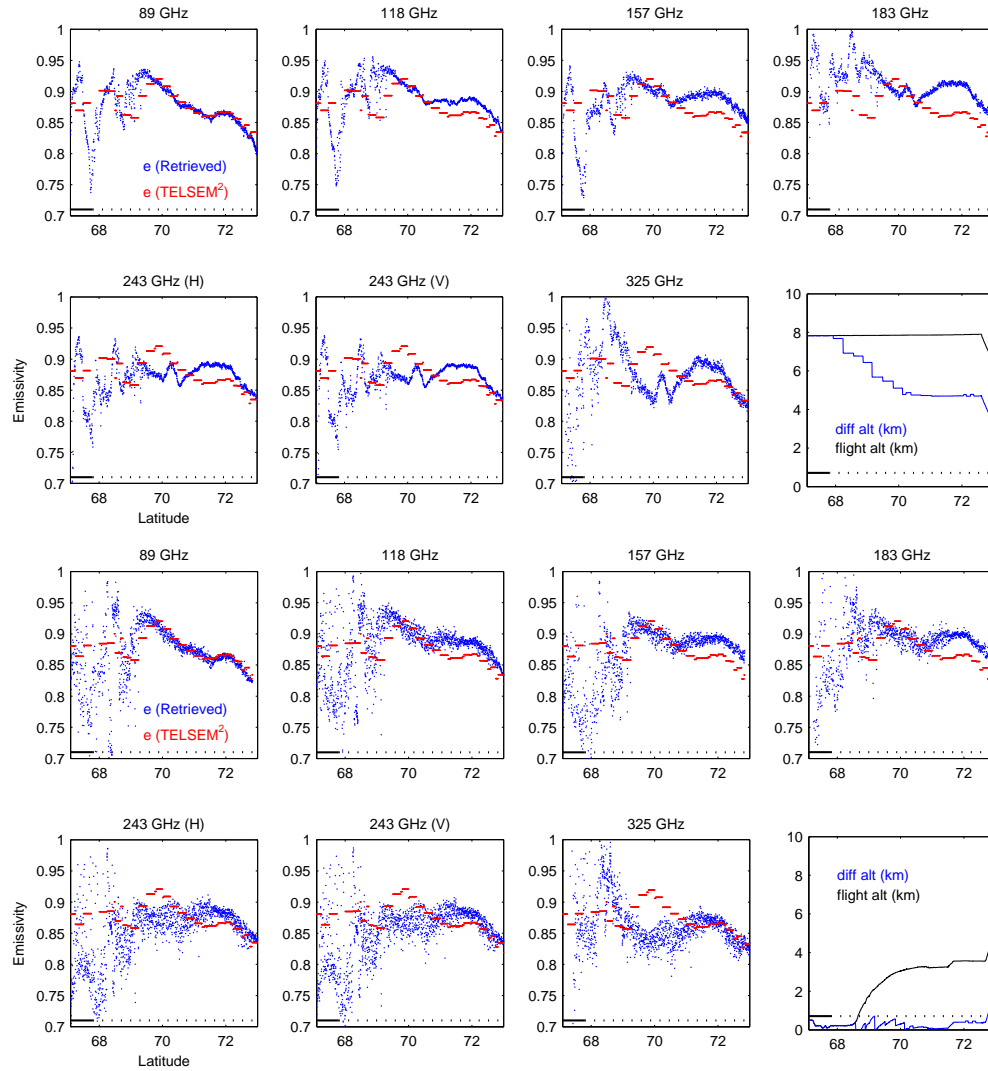


FIGURE 4.37: The retrieved emissivities from MARSS and ISMAR observations for flight B896 as a function of latitude at 0° scan angle for 89, 118 ± 5 , 157, 183 ± 7 , 243, and 325 ± 9.5 GHz. Top two rows: on the way to Greenland. Bottom two rows: on the way back from Greenland. The results from TELSEM² on March at 0° are shown for comparison. The last panel indicates the flight altitude and the altitude difference between the aircraft and surface. On the x-axis, the solid black line indicates the presence of sea ice and the dotted line corresponds to the continent.

emissivity increases slightly between 89 and 183 GHz for H polarization (not shown). Therefore, it is possible that TELSEM² underestimates the surface emissivity for this type of continental ice between 89 and 183 GHz. In addition, some spatial structures in the emissivity retrieval that are visible at 70°N at 243 GHz are clearly not present at 89 GHz, either in the retrieved emissivities or in the TELSEM² estimates. This could be related to some specific snow and ice conditions that would induce emissivity changes at higher frequencies. These signatures are missed by TELSEM² that is anchored to emissivity estimates below 100 GHz, with limited reliable satellite-derived emissivity retrievals at frequencies above 100 GHz. Overall, the spatial variability is captured by TELSEM², despite the fact that TELSEM² is based on a monthly climatology.

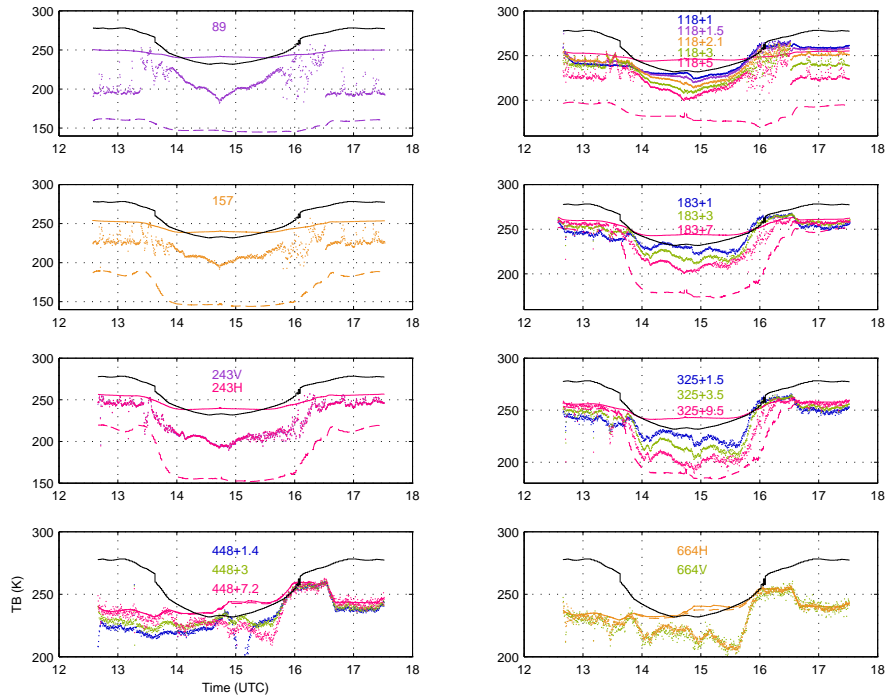


FIGURE 4.38: The ISMAR and MARSS downward observations for all channels as a function of the observation time for flight B896 at nadir (solid lines). The simulations are also presented for the window channels for surface emissivity of 0.5 (dashed lines) and of 0.9 (solid lines). The surface skin temperatures from the ERA-Interim database are indicated in black.

Over ice (sea and continental), the surface temperature is subject to large errors, which will cause errors in emissivity retrieval. The UK Met Office retrieved and analyzed the surface temperature estimated by several methods, directly from the aircraft estimates for flight B896. It includes infrared retrieval from the Advanced Remote-sensing Imaging Emission Spectrometer (ARIES) spectrometer (Wilson et al., 1999), as well as estimates from an infrared Heimann sensor. Figure 4.39 shows the results from this work, on the way from Greenland. Notice the large T_s gradient between 68°N and 70°N , along with the large difference between the aircraft estimates and the ECMWF T_s . This is likely partly related to the spatial resolution differences between these estimates, in an area of large spatial heterogeneity (fjords and mountains). The T_s differences can be large between the T_s estimates, up to 10 K even between in situ estimates. For flight B896 at nadir (similar to Figure 4.37), the emissivities have been estimated, using different T_s . The changes in T_s estimates have a significant impact on the emissivity retrievals, as expected, but no T_s estimate does systematically improve the agreement with TELSEM². The emissivity aircraft retrievals in window frequencies are also presented for flight B898 (Figures 4.40) at nadir and 40° on the way back from Greenland. The agreement with TELSEM² is very reasonable, and the spatial variability between 69°N and 73°N is captured well. The histogram of the emissivity differences between the TELSEM² and retrieved results at nadir are shown in Figure 4.41 for the pixels only over the continental ice during the two flights, with mean difference and std for each frequency. At 89 GHz, the mean difference (-0.002) is much smaller than the mean difference between TELSEM²

and satellite estimations. As expected, the bias increases with atmospheric opacity, and it is larger near the water vapor lines at 183 GHz (0.017) and 325 GHz (-0.022) than in the window channels at 89 (-0.002), 157 (0.012), 243 H (-0.011), and 243 GHz V (-0.013). The mean difference and std are also calculated at 40° (not shown). The bias is very similar, and the std is lightly larger for each channel.

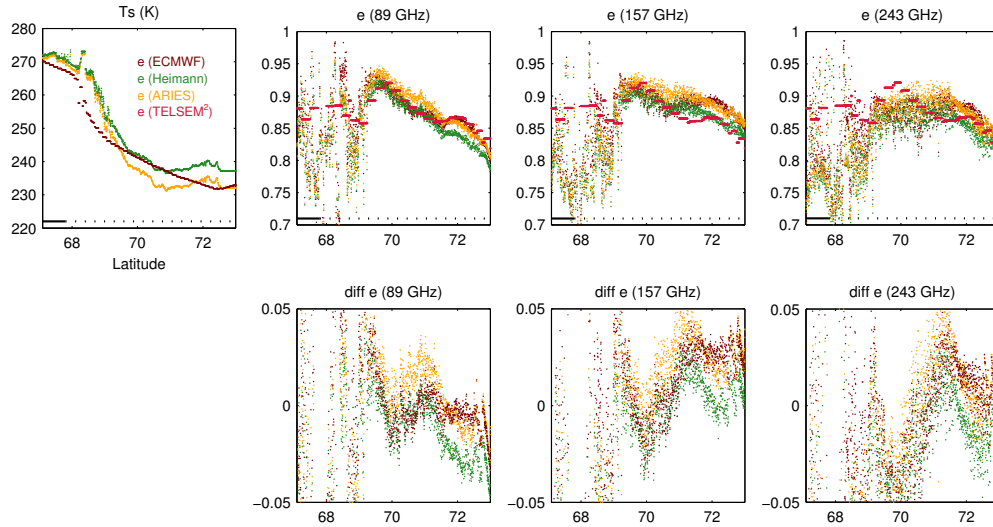


FIGURE 4.39: Top row: The first left panel shows the surface temperature derived directly from the aircraft observations, along with the ECMWF-Interim database estimates for the flight B896 on the way from Greenland. The three right panels show the corresponding emissivity at nadir from the aircraft measurements with the different T_s estimates, along with the corresponding TELSEM² emissivities. On the x-axis, the solid black line indicates the presence of sea ice and the dotted line corresponds to the continent. Bottom row: The three panels show the differences between aircraft retrieved emissivities and the TELSEM² emissivity ($e(\text{various airborne}) - e(\text{TELSEM}^2)$). The brown dots represent $e(\text{ECMWF}) - e(\text{TELSEM}^2)$; the green dots represent $e(\text{Heimann}) - e(\text{TELSEM}^2)$; the orange dots represent $e(\text{ARIES}) - e(\text{TELSEM}^2)$.

4.5 Conclusions

ISMAR, a passive remote sensing radiometer between 118 to 664 GHz, has been developed and operated onboard the FAAM BAe-146 research aircraft during two campaigns (STICCS-2 and COSMICS). It is the demonstrator of ICI that will equip the next generation of MetOp satellites. The ISMAR and MARSS observations are analyzed and compared to radiative transfer simulations with ARTS. The data quality is within the requirement or close to it for most channels. During the two campaigns, four flights with low-level runs are designed to estimate the surface emissivity. The surface emissivities have been calculated over ocean as well as over sea-ice and continental ice, directly from the upwelling and downwelling radiance measured at low altitudes. The estimated emissivities are compared with the surface emissivity models developed at LERMA, TESSEM² for the ocean and TELSEM² for the sea-ice and continental ice.

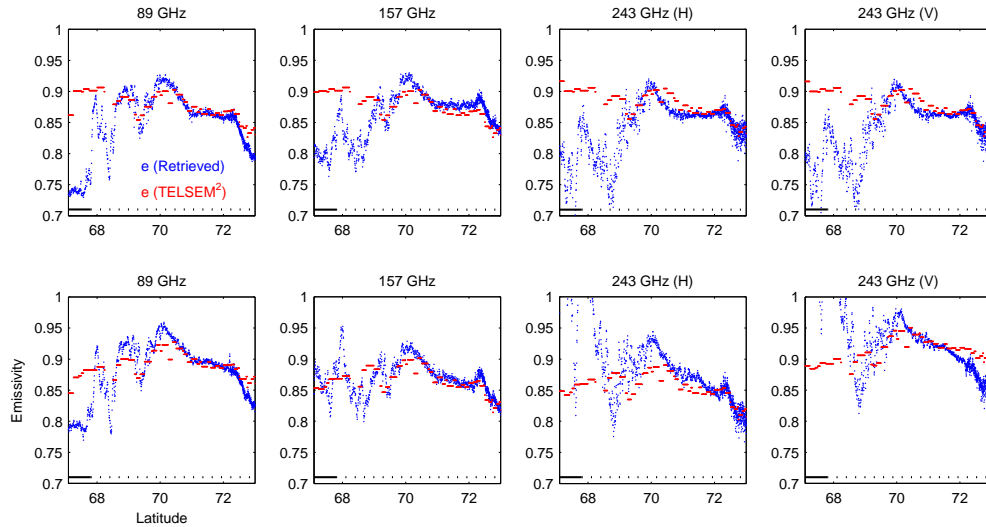


FIGURE 4.40: The retrieved emissivities from MARSS and ISMAR observations for flight B898 as a function of latitude on the way from Greenland at 89, 157, and 243 GHz (V and H). Top row: at 0° incidence angle; bottom row: at 40° incidence angle. On the x-axis, the solid black line indicates the presence of sea ice and the dotted line corresponds to the continent.

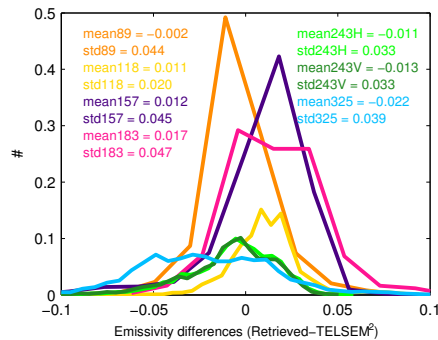


FIGURE 4.41: Histogram of the emissivity differences between retrieved and TELSEM^2 results at nadir with the pixels only over continental ice in flights B896 and B898 for different frequencies.

The sea surface emissivity model (TESSEM^2) has been compared to the aircraft emissivity retrievals, for low wind speed (3 to 5 m/s). The agreement is very encouraging up to 325 GHz, for all angles (except for 325 GHz at larger angles) and polarizations. At 325 GHz above, the atmospheric contribution was too high to provide any reliable estimate of the emissivity.

Above continental snow and ice up to 325 GHz, TELSEM^2 results are very consistent with the aircraft observations in spatially homogeneous regions. The frequency and angle dependences are well reproduced by this parameterization. The agreement at 89 and 157 GHz is very good, considering that TELSEM^2 is only assumed to provide a realistic climatological first guess of the emissivities at a monthly scale. In coastal regions, the agreement can be affected by the differences in spatial resolution between the two estimates. Over sea ice, the aircraft estimates are very variable spatially and temporally, and comparisons with TELSEM^2 model were not conclusive.

This is a first step toward evaluation of the emissivity parameterization at millimeter and sub-millimeter frequencies. More flights under a larger variety of surface and atmospheric conditions will have to be performed. The surfaces that should be targeted are: ocean surface for medium to high surface wind speeds under dry atmospheric conditions, sea-ice surfaces, and continental ice and snow.

Chapter 5

Simulations of the Microwave Polarized Scattering Signals over Frozen Clouds up to 874 GHz

5.1 Introduction

Passive microwave measurements from satellites have the capacity to penetrate the complex vertical cloud structure, providing information about the hydrometeors. As already presented in Chapter 3, at low microwave frequencies (below ~ 80 GHz), emission and absorption by the liquid clouds dominate. At higher frequencies, the cloud frozen particles scatter the microwave signals, providing additional information on the cloud ice microphysical characteristic. In this thesis, all cloud particles have been assumed as spheres or randomly oriented spheroid in radiative transfer simulations (in Chapter 3), and as a consequence did not generate any polarized scattering signal. However, several studies have already evidenced the impact of non-spherical oriented particles on the scattering signals at frequencies above 80 GHz.

Spencer et al. (1989) observed polarized scattering signatures at 85 GHz with the Special Sensor Microwave Imager (SSM/I) above cloud structures and attributed it to non-spherical particles with non-random orientation in stratiform regions, whereas in convective cores, the absence of polarization would be due to 'irregularly shaped graupels tumbling in a turbulent environment'. The sensitivity of the scattering to the particle shape and orientation has been simulated from both satellite observations and ground based measurements by Czekala et al. (2001). Prigent et al. (2001) carefully characterized the scattering-related positive polarization difference (vertical minus horizontal) observed at 85 GHz with the SSM/I and interpreted it with the help of a radiative transfer model to show that the presence of mostly horizontally oriented non-spherical particles is needed within the stratiform anvil part of convective systems to explain the larger polarization magnitudes observed. Concurrent passive and active microwave measurements on board the Tropical Rainfall Measurement Mission (TRMM) showed that under cloudy conditions, when a melting layer is detected by the precipitation radar, a polarized scattering signal at 85 GHz in passive mode is often observed (Galligani et al., 2013). Radiative transfer simulations confirmed the role of large horizontally oriented non-spherical particles on the polarized scattering signals and assessed the effect of changes in particle phase, from solid ice to dry snow to melting snow, on the radiative properties. Polarized scattering by frozen hydrometeors from satellite was investigated for the first time up to 157 GHz, based on the passive microwave observations of the Microwave Analysis and Detection of Rain and Atmospheric Structures (MADRAS) instrument on board the Indo-French Megha-Tropiques satellite mission (Defer et al., 2014). A comparison with time-coincident TRMM Microwave Imager (TMI) records confirmed the consistency of the coincident observations collected independently by the two instruments up to 89 GHz. Compared to the 89 GHz polarized channels that mainly sense large ice particles (snow and graupel), the 157 GHz polarized channel is sensitive to smaller particles and provides additional information on the cloud systems. The analysis of the radiometric signal at 157 GHz revealed that the ice scattering can induce a polarization difference of the order of 10 K at that frequency. In addition, the polarization differences have also been observed with a ground-based radiometer at 150 GHz, and their responses to the snow particle orientation were analyzed by Xie et al. (2012). During snowfall on Mount Zugspitze (German Alps), the polarization differences (V-H) reach up to -10 K at an elevation angle of 34.8° .

The Ice Cloud Imager (ICI) will focus on the remote sensing of ice clouds, and will become the first space radiometer with frequencies up to 664 GHz, for ice cloud monitoring (as presented in Chapter 1). Among other channels, ICI will have two window channel frequencies (243 and 664 GHz) with the capability of measuring both vertical and horizontal polarization signatures. With the capability of detecting, quantifying, and tracking ice particles at different cloud heights, ICI will provide new measurement possibilities, and understanding the scattering characteristics of frozen particles, including their polarization, is required for preparing this next generation of satellite instrument. ISMAR, the ICI demonstrator, has already provided some measurements of ice clouds up to 664 GHz, from airborne campaigns on the UK FAAM BAe-146 aircraft. Evident cloud polarization signals have been observed from several ISMAR flights at both 243 and 664 GHz, such as flight B897. This flight was over a precipitating frontal system, from thin and broken cirrus clouds to full-depth precipitating clouds. The ISMAR observed brightness temperatures at V polarization (TBV) at 243 and 664 GHz during this flight are shown in Figure 5.1 as a function of the polarization differences (vertical minus horizontal, TBVH) for different scan angles (0° and 40°). The flight altitude (km) is shown in color. No polarization was observed at 0° , as expected. The polarization difference induced by the ice clouds reaches 10 K at 243 GHz at 40° . At 664 GHz, the polarization analysis is difficult up to now, due to the scan-dependent warm bias in vertical polarization. Note that ISMAR will soon be upgraded with a dual polarization receiver at 874 GHz.

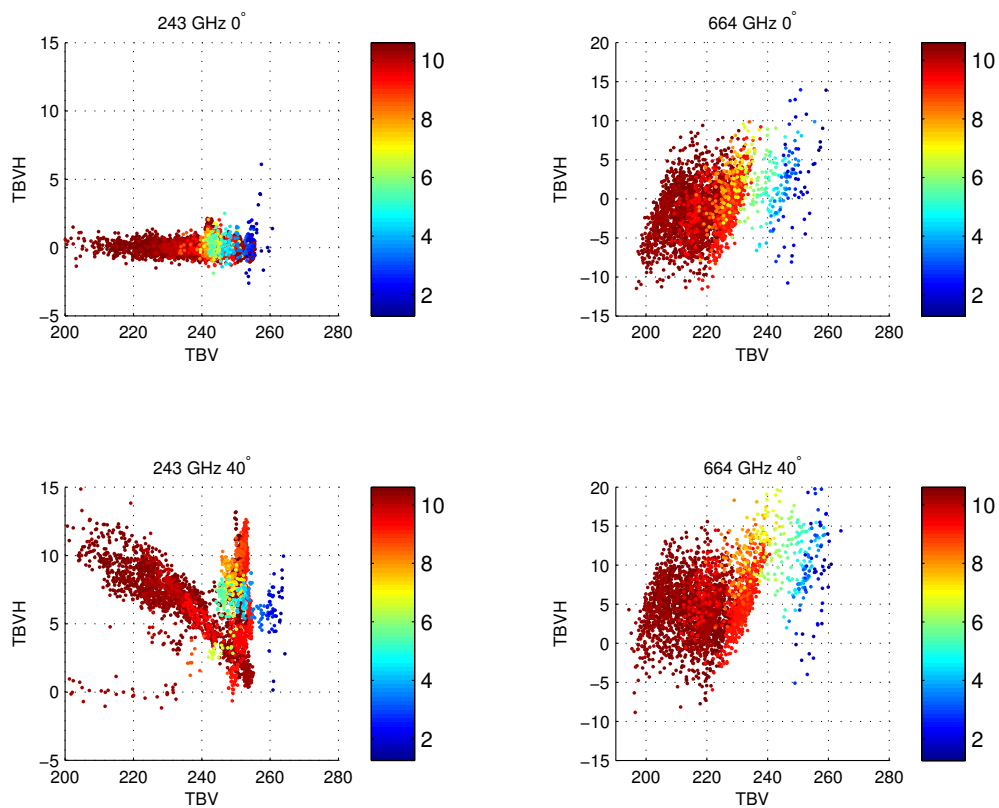


FIGURE 5.1: The brightness temperature polarization differences (TBVH) versus the brightness temperature in vertical polarization (TBV), at 243 and 664 GHz for scan angles at 0° and 40° , for flight B897.

In this chapter, the polarized scattering signatures are simulated by ARTS and analyzed for the first time at higher frequencies up to 874 GHz, where the sensitivity to smaller ice scattering is expected to be higher. The polarized scattering signals are simulated and discussed, for frozen hydrometeors, such as pure ice, dry snow, and wet snow.

5.2 Radiative transfer simulations setup

The radiative transfer simulations are performed with ARTS. We assume a 1D atmosphere for the simulations in this chapter, so the Discrete Ordinate ITERative (DOIT) algorithm (Emde et al., 2004), described in Section 2.3, is recommended and used to solve the radiative transfer equation. The basic atmospheric conditions (i.e., pressure, temperature, water vapor, oxygen, and nitrogen profiles) are extracted from the Fast Atmospheric Signature CODE (FASCOD) database (Anderson et al., 1986) in the tropics. The gas absorption model combination is: the Liebe MPM87 model (Liebe and Layton, 1987) for water vapor, the Liebe MPM92 model (Liebe et al., 1992) for oxygen, and the Liebe MPM93 model (Liebe et al., 1993) for nitrogen.

We assume that there is only one single cloud layer containing frozen hydrometeors located between 6 and 8 km in the atmosphere. To remove the possible contribution of the surface in the polarized signals, we assume a land surface with a fixed emissivity at 0.9, for both V and H polarizations, and a surface temperature at 300 K. The incidence angle is set to 53°, corresponding to the ICI geometry (and close to the geometry of the existing microwave conical scanners). In the first step, the frozen hydrometeors inside the clouds all have the same size. Under the assumption of monodisperse size distribution, the particle number density (PND) can be given as

$$n = \frac{3IWC}{4\pi\rho r_e^2} \quad (5.1)$$

where IWC is the ice water content (kg/m^3), ρ is the particle density (kg/m^3), and r_e is the particle mass-equivalent radius (m).

The dielectric properties of ice and liquid water are calculated from Matzler (2006) and from Liebe et al. (1993), respectively. For the multiphase hydrometeors (snow, graupel, and hail), the effective dielectric properties are calculated by the Maxwell-Garnett formula here, as in Galligani et al. (2013), Defer et al. (2014), and Eriksson et al. (2015). The snow can be dry or wet, depending on its liquid water content. The dry snow is composed of air and pure ice (ice matrix with air inclusions), and the wet snow contains liquid water and dry snow (dry snow inclusions in a water matrix). See Chapter 2 for more details.

The far-field scattering by ensembles of totally or azimuthally randomly distributed spheroids is calculated using the T-matrix method (Mishchenko et al., 2002) described in Section 2.3.2.2. Here, this code is used to calculate the scattering by spheres (giving the same results as Mie code) and by horizontally oriented spheroids (oblate spheroid).

Note that the mass-equivalent radius (r_e) is used to calculate single scattering properties (SSPs) for non-spherical hydrometeors.

5.3 Polarized scattering signatures of ice particles

We first simulate the radiative transfer in a cloud layer filled with pure ice particles. As discussed by [Brussaard and Watson \(1995\)](#), the larger ice particles exist in the natural clouds with preferred horizontal orientation owing to the effects of gravitational field and aerodynamic force, implicating they have longer horizontal axis than the vertical ones. We will not consider here the detailed shape of possible particles. Instead, the particles are regarded as spheroids, with a given aspect ratio (AR) to analyze the shape and orientation effects on the scattering signals ([Galligani et al., 2015](#), [Heymsfield et al., 2005](#), [Matrosov et al., 2005](#)). The AR is the proportional relationship between the maximum and minimum particle dimensions used to characterize the particle non-sphericity. According to aircraft observations ([Heymsfield personal communications](#)) and simulations by [Galligani et al. \(2013\)](#) and [Defer et al. \(2014\)](#), a realistic value for this AR is around 1.6. Therefore, the referred horizontally oriented spheroids in the following simulations are assumed with an AR of 1.6.

Since the hydrometeor scattering signatures are more evident at window channels, calculations are performed in window frequencies at 37, 89, 157, 243, 344, 462, 664, and 874 GHz. Figure 5.2 shows the TBV and the TBVH against the particle radius and against the size parameter (x , presented in Chapter 2). The integrated ice water path (IWP) is set to 0.2 kg/m^2 . At low frequency (37 GHz), the scattering signature is very limited (rather stable TBV), as already reported by [Prigent et al. \(2001\)](#) based on the SSM/I radiometric signatures and by [Galligani et al. \(2013\)](#) based on the TMI observations. At high frequencies (above 80 GHz), the scattering signals become more intense, with decreasing TBV and increasing ice particle size. However, with increasing frequency, the TBV reaches a plateau (around $x = 2.2$), and then increases again with increasing particle size. This can be attributed to the combined effects of less dense particle number (less number of larger particles assuming a fixed IWP) and the weaker scattering efficiency (see below). For these spherical particles, TBVH is very close to zero, regardless of the frequency and particle size.

Figure 5.3 is similar to Figure 5.2, but for horizontally oriented ice spheroids with an AR of 1.6. For this particle type, TBV has a similar behavior as for the spheres with the same equivalent radius. However, TBVH shows a very different signature above 80 GHz, with an increasing polarization difference up to a given particle size (TBV higher than TBH), followed by a TBVH decrease down to ~ 0 K. The maximum TBVH value is similar at 89 and 157 GHz (~ 20 K), but slowly decreases to less than 10 K at 874 GHz. The interpretation of this behavior is possibly the multiple scattering effects introducing more stochasticity in the scattering processes. For higher frequencies, the multiple scattering starts to occur at smaller particles. For example, the polarization difference approaches saturation around 8 K with particles radius of $50 \mu\text{m}$ at 874 GHz, while it is around 20 K with particle radius of $400 \mu\text{m}$ at 157 GHz. The polarization

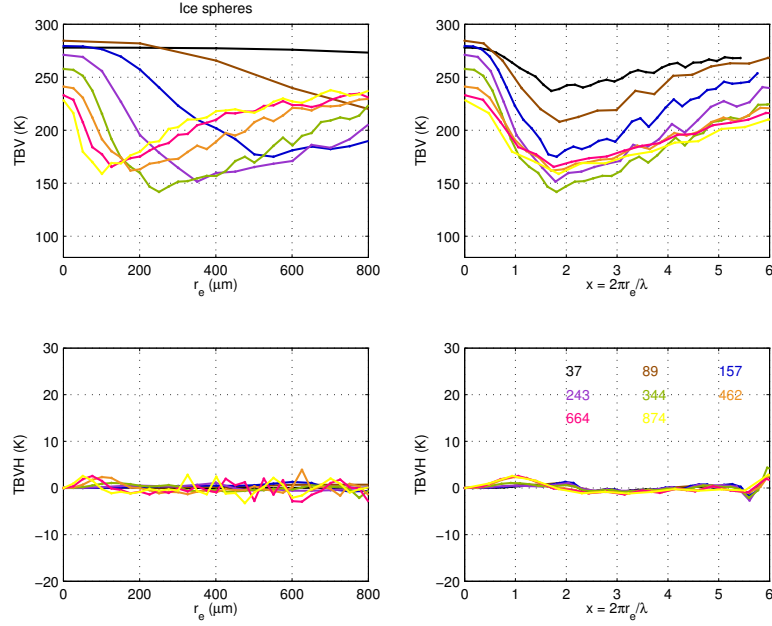


FIGURE 5.2: The sensitivities of the brightness temperature at vertical polarization (TBV) and the polarization differences (TBVH) for pure ice spheres at 37, 89, 157, 243, 344, 462, 664, and 874 GHz to r_e . The IWP is fixed to 0.2 kg/m^2 .

differences keep positive when x is less than 2.2, and their maxima emerge when $x = 1.2$ for all the frequencies mentioned above. When x is more than 2.2, slightly negative polarization differences appear, and polarization differences change following a series of peaks, which are probably explained by the morphology-dependence resonance. This resonance is a function of the particle morphology, meaning, its geometry and dielectric property. Any perturbation to its morphology (shape, size, or dielectric property) can cause a shift in the resonance. In addition, some tests have been done to investigate the sensitivity of the brightness temperature and the polarization to the particle aspect ratio (not shown here), under the assumption of three different AR values (1.3, 1.6, and 2). The brightness temperature depressions are slightly sensitive to the particle shape (particle AR) below certain frequency (e.g., 344 GHz in our case), while lose their sensitivity at much higher frequencies (e.g., 462 and 664 GHz). In terms of polarization, a similar trend is observed. The particle shape becomes less important to the polarized signals at higher frequencies, and even for larger particles at lower frequencies (the differences in TBVH between particles with AR of 1.6 and 2, at 243 GHz, decrease to nearly 0 for the particle radius larger than $250 \mu\text{m}$).

To better understand the scattering processes, the SSPs (i.e., the scattering efficiencies and the scattering cross sections) of horizontally oriented ice spheroids with AR of 1.6 are shown in Figure 5.4. At all the frequencies of concern, the scattering efficiency reaches a peak and then decreases largely with some ripples. The scattering efficiencies are directly related to the size parameter (x), the first peak is reached for $x \sim 3.2$. We also calculated the scattering properties for ice spheres against the particle mass-equivalent radius and the size parameter for comparison (not shown). For the spheres, the peak is reached for $x \sim 2.5$, which is consistent with the results from Kim (2006).

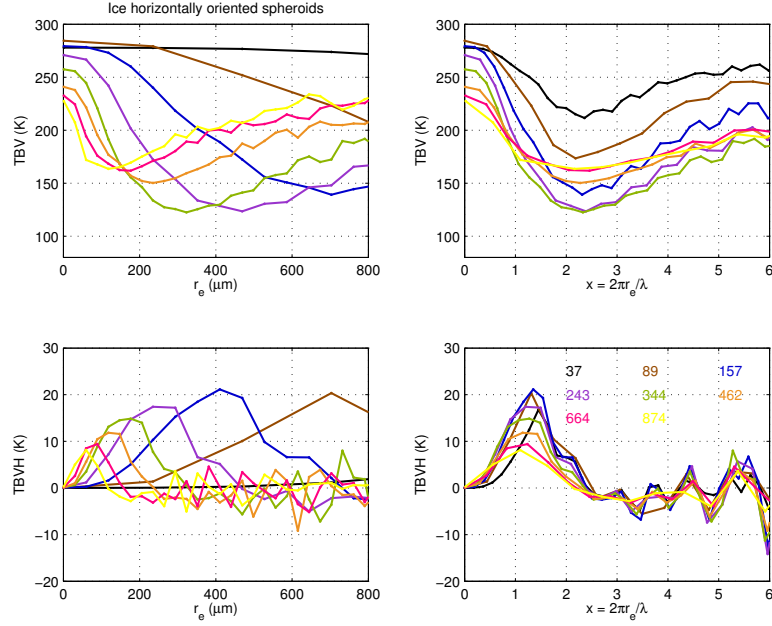


FIGURE 5.3: Same as Figure 5.2, but for horizontally oriented oblate spheroids with an AR of 1.6.

When the size parameter is large enough (in our case, $x > 3.2$ for the horizontally oriented ice spheroids) and the absolute value of the refractive index is close to 1 (~ 1.78 for pure ice at -20°C), we are in the anomalous diffraction regime and the electromagnetic energy is affected by the morphology-dependent resonances related to the surface wave (Chylek and Klett, 1991, Kim, 2006, Yang et al., 2004). The anomalous diffraction theory was firstly introduced by Van (1957) to describe light scattering for optically soft spheres, and it can be expressed as

$$Q_{ext} = 2 - \frac{4 \sin p}{p} + \frac{4(1 - \cos p)}{p^2} \quad (5.2)$$

where Q_{ext} is the extinction efficiency (in this approximation, the refractive index is assumed to be real, leading to $Q_{abs} = 0$, and thus $Q_{ext} = Q_{sca}$), $p = 4\pi r_e(n - 1)/\lambda$ is equivalent to the phase delay of the wave passing through the center of the particle, n is the ratio of refractive indices inside and outside of this particle. Therefore, the scattering efficiency Q_{sca} is determined largely by p , meaning the interference of diffraction and transmission, which depends on the particle surface geometry. In addition, the edge effect (Ackerman and Stephens, 1987), induced by the interaction between the photon that cannot pass through the particle and the particle itself, is an additional term in the extinction efficiency function. The edge corrections are essentially wave optics corrections to geometrical optics results, including a term describing the interference between surface waves that gives rise to the ripple structure in the extinction efficiency curve (Kim, 2006, Kneifel et al., 2010).

Figure 5.5 explores the effects of the ice quantities on the brightness temperatures and on their polarization differences (with IWPs from 0 to 0.6 kg/m^2) for different ice particle

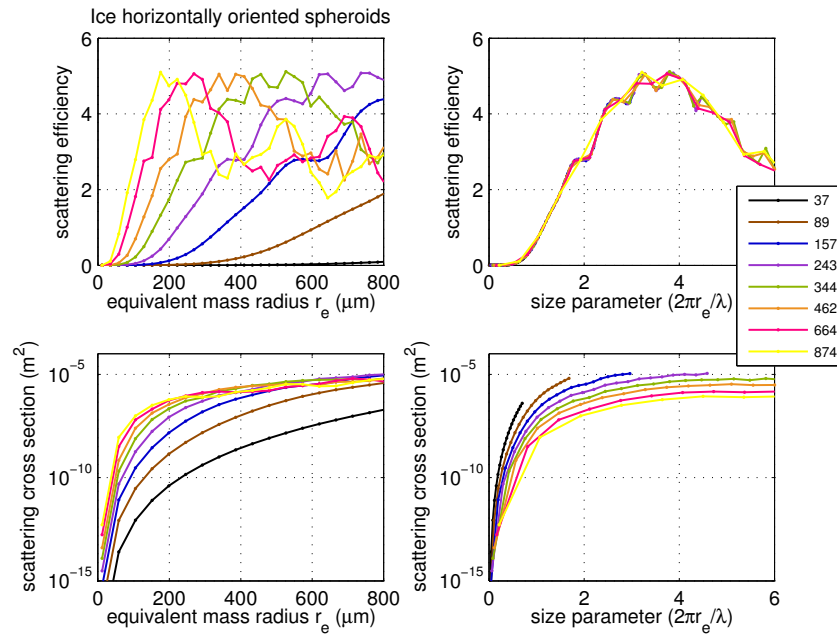


FIGURE 5.4: The scattering efficiencies and the cross sections of pure ice horizontally oriented spheroids ($AR = 1.6$) against r_e and x at 37, 89, 157, 243, 344, 462, 664, and 874 GHz.

sizes (mass-equivalent radius r_e from 0 to 800 μm). When increasing the IWP or the particle size, an enhancement of the scattering effect is expected thanks to an increase of the particle concentration or to the scattering efficiency. However, when the IWP and particle size are large enough, the multiple scattering effect (determined by the cloud optical depth) intervenes. The higher frequencies are more sensitive to smaller particles and lower IWP. With increasing opacity at these high frequency channels, the multiple scattering occurs earlier. The polarization difference saturates for lower particle size and lower IWP. With larger IWP, the critical opacity is reached with smaller particles, and thus the polarization difference starts to saturate for these particles.

5.4 Polarized scattering signatures of frozen particles

The frozen particles, including snow and graupel, produce strong scattering signatures in the millimeter and sub-millimeter wave range, while their emission effects are limited. Their scattering characteristics differ from the pure ice and largely depend on the hypothesis on the particle microphysical parameters, such as the particle shape, the particle orientation, the particle mass, and the PSD, particularly for high size parameters, as presented in Chapter 2.

5.4.1 Dry snow

First, we concentrate on the dry snowflakes, assuming a cloud layer of dry snow particles with snow water path (SWP) of 1 kg/m^2 . The cloud temperature (T) is set to -20°C ,

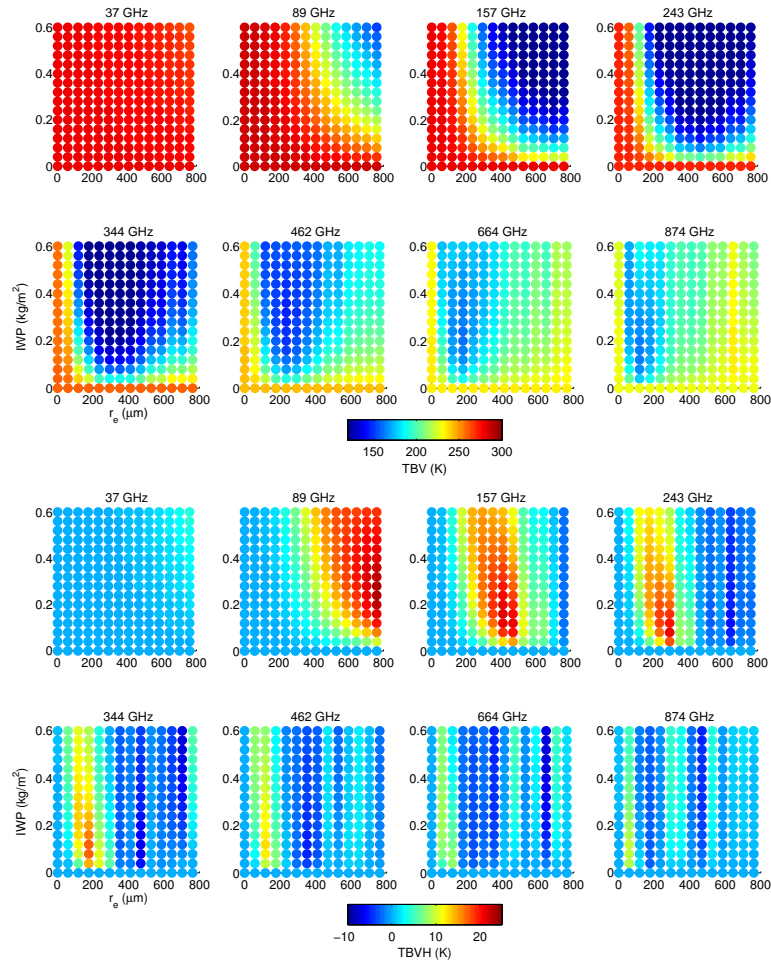


FIGURE 5.5: The sensitivity of the brightness temperature at vertical polarization (TBV) (top) and the polarization difference (TBVH) (bottom) at 37, 89, 157, 243, 344, 462, 664, and 874 GHz for horizontally oriented ice spheroids ($AR = 1.6$), as a function of r_e and IWP.

which is low enough to ignore the wetness percentage ($W, \%$) of snow particles ($W = 0$ for $T < -15^\circ\text{C}$; $W = T - 258.15$ for $-15^\circ\text{C} < T \leq 0^\circ\text{C}$; $W = 15$ for $T > 0^\circ\text{C}$, Skofronick-Jackson et al., 2002). The density of dry snow is fixed to 100 kg/m^3 . Considering that the spheres produce identical scattering signals for both orthogonal polarizations, we only focus on oriented spheroids (as reported by Defer et al. (2014), Prigent et al. (2005)), with an AR of 1.6. The vertical brightness temperatures and the polarization differences for randomly oriented dry snow spheres and horizontally oriented dry snow spheroids are shown in Figures 5.6 and 5.7, respectively. Note that T-matrix method is very challenging and is limited in the application to very large size parameters, especially with large aspect ratios, due to the numerical instability and non-convergence (Wendisch and Yang, 2012). It explains the missing results for larger particles at lower frequencies in the figures. The similar trends of dry snow scattering signal and polarization difference in terms of particle size are obtained as for the pure ice in Section 5.3. The TBV decreases with increasing particle size, reaches a saturation state or a certain particle range, and increases for larger particles. There is no polarization signal for the dry snow spheres, as expected. For the horizontally oriented dry snow spheroids,

the TBVH reaches more than 10 K at some frequencies (e.g., 89, 157, and 243 GHz), for $x \sim 2.2$, which is consistent with the satellite observations (Defer et al., 2014) and ISMAR airborne measurements as mentioned above.

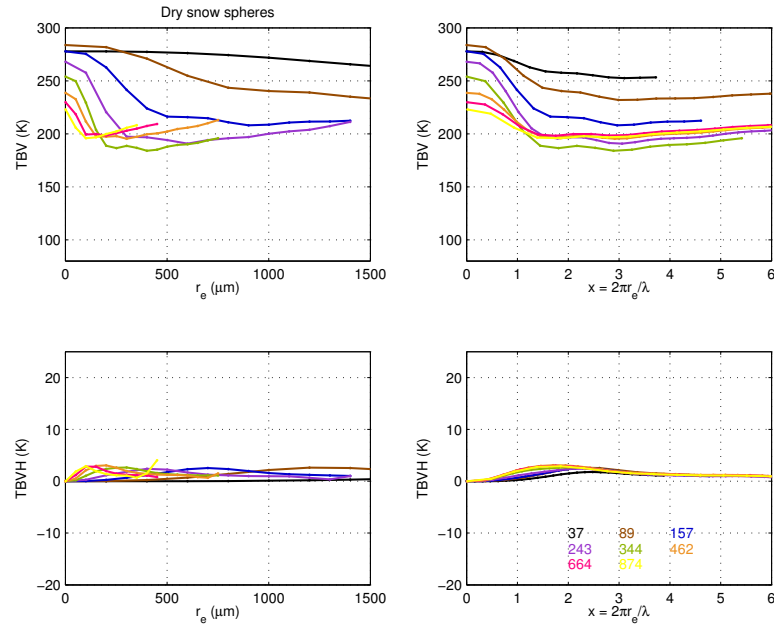


FIGURE 5.6: The sensitivities of the brightness temperature at vertical polarization (TBV) and the polarization differences (TBVH) for dry snow spheres at 89, 157, 243, 344, 462, 664, and 874 GHz as a function of r_e and x . The SWP is fixed to 1 kg/m^2 .

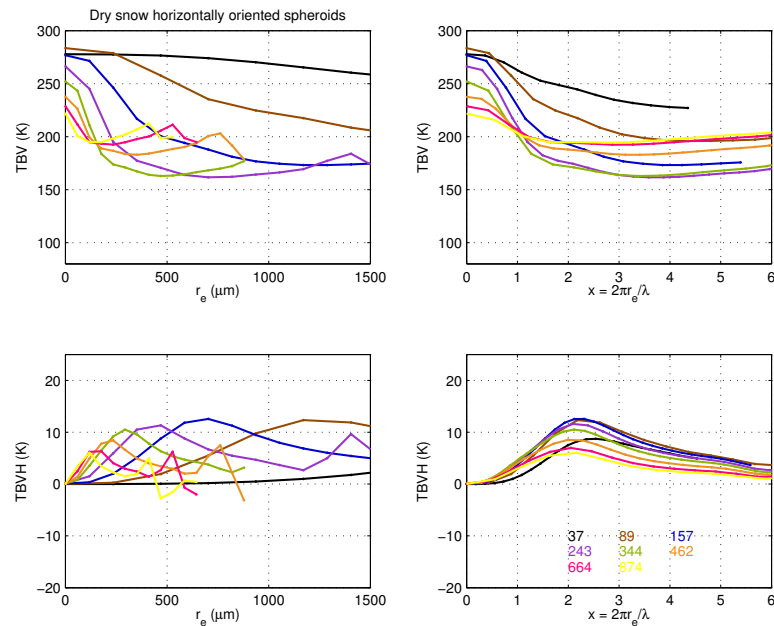


FIGURE 5.7: Same as Figure 5.6, but for horizontally oriented dry snow spheroids ($AR = 1.6$).

The scattering properties of dry snow horizontally oriented spheroids are presented against r_e and size parameter in Figure 5.8 for all the concerned frequencies. The dry snow scattering efficiency can reach up to 7 at very large particles (radius of 2000

μm at 874 GHz). Note that, unlike the ice particles, the sharp peaks only appear for much larger size parameters ($x > 32$). The physical interpretation is given by [Guimaraes and Nussenzweig \(1992\)](#). The real part of dielectric property is a critical parameter for understanding morphology-dependent resonances (presented in Section 5.3). The real part of the effective dielectric permittivity is a function of the volume fraction of the inclusion (in this case, the air) determined by the dry snowflake density (see Chapter 2, Section 2.3.2). The snow particles with lower density (100 kg/m^3) have lower dielectric constant hence less scattering efficiency compared with ice particles on the same size producing weaker resonance effect.

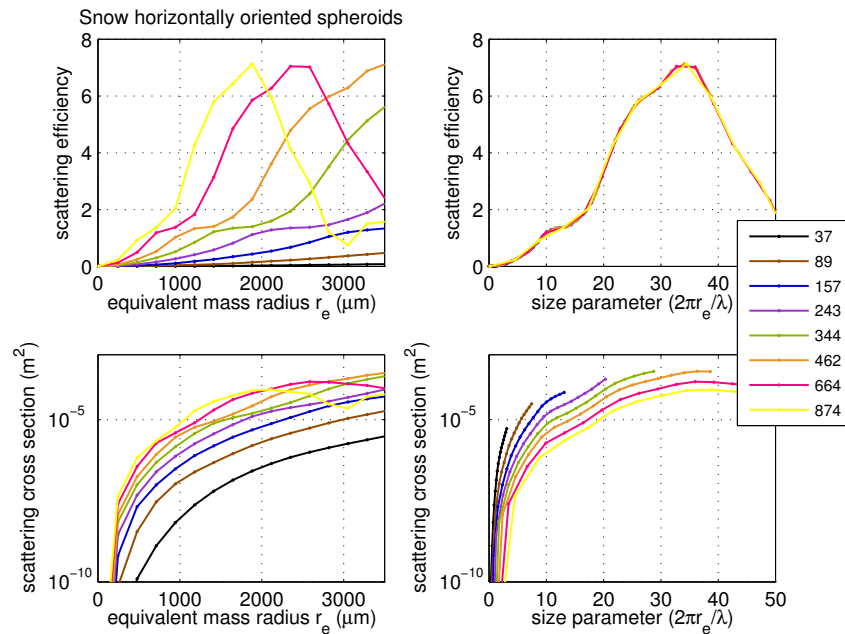


FIGURE 5.8: The scattering efficiencies and the cross sections of dry snow horizontally oriented spheroids ($AR = 1.6$) against r_e and x at 37, 89, 157, 243, 344, 462, 664, and 874 GHz.

Figure 5.9 explores the effects of the dry snow quantities on the brightness temperatures and the polarization differences with SWPs (from 0 to 2 kg/m^2) and different dry snow particle sizes (r_e from 0 to $600 \mu\text{m}$). As discussed for ice particles, scattering effects strengthen with increasing particle concentration and particle size. However, the multiple scattering effect also occurs when the SWP and particle size are large enough. Higher frequencies are more sensitive to smaller dry snow particles and lower IWP.

The monodisperse size distribution has been used in the simulations in previous sections, assuming single size particle in the clouds. In reality, the different types of particles exist with their various sizes and shapes. Therefore, some sensitivity simulations have been performed to study the response of polarized scattering signals to the snow PSD. The [Field et al. \(2007\)](#) snow PSD is chosen for this comparison, which is used in RTTOV radiative transfer code as discussed in [Geer and Baordo \(2014\)](#). It is a moment estimation parameterized PSD, based on the aircraft measurements of the tropical anvils and mid-latitude stratiform clouds, with reference to the second moment of the PSD (proportional to the ice water content). Figure 5.10 shows the TBV and TBVH of horizontally oriented

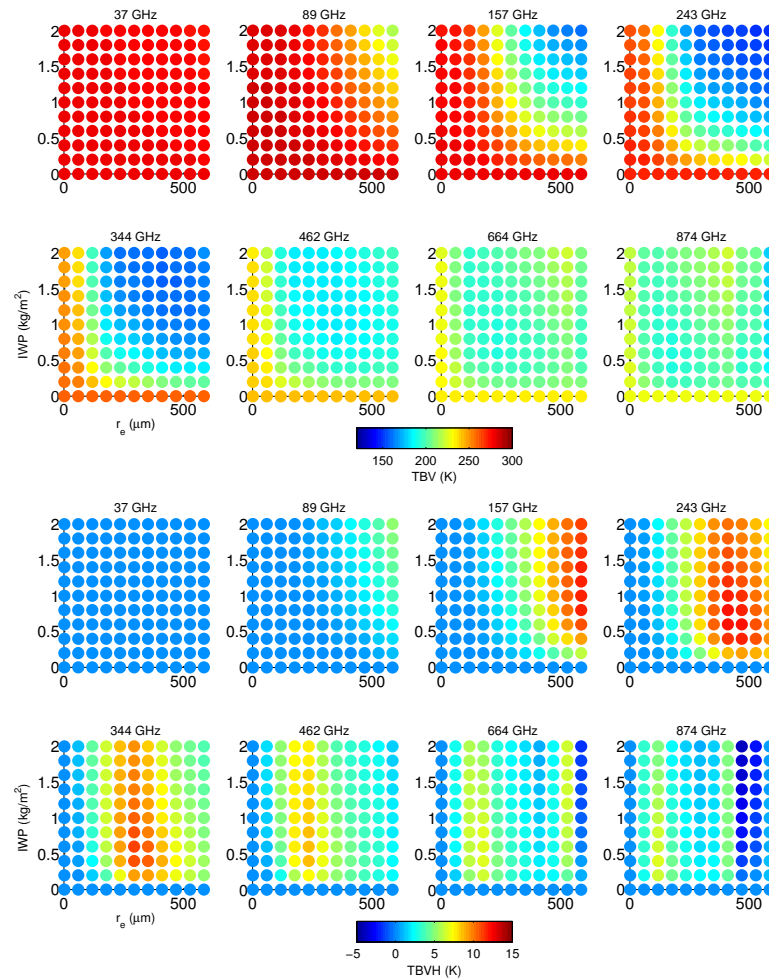


FIGURE 5.9: The sensitivity of the brightness temperature at vertical polarization (TBV) and the polarization difference (TBVH) at 37, 89, 157, 243, 344, 462, 664, and 874 GHz for horizontally oriented dry snow spheroids, as a function of r_e and IWP.

dry snow spheroids ($AR = 1.6$), calculated with different PSD assumptions (Field et al. (2007) and monodisperse ($r_e = 300 \mu m$) PSDs), as a function of SWP (from 0.1 to $2 kg/m^2$). The polarized scattering largely differs from one PSD to the other. With increasing SWP, Field et al. (2007) PSD provides more particles in a large particle range, inducing stronger scattering effect, as well as the polarization signals. As discussed above, a saturation of the polarization scattering signal appears under the monodisperse size distribution assumption at each concerned frequency.

5.4.2 Wet snow

The melting snow is a very significant component of the stratiform clouds. It produces a sharp increase in the radar reflectivity (from satellite- and ground-based), called the bright band, and is located just below the $0^\circ C$ isotherm level. Generally, the frozen particles grow through deposition and fall down to $2.5 km$ above the $0^\circ C$ level, and the aggregation of snow particles occurs frequently within $1 km$ of this level (Robert and Houze, 1993). The aggregation process allows the snowflakes to become larger with

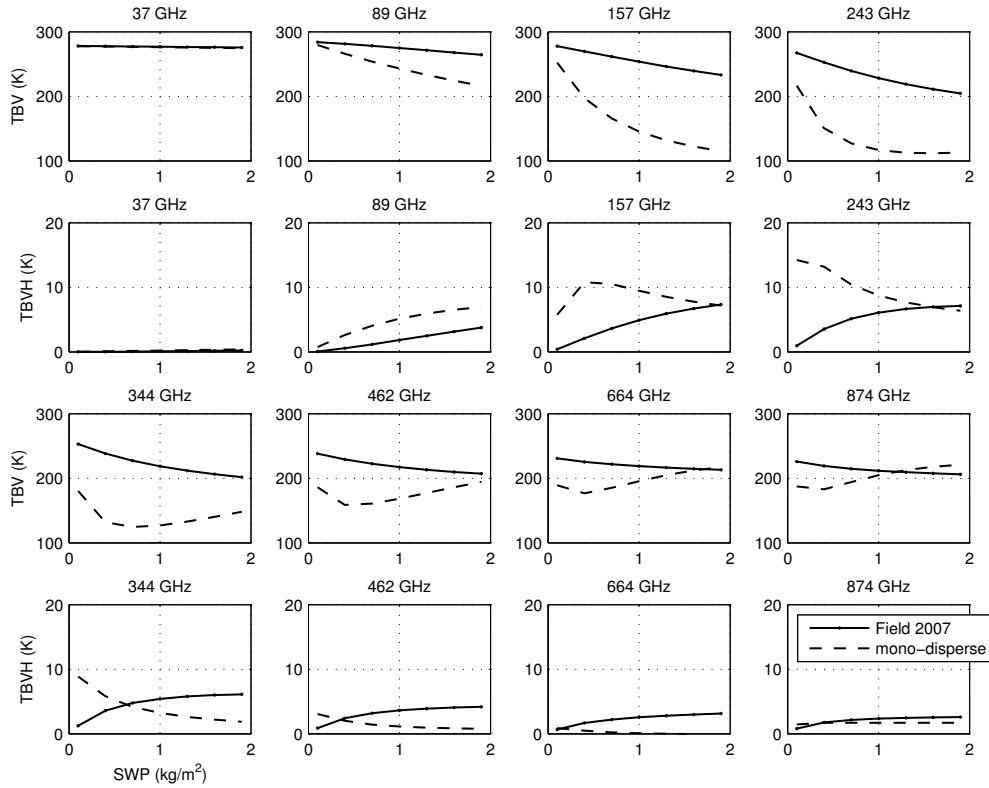


FIGURE 5.10: The sensitivity of the brightness temperature at vertical polarization (TBV) and the polarization difference (TBVH) at 37, 89, 157, 243, 344, 462, 664, and 874 GHz for horizontally oriented dry snow spheroids, for monodisperse ($r_e = 300 \mu m$) and for Field et al. (2007) PSDs, as a function of IWP.

irregular shapes. During the aggregation, the total mass of the frozen particles remains almost constant, but the number of large particle increases. Then the snowflakes collapse into smaller raindrops and they precipitate.

In this study, the cloud layer is set to 4 km close to 0°C isotherm level, with SWP of 1 kg/m². We assume that the melting snow is composed of water (as inclusion) and dry snow (as environment), as mentioned in Chapter 2, Section 2.3.2. As for dry snow, the Maxwell-Garnett formula (Garnett, 1906) is employed to calculate the effective dielectric property of wet snow, but twice here. The wetness definition is linked to the cloud temperature (Skofronick-Jackson et al., 2002), as given in Section 5.4. The cloud temperature is set to 250 K, 260 K, and 273 K, corresponding to a wetness of 0 % (dry snow), 2 %, and 15 %, respectively. Figure 5.11 reveals the influences of snow wetness on the polarized signatures. At low frequencies (e.g., 37 GHz), the liquid water absorption and emission are the main processes, and dry or wet snow particles have a limited impact over the warm surface background. At 89, 157, 243, and 344 GHz, the scattering effect and polarization signature for the wet snow particles are very limited compared to the dry snow particles. On one side, an increase in wetness translates into an increase in snow density and a decrease in snow particle number concentration, tending to decrease the scattering effect. On the other side, the increased wetness is a result of the increase in cloud temperature and fraction of liquid phase, leading to a larger dielectric property, hence stronger scattering effect. In our case, the effects of the

increase in dielectric property on the snow scattering signals and polarization difference are largely compensated by the effect of the decrease in particle number concentration. In a real cloud, during the melting process, the transition from dry snow particles to wet ones will not lead to a evident change of particle number, but an increase in snow density, inducing a higher dielectric property, thus stronger scattering signals. Note that, at 462, 664, and 874 GHz, there is no effect of the frozen particles at 4 km, because of the large atmospheric opacity above the clouds. The polarization differences decrease as the snow wetness increases, and the maxima appear at smaller particles.

According to observations from TMI (Galligani et al., 2013) and MADRAS (Defer et al., 2014), the stratiform clouds present higher polarization differences at 85 and 157 GHz, and this is likely related to the snow particles just above the melting layer. The observations of snowfalls at mid-latitude from the ground-based in situ measurements with optical disdrometers (e.g., Brandes et al., 2007, Huang et al., 2010) reveal that the large snowflakes aggregate in complex shapes in the stratiform clouds. The typical and classic snowflakes, such as hexagonal columns, plates, or dendrites, are only representative of the small particles. As shown by our simulation, the large polarization signatures originate from the large dry snow aggregates, likely above the melting layer. During the melting process, the large wet snow aggregates could also provide a relative large polarization differences, although our analysis tends to show that their contribution to the polarized signatures is more limited.

The sensitivity of snow density is also investigated by substituting the constant density (100 kg/m^3) by a more realistic parameterized density from Fabry and Szyrmer (1999) (in Figure 5.11). The size-density relationship is given as $\rho = 0.012D^{-1}$, in cgs units. In this parameterization, the snow density decreases rapidly with the particle size from the maximum limit 917 kg/m^3 (pure ice density) to nearly 100 kg/m^3 . This assumption leads to an increase of scattering and polarization differences for smaller and denser particles for the reason that the effective refractive index of snow is proportional to the density (see Section 2.3.2).

5.5 Conclusion

The polarized scattering signatures of frozen clouds have been simulated over a large frequency range from 37 to 874 GHz, for spheres as well as for horizontally oriented spheroids, using ARTS with DOIT.

At low frequencies (below 80 GHz), very limited scattering signatures are observed. At higher frequencies, the polarized scattering signatures derive from the interaction of the radiation with oriented non-spherical particles. The brightness temperature depression as well as the polarization difference increases with particle size and with particle contents. However, the brightness temperature depression tends to reach a maximum and then reduces. The maximum depression tends to be more limited for large frequencies. The same happens for the polarization difference: for large frequencies, it reaches a maximum and then decreases, with the value of the maximum reducing with increasing

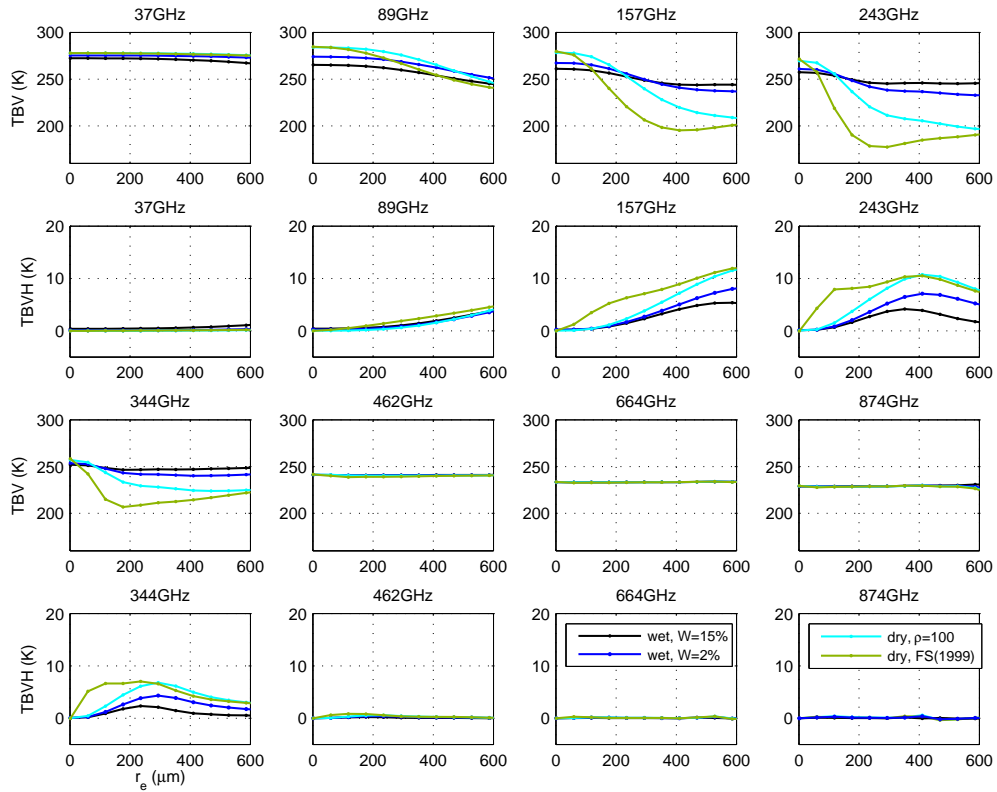


FIGURE 5.11: The simulated brightness temperature at vertical polarization (TBV) and the polarization difference (TBVH) at 37, 89, 157, 243, 344, 462, 664, and 874 GHz for dry snow and wet snow horizontally oriented particles ($AR = 1.6$) with different wetness (W) as a function of r_e .

frequency. This can be interpreted by the increased opacity with increasing frequency and thus increased multiple scattering effects. The simulated polarization differences are consistent with satellite observations (at 89 and 157 GHz) and ISMAR airborne measurements (at 243 GHz).

In this study, only the spheres and spheroids are discussed. For more irregular shapes, the discrete dipole approximation method (DDA, [Draine and Flatau, 1994](#)) is a promising way to calculate realistic scattering properties as discussed in Chapter 2 and used for realistic radiative transfer simulations in Chapters 2 and 3. It can handle more realistic frozen particles such as columns, plates, rosettes, or dendrites (e.g., [Evans et al., 2005](#), [Noh et al., 2006](#)). For small ice particles ($< 30 \mu\text{m}$), the scattering signals do not depend strongly on the particle shapes even at 664 GHz. However, for larger snowflakes, they will have to be accounted for. However, at present the DDA calculations do not provide polarization information. Efforts are underway to overcome this limitation.

Note that the polarization differences discussed here are rather significant, often of the order of 10 K. This will have to be taken into account in the retrieval of the frozen quantities. However, at this stage and in a first step, the quantification of the polarized signal is still difficult, and it is recommended to neglect the polarization signal in the retrieval, knowing that this can introduce errors. This is what has been done in the cloud parameter retrievals in Chapter 3.

Chapter 6

Conclusions and Perspectives

6.1 Conclusions

The second generation of the EUMETSAT Polar System (EPS-SG) will provide meteorological data starting in 2021. EUMETSAT will operate three passive microwave instruments on these polar platform: the Microwave Sounder (MWS), the Microwave Imager (MWI), and the Ice Cloud Imager (ICI). ICI will have 9 channels measuring radiance at 183, 243, 325, 448, and 664 GHz. The window channels at 243 and 664 GHz will have dual polarization measurements (V and H). It will provide unprecedented measurements in the sub-millimetre spectral range, above 200 GHz, contributing to an innovative characterization of ice clouds over the globe. The European scientific community is getting prepared to this new potential, with a series of technical and scientific studies. It includes several research groups such as the Observatoire de Paris, Hambourg University, Cologne University, UK Met Office, or Chalmers University.

This thesis is a contribution to the preparation of this upcoming satellite-borne sub-millimeter imager, ICI, with a strong collaboration with the other research groups involved in these developments. It focuses on the following aspects:

- sensitivity analysis of the passive millimeter and sub-millimeter responses to frozen hydrometeors and realistic simulations of the radiometric signals at ICI frequencies;
- development a statistical retrieval algorithm for the characterization of ice clouds with ICI;
- estimation of the surface emissivities using airborne ISMAR observations at millimeter and sub-millimeter waves;
- analysis of the polarized scattering signals from ice clouds in the millimeter and sub-millimeter range using radiative transfer modeling.

6.1.1 Realistic radiative transfer simulations of ICI observations

First, realistic radiation transfer simulations have been prepared for real scenes in the millimeter and sub-millimeter range to better understand the scattering in frozen clouds and to generate the ice cloud parameters retrieval database (in Chapter 2). The radiative transfer simulations have been performed with the Atmospheric Radiative Transfer Simulator (ARTS) using realistic atmospheric profiles from the Weather Research and Forecasting (WRF) model, for twelve European mid-latitude scenes. When coupling these two models, special attention has been paid to the selection of the microphysics scheme in WRF and the calculation of the single scattering properties (SSPs) for ARTS. The WRF WSM6 microphysical scheme has been selected as it provides robust results and runs fast enough, predicting the mixing ratios of five hydrometeors (cloud ice, snow, graupel, rain, and cloud water). My experience in atmospheric modeling with WRF has been gained during my master thesis about local circulation and thunderstorm studies in mid-latitude (two papers have been published, Wang et al., 2013, 2015). Extensive

sensitivity tests were performed on the ice scattering properties. A Discrete Dipole Approximation (DDA) pre-calculated database has finally been adopted to provide realistic SSPs for snow particles (with aggregates from the Hong DDA database finally selected due to a closer match to the WRF microphysical assumption WSM6). The performance of the coupling model results has been evaluated by comparison with existing satellite observations from SSMIS up to 190 GHz. A good agreement has been obtained for all the twelve cases at the investigated frequencies, giving us confidence in these WRF+ARTS simulations.

6.1.2 Development of a statistical retrieval algorithm for ICI

The second part of this thesis concerned the development of a statistical retrieval of the ice cloud parameters from ICI based on Neural Network (NN) methodologies (in Chapter 3). Combination of ICI and MWI observations has also been explored, with frequencies from 19 to 664 GHz. The simulation database prepared in the first part of this study is used: it includes the atmospheric variables of interest describing the 12 cases and the corresponding simulated brightness temperatures at ICI and MWI channels. It ensures that the database is physically satisfactory for the retrieval. Additionally, the quality of this database needs to be investigated statistically. PCA and correlation analyses have been performed on the integrated hydrometeor contents, the hydrometeor profiles, and the simulated brightness temperatures at frequencies of interest. The potentials of the ICI channels for the frozen particle retrieval and the advantage of the MWI channels in improving the liquid particle retrieval are revealed from correlation analyses. A standard multiplayer feed-forward NN classifier and retrieval algorithm have been used to detect and quantify each cloud hydrometeor by using the prepared retrieval database for ICI-only and for ICI+MWI channels. The classifier gives very reasonable accuracy in detecting the cloud frozen hydrometeors when using ICI-only channels, with an accuracy of 88.9 % over land (similar over sea). For the cloud hydrometeor quantification, the retrieved cloud frozen phase contents are satisfactory with ICI-only channels for ice water path (IWP) above 0.05 kg/m^2 . The absolute error is larger than 0.04 kg/m^2 for IWP less than 0.05 kg/m^2 , showing the difficulty in lower IWP retrieval. Adding the MWI channels improves the detection and quantification essentially for the cloud liquid phases, as expected. For the hydrometeor profiles, the retrieval algorithm can capture the major vertical structures of the cloud profiles, but fail to detect the details.

This work has been presented in the 4th ISMAR workshops in Hamburg, Jun. 2016 and has been accepted for oral presentation at the 8th IPWG and 5th IWSSM Joint Workshop in Bologna, Oct. 2016. A paper describing the database simulations and the retrieval development has been published in IEEE Transaction on Geophysics and Remote Sensing (see Appendix D).

6.1.3 Surface emissivity estimation using airborne ISMAR observations

No effort had been made toward the estimation of the surface emissivity at frequencies above 200 GHz, due to the lack of observations for the evaluation. The ISMAR is a unique opportunity to document the surface emissivity in the sub-millimeter range, above 220 GHz. Another instrument, the Microwave Airborne Radiometer Scanning System (MARSS), was also operated on board the same aircraft, at frequencies from 89 to 183 GHz. First, the ISMAR and MARSS observations have been analyzed using radiative transfer modeling with ARTS for the uplooking observations. The data quality is within the requirements or close to it for most channels. Second, the ISMAR instrument noise has been estimated statistically for all 15 flights, separately for the upwelling and downwelling views at zenith and nadir. The evaluated noise is comparable to the specification for each channel, except for the 243 GHz V and 448 ± 7 GHz. Third, the measured upwelling and downwelling radiances by the ISMAR and MARSS at low altitudes from four flights during two campaigns have been used to estimate the surface emissivities for different surface types (i.e., sea, sea-ice, and continental ice surfaces). Two emissivity parameterizations, the Tool to Estimate Land Surface Emissivity from Microwave to sub-Millimeter waves (TELSEM²) and the Tool to Estimate Sea Surface Emissivity from Microwave to sub-Millimeter waves (TESSEM²), have been developed at LERMA to provide realistic surface emissivities over land and sea, for frequencies up to 664 GHz. These two emissivity parameterizations are evaluated with the ISMAR aircraft observations in this thesis in Chapter 4. Four flights have been selected for emissivity estimation, considering their limited cloudiness and low level runs. For ice-free sea surface, the agreement between the retrieved and modeled emissivities by TESSEM² is very encouraging up to 325 GHz, for all the polarizations and angles (except for 325 GHz at larger angles that is contaminated by the atmosphere contribution), and for low wind speeds (3 to 5 m/s). Above continental snow and ice up to 325 GHz, TELSEM² is very consistent with the aircraft observations in spatially homogeneous regions. Over sea ice, the aircraft estimates are very variable spatially and temporally, and the comparisons with TELSEM² model were not conclusive at this stage. Above 325 GHz, the atmospheric contribution is too high to provide any estimate of the emissivities. These two surface emissivity models have already been used to provide reasonable land and ocean surface emissivities for the preparation of the cloud parameter retrieval database in Chapters 2 and 3.

This study has been partly supported by a EUMETSAT contract 'Study on surface emissivity at microwave and sub-millimeter frequencies' (EUM/CO/14/4600001473/CJA). The work has been presented at EUMETSAT (Darmstadt, Jan. 2016), at the 3rd and 4th ISMAR workshops (Paris, Sep. 2015 and Hamburg, Jun. 2016), and at the 4th workshop on remote sensing and modeling of surface properties (Grenoble, Mar. 2016). One paper about the ocean emissivity has been published in Quarterly Journal of the Royal Meteorological Society (QJRMS) and one paper about the land emissivity has been submitted to Journal of Atmospheric and Oceanic Technology (JAOT). They are attached in Appendices B and C

6.1.4 Analysis of the polarization signal with ICI

Polarized scattering signals of frozen clouds have not been taken into account in the development of the retrieval algorithm in Chapter 3. We assumed a random orientation of all the cloud hydrometeors in the radiative transfer simulations. Note that the DDA databases so far do not provide calculations for oriented particles. Nevertheless, we are aware that orientation of non-spherical particles can impact the polarized signals at microwave to sub-millimeter frequencies. Analysis of the scattering polarized signals can provide information on particle shapes and orientations, and help understand the cloud microphysical properties. It should be taken into account to improve the ice cloud retrieval performance. In Chapter 5, we investigated expected polarization effects using radiative transfer modeling (ARTS with the Discrete Ordinate Iterative, DOIT) over a large frequency range from 37 to 874 GHz at window channels, for horizontally oriented spheroids. The SSPs are calculated with the T-matrix method. The scattering signatures are limited at low frequencies (below 80 GHz), while they are more evident at higher frequencies for oriented non-spherical particles. With increasing particle size or ice content, the brightness temperature depression and the polarization difference tend to reach a maximum and then become smaller again. Simulations show that with increasing frequency, this maximum increases reach a plateau and decreases. The decrease could be attributed to the increasing multiple scattering effects. The simulated polarization differences are consistent with satellite observations at 89 and 157 GHz (e.g., MADRAS and TMI), in agreement with previous studies. The polarization signals observed during the ISMAR campaigns have been analyzed, reaching ~ 10 K at 243 GHz at a scan angle of 40° . These observations agree well with our radiative transfer simulations.

6.2 Perspectives

More work still need to be done in the coming years for the exploitation of MWI/ICI data on METOP-SG for operational applications. This includes efforts in better understanding and simulating the interaction of radiation at ICI frequencies with the atmosphere and the surface, and in the development of optimized retrieval methods. Analysis of more ISMAR observations under a large variety of environments is necessary. Synergy with active microwave observations could also be considered.

6.2.1 Efforts in radiative transfer understanding and modeling up to sub-millimeter frequencies

Continued efforts need to be made to better understand the microphysical properties of frozen hydrometeors and their responses to the millimeter and sub-millimeter waves, since the misrepresenting of them can induce large uncertainty in ice mass retrieval, as discussed in Chapter 2. Approximations for the shape of frozen particles cannot be avoided, directly related to the calculation of their single scattering properties. The DDA method is promising for calculating the SSPs of frozen hydrometeors, without restrictions on their shapes. In this thesis, the Hong DDA database has been selected, according to the investigation of the compatibility of the hypotheses adopted in the DDA calculation and in the WRF WSM6 microphysical scheme. However, the selection of frozen particle habits from existing DDA databases is still questionable and inconclusive. Therefore, the idea is to compare the simulated brightness temperatures by WRF+ARTS model (with different WRF microphysical schemes and SSPs from corresponding DDA database for snow particles) with available satellite observed ones to find an 'ideal' combination. This would minimize the uncertainties induced by the microphysical assumption, and thus improving the ice cloud parameter retrieval performance. This work is ongoing (in collaboration with V.S. Galligani, UBA-CONICET), using WRF+ARTS model, as well as WRF+RTTOV, for Tropical cases. In addition, more cases at mid-latitude should be studied under different meteorological situations in the next step.

The existing DDA databases do not cover the full frequency range. In addition, they do not handle oriented particles that have been shown to play a key role on the polarized signals. Development of new DDA databases is required, for the preparation of the MWI and ICI instruments, for various frozen habits over the full frequency spectrum and including oriented particles. Work is ongoing in Chalmers University by R. Ekelund for preparing a database of SSPs of ice particles covering frequencies from 18 to 884 GHz, at three temperatures, for complex ice habits (reaching a volume-equivalent diameter of 5 *mm*), such as columns, graupel, pristine snowflakes, and aggregates. Randomly orientated frozen particles are considered in the first step. Horizontally orientated hydrometeors are expected to be simulated in the next stage.

For the analysis of polarized scattering, we expect to analyze thoroughly the Global Precipitation Measurement (GPM) Microwave Imager (GMI) observations, on board GPM mission. It is the first conically-scanning passive microwave radiometer to measure

polarized radiation above 100 GHz (166 GHz), outside the Tropical zone (MADRAS on board Megha-Tropique observed polarized scattering at 157 GHz only in Tropics). According to preliminary analysis at NASA, polarization differences exceeding 10 K in tropical and mid-latitude stratiform rain associated with mesoscale convective systems have been observed, as well as more than 20 K in frontal stratiform rainfall and tropical cyclones undergoing extratropical transition.

RTTOV is a fast community code developed for use in Numerical Weather Prediction centers. It is based on the parameterization of a line by line radiative transfer code, and includes scattering calculation. The code has been recently extended to the ICI frequencies, under clear sky assumptions. We did some preliminary comparisons with ISMAR observations and ARTS simulations. This work has to be continued. There is also a need to extend the RTTOV scattering calculations to the millimeter and sub-millimeter range. This work will have to be done in close collaboration with the UK Met Office.

6.2.2 Developments in retrieval methodologies

A statistical retrieval algorithm has been developed for the ice cloud parameters in this thesis in Chapter 3. This work is based on realistically simulated brightness temperatures with WRF+ARTS model, to have a valid assessment of the retrieving capacity of the ICI and MWI instruments. However, some sources of uncertainty have not yet been accounted for, which may affect the retrieval performance. The instrumental noises have been taken into account in the ice cloud parameter retrievals in Chapter 3, but not the uncertainties in WRF modeling/parameterization and in the radiative transfer modeling with ARTS, which could have a major impact on the retrieval performance. In our study, the simulations (training and test databases) of 12 diverse and fairly representative events have been compared and validated with existing satellite observations up to 200 GHz (which is rarely done in this field). This gives us confidence about the current simulation setups at those frequencies. Nevertheless, this retrieval algorithm needs to be studied once real satellite observations become available (specially at the higher frequencies).

The training database will have to be extended to the globe. We concentrated on European situations so far. Mid-latitude situations were deserving special attention: snow is recognized to be a key problem in the radiative transfer in this frequency range and is often present in mid-latitude cases (in the clouds as well as in precipitation). Tropical situations as well as polar cases will have to be added to the database. For that, cloud model simulations will have to be performed and it is advised to simulate real scenes that have been observed by the current satellites, for an evaluation of the radiative transfer simulations up to 200 GHz.

6.2.3 The key role of the ISMAR aircraft observations

The role of ISMAR observations in the preparation of ICI exploitation is two fold:

- analysis and evaluation of the radiative transfer simulations
- evaluation of the retrieval performance

In addition to the two aircraft campaigns operated during this Ph.D period, the Met Office flew ISMAR on a number of flights on February and March 2016 as part of the WINTeX campaign, based out of Cranfield airport. Various flights were designed to look at clear sky, cirrus, and thicker cloud measurements. The flight information is given in Table 6.1 and the database is available to the community.

6.2.3.1 Analysis of the high frequency signals and evaluation of the radiative transfer simulations

With both upward and downward views over a large range of incidence angles, ISMAR can help understand the radiometric signals at high frequencies, as well as evaluate the radiative transfer model/parameterization, for the atmospheric gas contribution, for the cloud interaction, and for the surface emissivity.

In terms of gaseous absorption, with its upward looking views, ISMAR observations are suitable to test the line parameters as well as the absorption continua up to 664 GHz, under a large range of altitudes. We performed comparisons with ARTS simulations. RTTOV simulations have also been conducted at LERMA (not presented in this thesis). Other spectroscopic assumptions are under consideration with the Atmospheric Transmission at Microwave model (ATM, Pardo et al., 2001). These evaluations have to be encouraged, for a large variety of atmospheres, as well as the associated model developments.

Chapter 4 is a first step toward the evaluation of the emissivity parameterizations (TESSEM² and TELSEM²) at millimeter and sub-millimeter frequencies using ISMAR observations. There are only four flights during the first two ISMAR campaigns suitable for the surface emissivity calculations with low-level runs and limited cloudiness, over ice-free ocean, sea-ice, or continental ice. It shows the difficulties in evaluating the emissivity parameterizations conclusively. More flights under a larger variety of surface and atmospheric conditions are expected. During the ISMAR WINTeX-2016 campaign described above, Flight B940 was designed for the sea surface emissivity study and clear-sky radiative transfer comparisons, with low-level runs at 500 *ft* and near-surface winds of 5-10 *m/s*. However, the cloud conditions were not ideal with some cumulus around. The measurements during this flight will be analyzed and used in sea surface emissivity retrieval to evaluate the TESSEM² for slightly higher wind speed condition than during the first two campaigns (3-5 *m/s*). The following surfaces should be targeted during the future ISMAR campaigns: ocean with medium to high surface wind speeds under dry atmospheric conditions, sea-ice surfaces, and continental ice and snow.

The major objective of ICI is the characterization of the ice clouds. Careful analysis of ISMAR flights have to be conducted under cloudy conditions. With the FAAM aircraft flying rather low, observations from above the clouds as well as from below the clouds

have to be considered. During the first two campaigns, the UK Met Office performed a very careful analysis of the instruments and showed the good performance of the ISMAR instrument. Detailed study of the scattering effect can now be performed, including the analysis of the polarized signals for the window channels at 243 and 664 GHz. A preliminary examination has been provided in Chapter 4. We plan a further analysis in the near future.

6.2.3.2 Evaluation of the retrieval performance

The airborne observations from ISMAR can also be used to test the performance of the retrieval algorithm. Several flights during the two first campaigns were designed for the cloud and precipitation studies. Flights B879, B884, and B892 were under stratocumulus cloud conditions. Flight B897 was over a precipitating frontal system, with the clouds varying from thin and broken cirrus clouds to full-depth precipitating clouds. In addition, various flights during the WINTEX campaign were designed to look at clear sky, cirrus, and thicker cloud measurements. Flight B949 aimed to measure the radiative signatures of an extensive cloud feature off the East coast of Scotland caused by a low pressure system and associated occluded fronts. Other ice retrieval methodologies for ICI have been developed at Chalmers and Hamburg Universities, based on Monte Carlo Integration and making use of the retrieval of frozen quantities from CloudSat. Retrieval algorithms have been developed specifically for ISMAR and are being tested with ISMAR airborne observations from the first two campaigns. Some primary results have already been presented by these groups. Our retrieval could also be adapted to aircraft situations and tested with ISMAR observations. Some challenging issues related to the 'in situ' estimation of the ice parameters during these ISMAR flights, also need to be considered.

TABLE 6.1: Flight characteristics during the WINTeX campaign.

Flight	Comments
B938	This was an instrument test flight, that took place in variable amounts of cloud over East Anglia. In-cloud runs at two altitudes and high-level above-cloud run at 31000 <i>ft</i> . ISMAR operated successfully.
B939	A flight measuring cirrus, mostly over land but partly over sea. Fairly extensive cirrus cover, although some variability in cloud thickness along track and patchy low cloud underneath. Sets of runs above cloud, in cloud tops, mid-cloud, cloud base, and below cloud. ISMAR operated successfully.
B940	A flight looking at clear sky measurements with ISMAR for sea surface emissivity and clear-sky radiative transfer comparisons. Cloud conditions were not ideal with some cumulus around. The flight contains low-level runs at 500 <i>ft</i> above the sea for emissivity measurements (sometimes affected by cloud above the aircraft, near-surface winds 5-10 <i>m/s</i>), high-level runs above the tropopause (can use the lidar to identify when above low cloud), and a series of 2 minute runs spaced at 2000 <i>ft</i> throughout the depth of the troposphere. ISMAR operated successfully throughout the flight.
B941	A repeat of the plan for B939 looking at cirrus cloud. Cirrus was mostly optically thin with quite a lot of variability at some low cloud underneath. Sets of runs above, in and below the cirrus at various levels. ISMAR operated successfully throughout the flight.
B945	Another repeat of the previous cirrus flights. Cirrus was very tenuous and patchy, with further patches of mid-level cloud underneath which could make analysis challenging. Single set of above and in and below-cloud runs at varying altitudes. ISMAR operated successfully throughout the flight.
B949	A flight measuring the radiative signature of an extensive cloud feature off the East coast of Scotland caused by a low pressure system and associated occluded fronts. Above-cloud and in-situ measurements were made, focusing on the upper parts of the cloud (between 20000 and 30000 <i>ft</i>). ISMAR operated successfully throughout the flight.
B951	A flight aimed at validating up-looking clear-sky radiative transfer modeling and ISMAR characterization that took place above fairly extensive low cloud over East Anglia. Contains a series of runs spaced at 2000 <i>ft</i> from 30000 to 4000 <i>ft</i> (all above cloud), ascending and descending profiles at faster rates than standard, and a series of longer runs spaced at 5000 <i>ft</i> intervals between 10000 and 30000 <i>ft</i> . Some ISMAR issues were encountered during this flight-instability in 325 GHz receiver voltage outputs and failure of the 448GHz receiver during a large proportion of the flight.
B952	A repeat of the plan for B940, this time in fully clear conditions. High level runs were below the tropopause for this case due to the high tropopause height. ISMAR issues with 325 and 448 GHz receivers remained, although the 448 GHz receiver operated for most of the stacked descending runs at 2000 <i>ft</i> intervals.

Appendix A

Comparison of Passive Radiative Transfer Simulations for a Tropical Case

A.1 Introduction

The development of the retrieval algorithms for cloud parameters is based on radiative transfer simulations, meaning that the accuracy of the algorithm largely depends on the ability of the simulations to reproduce the observations. The retrieval database in Chapter 3 for the detection and quantification of cloud parameters is provided by the coupling of the WRF model and the ARTS. Other cloud resolving models (e.g., the Méso-NH and the MetOffice Mesoscale model (UKMES)) can also be used for the retrieval database preparation by providing inputs for radiative transfer codes, such as the Atmospheric Transmission at Microwave (ATM), or the RTTOV (Galligani et al., 2015, Meirold-Mautner et al., 2007, Wiedner et al., 2004). Recently, Geer and Baordo (2014) simulated both tropical and mid-latitude cases, using RTTOV with the atmospheric profiles from the ECMWF 4D-Var data assimilation system. They first presented a Tropical case, the Irene hurricane, that they simulated using the Mie theory. Then, from comparisons with satellite observations, they concluded that the use of the DDA from Liu for the sector snowflakes provides better results.

In this appendix, we compare the results of our WRF+ARTS simulations with the Geer and Baordo (2014) RTTOV simulations, for this Tropical cyclone Irene, using first the Mie theory for both simulations. Comparisons are also provided with satellite observations from TMI and SSMIS. These comparisons is a step forward to extend the training database generated in Chapters 2 and 3 to the global scale.

A.2 Case description

The hurricane Irene, a strongly destructive tropical cyclone, affected the Caribbean and East Coast of the United States during late August 2011. It originated from a well-defined Atlantic tropical wave, with a progressively favorable environment situated ahead of the wave. It was classified as Tropical Storm Irene near the Lesser Antilles on August 20, 2011. Then Irene developed over the west-central Atlantic. On August 21, Irene strengthened to near hurricane force, thanks to a favorable vertical structure (deep convection at surface and anticyclone aloft), as well as light wind shear and high sea surface temperature. Irene weakened briefly on August 23 after its initial landfall, and then redeveloped and quickly intensified into a Category 3 major hurricane. It subsequently underwent a partial eye-wall replacement, resulting in a reduction in its wind speed. On August 27, it made landfall near Cape Lookout with a wind speed of 140 *km/h* and a surface pressure of 951 *hPa*. After about 10 hours over land, Irene re-emerged into the Atlantic and continued northward, weakening to a tropical storm early on August 28. Finally, Irene made landfall with 100 *km/h* wind speed in the Coney Island neighborhood of Brooklyn, New York. During intensifying and developing, Irene made ninth landfalls and caused serious flooding and extensive wind destruction particularly in mid-Atlantic, Eastern New York, large part of the New England, and the Long Island coast.

A.2.1 Model configurations

The atmospheric and hydrometeor information are provided by the ECMWF 4D-Var data assimilation system, which contains 107171 profiles on 91 vertical layers. They include the 2-m temperature and humidity, the 10-m wind speed, the surface pressure and temperature, the rain flux, the pressure, temperature, and specific humidity profiles, and the mixing ratios of rain, snow, cloud water, and cloud ice, along with the cloud fraction. The ARTS model (see Chapter 2 for the description) with the Monte-Carlo module is used to simulate the brightness temperatures in this study, with the inputs and configurations for ARTS remaining the same as for RTTOV-10 in Geer and Baordo (2014) to facilitate the comparison between these two models. Note that in RTTOV, the total rain mixing ratio is the sum of the rain mixing ratio and the rain flux (large-scale and convective). The rain flux can be converted to mixing ratio in terms of the rain PSD and the rain fall speed (Bauer, 2001, Geer and Baordo, 2014). To keep the consistency, we used the same solution for the rain mixing ratio in ARTS. Figure A.1 presents the vertically integrated contents of four hydrometeors, along with the water vapor content, the surface temperature, and the 10-m wind speed provided by the ECMWF 4D-Var data assimilation system.

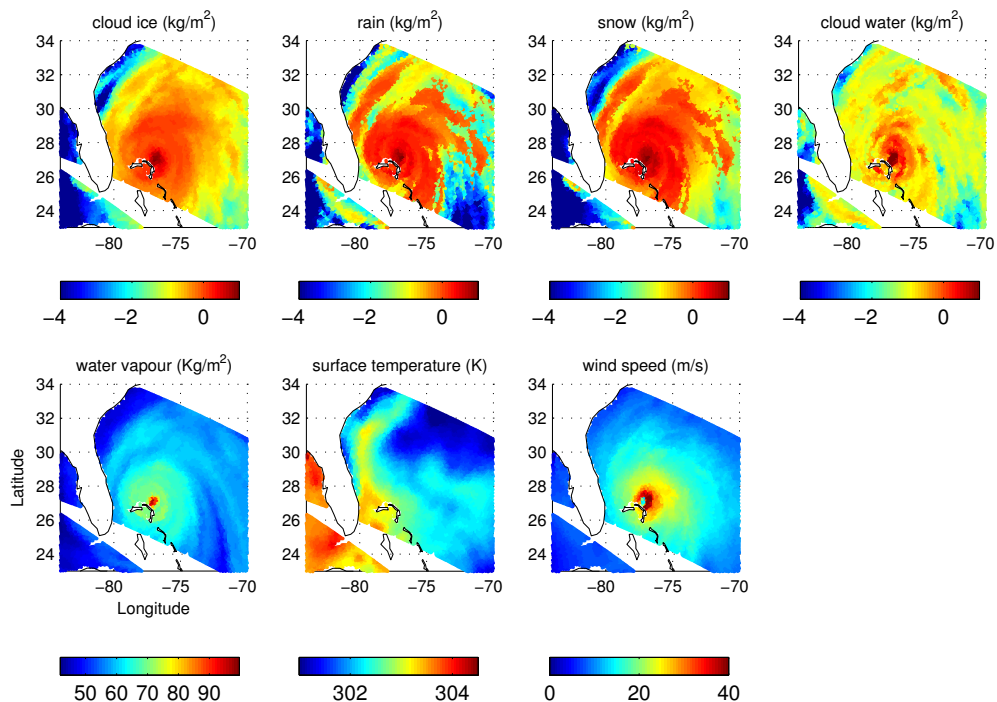


FIGURE A.1: The mass contents of the hydrometeors and the water vapor, the surface temperature, and the 10-m wind speed from the ECMWF 4D-Var data assimilation system for the Irene case, on August 25, 2011 at TMI over-pass time (21:18 UTC).

To be close to RTTOV-10: the MPM87 absorption model (Liebe and Layton, 1987) for water vapor, the MPM92 absorption model (Liebe et al., 1992) for oxygen, and the MPM93 absorption model (Liebe et al., 1993) for nitrogen are used in ARTS. All the particles are assumed to be spheres with constant densities. A four parameter modified gamma particle size distribution (Petty and Huang, 2011) is defined for cloud water

and ice particles. For rain and snow particles, the PSDs are determined by [Marshall and Palmer \(1948\)](#). The more detailed microphysical information of particles can be found in [Table A.1](#). It follows the [Geer and Baordo \(2014\)](#) selections as close as possible for comparison purposes. Some parameters are undefined in the PSD functions, which can be calculated in terms of given mass contents. The scattering properties of all the hydrometeors are calculated by the Mie theory (presented in [Chapter 2](#)). For the liquid phases (i.e., cloud water and rain), the dielectric properties are calculated from [Liebe et al. \(1991\)](#) model. For the cloud ice, the [Matzler \(2006\)](#) model is chosen. For the snowflakes, the Maxwell-Garnett formula is used, while the approach of [Bohren and Battan \(1982\)](#), [Fabry and Szyrmer \(1999\)](#) is used in RTTOV. Different mixing formulas could not induce large discrepancies in this case as discussed by [Geer and Baordo \(2014\)](#). The ocean surface emissivities are simulated by the FAST microwave Emissivity model (FASTEM-4), which is coupled with RTTOV-10.

TABLE A.1: Microphysical assumptions in the ECMWF 4D-Var data assimilation system for four hydrometeors, including the particle size distribution (PSD), their shapes, and their densities. n_0 is the intercept parameters; λ is the slope parameters; D is the spherical diameter; μ is the dispersion; R is the rainfall rate in mm/hr .

Hydrometeor	PSD	PSD parameters	Shape	Density (kg/m^3)
Rain	$n(D) = n_0 e^{-\lambda D}$ (Marshall and Palmer, 1948)	$n_0 = 8 \times 10^6$ $\lambda = 41R^{-0.12} cm^{-1}$	sphere	1000
Snow	$n(D) = n_0 e^{-\lambda D}$ (Marshall and Palmer, 1948)	$n_0 = 8 \times 10^6$ $\lambda = 41R^{-0.12} cm^{-1}$	sphere	100
Cloud water	$n(D) = n_0 D^\mu e^{-\lambda D}$ (Petty and Huang, 2011)	$\lambda = 2.13 \times 10^5$ $\mu = 2$	sphere	1000
Cloud ice	$n(D) = n_0 D^\mu e^{-\lambda D}$ (Petty and Huang, 2011)	$\lambda = 2.05 \times 10^5$ $\mu = 2$	sphere	900

A.2.2 Comparison between satellite observations and simulations

The simulated brightness temperatures with ARTS are compared to the observed ones in [Figures A.2 and A.3](#), at some channels (i.e., 10, 19, 37, 85, 150, and 183 GHz) of TMI and SSMIS. At all the presented frequencies, the global cloud structures (with some spatial shifts), corresponding to the cloud emission and scattering, are fairly well reproduced by ARTS. At lower frequencies (below 85 GHz), the cloud liquid phase absorption dominates, over the cold oceanic background. Therefore, the agreement between observations and simulations at these frequencies suggests the good reproduction of liquid cloud characteristics by ECMWF 4D-Var data assimilation system and the realistic surface emissivities from FASTEM (at least at these channels). At 85 and 150 GHz, the brightness temperature depressions related to the scattering effect by the cloud frozen particles, are reasonably simulated but with certain underestimations. These insufficient scattering can be mainly attributed to the uncertainty in the SSPs calculations using the Mie code (as discussed in [Chapters 2 and 3](#)). Note that the cloud frozen phases are presented by two hydrometeors (i.e., cloud ice and snow) in ECMWF 4D-Var data assimilation system. Graupel is usually the dominant frozen hydrometeor (more denser than the snow) in a hurricane rain-producing process ([Franklin et al., 2005](#)), and it is not accounted for here. In addition, the radiative transfer simulations have also been

done for three channels centered at water vapor absorption line 183 GHz (183 ± 1 , ± 3 , and ± 7 GHz). The water vapor absorption masks the lower cloud signals and the surface contribution, in varying degrees. With varying atmospheric opacity, these three channels reach their saturations at different altitudes. A good agreement between the observations and the simulations at these frequencies reveals a realistic water vapor content provided by ECMWF 4D-Var data assimilation system.

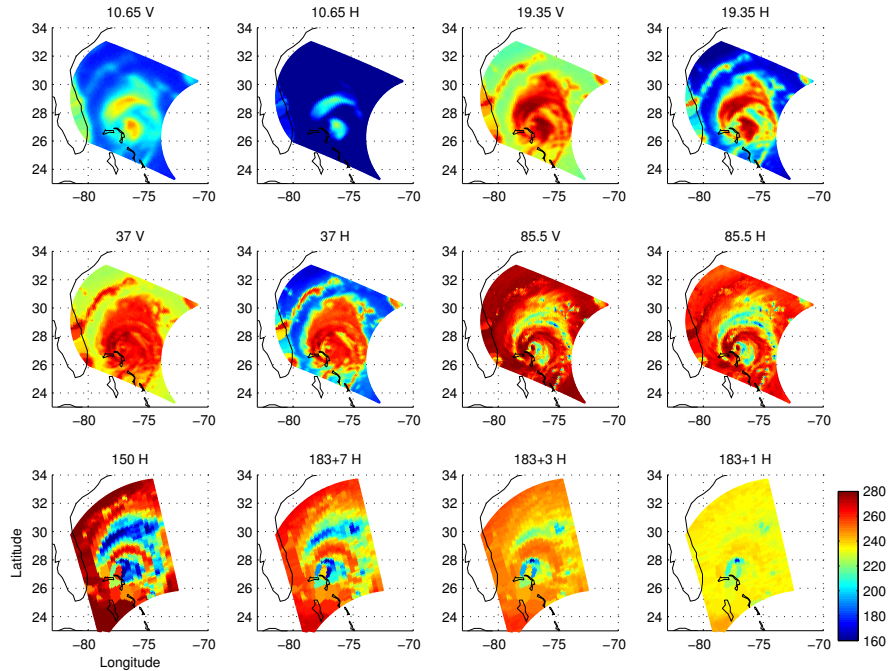


FIGURE A.2: The TMI (for 10, 19, 37, and 85 GHz) and SSMIS (for 150 and 183 GHz) observations for the Irene case.

The simulated brightness temperatures with RTTOV are shown also in Figure A.4, as provided by ECMWF using the Mie theory. Compared with the satellite observations (Figure A.2), much more brightness temperature depressions are simulated by RTTOV at higher frequencies (85, 150, and 183 GHz). Note that at 37 GHz, unexpected scattering signals are simulated by RTTOV, where the liquid water emission dominates (discussed in Chapter 3). The reason for that is unclear, and an error in the Mie calculation in RTTOV is suspected. Discussions are underway with A. Geer.

For the reason that the cloud and precipitating patterns are generally misplaced in the cloud resolving models (the same for the WRF model, discussed in Chapter 3), the histograms of the observed and simulated brightness temperatures (with ARTS and RTTOV) are shown in Figure A.5 for comparison purposes. For the lower frequencies, good agreements are obtained between the observations and ARTS simulations, it degrades at 85 and 150 GHz. The depressions of brightness temperatures, related to the scattering by the cloud frozen phases, are underestimated. Clearly, much more scattering signals are simulated by RTTOV for frequencies at 37 GHz and above.

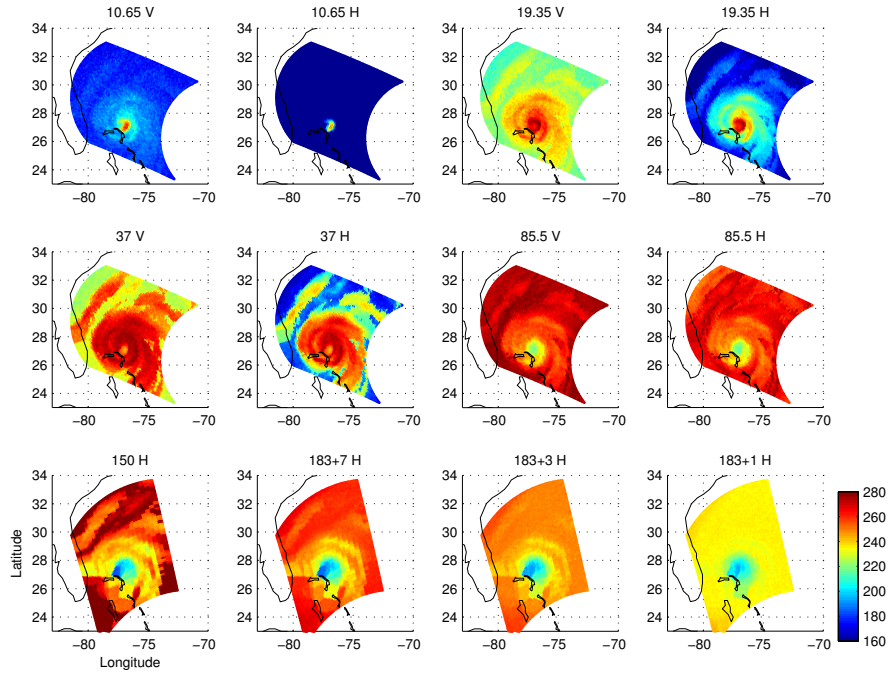


FIGURE A.3: The simulations with ARTS for the Irene case. The SSPs are calculated using the Mie code.

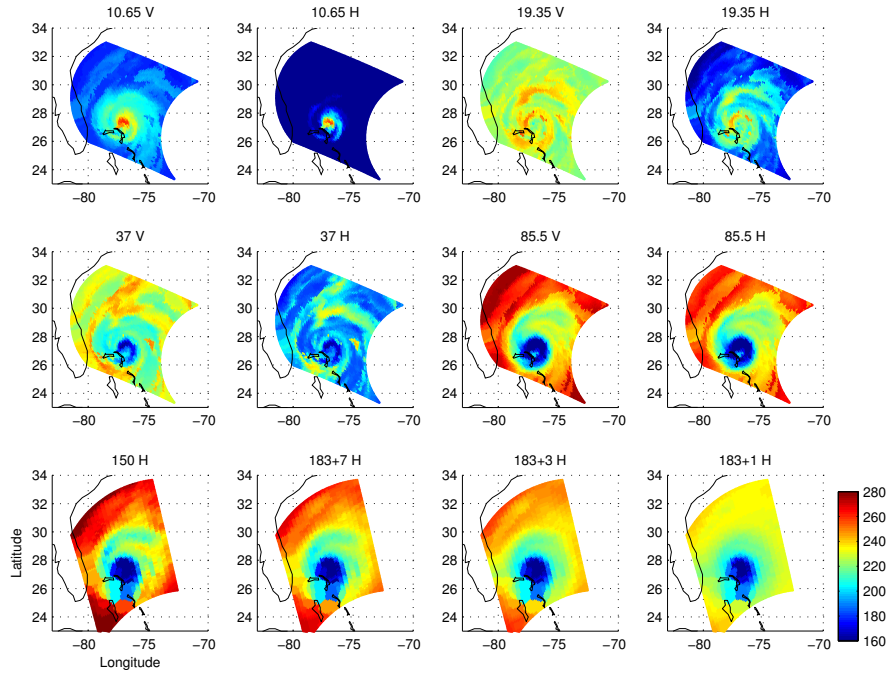


FIGURE A.4: The simulations with RTTOV for the Irene case. The SSPs are calculated using the Mie code.

A.2.3 Discussion about the sensitivity of the microwave simulations to the hydrometeor characteristics

Simulation of the scattering signals largely depends upon the uncertainties in the description of the physical properties of frozen particles (e.g., particle shape, particle size,

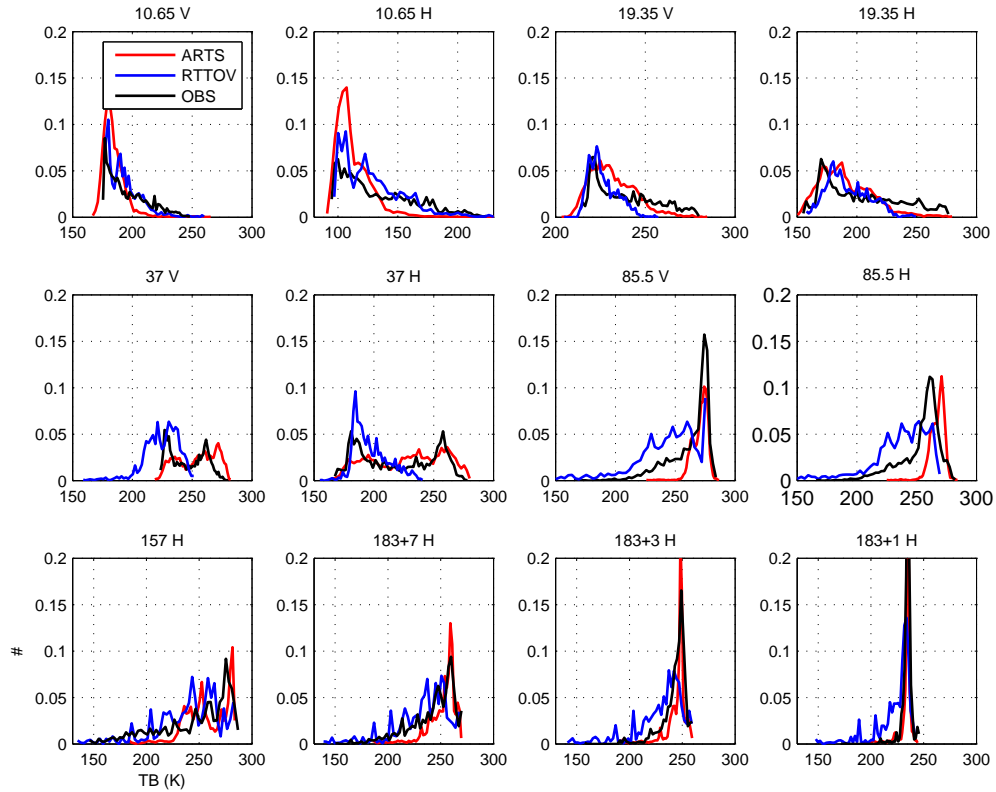


FIGURE A.5: Histograms of TMI and SSMIS observations, along with the simulated brightness temperatures by ARTS and RTTOV for the frequencies of interest for Irene case.

particle orientation, particle density, and particle SSP), as discussed by Galligani et al. (2013, 2015), Kulie et al. (2010), and in Chapters 2 and 3. Some sensitivity tests have been performed on some microphysical properties of the snow particles. Two transects through the center of the Irene hurricane are chosen for the tests, depending on the overpasses of TMI and SSMIS (Figure A.6 (left column)). The vertically integrated content of all the hydrometeors along the selected transects are presented in Figure A.6 (right column). The contents of all the hydrometeors are larger than 5 kg/m^2 (up to 7 kg/m^2 for snow). Generally, the strong hurricanes are surrounded by the eyewall with strong winds, while it seems that it is not the case for the Irene hurricane. In fact, at this time, the Irene hurricane was undergoing a partial eyewall replacement cycle, meaning that the distinct eye redeveloped and turned to a sufficiently small one, which can explain the relatively deepest convective and largest precipitation at its center.

Figure A.7 shows the observed brightness temperatures at 10, 19, 37, and 85 GHz, along with the simulations, adding successively the different hydrometeor types in the clouds in ARTS. Each orthogonal polarization is presented, along with the corresponding polarization differences. The impact of the liquid water emission in clouds is evident at lower frequencies, with an increase in brightness temperature and a decrease in the polarization difference over the ocean. Adding the cloud frozen phases, there is no evident change in simulated brightness temperature. At 85 GHz, the atmospheric opacity increases, and the ocean surface contribution (and its polarization difference) is masked

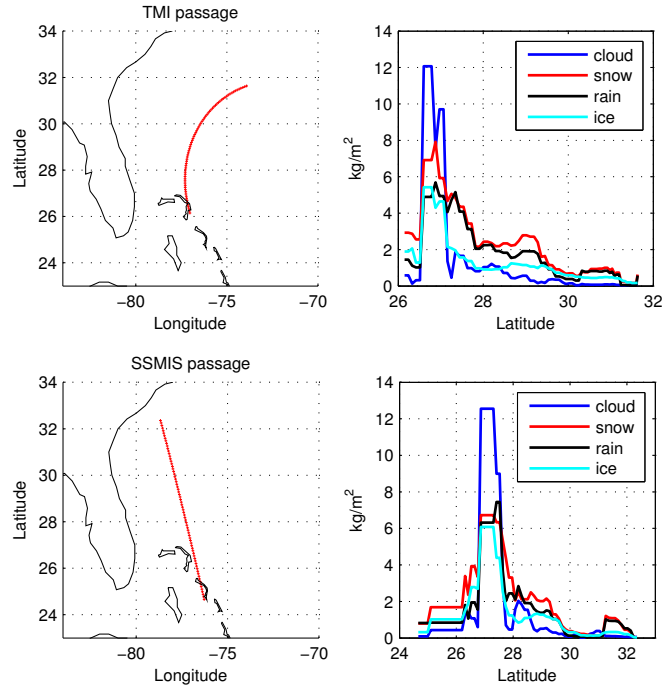


FIGURE A.6: Left: the selected transects for the sensitivity tests from TMI and SSMIS over-passes, respectively. Right: the integrated mass contents of different hydrometeors along both transects mentioned in the left column.

to a great extent. The brightness temperature depressions and the polarizations are related to the scattering by the frozen particles. It is similar at 150 and 183 ± 7 GHz (not shown).

Figure A.8 presents the simulated brightness temperatures under different microphysical hypotheses (listed in Table A.2) and the observations at 85, 150, and 183 ± 7 GHz along the specified transects in Figure A.6. The initial simulation was performed following the microphysical scheme in ECMWF 4D-Var data assimilation system. The Mie method was used to calculate the SSPs for all the hydrometeors. Compared with the observations, an underestimated scattering (~ 20 K, ~ 30 K, and ~ 20 K of brightness temperatures at 85, 150, and 183 ± 7 GHz, respectively) is revealed as discussed in previous sections. Next, four sensitivity tests are performed with different changes in the snow microphysical parameters. All the tests were implemented under the precondition of keeping the same total snow mass, except for the test D. Note that the microphysical parameters for other hydrometeors remain the same as in the initial simulation.

TABLE A.2: The sensitivity tests.

Test	The changes of parameters
A	The original ECMWF microphysical scheme
B	The density of snow is set to 250 kg/m^3
C	The spheres are replaced by horizontally aligned spheroids (aspect ratio 1.6)
D	The snow mass content is multiplied by 1.25
E	The SSP of Liu sector from DDA database are used

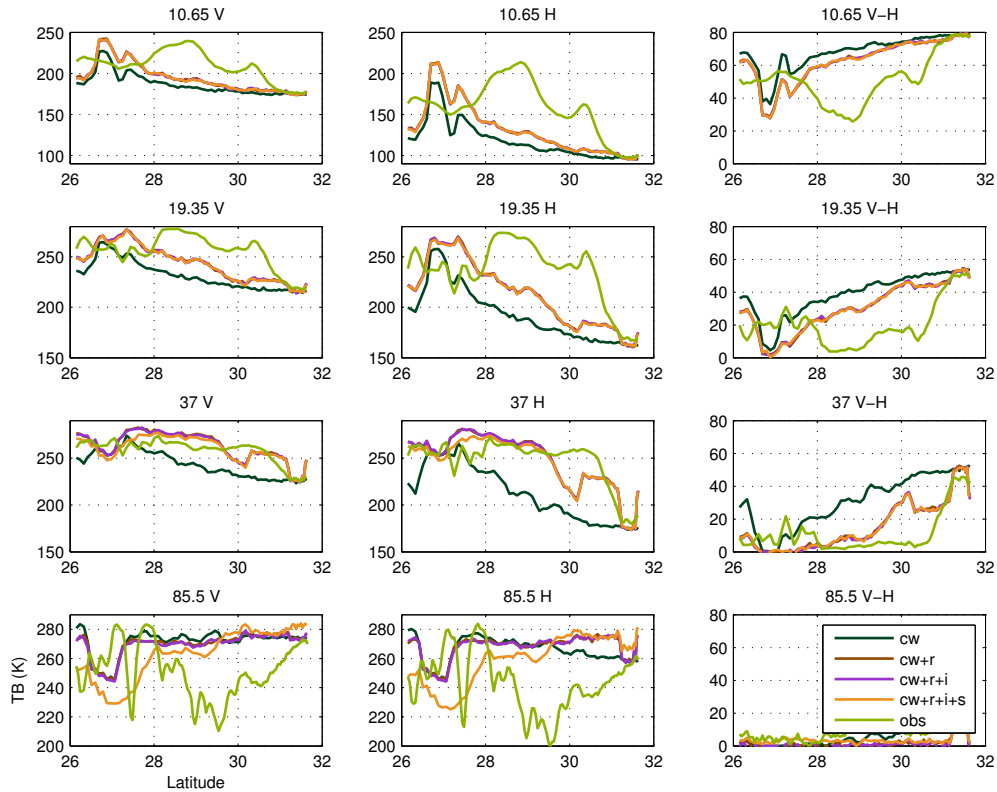


FIGURE A.7: The simulated and observed brightness temperatures at 10, 19, 37, and 85.5 GHz (from top to bottom) with different types of hydrometeors in the radiative transfer simulations, as well as the correspondent polarization differences.

The density is a key parameter in the SSP calculation, which directly affects the particle dielectric property (discussed in Chapter 2). A sensitivity test has been done by changing the snow density from 100 kg/m^3 (in original simulation) to 250 kg/m^3 in the radiative transfer simulations, considering the fact that denser particles (graupels) are missing in the ECMWF outputs. In addition, the snow density is generally parameterized as a function of its size, from pure ice density for very small particles to a constant close to 100 kg/m^3 for large particles. The density-induced depressions in brightness temperatures of the order of $\sim 40 \text{ K}$, $\sim 50 \text{ K}$, and $\sim 30 \text{ K}$ at 85, 150, and $183 \pm 7 \text{ GHz}$ in the storm center. As discussed in Chapter 2, the SSPs for snowflakes calculated under the hypothesis of spheres using the Mie code, lead to discrepancies in radiative transfer simulations. A test is made with the snow particles assumed to be horizontally aligned oblate spheroids of aspect ratio 1.6 in the sensitivity test. The SSPs are calculated using the T-matrix method. Clear changes are found in the simulations along the transects in our case (20 K, 45 K, 20 K, and 20 K for the 85 V, 85 H, 150, and $183 \pm 7 \text{ GHz}$, respectively), while the polarization differences reach up to $\sim 15 \text{ K}$ for 85 GHz, which is consistent with the analysis in Chapter 5. In addition, the sensitivity to the snow content in the radiative transfer simulations is also investigated: when multiplied by 1.25, the decrease in the brightness temperature is not obvious at 150 and $183 \pm 7 \text{ GHz}$, while with a magnitude of $\sim 10 \text{ K}$ at 85 GHz. Finally, the SSPs of the Liu DDA database for sector snowflake, suggested by Geer and Baordo (2014) for the new development of the RTTOV model, is tested. The results are encouraging and consistent with the

observations, with a decrease of ~ 20 K, ~ 40 K, and ~ 40 K compared to the original one at 85, 150, 183 \pm 7 GHz, respectively. Therefore, ARTS simulations were performed using the SSPs from the Liu DDA sector snowflake for the whole scene (see Figure A.9). The simulations agree well with the observations at high frequencies (above 85 GHz).

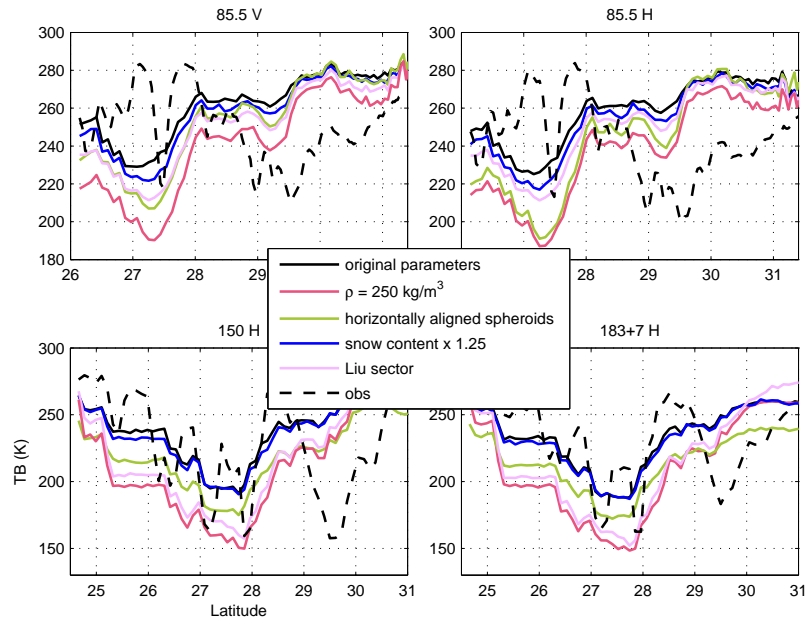


FIGURE A.8: The observed and simulated brightness temperatures under different microphysical assumptions for snow particles at 85.5, 150, and 183 \pm 7 GHz for the transects shown in Figure A.6.

As mentioned above, the ECMWF predicts four hydrometeors (i.e., cloud water, cloud ice, snow, and rain). In other cloud resolving models, such as WRF, five or six hydrometeors can be given (graupel or hail added). Figure A.10 shows the integrated mass contents of different hydrometeors from two models along the TMI transect shown in Figure A.6 for the Irene case. The graupel content produced by the WRF model is of the order of 4 kg/m^2 : clearly, this can not be ignored in this case. According to Wiedner et al. (2004), the good agreement between the observation and the simulation can be obtained in the Tropical regions where graupels dominate.

A.2.4 Conclusions

For hurricane Irene, simulations at TMI and SSMIS frequencies are performed by coupling ARTS with the atmospheric fields from ECMWF 4D-Var data assimilation system, for comparisons with the work from Geer and Baordo (2014) using RTTOV. The Mie code is used for both simulations. With ARTS, reasonable agreement is obtained with the observations, with a slight underestimation of the brightness temperatures above 85 GHz. The Geer and Baordo (2014) simulations with the Mie code show a large overestimation of the scattering, even at 37 GHz. This is still not explained and there are on going discussions to interpret it. The sensitivity of radiative transfer simulations to the snow microphysical properties (e.g., its content, its density, and its SSP) is investigated

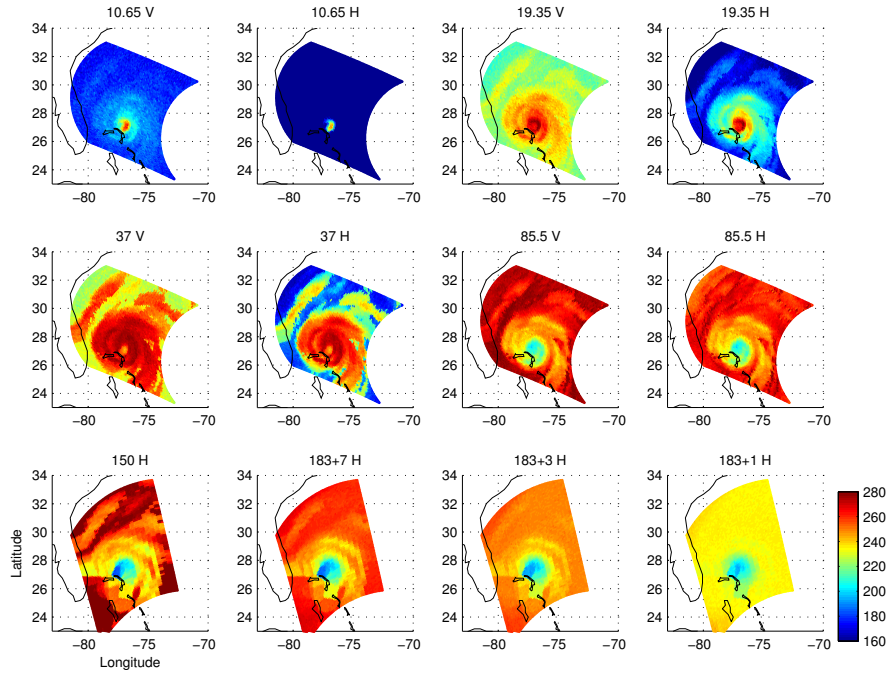


FIGURE A.9: Simulated brightness temperatures at some TMI and SSMIS channels with ARTS. The SSPs for snow particles are from the Liu DDA database for sector snowflakes.

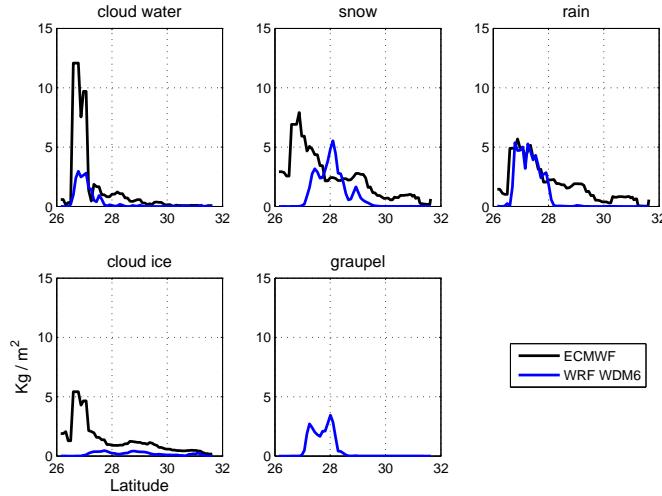


FIGURE A.10: The integrated mass contents of different hydrometeors from the WRF with the WDM6 microphysical scheme and the ECMWF 4D-Var data assimilation system along the first transect in Figure A.6.

with the ARTS model. The use of the DDA calculation from Liu sector snowflakes in the ARTS code improves the agreement with the observations at high frequencies (always using the initial microphysical properties from the ECMWF 4D-Var data assimilation system). The reasonable agreement between the ARTS simulations and the observations for a Tropical case is a first step toward the extension of our retrieval training database to the global scale.

Appendix B

Paper A: Sea surface emissivity parameterization from microwaves to millimeter waves

Authors:

C. Prigent, F. Aires, D. Wang, S. Fox, and C. Harlow

Paper published in:

Quarterly Journal of the Royal Meteorological Society, 2016



Sea surface emissivity parameterization from microwaves to millimeter waves

C. Prigent ^{*a b}, F. Aires ^{a b}, D. Wang ^a, S. Fox ^c, and C. Harlow ^c

^a CNRS, Laboratoire d'Etudes du Rayonnement et de la Matière en Astrophysique, Observatoire de Paris, Paris, ^b

Estellus, Paris, France, ^c Met Office, EX1 3PB Exeter, United Kingdom

*Correspondence to: LERMA, Observatoire de Paris, 61 avenue de l'Observatoire, 75014 Paris, France

In preparation for the new observations on board the next generation of European operational meteorological satellite (EUMETSAT Polar System - Second Generation - EPS-SG), a parameterization of the sea surface emissivity is proposed from 10 to 700 GHz: TESSEM² (Tool to Estimate Sea Surface Emissivity from Microwave to sub-Millimeter waves). It is based on the community model FASTEM (FAST microwave Emissivity Model, (*English and Hewison 1998; Liu et al. 2011*)) at frequencies up to 200 GHz where FASTEM has been operationally calibrated and validated. It follows a physical emissivity model at higher frequencies (*Prigent and Abba 1990*). A preliminary evaluation of TESSEM² has been conducted with success, by comparison with airborne International Sub-Millimetre Airborne Radiometer (ISMAR) observations (*Fox et al. 2014*) from 118 to 325 GHz, under low wind speed (3 to 5 m/s) off the coast of Scotland. TESSEM² is a fast parameterization that can easily be implemented in a community radiative transfer model. The code is available to the community and will be distributed with the next version of RTTOV. Copyright © 0000 Royal Meteorological Society

Key Words: Satellite observations, sea surface emissivity, microwave and millimeter waves

Received...

Citation:...

1. Introduction

The EUMETSAT Polar System Second Generation (EPS-SG) will provide continuity of observations of the current EPS, in the microwave domain up to 200 GHz, but it will also include innovative measurements in the millimeter range up to 664 GHz. The Micro-Wave Sounding (MWS), the Micro-Wave Imaging (MWI) and the Ice Cloud Imaging (ICI) instruments will cover the 18 to 664 GHz range to respond to the increasing user requirements (Stoffelen *et al.* 2006; Rizzi *et al.* 2006). In preparation for EPS-SG, operational radiative transfer models have to be extended up to 700 GHz. With increasing frequencies, the atmosphere becomes progressively more opaque due to the increasing contribution of absorption lines from different gases along with the increased continuum absorption. However, observations can be surface sensitive at high frequencies in the case of very dry atmospheres commonly present in polar and sub-polar regions or at lower latitudes, in the case of cold air outbreaks. Consequently, the representation of surface emissivity is of importance even at high frequencies to ensure efficient use of these observations for data assimilation or for retrievals.

Over open ocean, the emissivity varies primarily with the surface wind speed, and models have been developed to estimate the emissivity as a function of surface wind speed and direction, sea surface temperature, and salinity. The emissivity of a flat water surface can be calculated from the Fresnel equations for any incidence angle and orthogonal polarization, with the water permittivity calculated as a function of temperature and salinity. When the wind strengthens above the ocean, waves appear and the surface gets rough. The large-scale waves can be treated as an ensemble of facets, for which the Fresnel reflection applies, following geometric optics. The total emissivity is the sum of the contribution from each facet, weighted by the slope distribution. Small-scale roughness related to ripples has been added and models include these two scales of roughness. In addition, above a certain wind speed, foam

can appear. With an emissivity close to one (as compared to the low emissivity of water), the presence of foam can modify the surface emissivity. Estimating the surface coverage of foam and its emissivity is difficult, and several models exist.

The FAST microwave Emissivity Model (FASTEM) (English and Hewison 1998; Liu *et al.* 2011) is currently used in major Numerical Weather Prediction (NWP) centres up to 200 GHz and provides realistic estimates of the sea surface emissivities. The distributed version of FASTEM corresponds to a parameterization of a two-scale physical model. The parameterization is optimized for frequencies below 200 GHz. It has been calibrated and validated in operational frameworks. The objective of this study is to extend this capability to higher frequencies, while maintaining an accuracy and a computational efficiency compatible with operational systems. The physical model used to derive FASTEM is no longer available, but a model based on similar principles and developed in Paris Observatory, can be adopted for the extrapolation to higher frequencies (Prigent and Abba 1990). Here we propose an emissivity parameterization that is based on FASTEM for frequencies up to 200 GHz where FASTEM has been thoroughly evaluated and that follows our physical emissivity model (Prigent and Abba 1990) where FASTEM is not valid. Another solution would be to use our physical model for the full frequency range, but this would ignore all the work done in NWP centres along the years to improve the agreement between FASTEM and the satellite observations. The parameterization of a carefully evaluated physical model for the full spectrum and environmental conditions is the ultimate goal to achieve, but at this stage such a physical model is not available.

The two models (FASTEM and our physical model) are briefly presented and are compared (Section 2). A parameterization of the emissivity (Tool to Estimate the Sea Surface Emissivity at Microwaves and Millimeter waves, TESSEM²) is developed: it mimics FASTEM up to 200 GHz and transitions smoothly to our physical

Sea surface emissivity up to 700 GHz

3

model for higher frequencies (Section 3). The International Sub-Millimetre Airborne Radiometer (ISMAR) is a demonstrator of ICI that flies on the UK Facility for Airborne Atmospheric Measurements (FAAM) aircraft (Fox *et al.* 2014). A preliminary evaluation of TESSEM² is conducted in Section 4, by comparison with ISMAR observations from 118 to 325 GHz, under low wind speed (3 to 5 m/s) off the coast of Scotland. Conclusions are presented in Section 5, along with the main characteristics of the TESSEM² code to be distributed to the community.

2. The two models and their comparison

2.1. FASTEM

Several groups contributed to the development of FASTEM. It is based on a full physical emissivity model. For computational efficiency, the full model has been parameterized for current satellite observations up to 200 GHz and up to 65° incidence angle. FASTEM has undergone several updates, from FASTEM-1 to FASTEM-6. The changes from one version to the other are documented in Bormann *et al.* (2012). The first FASTEM versions were based on the geometric optics model, to account for the large scale roughness, with the inclusion of the foam contribution. FASTEM-4 (Liu *et al.* 2011) added the small scale roughness to the large scale roughness, with a new permittivity model and a change in foam coverage. FASTEM-5 reverted to the former foam cover model (Monahan and O’Muircheartaigh 1986), and constraints have been added to have the same emissivity for the two orthogonal polarizations at nadir. In FASTEM-4 and 5, the foam emissivity is modeled following the polarization and zenith dependence from Kazumori *et al.* (2008), with the frequency dependence from Stogryn (1972). It increases with frequencies for both V and H polarizations, and reaches values very close to unity for both polarizations above 100 GHz. Note that the foam cover is usually rather limited: at 20 m/s, it is below 5%, meaning that it is not a major source of emissivity error up to this wind speed. The use of FASTEM-5 at European

Center for Medium-range Weather Forecast (ECMWF) led to an overall reduction of the biases for the sounders, as compared to versions 3 and 4, and for the imagers, part of the remaining bias is expected to come from problems in the absolute calibration of the instruments. FASTEM-6 is very close to FASTEM-5, except for a change in the wind direction model to represent the azimuthal variations of the emissivities in vertical and horizontal polarizations (Kazumori and English 2015). In the following, FASTEM-6 is used (it is equivalent to FASTEM-5 without taking into account the wind direction), and FASTEM will stand for FASTEM-6. The ideal would be to adopt the original model used to derive FASTEM and to extend it to higher frequencies. However, this initial model is not available anymore. As a consequence, another physical model, based on the same physical principles is used instead and is now briefly described.

2.2. Paris Observatory sea surface emissivity model

Our model (Prigent and Abba 1990; Greenwald and Jones 1999) is a geometric optics model, with the sea surface described as a set of flat surfaces with a bi-directional slope distribution, derived from Cox and Munk (1954) from photographic observations of the sun glitter on the sea. Our emissivity model does not account for the small scale roughness. The small scale roughness is expected to have maximum effect at low frequencies. The higher the frequency, the more valid the geometric optics approach, making this model very suitable for millimeter to sub-millimeter frequencies. Our initial model has been updated using the FASTEM-6 modeling for the dielectric properties of sea water, for the foam cover, and for the foam emissivity. The sea water dielectric properties used in FASTEM is based on a large range of measurements of pure and sea water from 1.7 to 410 GHz (Liu *et al.* 2011). Above 410 GHz, the frequency dependence of the water dielectric properties is expected to be smooth, and extrapolation of the model should be realistic.

2.3. Comparisons of the two sea surface emissivity models

Figure 1 shows the comparisons of FASTEM and our model (the original one and the one with FASTEM updates), at 100, 200 and 300 GHz, for 4 different wind speeds (0, 7, 14, 21 m/s), at 293 K, and a salinity at 36 psu. At 0 m/s, results are also compared with the Fresnel calculation using the same dielectric properties as FASTEM. The change in dielectric properties from our original model to the updated model does not impact the emissivity much at temperatures around 293 K. Changes are more pronounced at lower temperatures (~ 273 K, not shown), as the new dielectric model was modified to account for more recently available dielectric measurements at these low temperatures. It can be seen that the FASTEM model does not strictly follow the Fresnel model for the specular surface at 0 m/s wind speed, with significant departures especially above 50° incidence angle. Unrealistic emissivities are calculated with FASTEM for large angles. This is expected as FASTEM was not parameterized to operate at large incidence angles. However, this is now problematic when simulating radiative transfer in scattering atmospheres where the upwelling radiation from the surface needs to be calculated in all directions. There is a need for emissivity estimates for radiative transfer codes that use all the scattering streams such as Monte Carlo methods, and reasonable emissivity parameterization should be provided also for these applications. Up to 200 GHz, the differences between our updated model and FASTEM are limited at moderate wind speed (up to 7 m/s), for angles below 40° . The differences increase with wind speed and is significant at 21 m/s. As the foam contribution is the same for the two models (FASTEM and our updated model), the difference results from the treatment of the wind-roughened surface. At 300 GHz, the models differ more as can be expected from the optimization of the FASTEM parameterization for frequencies below 200 GHz. Note that in this study, the emissivity dependence with the azimuthal angle with

respect to the wind direction is not accounted for (although our physical model can handle it). The dependence is usually limited (of the order of 0.5 K) and there are debates today about the validity of this azimuthal dependency in the FASTEM / RTTOV community.

Figure 2 shows the frequency dependence of the models, at 0° and 50° incidence angles. It emphasizes the large differences in behaviours between FASTEM and our model below 200 GHz, for the horizontal polarization for large wind speeds. The frequency dependence of the dielectric properties of sea water predicts a smooth increase of the emissivities with frequency. Our model provides a smooth increase of the emissivities after 200 GHz, consistent with the theory.

The FASTEM model uses the sea surface roughness spectrum of *Durden and Vesecky* (1985). This model has been shown to be optimal at L-band (*Dinnat et al.* 2003). *Liu et al.* (2011) compared the *Cox and Munk* (1954) and *Durden and Vesecky* (1985) slope variances. The two slope variances agree well and *Liu et al.* (2011) specify that the *Cox and Munk* (1954) model can be used at higher frequencies. As a consequence, our use of the *Cox and Munk* (1954) slope variances is legitimate for the millimeter and sub-millimeter ranges.

FASTEM has been run without the small scale roughness effect, and the results are compared with the full FASTEM simulations (Figure 3). The small scale effect is rather limited. A decrease of the small scale roughness with frequency was expected (at least up to 200 GHz for which FASTEM is valid). On the contrary, it tends to increase with frequency for the H polarization. Note that depending on the windspeed, it induces a decrease or an increase of the emissivities in H polarization. This behavior is likely related to the parameterization of the initial physical model, not to the physics itself.

Sea surface emissivity up to 700 GHz

5

3. A unified emissivity parameterization up to 700 GHz: TESSEM²

A new parameterization, TESSEM² (Tool to Estimate the Sea Surface Emissivity at Microwaves and Millimeter waves), has been developed that fits as close as possible FASTEM in its range of validity (up to 190 GHz and for angles up to 60°), and that smoothly transitions to our physical model for larger angles and for higher frequencies.

For that, a statistical parameterization of the emissivity is proposed. A neural network parameterization is adopted to represent the multi-variate and non-linear behavior of the sea surface emissivity. It is a classical feedforward multi-layer perceptron (Rumelhart *et al.* 1986). This type of neural network architecture is well suited to model continuous relationships (Hornik *et al.* 1990). The network has 5 inputs in its input layer corresponding to the model (frequency, incidence angle, wind speed, sea surface temperature, and salinity), 15 neurons in the hidden layer, and 2 outputs, corresponding to the two orthogonal polarizations of the emissivities. The nonlinearities are represented by tanh sigmoid functions (in the hidden and output layer).

The learning of the neural network model aims to find the appropriate parameters (i.e., synaptic weights) of the NN model. It is performed using the so-called error back-propagation algorithm (Rumelhart *et al.* 1986). Its objective is to minimize the differences between the NN outputs and 1) FASTEM over its validity range, and 2) our physical emissivity model for the larger angles and higher frequencies. It is therefore asked to fit, at the same time, the two emissivity models and interpolate smoothly between the two emissivity ranges. During the learning stage, the NN parameters are changed to minimize the NN errors on the two ranges. This process is stopped once the differences converge to a minimum. To ensure a smooth transition in angles and frequencies between the two models, no data constraint is imposed on a range of frequencies (between 190 and 300 GHz) and angles (between 60° and 75°) so that the statistical model can interpolate smoothly over these

ranges. The optimization is stable and a smooth behavior of the neural network scheme is observed. This proves that the NN emissivity model was able to make the right compromise in its interpolation.

This microwave ocean emissivity parameterization provides fast and realistic estimates of the ocean emissivities in the frequency range from 10 to 700 GHz, for both orthogonal polarizations. The required inputs are the same as FASTEM (except for the azimuthal angle that is not accounted for in TESSEM²):

- the frequency in GHz,
- the incidence angle (in degrees),
- the wind speed in m/s (at 10 m altitude),
- the surface skin temperature in K,
- the salinity (in practical salinity units (psu)).

The outputs are the surface emissivities for the two orthogonal polarizations corresponding to the observing and environmental conditions.

Figure 4 shows the angular dependence of the resulting emissivity parameterization, along with FASTEM and our model, for different frequencies and wind speeds at 283 K, along with the suggested emissivity parameterization. Figure 5 presents the frequency dependence, with the same conventions, for three incidence angles (0°, 25°, and 50°).

The new emissivity parameterization fits the two models in their validity ranges, with a root mean square (rms) error of 0.007 in emissivity for both polarizations. The angular and frequency dependences are consistent with the expected models over their validity ranges, and provide smooth transitions between the 180-300 GHz domain in frequency, and between the 55°-75° domains in incidence angle, for both polarizations.

Over the FASTEM validity range (below 200 GHz and 55° incidence angle), the rms error is 0.009 for both V and H polarizations. The NN model tries to provide the closer and smoother parameterization over the full frequency range (and environmental conditions). The discrepancy is larger over the FASTEM range from 10 to 200 GHz as this is

where the largest frequency dependence is observed. Rather limited emissivity variations are observed above 200 GHz, making the model fit easier and less noisy.

For illustration purposes, FASTEM and TESSEM² are compared for the Advanced Technology Microwave Sounder (ATMS) window frequencies (31.4, 50.3, 89.5, and 165.5 GHz) as a function of zenith angle, sea surface wind speed, and sea surface temperature (Figure 6, with nominal conditions at zenith angle of 50°, 8 m/s, 290 K, and 35 psu). The ATMS polarization is a mixture of the orthogonal polarizations, with V (respectively H) dominating close to nadir at 31.4 and 89.5 GHz (respectively at 50.3 and 165.5 GHz).

In addition to the emissivity estimation, one can test that the model is physically sound by analyzing its sensitivity with respect to the major geophysical parameters (test of the tangent-linear of the model). This is particularly important in the framework of the NWP variational assimilation where this information is directly used. The Jacobians of the emissivity model with respect to the surface wind speed (the first derivative of the emissivity with respect to the surface wind speed) have been calculated by finite differences, and compared to the FASTEM ones (Figure 7). The Jacobians have similar behaviours, even if some differences can be noted especially at high incidence angle and for high wind speeds.

On a large number of simulations (7 million calculations on a MacBookPro with a 2.8 GHz Intel Core i7), it has been noted that TESSEM² was slightly slower than FASTEM (10% slower).

4. Preliminary evaluation of TESSEM² with ISMAR observations

ISMAR is an along-track scanning radiometer that has five channels in the oxygen line at 118.75 GHz, three in the 325.15 and the 448 GHz water vapor lines, and two window channels at 243.2 and 664 GHz (Fox *et al.* 2014). The two window channels have two orthogonal polarizations which rotate with scan angle, giving both V and H polarizations in

the +50° downward view. For the other channels, only one polarization is observed, corresponding to V polarization at +50° for the downward view (Fox 2015). The instrument viewing angles are between +55° and -10° downward and between +10° and -40° upward. ISMAR operates on board the FAAM BAe-146 research aircraft at altitudes from 50 to 35000 ft. Two scientific campaigns have been analyzed so far: STICCS-2 (Sub-millimeter Trial in Cirrus and Clear Skies), out of Prestwick (Scotland, UK) between November 26, 2014 and December 15, 2014, and COSMICS (Cold-air Outbreak and Sub-Millimeter Ice cloud Study) during the period March 4-25, 2015, also from Prestwick, with flights up to Greenland.

Two flights from these campaigns are studied here, for their low flying transects over the ocean, under clear sky conditions. Flight B875 took place on November 28, 2014, during the STICCS-2 campaign. The sea surface temperature was ~284 K, the wind speed ~5 m/s, and the integrated water vapor ~11 kg/m², during the low level run at 100 ft. Flight B893 took off the east coast of Scotland on March 10, 2015, under clear sky conditions. A number of low-level runs were performed at 100, 500, and 1000 ft above the surface. The conditions were rather cold and dry (sea surface temperature ~280 K and integrated water vapor content ~7 kg/m²), with low wind speed between 3 and 4 m/s.

During the low level runs from these two flights, radiative transfer calculations have been performed using TESSEM², for comparison with the aircraft measurements. Same calculations have also been conducted with FASTEM. The Atmospheric Radiative Transfer Simulator (ARTS) (Eriksson *et al.* 2011) is used, along with the atmospheric and surface information extracted from the closest in space and time ERA Interim reanalyses, at 0.125° × 0.125° spatial resolution. The pitch, roll, and orientation angles of the aircraft are taken into consideration in the simulations, along with the polarization mixture that depends upon the incidence angle and frequency. Both the upward and downward views have been simulated and analyzed

Sea surface emissivity up to 700 GHz

7

(see *Estellus* (2016) for more details). Figure 8 presents the comparisons between the simulated and observed brightness temperatures, for the low level runs for the downward views for three different incidence angles, and for the window frequencies below 400 GHz. Note that depending on the scanning angle and frequency, the polarization status varies (*Fox* 2015). The estimated noise for the channels are: 0.5 K at 118 ± 5 GHz, 0.5 K at 243 GHz, and 1 K at 325 ± 9.5 GHz. It is observed at 325 GHz that the sensitivity to the surface emissivity is very limited, given the lack of contrast between the direct surface contribution and the reflected downwelling radiation. Above 400 GHz, the atmospheric opacity is larger and the emissivity effect is not observable. At nadir, for the very low transect at 100 ft, the bias is large for all frequencies that are sensitive to the surface (all the transect for B875 and first part of the transect for B893). This higher T_b s observed at nadir cannot be explained in terms of atmospheric or surface variability. This effect is not observed at 20° and above. It is attributed to the reflection of the aircraft at the surface, with the aircraft having warmer T_b s than the atmosphere in these window channels (*S. Fox*, personal communication). TESSEM² provides rather low differences with the observations, for most valid observations (i.e., avoiding the transects at 100 ft at nadir). Larger biases are observed at 243 GHz for the polarization close to H, for both flights. Higher sensitivity to wind speed is expected for this polarization at larger angles, and the emissivity dependence to the wind speed might have to be revised when more observations will be available. This can also be related to error in the atmospheric contribution that is more important at large angles for polarization H in this window channel. Note also more noise in the 243 GHz V polarization results for flight B875, likely related to instrument calibration problems.

From these preliminary tests, we can conclude that for low wind speeds (below 5 m/s), TESSEM² provides reasonable results at frequencies above 200 GHz and up to 325 GHz (and better results than FASTEM). At 118

GHz under the same conditions, TESSEM² and FASTEM provide rather similar results. At this stage, we do not unfortunately have ISMAR observations over ocean under much different environments (medium to high wind speeds, other surface temperature range) for a more thorough evaluation.

5. Conclusion

A fast parameterization of the sea surface emissivity is proposed from 10 to 700 GHz: TESSEM² (Tool to Estimate Sea Surface Emissivity from Microwave to sub-Millimeter waves). It is based on FASTEM at low frequencies up to 200 GHz where FASTEM has been thoroughly evaluated. It follows our physical emissivity model elsewhere.

The advantages of this approach is many-fold:

- It capitalizes on the realism of FASTEM at frequencies where FASTEM has been thoroughly evaluated (up to 190 GHz);
- It exploits a physical model where FASTEM is not valid;
- It is a fast parameterization that can easily be implemented in community radiative transfer codes;
- The Jacobians can be estimated analytically, with respect to the environmental variables (wind speed, surface temperature, and salinity) for the assimilation,
- The parameterization could be easily updated to integrate any new development in the physical model, any new version of FASTEM, or any new observations to calibrate the parameterization.

The code has been written in Fortran 90, following a structure similar to FASTEM for an easier use by community models such as RTTOV, CRTM, or ARTS. Its inputs are: the frequency (GHz), the incidence angle (deg), the wind speed at 10 m (m/s), the surface temperature (K), and the salinity (psu). From these inputs, the surface emissivities are calculated for the two orthogonal polarizations. The code is available to the community upon request to the authors.

ISMAR, the demonstrator of the ICI instrument, already flew on the UK FAAM aircraft, with frequencies between 118 and 664 GHz. For low altitude runs off the coast of Scotland, preliminary comparisons of TESSEM² have been conducted, up to 325 GHz. The first results are very encouraging with limited biases as compared to the ISMAR observations, for ocean surface wind speeds below 5 m/s. The evaluation will be consolidated when more observations are available, under more diverse conditions (medium to high surface wind speeds along with a larger range of surface temperatures).

A parallel emissivity parameterization has been developed over the continents and sea-ice, for frequencies up to 700 GHz : the Tool to Estimate the Land Surface Emissivity at Microwaves and Millimeter waves (TELSEM²). Both TESSEM² and TELSEM² will be distributed in the new RTTOV version V12, to be available in 2017.

Acknowledgement

This study has been partly supported by a EUMETSAT contract 'Study on surface emissivity at microwave and sub-millimeter frequencies' (EUM/CO/14/4600001473/CJA). The aircraft ISMAR data have been provided by the UK Met Office. We would also like to thank Clare Lee and all personnel involved in the aircraft campaigns. The BAe-146 research aircraft was operated by Directflight Ltd/Avalon and managed by the FAAM, which is jointly funded by the Met Office and Natural Environment Research Council (NERC). Die Wang is very grateful to the CNES and AIRBUS for their financial support during her PhD. Financial support to participate to the aircraft campaign has also been provided by the CNES, through a TOSCA grant. We thank Christophe Accadia, Vinia Mattioli, and Tim Hewison (EUMETSAT), Stephen English (ECMWF), Fuzhong Weng (NOAA), and James Hocking (UK Met Office) for stimulating discussions on these model developments. We also thank two anonymous reviewers for their careful reading of the manuscript and their constructive comments.

References

- Bormann, N., A. Geer, and S. English (2012), Evaluation of the microwave ocean surface emissivity model fastem-5 in the ifs, *Tech. rep.*, Tech Memo 667, ECMWF, Reading, U. K.
- Cox, C., and W. Munk (1954), Measurement of the roughness of the sea surface from photographs of the suns glitter, *Journal of Optical Society of America*, 44(11), 838–850.
- Dinnat, E. P., J. Boutin, G. Caudal, and J. Etcheto (2003), Issues concerning the sea emissivity modeling at l band for retrieving surface salinity, *Radio Science*, 38(4).
- Durden, S. L., and J. F. Vesecky (1985), A physical radar cross-section model for a wind-driven sea with swell, *IEEE Journal of Oceanic Engineering*, 10(4), 445–451.
- English, S. J., and T. J. Hewison (1998), Fast generic millimeter-wave emissivity model, in *Asia-Pacific Symposium on Remote Sensing of the Atmosphere, Environment, and Space*, pp. 288–300, International Society for Optics and Photonics.
- Eriksson, P., S. Buehler, C. Davis, C. Emde, and O. Lemke (2011), Arts, the atmospheric radiative transfer simulator, version 2, *Journal of Quantitative Spectroscopy and Radiative Transfer*, 112(10), 1551–1558.
- Estellus (2016), Study on surface emissivity at microwave and sub-millimeter frequencies, final report, *Tech. rep.*, EUMETSAT contract no EUM/CO/14/4600001473/CJA.
- Fox, S. (2015), Microwave radiometer polarization description, *Tech. rep.*, Tech Report, UK Met Office, Exeter, U. K.
- Fox, S., C. Lee, I. Rule, R. King, S. Rogers, C. Harlow, and A. Baran (2014), ISMAR: A new submillimeter airborne radiometer, *13th Specialist Meeting on Microwave Radiometry and Remote Sensing of the Environment, MicroRad 2014 - Proceedings*, pp. 128–132, doi: 10.1109/MicroRad.2014.6878923.
- Greenwald, T. J., and A. S. Jones (1999), Evaluation of seawater permittivity models at 150 ghz using satellite observations, *IEEE Transactions on Geoscience and Remote Sensing*, 37(5), 2159–2164.
- Hornik, K., M. Stinchcombe, and H. White (1990), Universal approximation of an unknown mapping and its derivatives using multilayer feedforward networks, *Neural networks*, 3(5), 551–560.
- Kazumori, M., and S. J. English (2015), Use of the ocean surface wind direction signal in microwave radiance assimilation, *Quarterly Journal of the Royal Meteorological Society*, 141(689), 1354–1375.
- Kazumori, M., Q. Liu, R. Treadon, and J. C. Derber (2008), Impact study of amsr-e radiances in the ncep global data assimilation system, *Monthly Weather Review*, 136(2), 541–559.

- Liu, Q., F. Weng, and S. J. English (2011), An improved fast microwave water emissivity model, *IEEE Transactions on Geoscience and Remote Sensing*, 49(4), 1238–1250, doi: 10.1109/TGRS.2010.2064779.
- Monahan, E. C., and I. G. O’Muircheartaigh (1986), Whitecaps and the passive remote sensing of the ocean surface, *International Journal of Remote Sensing*, 7(5), 627–642.
- Prigent, C., and P. Abba (1990), Sea surface equivalent brightness temperature at millimeter wavelength, *Ann. Geophys.*, 8, 627–634.
- Rizzi, R., P. Bauer, S. Crewell, M. Leroy, C. Matzler, W. Menzel, B. Ritter, J. Russel, and A. Thoss (2006), Position paper: Cloud, precipitation and large scale land surface imaging (cpl) observational requirements for meteorology, hydrology, and climate, *Tech. rep.*, EUMETSAT, Darmstadt, Germany.
- Rumelhart, D. E., G. E. Hinton, and R. J. Williams (1986), Learning internal representations by error propagation, in *Parallel distributed processing: explorations in the microstructure of cognition, vol. I.*, edited by D. E. Rumelhart, J. L. McClelland, and the PDP Research Group, pp. 318–362, MIT Press, Cambridge, Mass.
- Stoffelen, A., M. Bonavita, J. Eyre, M. Goldberg, H. Jarvinen, C. Serio, J.-N. Thepaut, and V. Wulfmeyer (2006), Position paper: Post-EPS developments on atmospheric sounding and wind profiling, *Tech. rep.*, EUMETSAT, Darmstadt, Germany.
- Stogryn, A. (1972), The emissivity of sea foam at microwave frequencies, *Journal of Geophysical Research*, 77(9), 1658–1666.

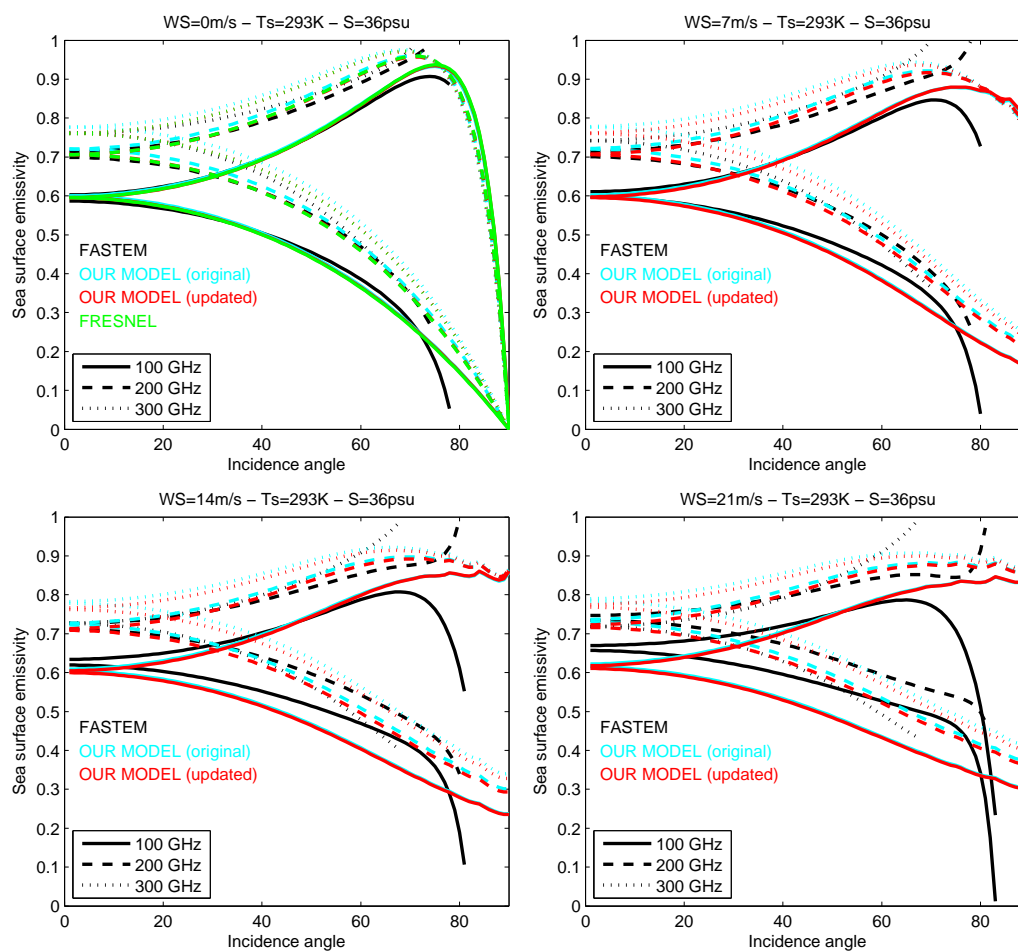


Figure 1. Comparison of different modeled emissivity as a function of incidence angle, for both V (upper curves in each panel) and H polarizations (lower curves in each panel), at 293 K, and a salinity of 36 psu. Upper left: windspeed of 0 m/s; upper right: windspeed of 7 m/s; lower left: windspeed of 14 m/s; lower right: windspeed of 21 m/s. Black: the FASTEM model; red: our model with the FASTEM updates for the dielectric properties of water and for the foam (cover and dielectric properties); cyan: our original model; green at 0 m/s: the Fresnel calculation for a specular surface.

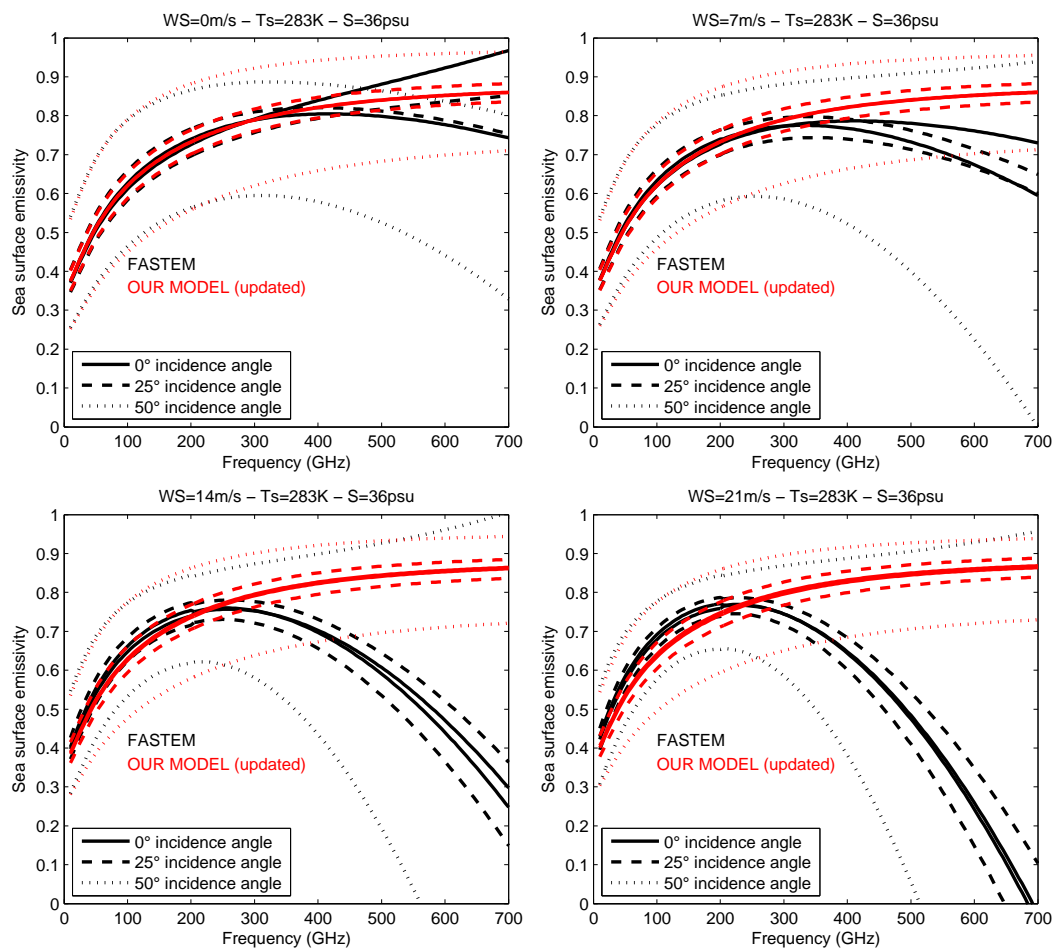


Figure 2. Similar to Figure 1 but for the analysis of the frequency dependence of FASTEM and our updated model, at 0°, 25°, and 50° incidence angle. Black: FASTEM; red: our model updated with FASTEM dielectric properties and foam treatment.

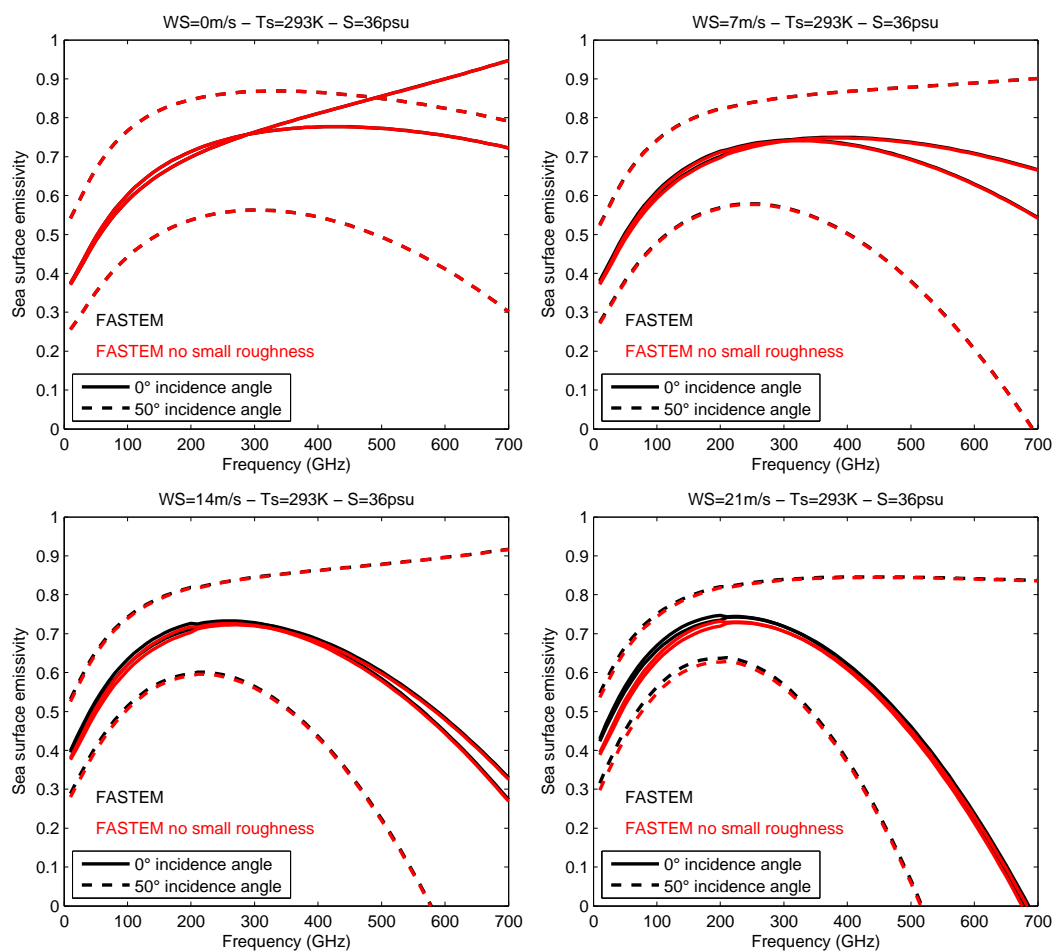


Figure 3. Sensitivity of FASTEM to the small scale roughness, for different wind speeds, and with two incidence angles (nadir and 50°). In black the full FASTEM model; in red the FASTEM model without the small scale roughness. At nadir for 0 m/s wind speed, there is no small scale roughness and the black line is below the red line.

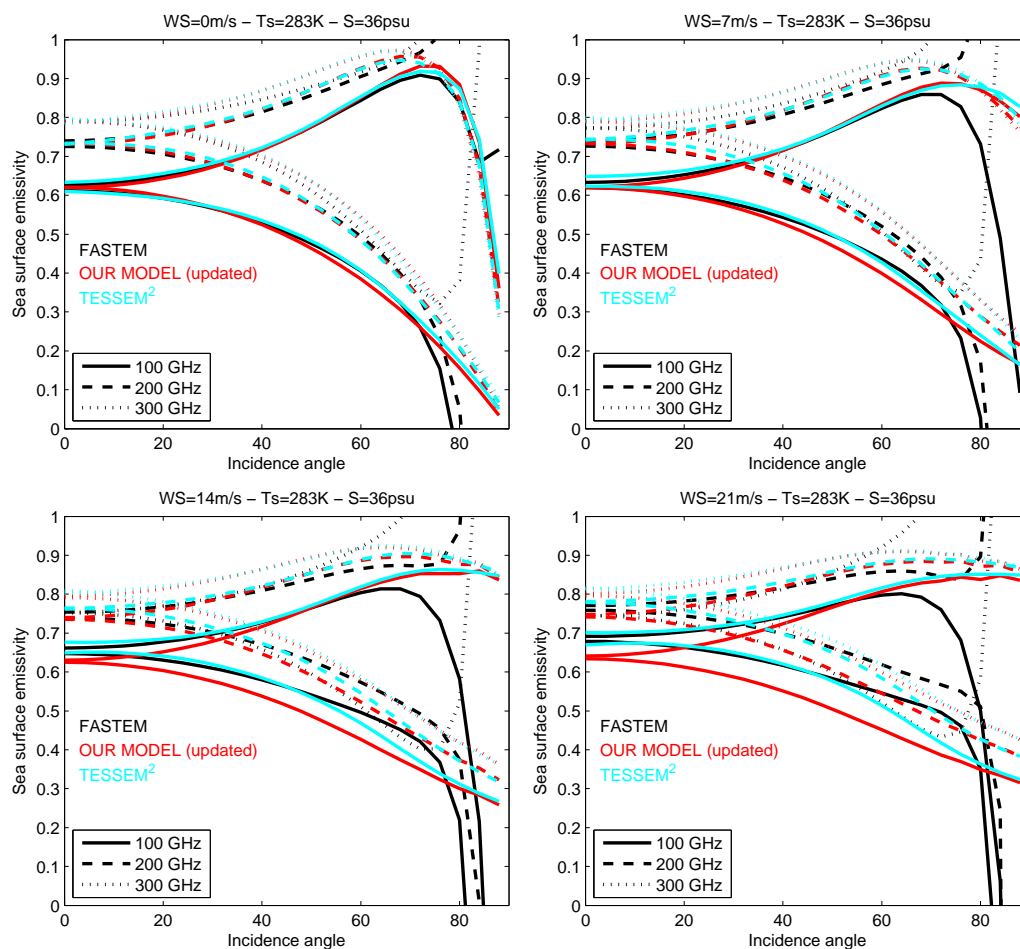


Figure 4. The emissivity angular dependence, as derived from the new parameterization TESSEM² (cyan). For comparison, the emissivity from FASTEM (black) and from our physical model (with the FASTEM updates in red). Results are presented for four wind speeds and for three frequencies (100, 200, and 300 GHz).

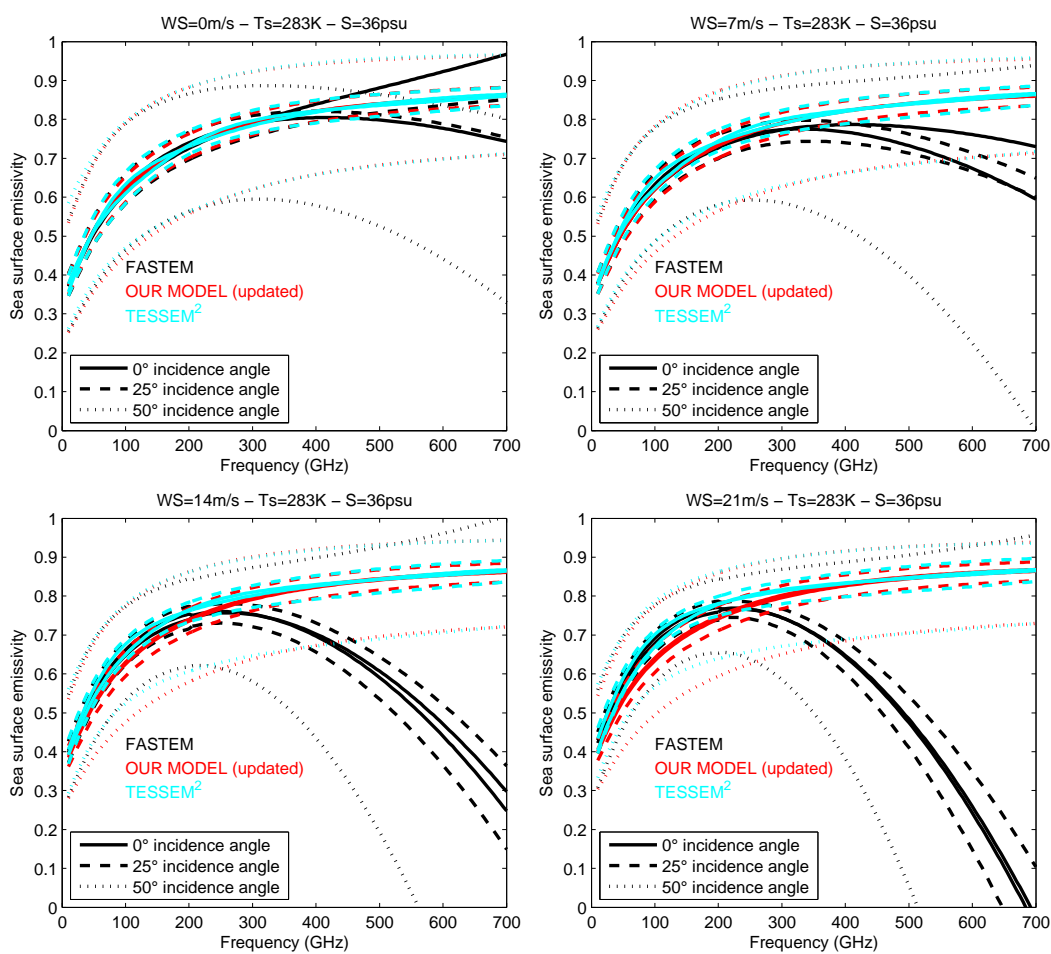


Figure 5. Same as Figure 4 but for the frequency dependence, for three incidence angles (0°, 25°, and 50°).

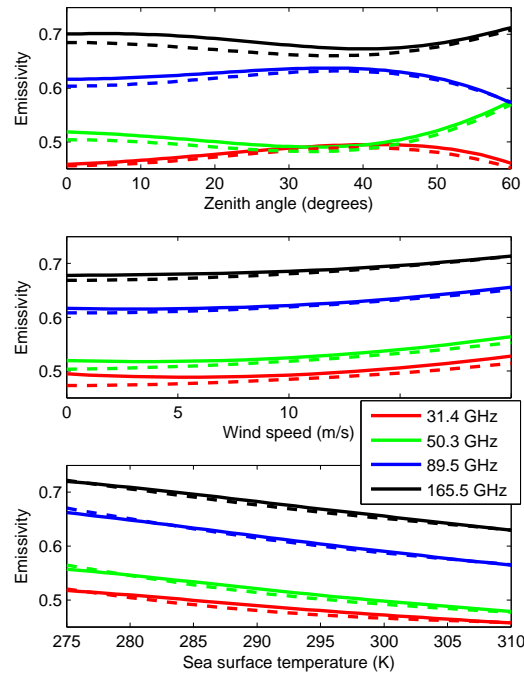


Figure 6. Comparison of TESSEM² (solid lines) and FASTEM (dashed lines) emissivities for ATMS window channels as a function of zenith angle (top), wind speed (middle), and sea surface temperature (bottom). The nominal conditions are: zenith angle at 50°, wind speed at 8 m/s, sea surface temperature at 290 K, and salinity at 35 psu.

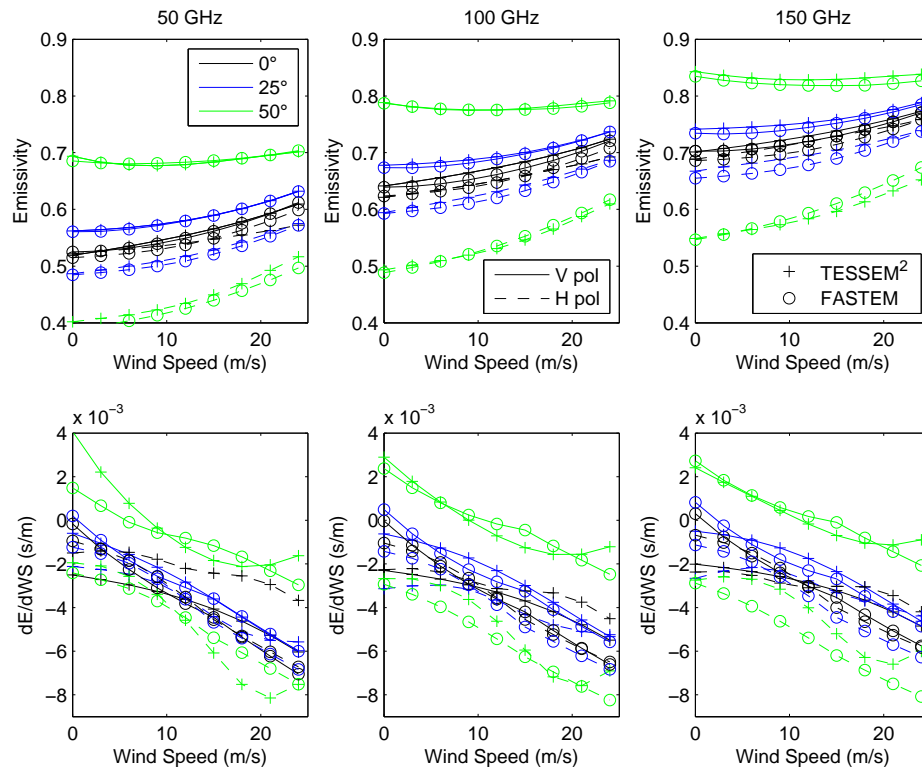


Figure 7. The emissivity as a function of wind speed (top row), as calculated from TESSEM² (+) and FASTEM (o), for both polarizations, and three incidence angles, for three frequencies (50 GHz left, 100 GHz middle, and 150 GHz top), along with the Jacobians of the emissivity with respect to the surface wind speed (bottom row).

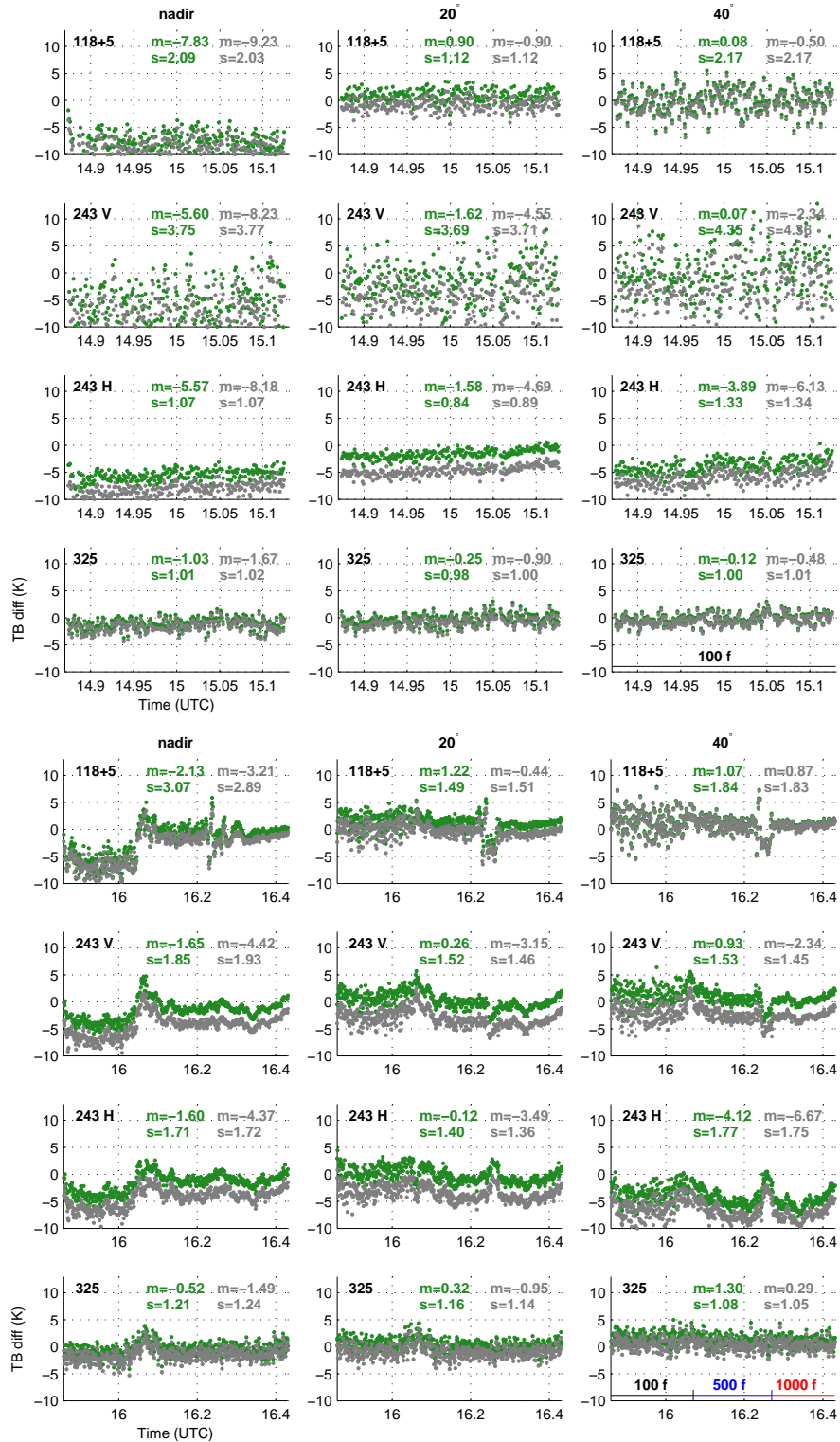


Figure 8. Difference between simulated and observed brightness temperatures for selected ISMAR frequencies as a function of time, for flight B875 (top four rows) and for flight B893 (bottom four rows), at 118.75±5 GHz, 243 GHz (V), 243.2 GHz (H), and 325.15±9.5 GHz, at nadir (left column), at 20° (middle column), and at 40° (right column). Results are in green for TESSEM² and in grey for FASTEM. Mean and standard deviations are mentioned. For each flight, the altitude is indicated in the right panel in the fourth row.

Appendix C

Paper B: Surface emissivity at microwaves to millimeter waves over polar regions: parameterization and evaluation with aircraft experiments

Authors:

D. Wang, C. Prigent, L. Kilic, S. Fox, C. Harlow, C. Jiménez, F. Aires, C. Grassotti, F. Karbou

Paper submitted to:

Journal of Atmospheric and Oceanic Technology, 2016

1 **Surface emissivity at microwaves to millimeter waves over polar regions:**

2 **parameterization and evaluation with aircraft experiments**

3 D. Wang*

4 *Laboratoire d'Etudes du Rayonnement et de la Matière en Astrophysique (LERMA), Observatoire*
5 *de Paris, Paris, France*

6 C. Prigent

7 *LERMA, CNRS, Observatoire de Paris, Paris, France*

8 L. Kilic

9 *LERMA, Observatoire de Paris, Paris, France*

10 S. Fox

11 *Met Office, EX1 3PB Exeter, United Kingdom*

12 C. Harlow

13 *Met Office, EX1 3PB Exeter, United Kingdom*

14 C. Jimenez

15 *LERMA, Estellus, Paris, France*

16 F. Aires

17 *LERMA, CNRS, Observatoire de Paris, Paris, France*

18

C. Grassotti

19

Earth System Science Interdisciplinary Center/Cooperative Institute for Climate and

20

Satellites-Maryland, University of Maryland College Park, MD, United States

21

**STAR/NESDIS/NOAA Affiliate*

22

F. Karbou

23

CNRM-GAME, Météo-France, CNRS, Saint Martin d'Hères, France

24 **Corresponding author address: D. Wang, Observatoire de Paris, 61 Avenue de l'Observatoire,*

25 *75014 Paris.*

26 *E-mail: die.wang@obspm.fr*

ABSTRACT

27 The Tool to Estimate Land Surface Emissivity from Microwave to sub-
28 Millimeter waves (TELSEM²) is a parameterization to provide surface emis-
29 sivity calculations up to 700 GHz, in the framework of the preparation for
30 the Ice Cloud Imager (ICI) on board Meteorological Operational Satellite
31 - Second Generation (MetOp-SG). It is an updated version of the Tool to
32 Estimate the Land Surface Emissivity in the Microwaves (TELSEM, Aires
33 et al. 2011). In this study, we present the parameterization of continental
34 snow and ice and sea ice emissivities in TELSEM². It relies upon satellite-
35 derived emissivities up to 200 GHz, and it is anchored to the Special Sensor
36 Microwave / Imager (SSM/I) TELSEM monthly climatology dataset (19 -
37 85 GHz). Emissivities from Météo-France and National Oceanic and Atmo-
38 spheric Administration (NOAA) at frequencies up to 190 GHz were used, cal-
39 culated from the Special Sensor Microwave Imager/Sounder (SSMIS) and the
40 Advanced Microwave Sounding Unit-B (AMSU-B) observations. TELSEM²
41 has been evaluated up to 325 GHz with the observations of the International
42 Sub-Millimeter Airborne Radiometer (ISMAR) and the Microwave Airborne
43 Radiometer Scanning System (MARSS) which were operated on board the
44 Facility for Airborne Atmospheric Measurements (FAAM) aircraft during the
45 Cold-air Outbreak and Sub-Millimeter Ice Cloud Study (COSMICS) cam-
46 paign over Greenland. Above continental snow and ice, TELSEM² is very
47 consistent with the aircraft estimates in spatially homogeneous regions, espe-
48 cially at 89 and 157 GHz. Over sea ice, the aircraft estimates are very variable
49 spatially and temporally, and the comparisons with the TELSEM² were not
50 conclusive. TELSEM² will be distributed in the new version of the RTTOV
51 radiative transfer community code, to be available in 2017.

52 **1. Introduction**

53 The current passive microwave instruments on board meteorological satellites are limited in fre-
54 quencies to 200 GHz. The Ice Cloud Imager (ICI), on board the next generation of European
55 operational meteorological satellite (EUMETSAT Polar System - Second Generation - EPS-SG),
56 will observe the frequencies up to 664 GHz. It will expand the current capabilities for the charac-
57 terization of the cloud frozen phase, but this is challenging as the radiative transfer models have
58 not been fully developed and evaluated yet up to these frequencies. More specifically, no effort
59 has been made yet toward the estimation of the surface emissivity at frequencies above 200 GHz.

60 Under a large range of atmospheric conditions, satellite observations above 200 GHz will not
61 be sensitive to the surface contribution, due to the increased atmospheric opacity with frequency.
62 However, for dry atmospheres, a portion of the signal received by the satellite can come from the
63 surface (see Figure 1 that presents the total atmospheric transmission at nadir, as calculated by the
64 Atmospheric Radiative Transfer Simulator (ARTS, Eriksson et al. 2011), for five standard atmo-
65 spheres from the Fast Atmospheric Signature Code (FASCOD)). Under dry and cold conditions,
66 a reliable estimate of the surface emissivity is necessary to account for the surface contribution
67 and perform an accurate retrieval of the atmospheric properties. Atmospheric transmission at high
68 frequencies occurs primarily around the poles and at mid-latitude during winter, even up to 480
69 GHz (Figure 1).

70 Physical modeling (e.g., numerical modeling, theoretical modeling) of the emissivity of snow
71 and ice at microwave frequencies is particularly complex, given the large variety of the snow and
72 ice signatures in this frequency range. The interaction between the radiation and snow / ice in-
73 volves both volume and surface scattering, and the mechanisms are very variable in space and
74 time. A variety of models exists (see Matzler (2006) for a review). Four major models are avail-

75 able to the community: the Community Radiative Transfer Model (CRTM) from NOAA (Weng
76 et al. 2001), the single-layer model from Helsinki University of Technology (HUT) (Pulliainen and
77 Grandeil 1999), the Microwave Emission Model of Layered Snowpack (MEMLS) from Univer-
78 sity of Bern (Wiesmann and Matzler 1999), (adapted by Tonboe (2010) for sea ice), and the Dense
79 Media Radiative Transfer (DMRT) snow models (Tsang et al. 2007; Picard et al. 2013). However,
80 the need for a detailed description of the snow and ice parameters (e.g., the snow grain size distri-
81 bution, the stratification of the snow medium, and the quantification of the brine inclusion in sea
82 ice) makes it very difficult to provide realistic estimates at continental scales where such informa-
83 tion is clearly not available. Even if a perfect model existed, the lack of reliable input parameters
84 would jeopardize its robustness. Modeling results above 100 GHz can be very misleading as the
85 complexity of the interaction of the radiation and the surface might not be taken into account at
86 high frequencies. Some efforts to validate the MEMLS model have been conducted, with airborne
87 measurements between 89 and 190 GHz (Harlow 2011; Harlow and Essery 2012). However, even
88 under controlled environments, the modeling of emissivity above 100 GHz is very challenging.

89 Microwave emissivities have also been calculated directly from satellite observations, removing
90 the atmospheric contribution (gas and clouds) and the modulation by the land surface temperature.
91 This technique has been applied to conical imagers such as the SSM/I, the Tropical Rainfall Mea-
92 surement Mission (TRMM) Microwave Instrument (TMI), the Advanced Microwave Scanning
93 Radiometer-E (AMSR-E) (e.g., Prigent et al. (1997, 2005, 2006); Moncet et al. (2011)) but also to
94 cross-track sounders such as AMSU (e.g., Prigent et al. (2005); Karbou et al. (2005); Karbou and
95 Prigent (2005)). These estimates capture well the spatial and temporal variabilities of the emissiv-
96 ities. An analysis of the spectral, angular, and polarization dependences of these satellite-derived
97 emissivities was conducted (Prigent et al. 2008), and led to the development of the TELSEM.
98 TELSEM provides a parameterization of the emissivity for all observing conditions and for all

99 continental surfaces, given the surface location and month in the year, for frequencies from 19 to
100 90 GHz. It is anchored to a robust climatology of 19 to 85 GHz emissivities, calculated from 15
101 years of SSM/I observations (Prigent et al. 2006). Compared to model calculations (e.g., CRTM),
102 TELSEM provides emissivity estimates that agree better with satellite observations up to 90 GHz,
103 especially over polar regions (Bernardo et al. 2013; Prigent et al. 2015).

104 Most satellite-derived emissivity studies focused so far on the frequency range up to 100 GHz,
105 where the atmospheric transmission is significant. Between 100 and 200 GHz, the need for rea-
106 sonable estimates of the emissivity at the AMSU / MHS (Microwave Humidity Sounder) / SSMIS
107 / ATMS (Advanced Technology Microwave Sounder) window channels around 160 GHz has trig-
108 gered some efforts (e.g., at Météo-France (Karbou et al. 2014), at NOAA, and at UK Met Office),
109 but they have not been consolidated yet. The snow and ice emissivities have been estimated from
110 aircraft observations at AMSU frequencies up to 190 GHz, on board the UK FAAM aircraft (Hewi-
111 son and English 1999; Hewison et al. 2002; Harlow 2009, 2011). These studies confirmed the large
112 variability of the snow, ice, and sea ice emissivities as a function of ice and snow types.

113 Here we propose a pragmatic approach to parameterize the snow and ice emissivities up to 700
114 GHz. It aims to provide realistic first guess estimations in practical applications. It makes ex-
115 tensive use of the existing satellite-derived emissivities to provide realistic estimates along with
116 reasonable spatial and temporal variabilities. It relies upon the experience already gained below
117 100 GHz, and upon available emissivity retrievals up to 200 GHz. The methodology, the data
118 sources, and the parameterization results are presented in Section 2. The ISMAR instrument is a
119 unique opportunity to document the surface emissivity above 200 GHz. It has been designed to op-
120 erate at the ICI frequencies (Fox et al. 2014, 2016). It flew on the FAAM BAe-146 aircraft during
121 two campaigns, including flights over Greenland. The snow and ice emissivity parameterizations

122 are partly evaluated by comparison with emissivity estimation from the ISMAR observations over
123 Greenland (Section 3). Conclusions are presented in Section 4.

124 **2. Parameterization of snow and ice emissivities above 90 GHz**

125 *a. The methodology to develop TELSEM²*

126 The satellite-derived estimates provide realistic emissivity estimates for all continental surface
127 types at the global scale, along with their annual dynamics. So far, consistent, long-term, and
128 robust land surface emissivity estimates have been calculated up to 90 GHz. At higher frequencies,
129 some datasets exist, but they need to be carefully analyzed and consolidated. As a consequence, the
130 basis of the emissivity parameterization up to 700 GHz is our SSM/I-derived TELSEM emissivity
131 dataset between 19 and 85 GHz (Prigent et al. 2006). From this dataset, two subsequent processing
132 steps need to be conducted to develop the new TELSEM²:

- 133 • extrapolate the dataset to higher frequencies
- 134 • provide a parameterization of the angular and polarization diversities.

135 To complement the SSM/I TELSEM emissivity database above 100 GHz, the Météo-France
136 and the NOAA emissivity calculations up to 190 GHz help characterize the emissivity frequency
137 dependence at high frequencies. Satellite-derived emissivities at frequencies above 100 GHz are
138 often considered problematic, due to the increasing atmospheric contribution in the signals. How-
139 ever, the surface types of interest here are also the ones that are the most reliably estimated from
140 the satellite observations, for reasons of low atmospheric water vapor contamination. The fre-
141 quency dependence of the emissivities above 100 GHz is analyzed, based on a joint analysis of the
142 SSM/I TELSEM database, the SSMIS and the AMSU-B Météo-France estimates, and the SSMIS
143 NOAA emissivities.

144 In terms of angular information above 100 GHz, SSMIS as well as all other imagers only provide
145 information around 53° . For cross-track scanners such as AMSU-B, a large range of incidence an-
146 gles are observed, and the statistics for a given location and the angle are limited : the AMSU-B
147 derived emissivities are often aggregated at larger incidence angles. Météo-France provides the
148 averaged emissivity for 2 ranges of angles (small angles ($\leq 30^\circ$) and large angles ($> 30^\circ$)), whereas
149 in the NOAA Microwave Integrated Retrieval System (MIRS) process the angular dependence is
150 not provided in the final emissivity product. In terms of polarization, the cross-track scanners such
151 as AMSU-B measure a mixed polarization. At 53° , there is an exactly equal mix of vertical and
152 horizontal polarization. Before the launch of the Global Precipitation Mission (GPM) on February
153 2014, the only imager that measured both polarizations above 100 GHz was the Microwave Anal-
154 ysis and Detection of Rain and Atmosphere Structure (MADRAS) microwave imager on board the
155 French-Indian Megha-Tropiques mission. However, it only covered the tropical latitudes, and as a
156 consequence did not observe the cold surfaces of interest here. The GPM Microwave Instrument
157 (GMI) now provides dual-polarization measurements at 166 GHz, but work on land surface emis-
158 sivities from this instrument is still to be done. The angular and polarization dependences have
159 been carefully analyzed up to 100 GHz during the TELSEM development and a parameterization
160 of these dependences has been suggested (see Aires et al. (2011) for more details). Here, given the
161 lack of information, we assume that these angular and polarization dependences are also valid for
162 higher frequencies. This is a rather crude hypothesis, but it is not possible to constrain a more real-
163 istic parameterization with the available information at this stage. Note that at Météo-France only
164 two angle ranges are considered (small and large angles), and that, in the NOAA/MIRS process-
165 ing of the sounding instrument (i.e., AMSU-A/B and MHS), the emissivities Empirical Orthogonal
166 Functions (EOFs) are assumed constant with angle for all surface types.

167 In the following, the satellite-derived emissivity datasets used in the development of the pa-
 168 rameterization of the high frequency (TELSEM²) are briefly described, and their consistency is
 169 evaluated for their common frequency range around 90 GHz. Then, a parameterization of the
 170 emissivity frequency dependence is proposed, for each surface type.

171 *b. The satellite-derived emissivity sources*

172 Under clear sky condition, assuming specular reflection, the radiative transfer equation, from a
 173 satellite or from an aircraft, can be written as:

$$T_{bp} = T_s \times \epsilon_p \times e^{-\tau(0,H)/\mu} + (1 - \epsilon_p)T_d \times e^{-\tau(0,H)/\mu} + T_u \quad (1)$$

174 The three terms stand for surface emission, downwelling atmospheric emission after reflection
 175 by the surface, and upwelling atmospheric emission, respectively. T_{bp} is the observed brightness
 176 temperature by the radiometer for polarization p ; T_s is the surface skin temperature; ϵ_p is the
 177 surface emissivity for polarization p ; τ is the atmospheric opacity; H is the sounder altitude; μ is
 178 the $\cos(\theta)$, where θ is the incidence angle; T_u is the upwelling brightness temperature from the
 179 atmospheric contribution only; T_d is the downwelling brightness temperature at the surface. See
 180 Prigent et al. (1997) for more details.

181 The surface emissivity can be deduced:

$$\epsilon_p = \frac{T_{bp} - T_u - T_d \times e^{-\tau(0,H)/\mu}}{e^{-\tau(0,H)/\mu} \times (T_s - T_d)} \quad (2)$$

182 Table 1 provides a summary of the satellite-derived emissivity estimates directly used in this
 183 study.

184 1) SSM/I-DERIVED EMISSIVITIES AND TELSEM

185 Our main source of information is the SSM/I-derived emissivity estimates (Prigent et al. 1997,
186 2006) at 19, 22, 37, and 85 GHz, calculated using ancillary data including the International Satel-
187 lite Cloud Climatology Project database (Rossow and Schiffer 1999) and atmospheric reanalysis
188 from NOAA NCEP (National Centers for Environmental Prediction) (Kalnay et al. 1996). Both
189 orthogonal polarizations are available at 53° incidence angle (except at 22 GHz). The calculations
190 are performed over 15 years, including the sea ice emissivities. Note that the sea ice surfaces were
191 not included in the first version of TELSEM. The dataset is available on an equal area grid of
192 $0.25^\circ \times 0.25^\circ$ at the equator, and monthly mean values are used here. With the help of AMSU-A
193 and TMI derived emissivities, TELSEM, which is an emissivity parameterization for all incidence
194 angles and for both orthogonal polarizations, has been developed (Aires et al. 2011).

195 2) SSMIS AND AMSU-B EMISSIVITIES FROM MÉTÉO-FRANCE

196 Based on the emissivity inversion in Eq. 2, emissivities have been calculated at Météo-France
197 from different sensors (Karbou et al. 2006). Short range forecast temperature and humidity pro-
198 files are used as inputs to the RTTOV (Radiative Transfer for the Television Infrared Observation
199 Satellite (TIROS) Operational Vertical Sounder) model to compute the atmospheric contribution
200 to the measured radiances. In this study, we use the AMSU-B and SSMIS estimates. Calculations
201 are performed only if the atmospheric transmission is above 0.5. The AMSU-B emissivities are
202 calculated at 89, 150, and 183 GHz, and are averaged for both low ($< 30^\circ$) and high ($> 30^\circ$) inci-
203 dence angles for a mixture of V and H polarizations. The SSMIS emissivities are calculated at 53°
204 incidence angle at 19, 37, and 91 GHz for both V and H polarizations, and at 150 and 183 GHz
205 for the H polarization (the instrument does not measure the V polarization at these frequencies).
206 One year (2014) of monthly mean estimates for both AMSU-B and SSMIS, with a $0.25^\circ \times 0.25^\circ$

207 spatial resolution, has been calculated and used here. Preliminary analysis of the SSMIS dataset
208 showed that the emissivities at frequencies greater than 150 GHz were problematic for F16 and
209 F17 due to reflector emissions on these spacecraft. The F18 spacecraft did not exhibit an emissive
210 reflector; however the 150 GHz channel failed, while the F19 reflector was recoated and as a result
211 did not exhibit this behavior (Steve Swadley, NRL, USA, personal communication).

212 3) SSMIS EMISSIVITY FROM NOAA/MIRS

213 At NOAA's Satellite and Information Service (NESDIS), a 1D-VAR retrieval algorithm named
214 MIRS (Boukabara et al. 2011), is run to estimate the surface emissivity and the surface temper-
215 ature systematically, along with the atmospheric parameters (humidity and water vapor profiles,
216 cloud and rain quantities), from most operational microwave instruments (i.e., AMSU-A/B, MHS
217 (Microwave Humidity Sounder), and SSMIS). We concentrate on the SSMIS estimates, as it pro-
218 vides emissivities up to 183 GHz with a scanning angle similar to SSM/I. NOAA/MIRS retrieves
219 the first five EOFs with SSMIS observations. The original EOF basis functions were computed
220 off-line, with separate sets for each of the four major surface types (ocean, sea ice, land, and
221 snow-covered land) treated by NOAA/MIRS. The data are available from the NOAA Comprehen-
222 sive Large Array-data Stewardship System (CLASS), on an orbit basis and the swath geometry.
223 As already mentioned, the SSMIS 150 and 183 GHz channels had a known contribution from re-
224 flector emission on the F16 and F17 missions. However, with the NOAA/MIRS retrievals based
225 on EOFs, some information were still extracted at this frequency, except for the F18 mission.

226 4) SATELLITE-DERIVED EMISSIVITY COMPARISONS AROUND 90 GHz OVER THE POLES

227 Observations around 90 GHz are available for both polarizations close to 50°, from all three
228 groups (85 GHz from SSM/I from TELSEM, 91 GHz from SSMIS from Météo-France and

229 NOAA/MIRS). The frequency dependence of the emissivities being limited, the emissivities at
230 these different frequencies are expected to be very close (Prigent et al. 2008). The consistency
231 of the three datasets is checked in this frequency domain. Figure 2 shows the emissivities esti-
232 mated around 90 GHz H polarization in March over the two poles from TELSEM, Météo-France,
233 and NOAA/MIRS. The three emissivity datasets show very similar spatial structures (linear spa-
234 tial correlation of 0.85 between TELSEM and Météo-France, and 0.76 between TELSEM and
235 NOAA/MIRS, similar values are calculated for the V polarization). The histograms of the emis-
236 sivities are presented for the same month, for the two poles, and at both polarizations, close to
237 90 GHz (Figure 3). For the V polarization (resp. H), the mean difference is 0.022 (resp. 0.015)
238 with a standard deviation (std) of 0.025 (reps. 0.031) between TELSEM and Météo-France, and
239 the mean difference is -0.005 (resp. 0.027) with a std of 0.053 (reps. 0.035) between TELSEM and
240 NOAA/MIRS. Compared to the differences observed between satellite and model estimates over
241 these surface types (mean differences of 0.048 (resp. 0.091) with a std of 0.063 (resp. 0.079) in
242 polarization V (reps. H), see Table 1 in Prigent et al. (2015)), the differences here are limited. Part
243 of the differences between the estimates is linked to the fact that TELSEM represents a monthly
244 climatology and that snow and ice areas can show significant variability from one year to the other.
245 Other differences can come from differences in surface temperature assumptions, as well as in the
246 estimation of the atmospheric contribution.

247 *c. Parameterization of frequency dependence of the continental snow and ice emissivity*

248 The emissivities of continental snow and ice have been estimated by all three groups (TELSEM,
249 Météo-France, and NOAA/MIRS). To ease the analysis of the frequency dependence, the conti-
250 nental snow and ice emissivities from TELSEM (from 19 to 85 GHz) are classified, using a k-mean
251 method with 6 classes. The result of the classification is presented in Figure 4 for January and July.

252 Note that the classes have been reordered (different as in TELSEM), to provide some continuity
253 from a class to the next, and to facilitate the interpretation. Classes 1 to 3 correspond mainly to
254 snow regions, whereas classes 4 to 6 are essentially present over continental ice in Antarctica and
255 Greenland. There are limited changes from January to July in Antarctica, slightly more in Green-
256 land. The corresponding frequency dependence for each class is indicated in Figure 5 (in black).
257 Classes 1 to 3 show a decrease of the emissivity with frequency, related to increasing scattering in
258 the snow pack. From classes 1 to 3, snow is getting dryer and thicker, with increasing snow grain
259 size. Class 1 is located mostly around mi-latitudes, where the snow can be wet and shallow. Class
260 3 corresponds to very dry and thick snow pack, with large grain sizes that induce strong scattering
261 around 90 GHz. For classes 4 to 6, the emissivities tend to increase with frequency, especially for
262 the H polarization. A detailed analysis of the sensitivity of the emissivity to the snow parameters
263 has been proposed by Cordisco et al. (2006) based on the SSM/I-derived emissivities as well.

264 The frequency dependence of the emissivity is now compared to the results from Météo-France
265 and NOAA/MIRS emissivity estimates. For each month, each location belongs to a class following
266 the climatologically-based TELSEM classification. The NOAA/MIRS and Météo-France emissiv-
267 ities are grouped by classes, based only on their geographical location and month, following the
268 TELSEM classification. The averaged frequency dependence per class is calculated and shown
269 in Figure 5, for the three databases. The SSMIS and SSM/I estimates correspond to the same
270 geometry (53° incidence angle), and SSMIS measured only the H polarization at high frequen-
271 cies. For the AMSU-B estimates, an average of all large angles ($> 30^\circ$) and average of V and H
272 polarizations (the case for 53° incidence angle) are presented here. The results show very similar
273 frequency dependence for TELSEM and NOAA/MIRS up to 90 GHz, but with a significant lower
274 value of NOAA/MIRS with respect to TELSEM for both polarizations (larger for the H polariza-
275 tion), for all classes except class 6 where the agreement is quite good. The SSMIS Météo-France

estimates are very close to SSM/I TELSEM at 19 and 37 GHz, but for most classes, the estimates around 90 GHz differ significantly, with lower emissivities obtained with SSMIS. The 89 GHz AMSU-B estimates from Météo-France are very close to the SSMIS estimates at V polarization from both Météo-France and NOAA/MIRS. This is not expected, since it should be close to the average of the V and H polarizations. For classes 4 to 6, the 89 GHz AMSU-B estimates are very close to the average of the V and H polarizations of the SSM/I TELSEM emissivities. The SSMIS estimates from NOAA/MIRS and Météo-France agree reasonably well around 90 and 183 GHz, with a rather limited frequency dependence between these two frequencies. Part of the differences in behaviors are due to the time mismatch between these datasets: TELSEM is a monthly mean climatology over 15 years, whereas Météo-France and NOAA/MIRS are representative of one year (2014). Other sources of discrepancies can come from the differences in the surface temperature used by the emissivity estimates, the differences in the water vapor, as well as calibration issues between the instruments. In addition, the TELSEM and Météo-France emissivities are representative of clear sky scenes only, whereas NOAA/MIRS processes all pixels, clear and cloudy. From this analysis, it is concluded that the frequency dependence of the continental snow and ice emissivities is limited, and the emissivities are assumed constant for frequencies above 85 GHz (equal to the 85 GHz emissivity) for both V and H polarizations.

d. Parameterization of the frequency dependence of the sea ice emissivity

Depending on its type (new ice, first-year ice, or multi-year ice), sea ice exhibits various emissivity behaviors, related to differences in dielectric and scattering properties. With age, the ice thickness increases, its salinity decreases, and the potential snow cover changes. These sea ice emissivities were not included in the first version of TELSEM, and the database is first updated to add the sea ice component. The presence of sea ice is derived from the National Snow and Ice

299 Data Center (NSIDC) analysis. Similar to the treatment of the continental snow and ice, a clas-
300 sification is applied to the monthly mean climatological emissivities, with a k-mean classification
301 with 6 classes. The result of the classification is presented in Figure 6 for the two poles on January
302 and July.

303 Over sea ice, the Météo-France emissivity estimates are not available above 100 GHz, so we
304 rely on the SSMIS NOAA/MIRS estimates for the frequency extrapolation of the emissivities.
305 The SSMIS NOAA/MIRS emissivities are grouped by class, following the SSM/I TELSEM clas-
306 sification for each location and month (as for continental snow and ice). The averaged frequency
307 dependence per class is calculated and shown in Figure 7, as compared to the SSM/I TELSEM
308 results (only the H polarizations are measured at high frequencies with SSMIS). Class 1 corre-
309 sponds to the presence of new sea ice likely mixed with open water: it is associated with low
310 emissivities at low frequencies, the emissivity increases with frequency, and this class is present
311 at the ice edge. Classes 2 and 3 are also associated with recent ice, with increasing emissivities at
312 low microwave frequencies. The three other classes have very different emissivity behaviors, with
313 rather high emissivities at low frequencies and decreasing emissivities with frequencies within
314 this frequency range. These classes are located closer to the poles. The emissivity decrease with
315 increasing frequency is related to scattering mechanisms over large particles. One immediately
316 notices that there are significant systematic differences between the SSM/I and the SSMIS results,
317 with the SSMIS emissivities generally lower than the SSM/I TELSEM emissivities. However, it
318 is very reassuring to observe that the frequency dependences are very similar for the two estimates
319 below 100 GHz, with close to parallel behaviors in frequencies for both polarizations. The first
320 three classes show a monotonic increase of the emissivity with frequency. For classes 5 and 6, the
321 emissivities decrease below 90 GHz, but increase slightly after 90 GHz. This behavior has also
322 been observed from aircraft measurements over multi-year ice (see Hewison and English (1999)).

323 As stated above, MIRS can retrieve an emissivity at 150 GHz via EOF with the information at
324 89 and 183 GHz, even if there is no measurement (bad channel). Whether it should actually be
325 used in this case is questionable, since the retrieval cost function will not include any radiometric
326 penalty term at 150 GHz.

327 To provide an idea of the variability of behaviors in the SSMIS dataset, Figure 8 presents the
328 frequency dependence of a few randomly selected pixels in the database for each class. The
329 mean behavior as obtained above is also added (thick solid black line). As expected, there is a
330 significant variability of behavior within a class as specified by the SSM/I TELSEM climatology,
331 but there is nevertheless a rather good consistency within a class. Due to factors such as matching
332 instantaneous values to a climatology, some pixels are clearly assigned to the wrong class, this can
333 be seen in many of the pixel groupings such as classes 4 and 5.

334 As a consequence, for the extrapolation of the emissivities in frequency, we suggest adopting
335 different strategies for the first three classes and for the last three ones. For the first three classes,
336 we propose to adopt the same frequency dependence as the one obtained with SSMIS, corrected
337 from the bias around 85 GHz. In the absence of any information for the V polarization, the same
338 frequency dependence is applied to both V and H polarizations: this is also justified by the rather
339 parallel behavior of the two polarizations between 37 and 85 GHz. For these first three classes, the
340 ratio of the emissivity versus frequency slopes between 150 and 85 GHz and between 85 and 37
341 GHz is assumed constant for a given class, as well as the ratio of the emissivity versus frequency
342 slopes between 183 and 150 GHz and between 150 and 85 GHz. This hypothesis appears to
343 be a reasonable and pragmatic approach at this stage, considering the limited information at our
344 disposal. Above 183 GHz, the emissivity is assumed constant with frequency. Occasionally in
345 the database, the emissivity does not increase with frequency between 37 and 85 GHz for these
346 three classes. In these cases, the emissivity is assumed constant above 85 GHz. For the last three

347 sea ice classes, the frequency dependence above 100 GHz is limited, and a conservative approach
348 is adopted: the emissivities are assumed constant with frequencies above 85 GHz. The resulting
349 extrapolation is presented in red in Figure 7 for each class.

350 **3. Evaluation of the emissivity parameterization with airborne observations**

351 The ISMAR instrument has been tested and operated in two field campaigns out of Prestwick,
352 Scotland, on December 2014 and March 2015, on board the FAAM BAe-146 research aircraft. The
353 MARSS complements the ISMAR on board this aircraft, with channels at 89, 157, and 183 GHz.

354 The emissivity can be directly calculated from the ISMAR and MARSS observations for each
355 frequency, polarization, and scan angle with Eq (2), taking into account the atmospheric contribu-
356 tion as well as the surface temperature. The airborne-derived emissivities are compared to the new
357 emissivity parameterization TELSEM². We are fully aware of the limited scope of the exercise,
358 with only a few flights available, and limited atmospheric and surface conditions.

359 *a. The aircraft radiometers*

360 ISMAR is an along-track scanning radiometer with five channels in the oxygen line at 118.75
361 GHz, three channels near the water vapor lines at 325.15 and 448 GHz, and two window channels
362 at 243.2 and 664 GHz. The two window channels have two orthogonal polarizations which rotate
363 with scan angle, giving both V and H polarizations in the +50° downward view. It is the same
364 for the other channels, but only V polarization is given in the +50° downward view (Fox 2015;
365 Fox et al. 2016). The instrument is calibrated against two blackbody targets, one at ambient
366 temperature, the other one heated. The instrument viewing angles are between +55° and -10°
367 downward and between +10° and -40° upward.

368 MARSS is also an along-track scanning radiometer. It observes in five channels corresponding
369 to AMSU-B, including two window channels (89 and 157 GHz) and three channels near the water
370 vapor line (183.31 GHz). Each scan takes 3 s, with scene views from -40° to $+40^\circ$) and 2 views of
371 the blackbody targets. A single linear polarization is measured in each channel, and the polariza-
372 tion rotates with scan angle. See Hewison (2006) for more details. The channel specifications for
373 both instruments are listed in Table 2.

374 *b. The COSMICS campaign*

375 The COSMICS campaign took place between March 4th and 25th, 2015 from Prestwick, Scot-
376 land, with flights up to Greenland. Two flights (B896 and B898) from this campaign are of special
377 interest for emissivity calculations over snow and ice: they provide level runs suitable for surface
378 emissivity calculation, under dry and rather clear conditions. The two flights started from Iceland
379 and aimed at the Greenland summit, with B898 east of B896. Figure 9 indicates the two flight pat-
380 terns and the flight altitudes. The atmospheric background during these flights are also presented
381 in Figure 9. The Greenland surface temperature was around 230 K, and the water vapor content
382 was less than 1 kg/m^2 .

383 Figures 10 - 11 present the observed brightness temperatures (TBs) at zenith and nadir respec-
384 tively for flight B896, along with corresponding radiative transfer simulations. From Iceland to
385 Greenland, flight B896 overpassed sea ice on its way toward the Greenland summit, and then flew
386 back to Iceland (Figure 9). The aircraft flew much closer to the surface on its way back to Iceland.
387 Some clouds were present during that flight (Figure 9), with some expected effects, especially at
388 high frequencies. Note that, according to the LIDAR measurements during this flight (not shown),
389 ERA-Interim was overestimating cloud cover: it was clear over the summit plateau, as well as
390 during flight B898. For B896, there was no cloud presence below the aircraft between 13.8 h

391 ($\sim 68.5^\circ\text{N}$) and 16.2 h (close to the coast). For B898, there was high cloud below the aircraft until
392 about 13.3 h (69.5°N), after which it was clear until 15.4 h (70°N). The atmospheric radiative
393 transfer is simulated with ARTS (Eriksson et al. 2011). The Rosenkranz (1998) and Rosenkranz
394 and Staelin (1998) models are selected, respectively for water vapor and oxygen. The atmospheric
395 profiles are extracted from the closest in space and time ERA-Interim reanalysis profiles at 0.125°
396 $\times 0.125^\circ$ spatial resolution. The pitch, roll, and orientation angles of the aircraft are taken into
397 consideration in the simulations. A clear sky condition is assumed for all the simulations.

398 In general, the upward-looking simulated and observed brightness temperatures are in rather
399 good agreement, although there are some discrepancies (Figure 10). Between 16.2 and 16.5 h, the
400 aircraft was close to the surface, and the differences are likely due to cloud presence above the
401 aircraft which is not included in the simulations. This effect is less pronounced in channels close
402 to the center of the absorption lines and at much higher frequencies (448 and 664 GHz) where
403 the atmosphere is opaque and radiates at a similar temperature to the cloud. Between 15 and
404 15.4 h, the differences are larger in channels sensitive to water vapor absorption and are thought
405 to be caused by errors in the ERA-Interim water vapor profile used in the simulations. Note that
406 neither of these discrepancies will affect the retrieval of emissivity during low-level flight since the
407 observed downwelling brightness temperature is used in Eq.(2). At 243.2 GHz, the observations
408 are warmer than the simulations, particularly at high altitude, and there is some difference between
409 the two polarizations which is not expected under clear sky conditions. A similar effect is seen
410 in the oxygen absorption band at 118 GHz where the difference between model and simulation
411 increases when moving away from the absorption line center. These differences are thought to be
412 caused by detector non-linearity, but they should not significantly affect the emissivity retrievals
413 as they are most pronounced at high altitude where the downwelling brightness temperature at the
414 surface is dominated by emission from the atmosphere between the aircraft and the surface.

415 For the downward-looking views (Figure 11), a large spatial variability is noticed up to ~ 14 h.
416 This corresponds to the over flying of coastal regions with large spatial variability (sea ice, fjord,
417 and mountainous areas). After 14 h, the aircraft overflew the Greenland plateau and the TBs are
418 smoother, especially at window frequencies. The downward-looking TBs have been simulated
419 with two assumed surface emissivities: 0.5 and 0.9. At 448 GHz and above, it is evident that there
420 is no sensitivity to the emissivity, both on the way to and from Greenland: the two simulations of
421 the down-looking TBs are identical, despite the large difference in emissivity. As a consequence,
422 it is not possible to estimate the emissivity from the observations at 448 GHz and above.

423 *c. Emissivity calculation over Greenland from the aircraft observations and comparison with*

424 *TELSEM²*

425 In the case of the aircraft observations, in Eq.(2), T_{bp} is the upward brightness temperature
426 measured by ISMAR or MARSS. The downwelling brightness temperature T_d is calculated at
427 the surface using a combination of the upward-looking aircraft observations down to the aircraft
428 altitude and simulations based on ERA-Interim database below the aircraft. The upwelling bright-
429 ness temperature T_u and the upwelling atmospheric emission τ are estimated with ARTS, using
430 the ERA-Interim database. The surface temperature T_s is taken from the ERA-Interim database.
431 For flight B896, T_s has been estimated from aircraft instrumentation at the UK Met Office: the
432 emissivity calculations are tested with these different T_s .

433 The TELSEM² estimates are systematically compared to the aircraft-derived emissivities. The
434 only inputs to TELSEM² are the latitude and longitude of the point, the month of observation, and
435 the observing conditions (frequency, incidence angle, and polarization). Figure 12 presents the
436 TELSEM² emissivities in the region for frequencies up to 325 GHz, at 40° for both sea and con-
437 tinental ices, along with the flight patterns for B896 and B898. The TELSEM² emissivity shows

438 a significant spatial variability, especially close to the coast both over sea and continental ices.
439 This is to be compared with the aircraft observations, keeping in mind that the spatial resolution of
440 TELSEM² is poor compared to the aircraft footprint. In these areas of marginal sea ice on March
441 and in coastal region with significant topography, the comparison is expected to be challenging.

442 Figure 13 shows the aircraft-retrieved emissivities at 0°, as a function of latitude for the win-
443 dow channels (89, 157, and 243 GHz) and the channels furthest from the absorption line centers
444 (118±5, 183±7, and 325±9.5 GHz). The top (resp. bottom) two rows present the emissivities
445 calculated on the way to (resp. from) Greenland. Sea ice is present from 67°N to 68°N in latitude;
446 the rest of the transect is over continental ice. The TELSEM² emissivities are also presented for
447 comparison, for the same frequencies, incidence angles, and polarizations. Over sea ice (from
448 67°N to 68°N), the aircraft retrieved emissivities show a very large variability. On the way to
449 Greenland, it is likely due to the natural spatial variability of the sea ice that is expected to be high,
450 but on the way back from Greenland, a poor temperature separation between the calibration tar-
451 gets is suspected, inducing an increased noise in the retrievals during this section of the flight. At
452 325 GHz, the estimates between 67°N and 68.5°N are very noisy, especially on the way back from
453 Greenland: this is due to the lack of sensitivity to the emissivity in this region (see the simulations
454 in Figure 11, with the two different emissivities, 0.5 and 0.9, that provide very similar brightness
455 temperatures). Over continental ice, from 69°N to 73°N, the agreement between the TELSEM²
456 and the aircraft estimates is good at 89 GHz, but degrades at higher frequencies. Beyond 71°N,
457 the differences between the aircraft retrievals and TELSEM² may be induced by two reasons.
458 The first reason maybe related to the errors in ERA-Interim water vapor profile as discussed in
459 Figure 10. The second one maybe related to our hypothesis made in TELSEM², assuming that
460 the surface emissivity is constant at frequencies higher than 90 GHz. Beyond 71°N, the region
461 is associated to class 5 (continental ice). The emissivity increases slightly between 89 and 183

462 GHz for H polarization (see Figure 5). Therefore, it is possible that TELSEM² underestimates
463 the surface emissivity for this type of continental ice between 89 and 183 GHz. In addition, some
464 spatial structures in the emissivity retrieval that are visible at 70°N at 243 GHz are clearly not
465 present at 89 GHz, either in the emissivity retrieval or in the TELSEM² estimates. This could be
466 related to some specific snow and ice conditions that would induce emissivity changes at higher
467 frequencies. These signatures are missed by TELSEM² that is anchored to emissivity estimates
468 below 100 GHz, with limited reliable satellite-derived emissivity retrievals at frequencies above
469 100 GHz. Overall, the spatial variability is captured by TELSEM², despite the fact that TELSEM²
470 is based on a monthly climatology.

471 Over ice (sea and continental), the surface temperature is subject to large errors, which will
472 cause errors in emissivity retrieval. The UK Met Office retrieved and analyzed the surface tem-
473 perature estimated by several methods, directly from the aircraft estimates for flight B896. It
474 includes infrared retrieval from the ARIES spectrometer (Wilson et al. 1999), as well as estimates
475 from an infrared Heimann sensor. Figure 14 shows the results from this work, on the way from
476 Greenland. Notice the large T_s gradient between 68°N and 70°N, along with the large difference
477 between the aircraft estimates and the ECMWF T_s . This is likely partly related to the spatial res-
478 olution differences between these estimates, in an area of large spatial heterogeneity (fjords and
479 mountains). The T_s differences can be large between the T_s estimates, up to 10 K even between
480 aircraft estimates. For flight B896 at nadir (similar to Figure 13), the emissivities have been esti-
481 mated, using different T_s . The changes in T_s estimates have a significant impact on the emissivity
482 retrieval, as expected, but none of the analyzed T_s estimate systematically improved the agreement
483 with TELSEM². The emissivity aircraft retrievals in window frequencies are also presented for
484 flight B898 (Figures 15) at nadir and 40° on the way back from Greenland. The agreement with
485 TELSEM² is very reasonable, and the spatial variability between 69°N and 73°N is captured well.

486 The histograms of the emissivity differences between the aircraft-derived estimates and TELSEM²
487 results at nadir are shown in Figure 16, over continental ice during the two flights, with the mean
488 difference and its std for each frequency. At 89 GHz, the mean difference (-0.002) is much smaller
489 than the mean difference between TELSEM and Météo-France and also between TELSEM and
490 NOAA/MIRS (discussed in section 2.2.4). As expected, the bias increases with atmospheric opac-
491 ity, and it is larger near the water vapor lines at 183 (0.017) and 325 GHz (-0.022) than in the
492 window channels at 89 (-0.002), 157 (0.012), 243 H (-0.011), and 243 V GHz (-0.013). The mean
493 difference and std are also calculated at 40° (not shown). The bias is very similar, and the std is
494 slightly larger for each channel.

495 **4. Conclusion**

496 A parameterization of the snow and ice emissivities has been developed, for frequencies up to
497 700 GHz, in the framework of the preparation for the ICI on board MetOp-SG. The objective is
498 to provide realistic first guess emissivity estimations for practical applications. Complex surface
499 emissivity models might better capture small scale spatial and temporal variability, but they require
500 input information (e. g., snow depth, snow water equivalent, grain size, surface roughness) that are
501 not available on a regular basis at global scale. Our parameterization relies upon satellite-derived
502 emissivities up to 200 GHz, and it is anchored to the SSM/I TELSEM monthly climatology dataset
503 (19 - 85 GHz). Météo-France and NOAA provided emissivities up to 190 GHz, calculated from
504 SSMIS and AMSU-B observations. For continental snow and ice, the frequency dependence after
505 100 GHz is limited. For sea ice, the frequency dependence is more important and it is parameter-
506 ized for some sea ice types. There is a general lack of information on the angular and polarization
507 dependence above 100 GHz. A conservative approach is adopted, following the polarization and
508 angular dependencies obtained below 100 GHz, which may require revisions when more high fre-

509 quency data are available in the future. The TELSEM fortran code has been updated to provide
510 emissivity calculations up to 700 GHz (TELSEM²) for all continents, including continental snow
511 and ice and sea ice. TELSEM² is available to the community. The inputs of the code are the
512 frequency, the incidence angle, the latitude, the longitude, and the month. It outputs the emissivity
513 for both orthogonal polarizations, along with the error covariance matrix, with a $0.25^\circ \times 0.25^\circ$
514 spatial resolution, at a monthly basis. TELSEM² will be included in the next version of the RT-
515 TOV package, a community radiative transfer code used by many Numerical Weather Prediction
516 centers, such as the UK Met Office, ECMWF, and Météo-France.

517 TELSEM² has been evaluated with observations between 89 and 325 GHz, on board the FAAM
518 aircraft, during the COSMICS campaign over Greenland. The surface emissivities have been es-
519 timated from the aircraft observations, from the upwelling and downwelling radiances measured
520 under dry conditions over Greenland, up to 325 GHz. At higher frequencies, the emissivity esti-
521 mates were not reliable, due to the large atmospheric contribution to the TBs even at low level.
522 Above continental snow and ice up to 325 GHz, TELSEM² is very consistent with the aircraft
523 observations in spatially homogeneous regions. The frequency and angle dependences are well
524 reproduced by the parameterization. The agreement at 89 and 157 GHz is even exceptional, con-
525 sidering that TELSEM² is only assumed to provide a realistic climatological first guess of the
526 emissivities at a monthly scale. In coastal regions, the agreement can be affected by the differ-
527 ences in spatial resolution between the two estimates. Over sea ice, the aircraft estimates are
528 highly variable both spatially and temporally, and comparisons with TELSEM² model were not
529 conclusive. This is a first step toward the evaluation of the emissivity parameterization at mil-
530 limeter and sub-millimeter frequencies over polar regions. More flights under a larger variety of
531 surface and atmospheric conditions will have to be performed.

532 *Acknowledgments.* This study has partly been supported by a EUMETSAT con-
533 tract 'Study on surface emissivity at microwave and sub-millimeter frequencies'
534 (EUM/CO/14/4600001473/CJA). We would like to thank the crew and personnel involved
535 in the COSMICS campaign. The BAe-146 research aircraft was operated by Directflight
536 Ltd/Avalon and managed by the FAAM, which is jointly funded by the Met Office and Natural
537 Environment Research Council (NERC). We thank Christophe Accadia, Vinia Mattioli, and
538 Tim Hewison (EUMETSAT), Stephen English (ECMWF), Fuzhong Weng (NOAA), and James
539 Hocking (UK Met Office) for stimulating discussions on these model developments. Die Wang is
540 very grateful to the CNES and AIRBUS for their financial support during her PhD. Some financial
541 support for the data processing has also been provided by the CNES, through a TOSCA grant.

542 **References**

- 543 Aires, F., C. Prigent, F. Bernardo, C. Jiménez, R. Saunders, and P. Brunel, 2011: A tool to esti-
544 mate land-surface emissivities at microwave frequencies (telsem) for use in numerical weather
545 prediction. *Quarterly Journal of the Royal Meteorological Society*, **137 (656)**, 690–699.
- 546 Bernardo, F., F. Aires, and C. Prigent, 2013: Atmospheric water-vapour profiling from passive mi-
547 crowave sounders over ocean and land. part ii: Validation using existing instruments. *Quarterly*
548 *Journal of the Royal Meteorological Society*, **139 (673)**, 865–878.
- 549 Boukabara, S. A., and Coauthors, 2011: MiRS: An all-weather 1DVAR satellite data assimilation
550 and retrieval system. *IEEE Transactions on Geoscience and Remote Sensing*, **49 (9)**, 3249–3272,
551 doi:10.1109/TGRS.2011.2158438.
- 552 Cordisco, E., C. Prigent, and F. Aires, 2006: Snow characterization at a global scale with passive
553 microwave satellite observations. 1–15 pp., doi:10.1029/2005JD006773.

- 554 Eriksson, P., S. Buehler, C. Davis, C. Emde, and O. Lemke, 2011: Arts, the atmospheric radia-
555 tive transfer simulator, version 2. *Journal of Quantitative Spectroscopy and Radiative Transfer*,
556 **112 (10)**, 1551–1558.
- 557 Fox, S., 2015: Microwave radiometer polarization description. Tech. rep., UK Met Office.
- 558 Fox, S., C. Lee, I. Rule, R. King, S. Rogers, C. Harlow, and A. Baran, 2014: ISMAR:
559 A new submillimeter airborne radiometer. *13th Specialist Meeting on Microwave Radiome-*
560 *try and Remote Sensing of the Environment, MicroRad 2014 - Proceedings*, 128–132, doi:
561 10.1109/MicroRad.2014.6878923.
- 562 Fox, S., and Coauthors, 2016: Ismar: an airborne submillimetre radiometer. *Atmos. Meas. Tech.*
563 *Discuss.*, doi:10.5194/amt-2016-310,2016.
- 564 Harlow, R. C., 2009: Millimeter microwave emissivities and effective temperatures of snow-
565 covered surfaces: evidence for Lambertian surface scattering. *Geoscience and Remote Sensing*,
566 *IEEE Transactions on*, **47 (7)**, 1957–1970.
- 567 Harlow, R. C., 2011: Sea ice emissivities and effective temperatures at MHS frequencies: An
568 analysis of airborne microwave data measured during two arctic campaigns. *IEEE Transactions*
569 *on Geoscience and Remote Sensing*, **49 (4)**, 1223–1237, doi:10.1109/TGRS.2010.2051555.
- 570 Harlow, R. C., and R. Essery, 2012: Tundra snow emissivities at MHS frequencies: MEMLS val-
571 idation using airborne microwave data measured during CLPX-II. *IEEE Transactions on Geo-*
572 *science and Remote Sensing*, **50 (11 PART1)**, 4262–4278, doi:10.1109/TGRS.2012.2193132.
- 573 Hewison, T. J., 2006: Aircraft validation of clear air absorption models at millimeter wavelengths
574 (89-183 GHz). *Journal of Geophysical Research Atmospheres*, **111 (14)**, 1–11, doi:10.1029/
575 2005JD006719.

- 576 Hewison, T. J., and S. J. English, 1999: Airborne retrievals of snow and ice surface emissivity
577 at millimeter wavelengths. *IEEE Transactions on Geoscience and Remote Sensing*, **37 (4)**,
578 1871–1879, doi:10.1109/36.774700.
- 579 Hewison, T. J., N. Selbach, G. Heygster, J. P. Taylor, and A. J. McGrath, 2002: Airborne Mea-
580 surements of Arctic Sea Ice, Glacier and Snow Emissivity at 24-183 GHz. *IEEE International*
581 *Geoscience and Remote Sensing Symposium*, **5**, 2851–2855.
- 582 Kalnay, E., and Coauthors, 1996: The ncep/ncar 40-year reanalysis project. *Bulletin of the Ameri-*
583 *can meteorological Society*, **77 (3)**, 437–471.
- 584 Karbou, F., F. Aires, C. Prigent, and L. Eymard, 2005: Potential of advanced microwave sounding
585 unit-a (amsu-a) and amsu-b measurements for atmospheric temperature and humidity profiling
586 over land. *Journal of Geophysical Research: Atmospheres*, **110 (D7)**.
- 587 Karbou, F., E. Gerard, and F. Rabier, 2006: Microwave land emissivity and skin temperature for
588 AMSU-A and -B assimilation over land. *Quarterly Journal of the Royal Meteorological Society*,
589 **132 (620)**, 2333–2355, doi:Doi10.1256/Qj.05.216, URL [⟨GotoISI⟩://000242468800011](#).
- 590 Karbou, F., and C. Prigent, 2005: Calculation of microwave land surface emissivity from satellite
591 observations: Validity of the specular approximation over snow-free surfaces? *IEEE Geoscience*
592 *and Remote Sensing Letters*, **2 (3)**, 311–314.
- 593 Karbou, F., F. Rabier, and C. Prigent, 2014: The assimilation of observations from the advanced
594 microwave sounding unit over sea ice in the french global numerical weather prediction system.
595 *Monthly Weather Review*, **142 (1)**, 125–140.
- 596 Matzler, C., Ed., 2006: *Thermal Microwave Radiation*. The Institution of Engineering and Tech-
597 nology.

- 598 Moncet, J. L., P. Liang, J. F. Galantowicz, A. E. Lipton, G. Uymin, C. Prigent, and C. Grassotti,
599 2011: Land surface microwave emissivities derived from AMSR-E and MODIS measurements
600 with advanced quality control. *Journal of Geophysical Research Atmospheres*, **116 (16)**, 1–98,
601 doi:10.1029/2010JD015429.
- 602 Picard, G., L. Brucker, a. Roy, F. Dupont, M. Fily, a. Royer, and C. Harlow, 2013: Simulation of
603 the microwave emission of multi-layered snowpacks using the Dense Media Radiative transfer
604 theory: the DMRT-ML model. *Geoscientific Model Development*, **6 (4)**, 1061–1078, doi:10.
605 5194/gmd-6-1061-2013, URL <http://www.geosci-model-dev.net/6/1061/2013/>.
- 606 Prigent, C., F. Aires, and W. B. Rossow, 2006: Land Surface Microwave Emissivities over the
607 Globe for a Decade. *Bulletin of the American Meteorological Society*, **87 (11)**, 1573–1584,
608 URL <http://journals.ametsoc.org/doi/abs/10.1175/BAMS-87-11-1573>.
- 609 Prigent, C., F. Chevallier, F. Karbou, P. Bauer, and K. G., 2005: Amsu-a surface emissivities for
610 numerical weather prediction assimilation schemes. *Journal of Applied Meteorology*, **44**, 416–
611 426.
- 612 Prigent, C., E. Jaumouillé, F. Chevallier, and F. Aires, 2008: A parameterization of the microwave
613 land surface emissivity between 19 and 100 GHz, anchored to satellite-derived estimates. *Geo-
614 science and Remote Sensing, IEEE Transactions on*, **46 (2)**, 344–352.
- 615 Prigent, C., P. Liang, Y. Tian, F. Aires, J.-L. Moncet, and S. A. Boukabara, 2015: Evaluation of
616 modeled microwave land surface emissivities with satellite-based estimates. *Journal of Geo-
617 physical Research: Atmospheres*, **120 (7)**, 2706–2718.
- 618 Prigent, C., W. B. Rossow, and E. Matthews, 1997: Microwave land surface emissivities estimated
619 from SSM/I observations. *Journal of Geophysical Research: Atmospheres*, **102 (D18)**, 21 867–

620 21 890.

621 Pulliainen, J. T., and J. Grandeil, 1999: HUT snow emission model and its applicability to snow
622 water equivalent retrieval. *IEEE Transactions on Geoscience and Remote Sensing*, **37 (3 I)**,
623 1378–1390, doi:10.1109/36.763302.

624 Rosenkranz, P. W., 1998: Water vapor microwave continuum absorption: A comparison of mea-
625 surements and models. *Radio Science*, **33 (4)**, 919–928, doi:10.1029/98RS01182.

626 Rosenkranz, P. W., and D. H. Staelin, 1998: Polarized thermal microwave emission from oxygen
627 in the mesosphere. *Radio Science*, **23 (5)**, 721–729, doi:10.1029/RS023i005p00721.

628 Rossow, W. B., and R. A. Schiffer, 1999: Advances in understanding clouds from isccp. *Bulletin*
629 *of the American Meteorological Society*, **80 (11)**, 2261–2287.

630 Tonboe, R. T., 2010: The simulated sea ice thermal microwave emission at window and sounding
631 frequencies. *Tellus, Series A: Dynamic Meteorology and Oceanography*, **62 (3)**, 333–344, doi:
632 10.1111/j.1600-0870.2010.00434.x.

633 Tsang, L., J. Pan, D. Liang, Z. Li, D. W. Cline, and Y. Tan, 2007: Modeling active microwave
634 remote sensing of snow using dense media radiative transfer (dmrt) theory with multiple-
635 scattering effects. *Geoscience and Remote Sensing, IEEE Transactions on*, **45 (4)**, 990–1004.

636 Weng, F., B. Yan, and N. C. Grody, 2001: A microwave land emissivity model. *Journal of Geo-*
637 *physical Research*, **106 (D17)**, 20 115, doi:10.1029/2001JD900019.

638 Wiesmann, A., and C. Matzler, 1999: Microwave emission model of layered snowpacks. *Remote*
639 *Sensing of Environment*, **70 (3)**, 307–316, doi:10.1016/S0034-4257(99)00046-2.

640 Wilson, S. H. S., N. Atkinson, and J. A. Smith, 1999: The development of an airborne infrared
641 interferometer for meteorological sounding studies. *Journal of Atmospheric and Oceanic Tech-*
642 *nology*, **16** (12).

643 **LIST OF TABLES**

644	Table 1.	Characteristics of the satellite-derived emissivity datasets used in this analysis.	
645		Note that the NOAA/MIRS retrieves the first five EOFs with SSMIS observa-	
646		tions. Freq. is Frequency; Spatial res. is Spatial resolution.	33
647	Table 2.	Channel characteristics of the ISMAR and MARSS instruments, including their	
648		frequencies, BandWidth (BW), instrument noise (measured Net Δ T on liquid	
649		nitrogen cooled target over 60 seconds, from Fox et al. 2016), polarization,	
650		Field-Of-View (FOV) angle (full-width at half-maximum), and main spectral	
651		features. The polarizations indicated here are the polarizations in the +50°	
652		downward view for all the channels. The MWI (MicroWave Imager) is an	
653		instrument on board the MetOp-SG as ICI.	34

654 TABLE 1. Characteristics of the satellite-derived emissivity datasets used in this analysis. Note that the
 655 NOAA/MIRS retrieves the first five EOFs with SSMIS observations. Freq. is Frequency; Spatial res. is Spatial
 656 resolution.

Dataset	Sensor	Surface type	Freq. (GHz)	Angle, polarization	Spatial res.	Temporal sampling	Temporal cover
TELSEM	SSM/I	Continents + sea ice	19, 37, 85	53°, V + H	.25°x.25°	Monthly mean	Climatology
Emissivity MIRS NOAA	SSMIS	All surfaces	19, 37, 91, 150, 183	53°, V + H (< 100 GHz), H (> 100 GHz)	.25°x.25°	Each satellite overpass	Mar. + Oct. 2014
Emissivity Météo-France	AMSU-B	Continents	89, 150, 183	Small and large angles separately, with mixed polar.	.25°x.25°	Monthly mean	2014
Emissivity Météo-France	SSMIS	Continents	19, 37, 91, 183	53°, V + H (< 100 GHz), H (> 100 GHz)	.25°x.25°	Monthly mean	2014

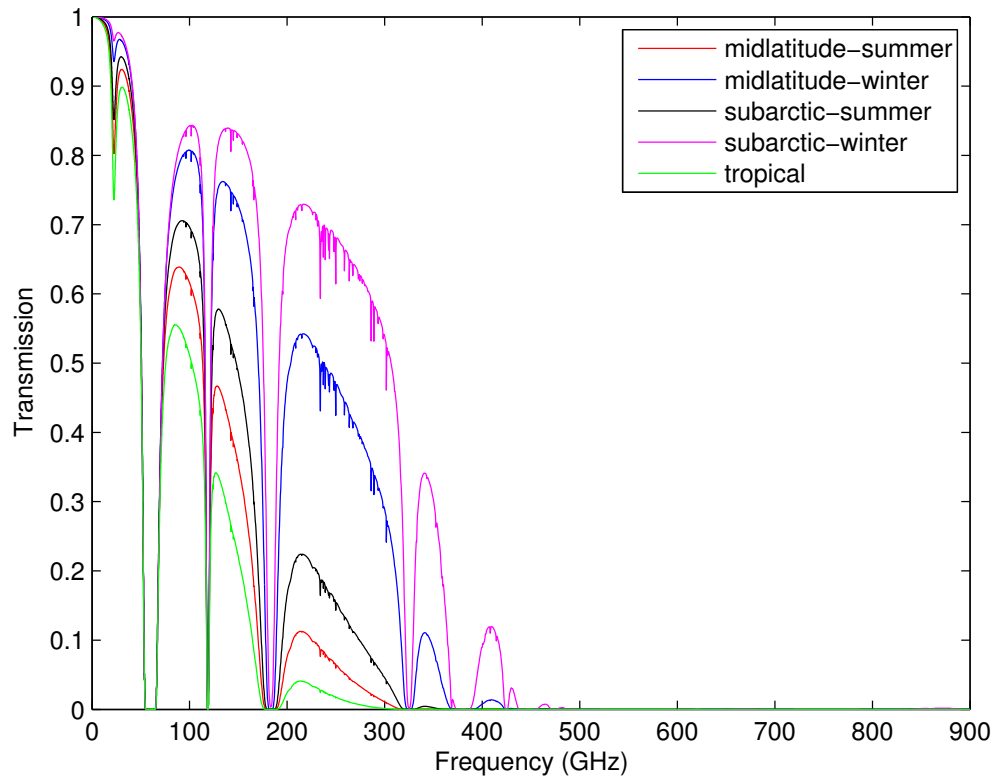
657 TABLE 2. Channel characteristics of the ISMAR and MARSS instruments, including their frequencies, Band-
658 Width (BW), instrument noise (measured Net Δ T on liquid nitrogen cooled target over 60 seconds, from Fox
659 et al. 2016), polarization, Field-Of-View (FOV) angle (full-width at half-maximum), and main spectral features.
660 The polarizations indicated here are the polarizations in the +50° downward view for all the channels. The MWI
661 (MicroWave Imager) is an instrument on board the MetOp-SG as ICI.

Instrument (GHz)	Centre freq. (GHz)	Freq. offset (GHz)	BW (GHz)	Net Δ T (K)	Polarization	FOV (deg)	Spectral feature
MARSS (MWI)	89	± 1.1	0.65	0.42	Mixed	12.0	Window
		± 1.1	0.4	0.4			
		± 1.5	0.4	0.4			
5 \times ISMAR (MWI)	5 \times 118.75	± 2.1	0.8	0.3	5 \times V	5 \times <3.8	5 \times O ₂
		± 3.0	1.0	0.3			
		± 5.0	2.0	0.3			
MARSS (MWI)	157.0	± 2.6	2.6	0.69	H	11.0	Window
		± 1.0	0.45	0.64			
3 \times MARSS (ICI)	3 \times 183.31	± 3.0	1.0	0.44	3 \times H	3 \times 6.2	3 \times H ₂ O
		± 7.0	2.0	0.35			
2 \times ISMAR (ICI)	2 \times 243.2	± 2.5	3.0	0.3	V	2 \times <3.6	2 \times Window
				0.4	H		
		± 1.5	1.6	1.6			
3 \times ISMAR (ICI)	3 \times 325.15	± 3.5	2.4	0.7	3 \times V	3 \times <3.6	3 \times H ₂ O
		± 9.5	3.0	1.1			
		± 1.4	1.2	1.1			
3 \times ISMAR (ICI)	3 \times 448.0	± 3.0	2.0	1.6	3 \times V	3 \times <3.6	3 \times H ₂ O
		± 7.2	3.0	2.8			
2 \times ISMAR (ICI)	2 \times 664.0	± 4.2	5.0	3.3	V	2 \times <3.8	2 \times Window
				1.3	H		

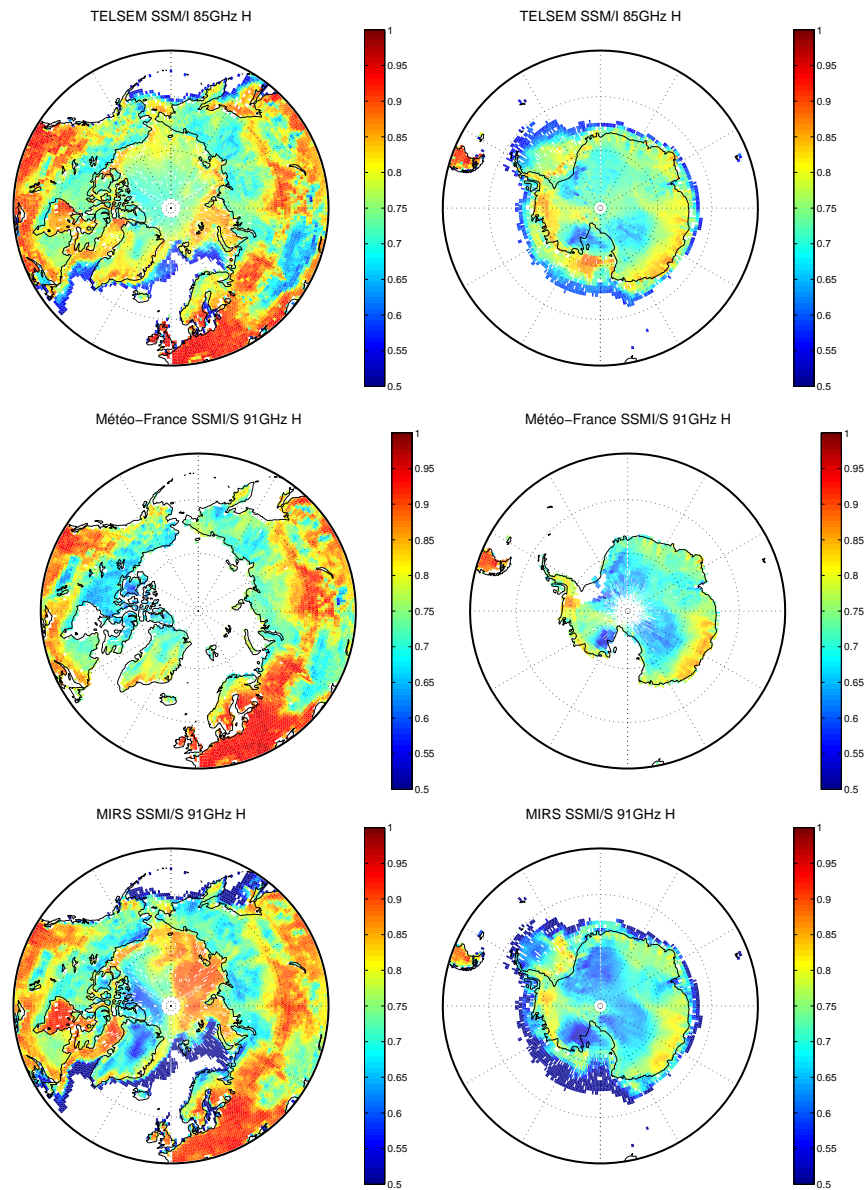
662 **LIST OF FIGURES**

663	Fig. 1.	Total transmission of the atmosphere at nadir, as calculated with ARTS, for five standard atmospheres from FASCOD.	37
664			
665	Fig. 2.	The emissivity around 90 GHz at H polarization as calculated from the different groups on March, for the North (left) and South poles (right). Top row: SSM/I (85 GHz) from TELSEM; middle row: SSMIS (91 GHz) from Météo-France; bottom row: SSMIS (91 GHz) from NOAA/MIRS.	38
666			
667			
668			
669	Fig. 3.	Histograms of the emissivity around 90 GHz as calculated from the different groups (TELSEM, Météo-France, and NOAA/MIRS) on March over the poles in both polarizations (V in black, H in red). Sea ice surfaces are excluded.	39
670			
671			
672	Fig. 4.	Results of the continental snow and ice emissivity k-mean classification from SSM/I TELSEM over the North pole (top) and the South pole (bottom) in January (left) and July (right). Six classes are used.	40
673			
674			
675	Fig. 5.	Frequency dependence of the snow and ice emissivities, for different classes, for SSM/I TELSEM, SSMIS NOAA/MIRS, and AMSU-B and SSMIS Météo-France.	41
676			
677	Fig. 6.	Results of the sea ice emissivity classification from SSM/I TELSEM over the North pole (top) and South pole (bottom) on January (left) and July (right).	42
678			
679	Fig. 7.	Frequency dependence of the emissivity per sea ice class, for both V and H polarizations, from SSM/I TELSEM (in black), from SSMIS NOAA/MIRS (in blue). The suggested extrapolation of the SSM/I TELSEM is indicated in red.	43
680			
681			
682	Fig. 8.	Frequency dependence of the SSMIS NOAA/MIRS emissivities, for a few randomly selected pixels per sea ice class (for H polarization only, as V polarization is not available at high frequencies). The mean behavior is indicated with a thick black line.	44
683			
684			
685	Fig. 9.	First two rows: The flight track of flights B896 (in black) and B898 (in grey) back and forth from Greenland (a). The flight altitudes as a function of the observation time (b). Bottom two rows: The surface skin temperature (c), integrated water vapor content (d), 10-m wind speed (e), and the fraction of total cloud from ERA-Interim database (f) as a function of the observation time during these two flights. Flight B896/B898 started from island at 12:37/12:01, reached its destination at 14:47/14:30, and came back to island at 17:41/16:30.	45
686			
687			
688			
689			
690			
691			
692	Fig. 10.	The ISMAR and MARSS upward brightness temperature observations for all channels as a function of the observation time for flight B896 at zenith (dotted lines). The brightness temperature simulations by ARTS are also presented (solid lines). Flight B896 started from island at 12:37, reached its destination at 14:47, and came back to island at 17:41.	46
693			
694			
695			
696	Fig. 11.	The ISMAR and MARSS downward brightness temperature observations for all channels as a function of the observation time for flight B896 at nadir (solid lines). The brightness temperature simulations are also presented for the window channels for a fixed surface emissivity of 0.5 (dashed lines) and 0.9 (solid lines). The surface skin temperatures from the ERA-Interim database are indicated in black. Flight B896 started from island at 12:37, reached its destination at 14:47, and came back to island at 17:41.	47
697			
698			
699			
700			
701			

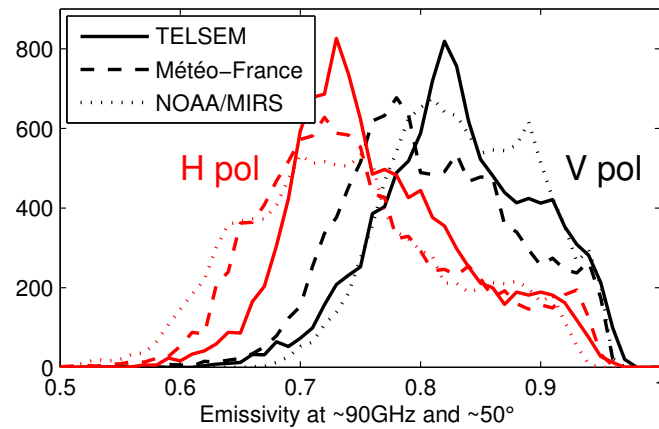
- 702 **Fig. 12.** B896 (black) and B898 (grey) flight patterns back and forth from Greenland, superposed
703 on the TELSEM² emissivities estimated at 40° for ISMAR and MARSS frequencies up to
704 325 GHz, for both sea and continental ices. The polarizations indicated in the titles are the
705 polarizations in the +50° downward view for these channels. 48
- 706 **Fig. 13.** The retrieved emissivity from MARSS and ISMAR observations for flight B896 as a func-
707 tion of latitude at 0° scan angle for 89, 118±5, 157, 183±7, 243, and 325±9.5 GHz. Top
708 two rows: on the way to Greenland. Bottom two rows: on the way back from Greenland.
709 The results from TELSEM² on March at 0° are shown for comparison. The last panel for
710 each 2 rows indicates the flight altitude and the altitude difference between the aircraft and
711 the surface. On the x axis, the solid black line indicates the presence of sea ice and the dotted
712 line corresponds to the continent. 49
- 713 **Fig. 14.** Top row : The first left panel shows the surface temperature derived directly from the air-
714 craft observations, along with the ECMWF-Interim database estimates for the flight B896
715 on the way from Greenland. The three right panels show the corresponding emissivity at
716 nadir from the aircraft measurements with the different T_s estimates, along with the corre-
717 sponding TELSEM² emissivity. On the x axis, the solid black line indicates the presence
718 of sea ice and the dotted line corresponds to the continent. Bottom row : The three panels
719 show the differences between aircraft retrieved emissivities and the TELSEM² emissivity
720 ($e(\text{various airborne})-e(\text{TELSEM}^2)$). The brown dots represent $e(\text{ECMWF})-e(\text{TELSEM}^2)$;
721 the green dots represent $e(\text{Heimann})-e(\text{TELSEM}^2)$; the orange dots represent $e(\text{ARIES})-$
722 $e(\text{TELSEM}^2)$ 50
- 723 **Fig. 15.** The retrieved emissivity from MARSS and ISMAR observations for flight B898 as a func-
724 tion of latitude on the way from Greenland at 89, 157, and 243 GHz (V and H). Top row: at
725 0° incidence angle; bottom row: at 40° incidence angle. On the x axis, the solid black line
726 indicates the presence of sea ice and the dotted line corresponds to the continent. 51
- 727 **Fig. 16.** Histograms of the emissivity differences between the aircraft-derived estimates and
728 TELSEM² results, at nadir, over continental ice during flights B896 and B898. Each chan-
729 nel is represented by a different color, and the corresponding statistics (mean and std) are
730 provided. 52



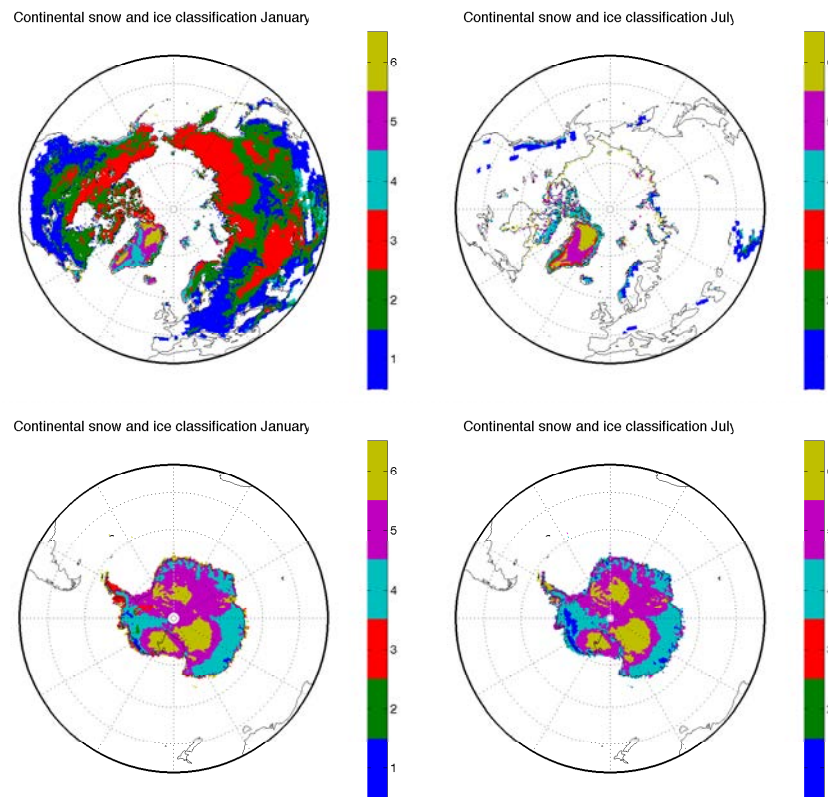
731 FIG. 1. Total transmission of the atmosphere at nadir, as calculated with ARTS, for five standard atmospheres
732 from FASCOD.



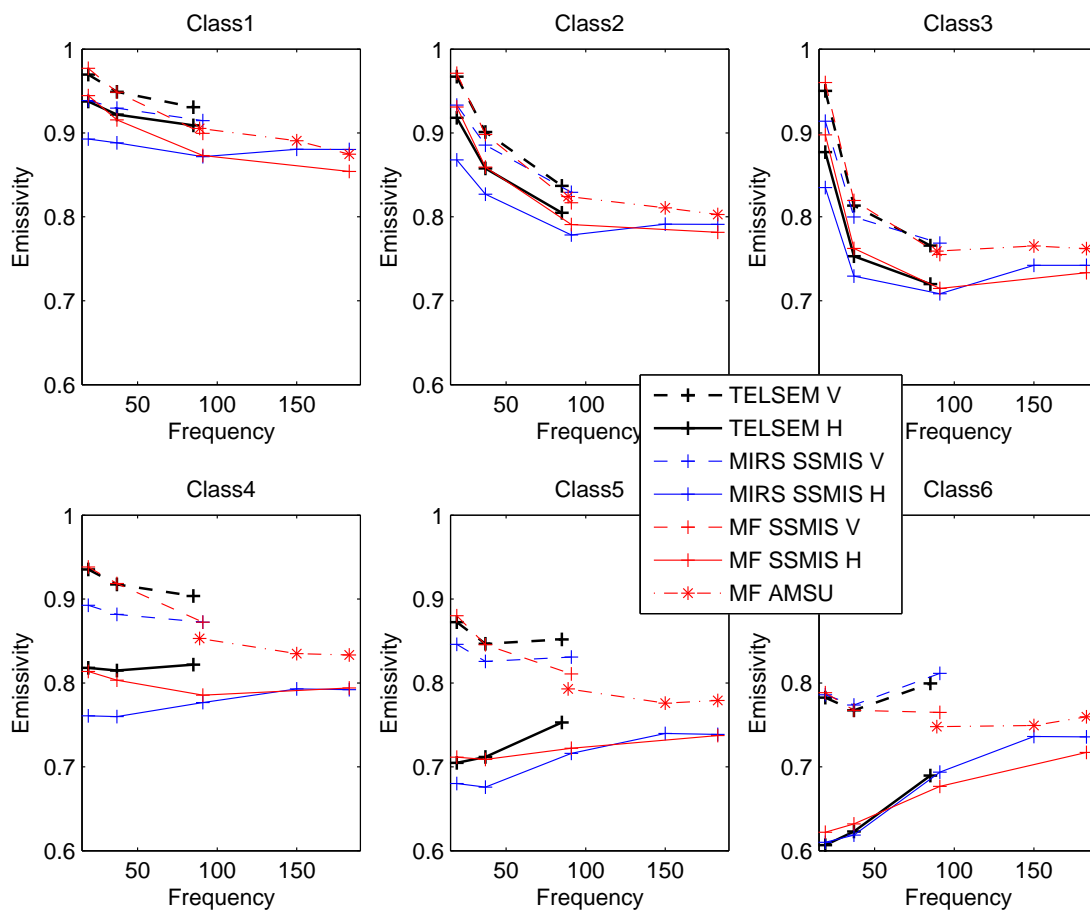
733 FIG. 2. The emissivity around 90 GHz at H polarization as calculated from the different groups on March, for
734 the North (left) and South poles (right). Top row: SSM/I (85 GHz) from TELSEM; middle row: SSMIS (91
735 GHz) from Météo-France; bottom row: SSMIS (91 GHz) from NOAA/MIRS.



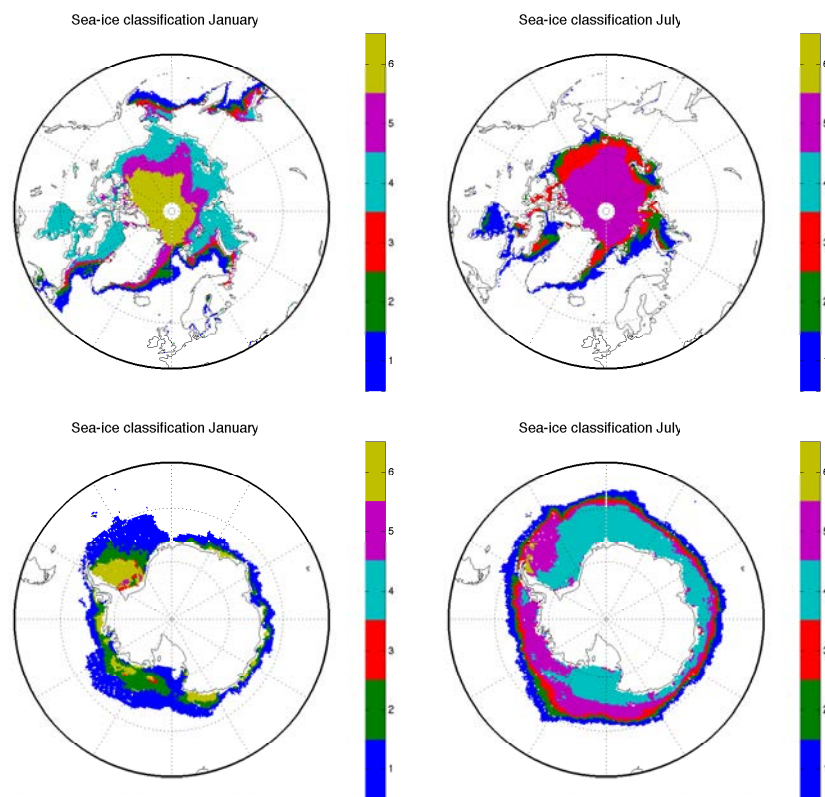
736 FIG. 3. Histograms of the emissivity around 90 GHz as calculated from the different groups (TELSEM,
737 Météo-France, and NOAA/MIRS) on March over the poles in both polarizations (V in black, H in red). Sea ice
738 surfaces are excluded.



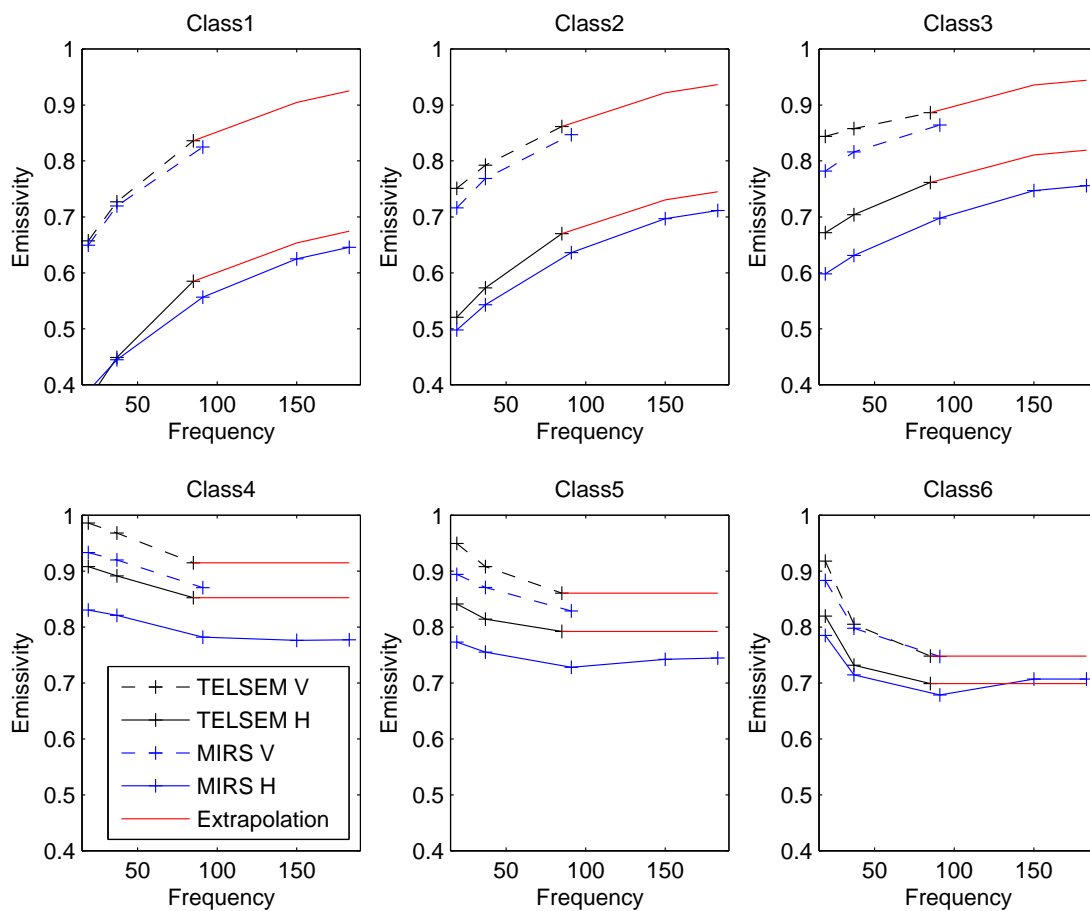
739 FIG. 4. Results of the continental snow and ice emissivity k-mean classification from SSM/I TELSEM over
740 the North pole (top) and the South pole (bottom) in January (left) and July (right). Six classes are used.



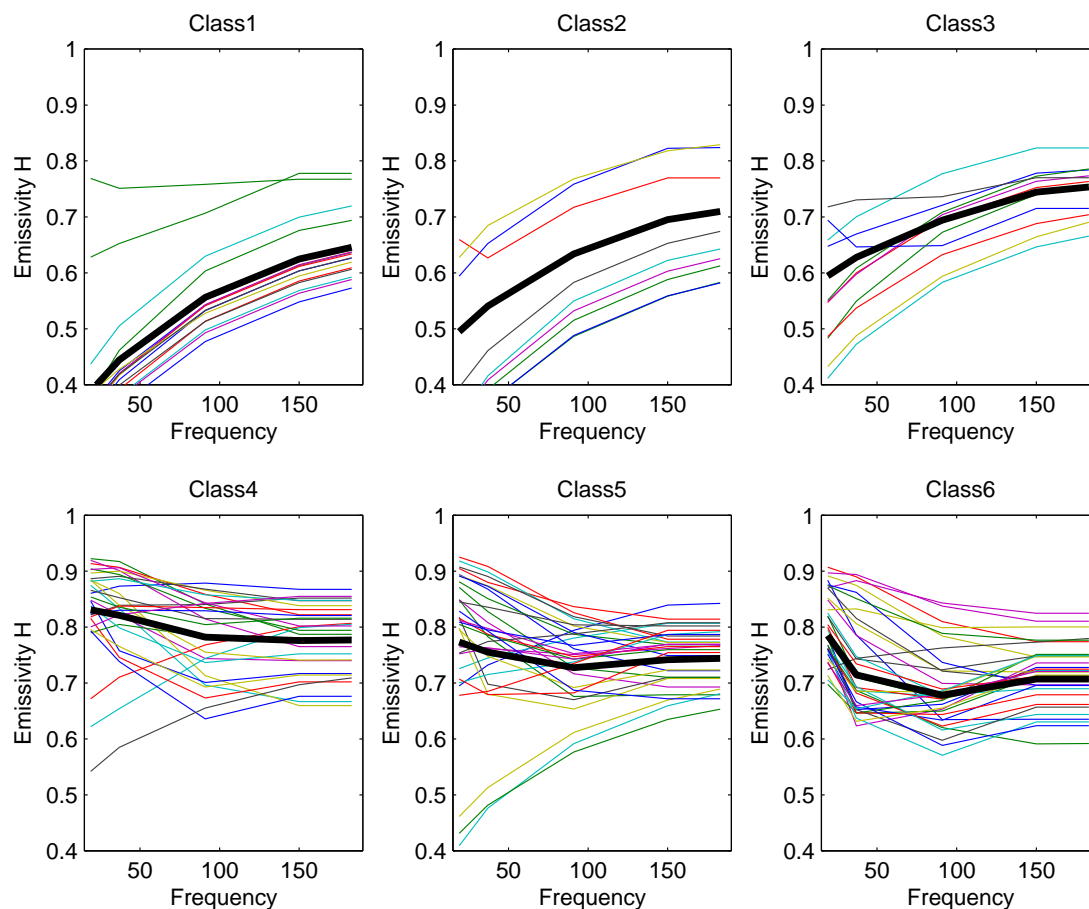
741 FIG. 5. Frequency dependence of the snow and ice emissivities, for different classes, for SSM/I TELSEM,
 742 SSMIS NOAA/MIRS, and AMSU-B and SSMIS Météo-France.



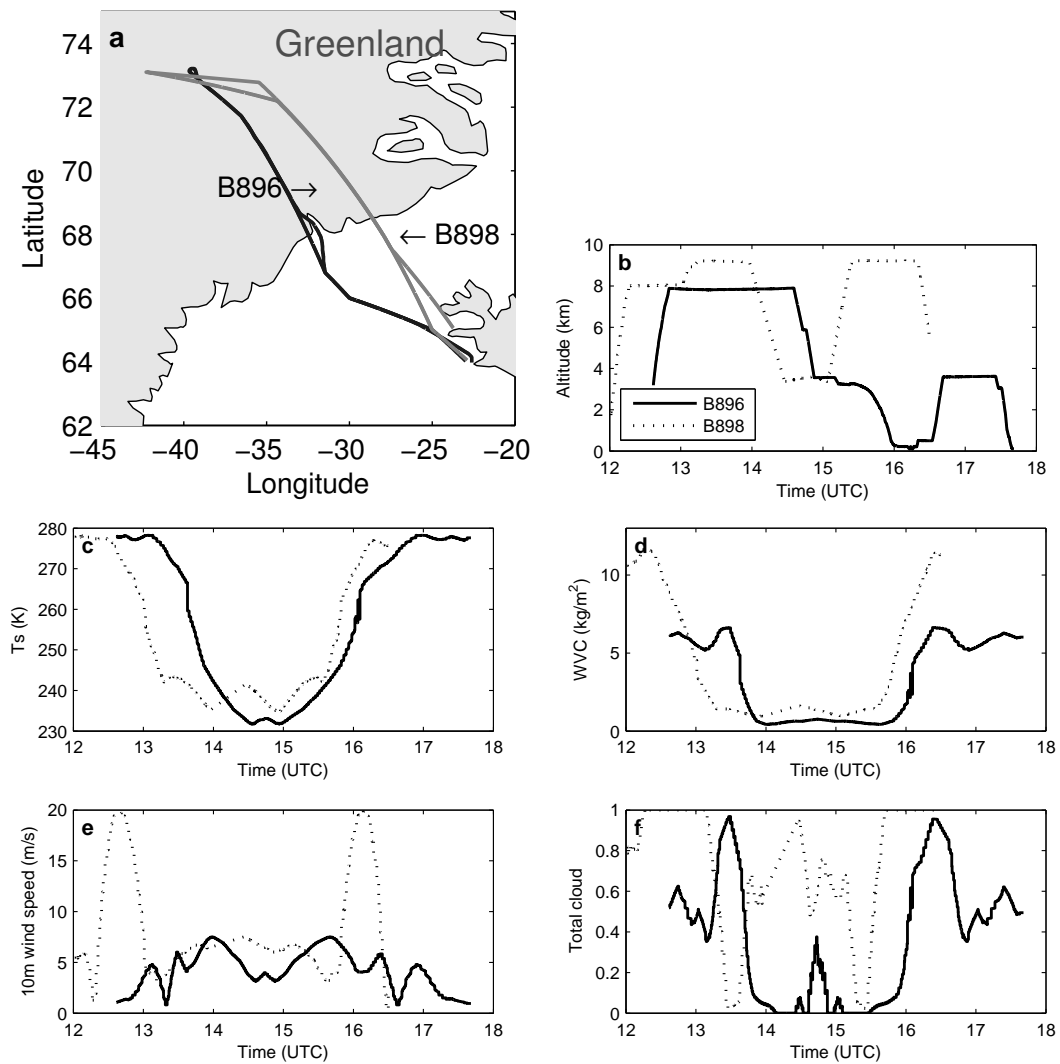
743 FIG. 6. Results of the sea ice emissivity classification from SSM/I TELSEM over the North pole (top) and
744 South pole (bottom) on January (left) and July (right).



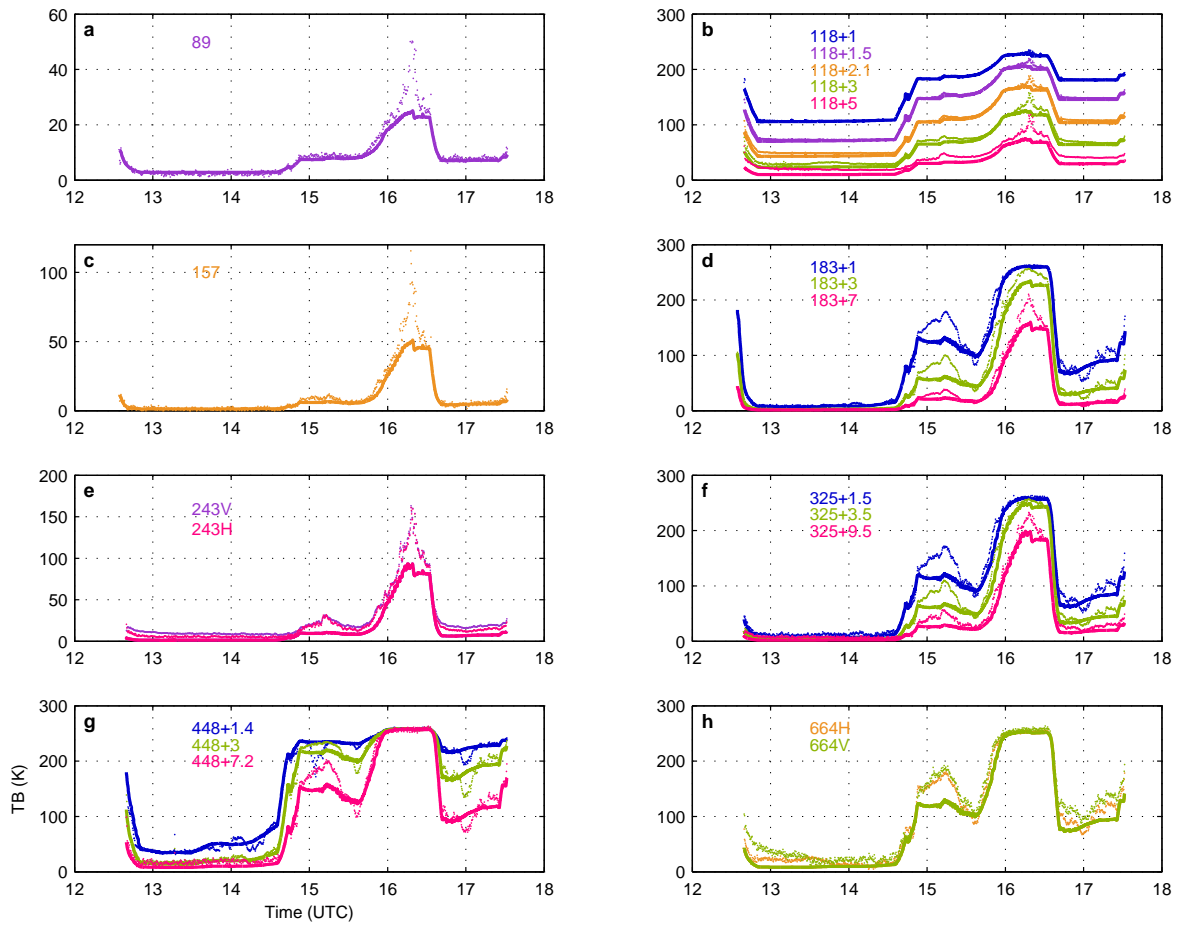
745 FIG. 7. Frequency dependence of the emissivity per sea ice class, for both V and H polarizations, from SSM/I
 746 TELSEM (in black), from SSMIS NOAA/MIRS (in blue). The suggested extrapolation of the SSM/I TELSEM
 747 is indicated in red.



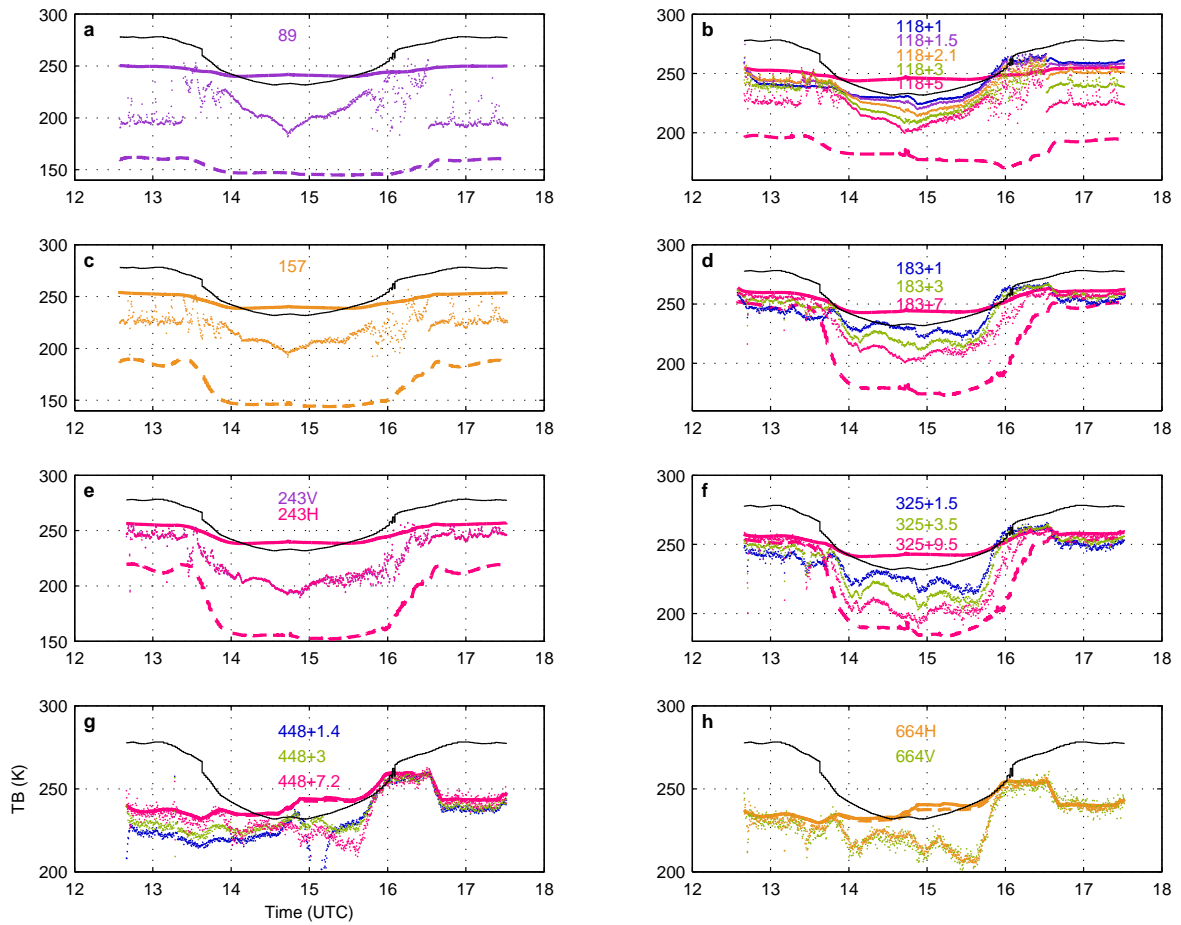
748 FIG. 8. Frequency dependence of the SSMIS NOAA/MIRS emissivities, for a few randomly selected pixels
749 per sea ice class (for H polarization only, as V polarization is not available at high frequencies). The mean
750 behavior is indicated with a thick black line.



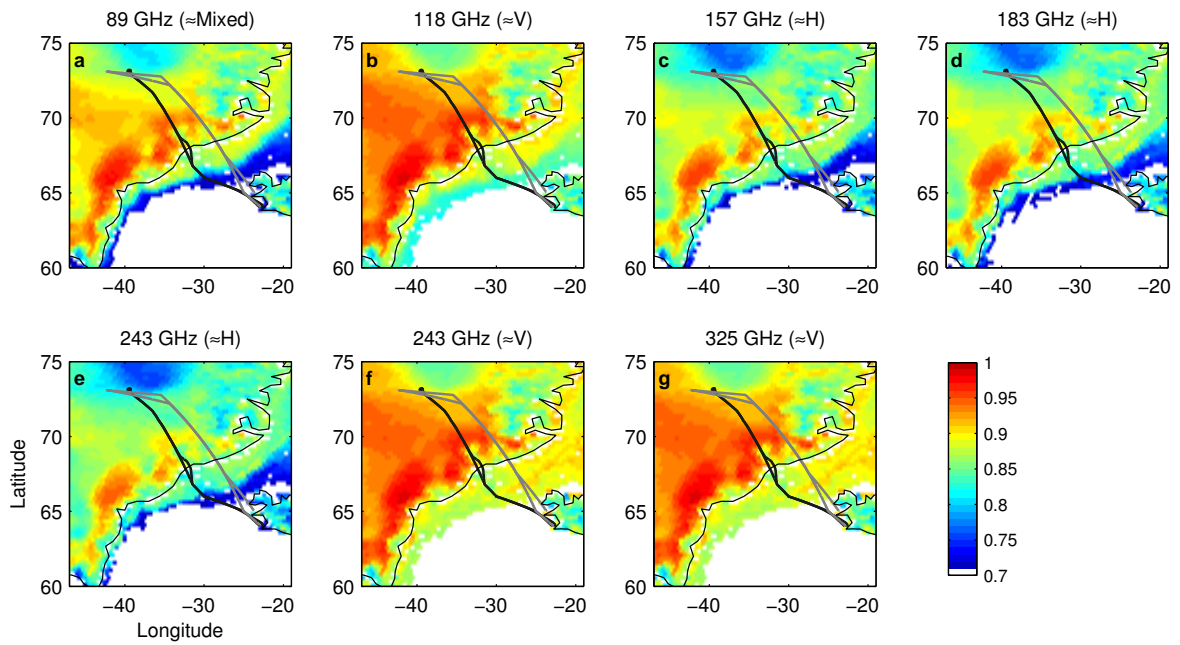
751 FIG. 9. First two rows: The flight track of flights B896 (in black) and B898 (in grey) back and forth from
 752 Greenland (a). The flight altitudes as a function of the observation time (b). Bottom two rows: The surface skin
 753 temperature (c), integrated water vapor content (d), 10-m wind speed (e), and the fraction of total cloud from
 754 ERA-Interim database (f) as a function of the observation time during these two flights. Flight B896/B898 started
 755 from island at 12:37/12:01, reached its destination at 14:47/14:30, and came back to island at 17:41/16:30.



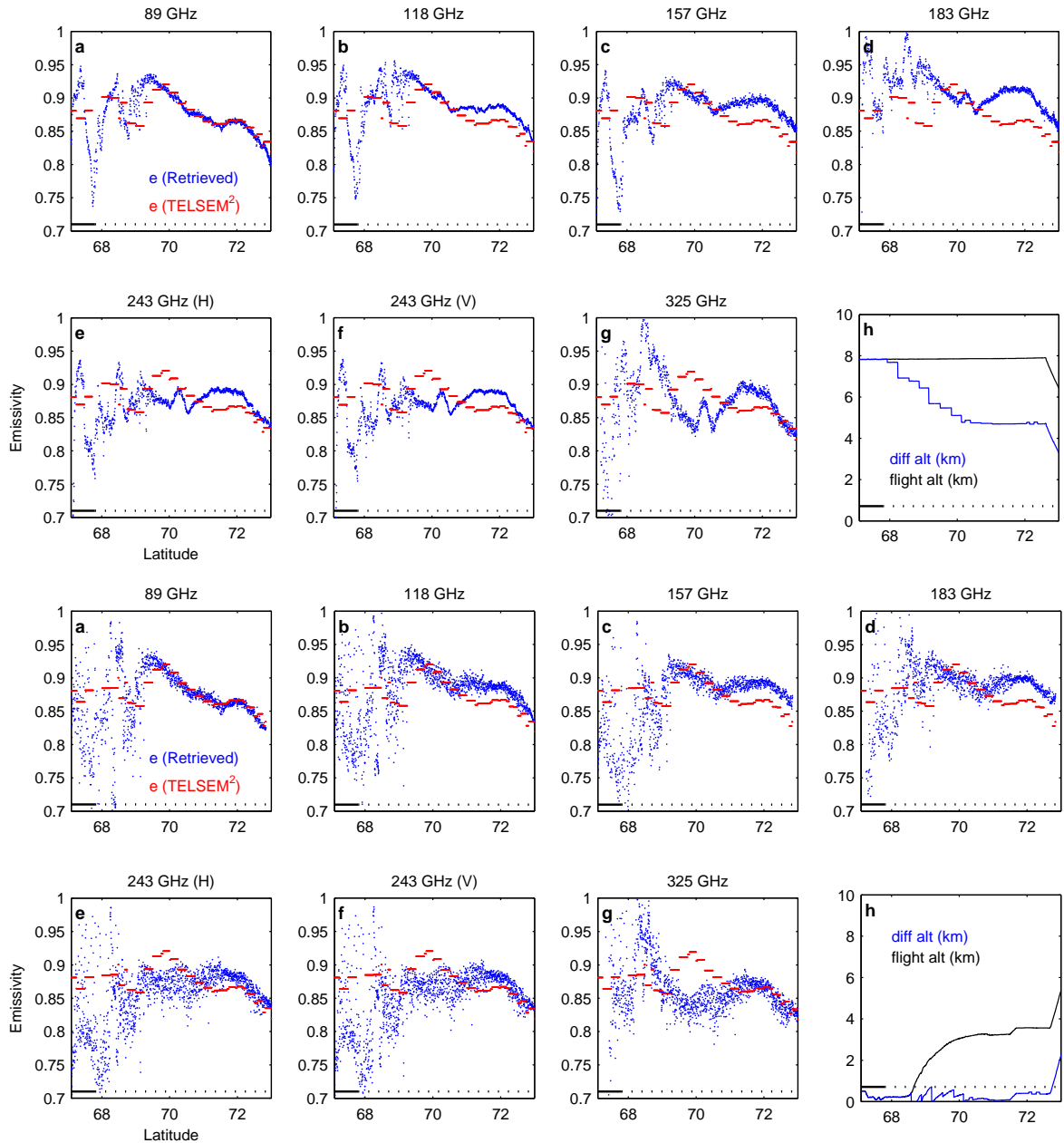
756 FIG. 10. The ISMAR and MARSS upward brightness temperature observations for all channels as a function
 757 of the observation time for flight B896 at zenith (dotted lines). The brightness temperature simulations by ARTS
 758 are also presented (solid lines). Flight B896 started from island at 12:37, reached its destination at 14:47, and
 759 came back to island at 17:41.



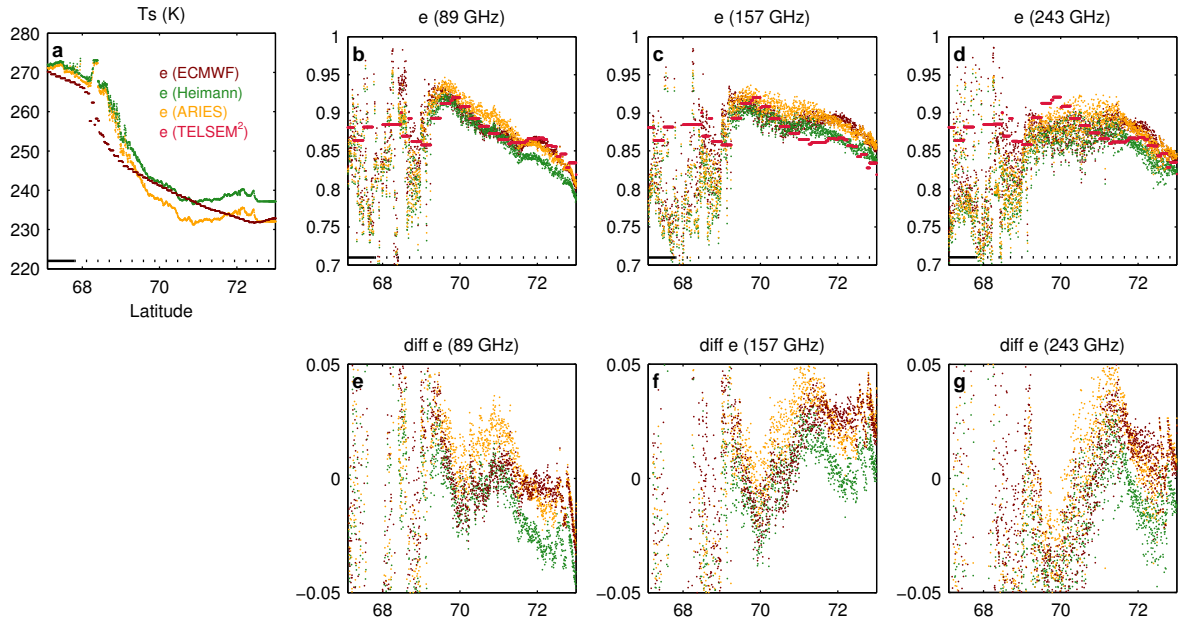
760 FIG. 11. The ISMAR and MARSS downward brightness temperature observations for all channels as a
 761 function of the observation time for flight B896 at nadir (solid lines). The brightness temperature simulations
 762 are also presented for the window channels for a fixed surface emissivity of 0.5 (dashed lines) and 0.9 (solid
 763 lines). The surface skin temperatures from the ERA-Interim database are indicated in black. Flight B896 started
 764 from island at 12:37, reached its destination at 14:47, and came back to island at 17:41.



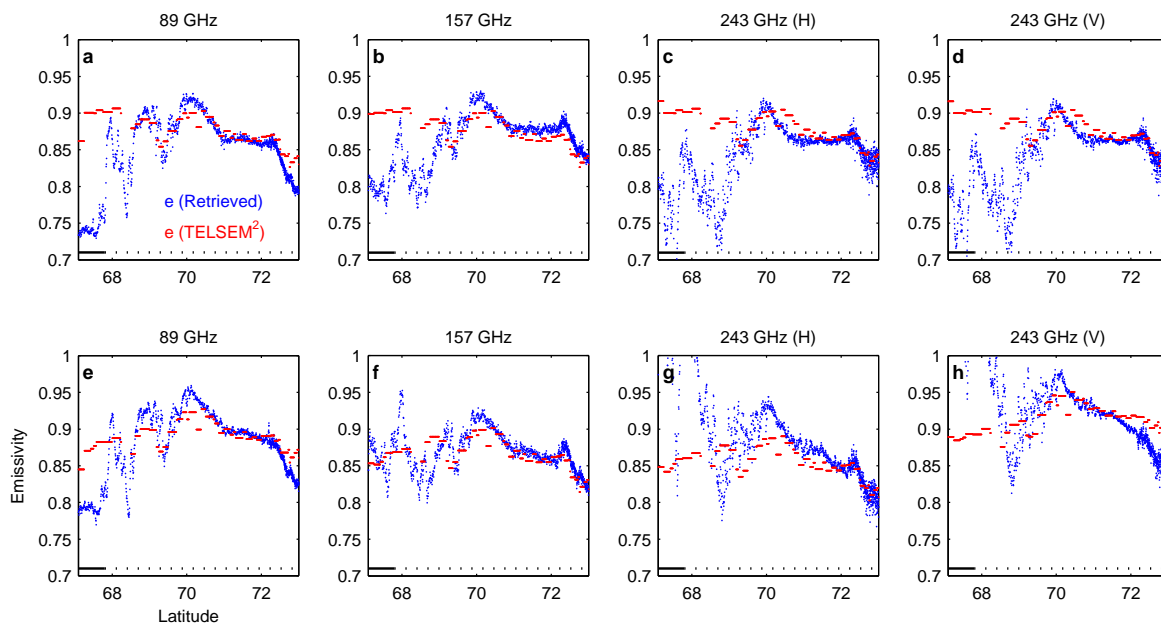
765 FIG. 12. B896 (black) and B898 (grey) flight patterns back and forth from Greenland, superposed on the
 766 TELSEM² emissivities estimated at 40° for ISMAR and MARSS frequencies up to 325 GHz, for both sea and
 767 continental ices. The polarizations indicated in the titles are the polarizations in the +50° downward view for
 768 these channels.



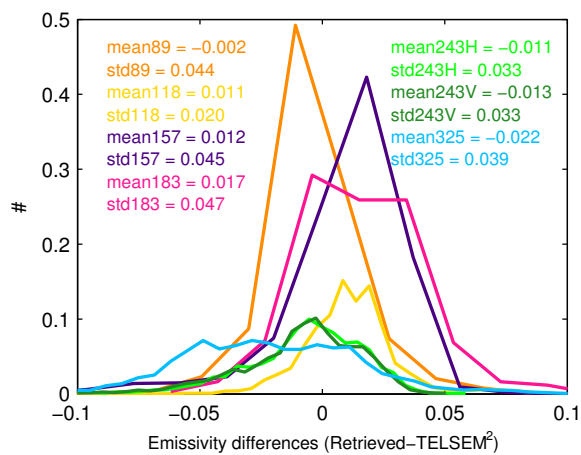
769 FIG. 13. The retrieved emissivity from MARSS and ISMAR observations for flight B896 as a function of
 770 latitude at 0° scan angle for 89, 118 ± 5 , 157, 183 ± 7 , 243, and 325 ± 9.5 GHz. Top two rows: on the way to
 771 Greenland. Bottom two rows: on the way back from Greenland. The results from TELSEM² on March at 0°
 772 are shown for comparison. The last panel for each 2 rows indicates the flight altitude and the altitude difference
 773 between the aircraft and the surface. On the x axis, the solid black line indicates the presence of sea ice and the
 774 dotted line corresponds to the continent.



775 FIG. 14. Top row : The first left panel shows the surface temperature derived directly from the aircraft ob-
 776 servations, along with the ECMWF-Interim database estimates for the flight B896 on the way from Greenland.
 777 The three right panels show the corresponding emissivity at nadir from the aircraft measurements with the dif-
 778 ferent T_s estimates, along with the corresponding TELSEM² emissivity. On the x axis, the solid black line
 779 indicates the presence of sea ice and the dotted line corresponds to the continent. Bottom row : The three panels
 780 show the differences between aircraft retrieved emissivities and the TELSEM² emissivity ($e(\text{various airborne})-$
 781 $e(\text{TELSEM}^2)$). The brown dots represent $e(\text{ECMWF})-e(\text{TELSEM}^2)$; the green dots represent $e(\text{Heimann})-$
 782 $e(\text{TELSEM}^2)$; the orange dots represent $e(\text{ARIES})-e(\text{TELSEM}^2)$.



783 FIG. 15. The retrieved emissivity from MARSS and ISMAR observations for flight B898 as a function of
 784 latitude on the way from Greenland at 89, 157, and 243 GHz (V and H). Top row: at 0° incidence angle; bottom
 785 row: at 40° incidence angle. On the x axis, the solid black line indicates the presence of sea ice and the dotted
 786 line corresponds to the continent.



787 FIG. 16. Histograms of the emissivity differences between the aircraft-derived estimates and TELSEM²
 788 results, at nadir, over continental ice during flights B896 and B898. Each channel is represented by a different
 789 color, and the corresponding statistics (mean and std) are provided.

Appendix D

Paper C: Development of ice water path retrievals at millimeter and sub-millimeter wavelengths for the Ice Cloud Imager preparation

Authors:

D. Wang, C. Prigent, F. Aires, C. Jiménez

Paper published in:

IEEE Transactions on Geoscience and Remote Sensing, 2016

Received September 12, 2016, accepted October 4, 2016. Date of publication xxxx 00, 0000, date of current version xxxx 00, 0000.

Digital Object Identifier 10.1109/ACCESS.2016.2625742

A Statistical Retrieval of Cloud Parameters for the Millimeter Wave Ice Cloud Imager on Board MetOp-SG

DIE WANG¹, CATHERINE PRIGENT¹, FILIPE AIRES¹, AND CARLOS JIMENEZ^{1,2}

¹Laboratoire d'Etudes du Rayonnement et de la Matière en Astrophysique, Observatoire de Paris, 75014 Paris, France

²Estellus, 75002 Paris, France

Corresponding author: D. Wang (die.wang@obspm.fr)

ABSTRACT The meteorological observations from satellites in the microwave domain are currently limited to below 190 GHz. The next generation of European Organization for the Exploitation of Meteorological Satellites Polar System-Second Generation will carry an instrument, the ice cloud imager (ICI), with frequencies up to 664 GHz, to improve the characterization of the cloud frozen phase. In this paper, a statistical retrieval of cloud parameters for ICI is developed, trained on a synthetic database derived from the coupling of a mesoscale cloud model and radiative transfer calculations. The hydrometeor profiles simulated with the weather research and forecasting model (WRF) for 12 diverse European mid-latitude situations are used to simulate the brightness temperatures with the atmospheric radiative transfer simulator (ARTS) to prepare the retrieval database. The WRF+ARTS simulations have been compared with the special sensor microwave imager/sounder observations up to 190 GHz: this successful evaluation gives us confidence in the simulations at the ICI channels from 183 to 664 GHz. Statistical analyses have been performed on this simulated retrieval database, showing that it is not only physically realistic but also statistically satisfactory for retrieval purposes. A first neural network (NN) classifier is used to detect the cloud presence. A second NN is developed to retrieve the liquid and ice-integrated cloud quantities over sea and land separately. The detection and retrieval of the hydrometeor quantities (i.e., ice, snow, graupel, rain, and liquid cloud) are performed with ICI-only, and with ICI combined with observations from the microwave imager (MWI, also on board MetOp-SG). The ICI channels have been optimized for the detection and quantification of the cloud frozen phase. Adding the MWI channels improves the performances of the vertically integrated content mostly for the cloud liquid phase. The relative error for the retrieved integrated frozen water content (FWP, i.e., ice+snow+graupel) is below $\sim 40\%$ for $0.1 \text{ kg/m}^2 < \text{FWP} < 0.5 \text{ kg/m}^2$ and below $\sim 20\%$ for $\text{FWP} > 0.5 \text{ kg/m}^2$.

INDEX TERMS Ice cloud imager, ice water path retrieval, radiative transfer simulation.

I. INTRODUCTION

Ice clouds play a significant role in the Earth's energy budget: they cool the atmosphere by reflecting the incoming solar radiation but also heat the atmosphere by absorbing and re-emitting outgoing infrared radiation. The ice cloud parameters such as the cloud optical thickness, the cloud altitude, and the ice particle effective radius determine their net radiative effect [1]–[3]. However, so far, we lack global measurements of these cloud parameters and there are large discrepancies in the cloud ice content predicted by the different global climate models [4], [5]. To handle this challenging issue, millimeter-wave and sub-millimeter-wave satellite observations have been suggested some time ago [6]–[8], for their sensitivity to the ice cloud parameters such as the integrated cloud ice

content, the cloud height, and the ice particle size. The visible and infrared radiometry techniques have been also studied to quantify the ice cloud properties [9], but they tend to saturate when the cloud optical thickness increases [10].

Sub-millimeter radiometers have already been launched for atmospheric chemistry (the Sub-Millimetre Radiometer (Odin-SMR) and the Earth Observing System Microwave Limb Sounder (EOS-MLS)) but in a limb-sounding mode, with coarse horizontal spatial resolution. No down-looking sub-millimeter satellite radiometer has been flown yet. The Ice Cloud Imager (ICI) will be the first instrument to equip a meteorological satellite in the millimeter to sub-millimeter wave domain [11]. It will have frequencies from 180 to 664 GHz and a conical scanning mechanism.

TABLE 1. Channel characteristics of the MWI and ICI radiometers, including their frequencies, bandWidth (BW), instrument noise (Net Δ T), polarization, and main spectral feature [11].

MWI					ICI				
Channels (GHz)	BW (GHz)	Net Δ T (K)	Polar.	Spectral feature	Channels (GHz)	BW (GHz)	Net Δ T (K)	Polar.	Spectral feature
18.7	0.2	0.7	V+H	Window	183.31 \pm 7.0	2 \times 2.0	0.7	V	H ₂ O
23.8	0.4	0.6	V+H	H ₂ O	183.31 \pm 3.4	2 \times 1.5	0.7	V	H ₂ O
31.4	0.2	0.8	V+H	Window	183.31 \pm 2.0	2 \times 1.5	0.7	V	H ₂ O
50.3	0.4	1.0	V+H	O ₂	243.2 \pm 2.5	2 \times 3.0	0.6	V+H	Window
52.61	0.4	1.0	V+H	O ₂	325.15 \pm 9.5	2 \times 3.0	1.1	V	H ₂ O
53.24	0.4	1.0	V+H	O ₂	325.15 \pm 3.5	2 \times 2.4	1.2	V	H ₂ O
53.75	0.4	1.0	V+H	O ₂	325.15 \pm 1.5	2 \times 1.6	1.4	V	H ₂ O
89.0	4.0	1.0	V+H	Window	448 \pm 7.2	2 \times 3.0	1.3	V	H ₂ O
118.7503 \pm 3.2	2 \times 0.5	1.2	V	O ₂	448 \pm 3.0	2 \times 2.0	1.5	V	H ₂ O
118.7503 \pm 2.1	2 \times 0.4	1.2	V	O ₂	448 \pm 1.4	2 \times 1.2	1.9	V	H ₂ O
118.7503 \pm 1.4	2 \times 0.4	1.2	V	O ₂	664 \pm 4.2	2 \times 5.0	1.5	V+H	Window
118.7503 \pm 1.2	2 \times 0.4	1.2	V	O ₂					
165.5 \pm 0.75	2 \times 1.35	1.1	V	Window					
183.31 \pm 7.0	2 \times 2.0	1.2	V	H ₂ O					
183.31 \pm 6.1	2 \times 1.5	1.1	V	H ₂ O					
183.31 \pm 4.9	2 \times 1.5	1.1	V	H ₂ O					
183.31 \pm 3.4	2 \times 1.5	1.1	V	H ₂ O					
183.31 \pm 2.0	2 \times 1.5	1.2	V	H ₂ O					

It will fly on the future generation of European Meteorological Operational satellites, MetOp-SG, to be launched in 2021 / 2022. The same platform (MetOp-SG-B) will also embark another MicroWave Imager (MWI) measuring at lower frequencies from 18 to 183 GHz. A MicroWave Sounder (MWS) will also be placed on the MetOp-SG suite at frequencies from 23 to 230 GHz, but on MetOp-SG platform A. The ICI and the MWI channel characteristics are presented in Table 1.

In preparation for the exploitation of the millimeter to sub-millimeter wave observations from satellites, statistical methodologies have been developed to estimate the ice cloud quantities. [12] retrieved the integrated cloud ice content, the cloud ice median mass equivalent sphere diameter, and the median cloud ice mass height, using two different training databases. The databases were derived from radiative transfer simulations applied to atmospheric profiles from the Atmospheric Radiation Measurements (ARM) program with the addition of randomly generated cloud quantities [13] for one, and from profiles combining Cloudnet radar data and European Center for Medium range Weather Forecasting (ECMWF) analysis [14] for the other. This work illustrated the sensitivity of the ICI frequencies to the cloud parameters, with a theoretical accuracy of 20% / 17% (median relative error) for IWP for a mid-latitude winter/tropical scenario.

In this study, our objective is to design a statistical retrieval algorithm to extract primarily the cloud ice parameters, based on an extensive database of simulations provided by realistic atmospheric scenarios over Europe. Statistical retrieval techniques are prone to very optimistic results when tested

without caution so we pay extra attention here to the robustness of our results: physical realism of the used databases, statistical representativity of the databases, and avoiding over-training phenomenon where the algorithm is able to perform well on the training dataset but unable to generalize on new data. Our analysis involves first the ICI instrument, but the methodology is also applied to the combination of the ICI and MWI channels to evaluate their potential synergy. The atmospheric profiles, clear and cloudy, are provided by a cloud resolving model. This ensures physical consistency among the different parameters. The Weather Research and Forecasting model (WRF) model is selected and run for a collection of diverse real cases over Europe. Radiative transfer simulations are performed on the resulting atmospheric profiles, using the Atmospheric Radiative Transfer Simulator (ARTS) along with carefully selected scattering properties of the hydrometeors. The database generation is described in Section II. The simulations are systematically compared to collocated Special Sensor Microwave Imager / Sounder (SSMIS) satellite observations below 200 GHz and the statistical representativity of the database is tested (also in Section II). Then statistical methods are developed, first to detect the clouds, second to quantify the cloud parameters, based on NN methodologies (Section III). Finally, Section IV concludes this study.

II. PREPARATION AND EVALUATION OF THE RETRIEVAL TRAINING DATABASE

Figure 1 presents the different steps to build the retrieval training database, along with the relevant tools. First, twelve diverse meteorological situations are collected to cover as well as possible the variability of the European situations, in

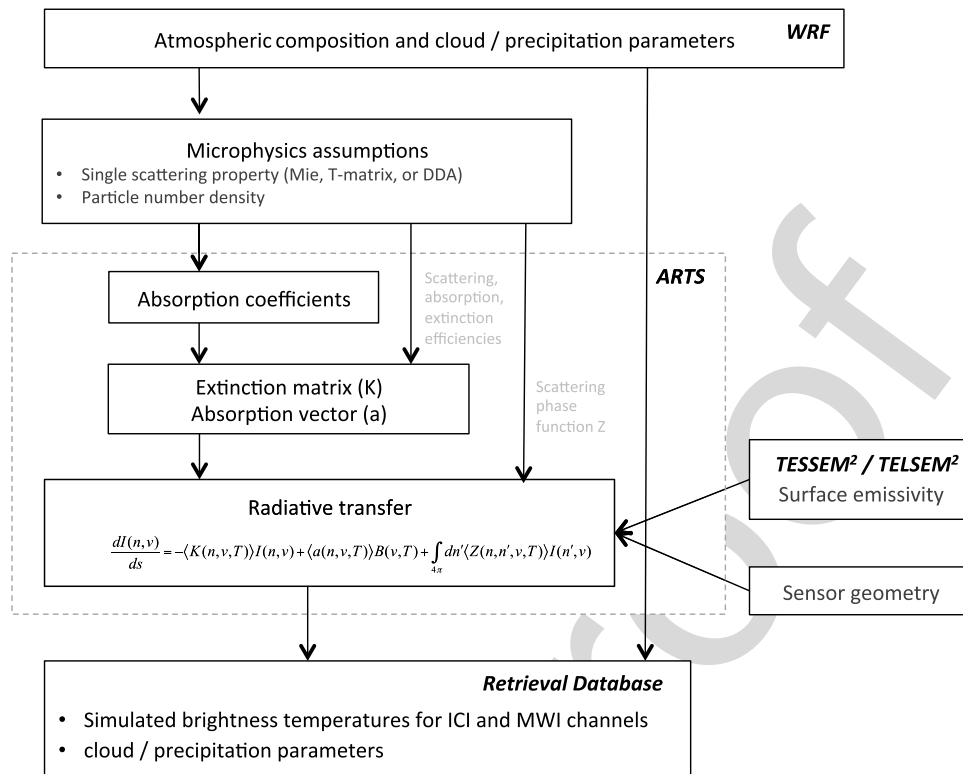


FIGURE 1. Schematic diagram showing the main necessary elements to prepare the retrieval training database.

terms of cloud parameters. These cases have been selected by considering the important atmospheric features associated with main weather systems across Europe (e.g., the Azores High, the Icelandic Low, the North Atlantic Oscillation, and the Siberian Anticyclone), for their different locations in Europe, their different seasons, their different synoptic backgrounds (both ocean and land cases), and their content of different precipitation types (convective, stratiform, and orographic precipitations), in order to meet the diversity requirement for the statistical training of the retrieval. Furthermore, we also checked that the selected scenes were observed by the SSMIS instrument, for comparison of the simulations with the satellite observations below 200 GHz. The meteorological cases are described in Table 2.

Here we present the tools that are implemented to generate the retrieval database, including the cloud resolving model (Section II-A) and the radiative transfer code (Section II-B). Coupling the cloud resolving model and the radiative transfer simulator requires specific care to maintain consistency between the cloud particles generated by the cloud resolving model and their scattering properties. The assumptions on the microphysical properties in the cloud resolving model and the calculation of the single scattering properties are discussed (in Section II-C).

A. THE CLOUD RESOLVING MODEL WRF

The WRF [15] version 3.5.1 with the ARW (Advanced Research WRF) dynamic core is used to generate realistic

atmospheric profiles and microphysical cloud parameters. WRF is a mesoscale numerical weather prediction system designed for both atmospheric research and operational forecasting needs. It is composed of a fully compressible and non-hydrostatic dynamical Euler core, with a terrain-following coordinate. In this study, the initial and lateral boundary conditions in WRF were obtained from the National Center for Environment Prediction (NCEP) Final Analysis (FNL) data every six hours. Two domains were selected for all the simulations, with 9 and 27 km horizontal grid spacing in the inner and the outer domains, respectively. The atmospheric fields in the inner domain with its 9 km resolution are compatible with the ICI horizontal resolution (16 km) and are used as inputs for the radiative transfer simulations. 104 vertical levels are defined from the surface to 50 hPa, with 20 levels within the lowest 2 km to better capture the characteristics of the planetary boundary layer. The spin-up times are at least 16 h. All the simulations were treated by the Noah 4-layer land surface model [16], the Monin-Obukhov surface scheme [17], the Yonsei University (YSU) planetary boundary layer scheme [18], the Rapid Radiative Transfer Model (RRTM) longwave radiative simulation [19], the Dudhia shortwave radiative simulation [20], and the Kain-Fritsch cumulus scheme [21].

Microphysical processes in the clouds control the formation, the growth, and the interactions of liquid droplets and frozen particles [22]. Furthermore, cloud microphysical processes interact with the macrophysics modules in the cloud

TABLE 2. Description of the 12 cases selected for the development of the retrieval database.

Name	Time	Description
C1	07/02/2007	Poland: A strong convective storm cell grew over the Sudety Mountains in Poland and expanded rapidly with wind speeds up to 90 km/h. The severe weather mainly took place in south-western and center Poland.
C2	03/01/2008	Central Europe: A severe extra-tropical cyclone named Emma was formed in the North Atlantic, passing northern UK on February 29, and arriving in Central Europe (e.g., Austria, Germany, Poland and the Czech Republic) on March 1st where winds reached up to 166 km/h (103 mph).
C3	05/20/2008	Hungary: A rapid tornado thunderstorm (2 hours) developed over Hungary inducing severe precipitation, hail (2-5 cm), even flash floods in several regions. This storm was defined as a cold-ring shaped supercell over Hungary and Serbia.
C4	12/08/2010	France: Huge plunges in the jet-stream allowed cold waves to build over Europe for the past few weeks, laying the groundwork for winter storms with heavy snowfall. An exceptionally heavy afternoon snowstorm hit France, inducing 11 cm of snow in Paris.
C5	08/18/2011	Belgium: An extremely severe thunderstorm system developed over Belgium, with particularly strong downdraft. It initiated over France around 12 UTC as a shallow low, and then deepened and propagated over Belgium, Netherlands and Germany.
C6	11/05/2011	Mediterranean: A typical extratropical system initiated in the Atlantic Basin and slowly moved westwards crossing Spain and the Balearic Islands. When it arrived over the Mediterranean Sea, the cut-off lows and warmer surface made it strengthen and transform into a tropical-like storm.
C7	06/28/2012	UK: A series of thunderstorms occurred across the UK, induced by a double structured cold front over western and northern parts of UK. Two tornadoes were observed in the Midlands. Exceptionally large hailstones were seen in Talgarth and Glasbury.
C8	09/12/2012	Italy: This case caused more than 100 mm of daily rainfall. The heavy rain and hail were associated with severe convective storms during two episodes. The first thunderstorm initiated and matured from 8 to 10 UTC, while from 15 to 19 UTC for the second one along the North Adriatic coast.
C9	08/26/2012	Italy: A cold front invaded western Europe on August 25, and passed the Alps region one day after. It went on through Poland, Slovakia, Hungary, northern Italy, Slovenia and western Balkan. Large hails and severe winds occurred in the Po Valley and along the Adriatic coast of Italy.
C10	11/20/2013	France: A remarkable snowfall was maintained for 24 hours by a depression fed by a flux from the Mediterranean at high altitudes with a wind draft from north in the lower layers. The orange alert was maintained for five departments since November 20 in the morning and extended to twenty other regions.
C11	01/19/2013	Portugal: An extreme windstorm (Gong) influenced the Portuguese coasts, with a central lowest pressure of 968 hPa and wind gusts of 140 km/h. This windstorm developed explosively between the Azores and the Iberian Peninsula, with the help of the southerly movement of the polar jet-stream.
C12	10/27/2013	UK: The St. Jude storm (Cyclone Christian), a severe European windstorm, formed in the western Atlantic on October 26, 2013, and strengthened under a strong jet-stream with incoming tropical airflow. The center low rapidly developed and intensified as it crossed the North Sea. The wind speed was up to 194.4 km/h on October 28 and the lowest pressure was 967.6 hPa.

model through the latent heating/cooling, the condensate loading, the surface mechanisms, and the radiative transfer processes, all very challenging to parameterize [23], [24]. A number of bulk microphysical schemes are available in WRF V3.5.1 to parameterize the cloud microphysical processes, including single- and double-moment approaches. The single-moment microphysical schemes predict the mixing ratio of each hydrometeor, while the double-moment schemes also provide the number concentrations for some hydrometeor species [25], [26]. However, information about key parameters controlling the scattering properties, namely the particle sizes, their density, or shape, are still largely simplified in all schemes.

In this study, the WRF Single Moment - 6 class (WSM6) [27] microphysical scheme has been selected after several tests: it provides robust results and runs fast enough. This scheme has been developed primarily by [28] and [29]. It includes a temperature dependent intercept parameter for snow, the auto-conversion of cloud water to rain, and the inclusion of sedimentation of ice particles [27], [30]. It predicts the mixing ratios of five hydrometeors (cloud ice, snow, graupel, rain, and cloud water). The major characteristics of

each hydrometeor type (Particle Size Distribution (PSD) and density) are indicated in Table 4.

The WRF configurations for the 12 selected cases are detailed in Table 3. The rainfall rate and the surface pressure pattern from WRF are shown in Figure 2 for the 12 cases at the SSMIS overpass times (indicated in the figure caption). The synoptic situations of these events show a large variability including extratropical cyclones (e.g., cases 2 and 12), tropical-like cyclones (e.g., case 6), cold fronts (e.g., case 9), and mesoscale convective systems (e.g., case 8), covering different ranges of precipitation (larger in cases 6, 7, and 11, smaller in cases 4 and 5). The histogram of the vertically integrated hydrometeor contents (i.e., Ice Water Path (IWP), Snow Water Path (SWP), Rain Water Path (RWP), Graupel Water Path (GWP), and Cloud Water Path (CWP)) are displayed in Figure 3. The different scenes show very variable distributions of cloud hydrometeor contents, especially for the SWP which has a large dynamical range (maximum values of SWPs between 1.5 and 4.5 kg/m²).

Note that in the literature, the IWP can represent the total integrated content of the frozen quantities in the cloud (ice, snow, graupel, as used in the introduction of this paper) or

TABLE 3. The WRF model configurations and the Special Sensor Microwave Imager / Sounder (SSMIS) overpass times for the 12 cases. The coordinated Universal Time (UTC) is used here.

Case	C1		C2		C3		C4	
Domains	D1	D2	D1	D2	D1	D2	D1	D2
Start time	07/02/07 00:00		03/01/08 00:00		05/19/08 12:00		12/07/10 12:00	
End time	07/04/07 00:00		03/03/08 00:00		05/21/08 12:00		12/09/10 12:00	
Grid points	100×100	142×142	90×90	121×121	100×100	106×88	100×100	124×124
Center	51°N, 15°E		45°N, 23°E		44°N, 18°E		50°N, 4°E	
OBS time	07/02/07 18:13		03/01/08 17:21		05/20/08 04:52		12/08/10 16:43	
Case	C5		C6		C7		C8	
Domains	D1	D2	D1	D2	D1	D2	D1	D2
Start time	08/18/11 00:00		11/05/11 00:00		06/28/12 00:00		09/12/12 00:00	
End time	08/20/11 00:00		11/07/11 00:00		06/30/12 00:00		09/14/12 00:00	
Grid points	100×100	100×100	120×120	169×169	110×110	172×172	100×100	112×112
Center	52°N, 6°E		43°N, 5°E		55°N, 5°W		45°N, 23°E	
OBS time	08/18/11 17:00		11/05/11 17:01		06/28/12 17:15		09/12/12 16:07	
Case	C9		C10		C11		C12	
Domains	D1	D2	D1	D2	D1	D2	D1	D2
Start time	08/26/12 00:00		11/20/13 00:00		01/18/13 00:00		10/26/13 00:00	
End time	08/28/12 00:00		11/22/13 00:00		01/20/13 00:00		10/28/13 00:00	
Grid points	120×90	160×148	100×100	112×112	100×100	136×136	100×100	106×106
Center	45°N, 15°E		50°N, 2.5°E		42°N, 6°W		54°N, 5°W	
OBS time	08/26/12 16:22		11/20/13 17:05		01/19/13 07:19		10/26/13 17:28	

TABLE 4. The particle size distribution (PSD), the intercept parameter, the slope parameter, and the particle density of each predicted hydrometeor in the WRF Single-Moment 6-Class Microphysics Scheme (WSM6, [27]). T is the air temperature in K; T_0 is the temperature of the triple point of water in K; D is the equivalent spherical diameter in m ; ρ is the particle density in kg/m^3 ; ρ_a is the air density in kg/m^3 ; q is the hydrometeor mixing ratio in kg/kg .

Hydrometeor	PSD ($/m^3$)	Intercept parameter ($/m^4$)	Slope parameter ($/m$)	Density (kg/m^3)
Rain	$N(D) = n_0 e^{-\lambda D}$	$n_0 = 8 \times 10^6$	$\lambda = (\pi \rho n_0 / \rho_a q)^{1/4}$	1000
Snow	$N(D) = n_0 e^{-\lambda D}$	$n_0 = 2 \times 10^6 e^{0.12(T-T_0)}$	$\lambda = (\pi \rho n_0 / 6 \rho_a q)^{1/4}$	100
Cloud water	$N = 1 \times 10^8$			1000
Cloud ice	$N(D) = 5.38 \times 10^7 (2.08 \times 10^{22} D^8)^{0.75}$			916
Graupel	$N(D) = n_0 e^{-\lambda D}$	$n_0 = 4 \times 10^6$	$\lambda = (\pi \rho n_0 / \rho_a q)^{1/4}$	500

only the ice particles. In the following, the IWP will represent the integrated content of the small ice particles, and the integrated content of all frozen quantities will be noted Frozen Water Path (FWP=IWP+SWP+GWP).

B. THE RADIATIVE TRANSFER MODEL ARTS

The radiative transfer simulations in the microwave and sub-millimeter wave range can be performed with ARTS [31]. This state-of-the-art model can solve the scattering radiative transfer with the Discrete Ordinate Iterative (DOIT) [32] method (adopted for the 1-dimension (1D) simulations) or the reverse Monte Carlo (MC) [33] method (for the 3D cases). In this study, a 3D atmosphere is simulated by WRF and therefore, the MC method is used for the radiative transfer simulation. The [34] gas absorption model is selected to calculate the absorptions of water vapor, oxygen, and nitrogen in all the simulations. Note that the choice of the absorption model may induce uncertainties in the radiative transfer simulations, especially at high frequencies. However, the uncertainties related to WRF modeling of the ice phase and to the simulations of the scattering properties in the radiative transfer will clearly dominate the error budget. Realistic surface emissivities are needed for the full frequency range. They are derived from the recently developed TELSEM² (Tool to Estimate Land Surface Emissivity from Microwave to sub-Millimeter waves, [35]) over land and TESSEM² (Tool to Estimate Sea Surface Emissivity from Microwaves to

sub-millimeter waves, [36]) over sea: these emissivity parameterizations provide surface emissivities up to 700 GHz, for all surface types.

C. SELECTION OF THE HYDROMETEOR SCATTERING PROPERTIES

Uncertainties in the description of the physical properties of the frozen particles (e.g., particle size, density, and shape) can lead to large uncertainties in the simulated brightness temperatures, and consequently large discrepancies with the satellite observations. The sensitivity of the radiative transfer simulations to the hydrometeor microphysical parameters has already been discussed and tested by comparison with available passive and active microwave observations up to 200 GHz (e.g., [37]–[41]). The hydrometeor Single Scattering Properties (SSP) are very sensitive to the hydrometeor microphysical parameters, especially their sizes and dielectric properties. For the frozen particle, the dielectric property strongly depends upon the particle density, from pure ice (density of 916 in kg/m^3) to light snow flakes (density below 100 in kg/m^3). In this study, the SSPs of the hydrometeors will be calculated using the Mie theory for spherical particles, except for snow. For liquid particles (cloud water and rain), and for frozen particles such as cloud ice and graupel, these assumptions have proved realistic [38], [39]. However, for snow, the Mie calculation has shown limitations [39], [41], with the difficulty to account for the ‘soft’ nature of the

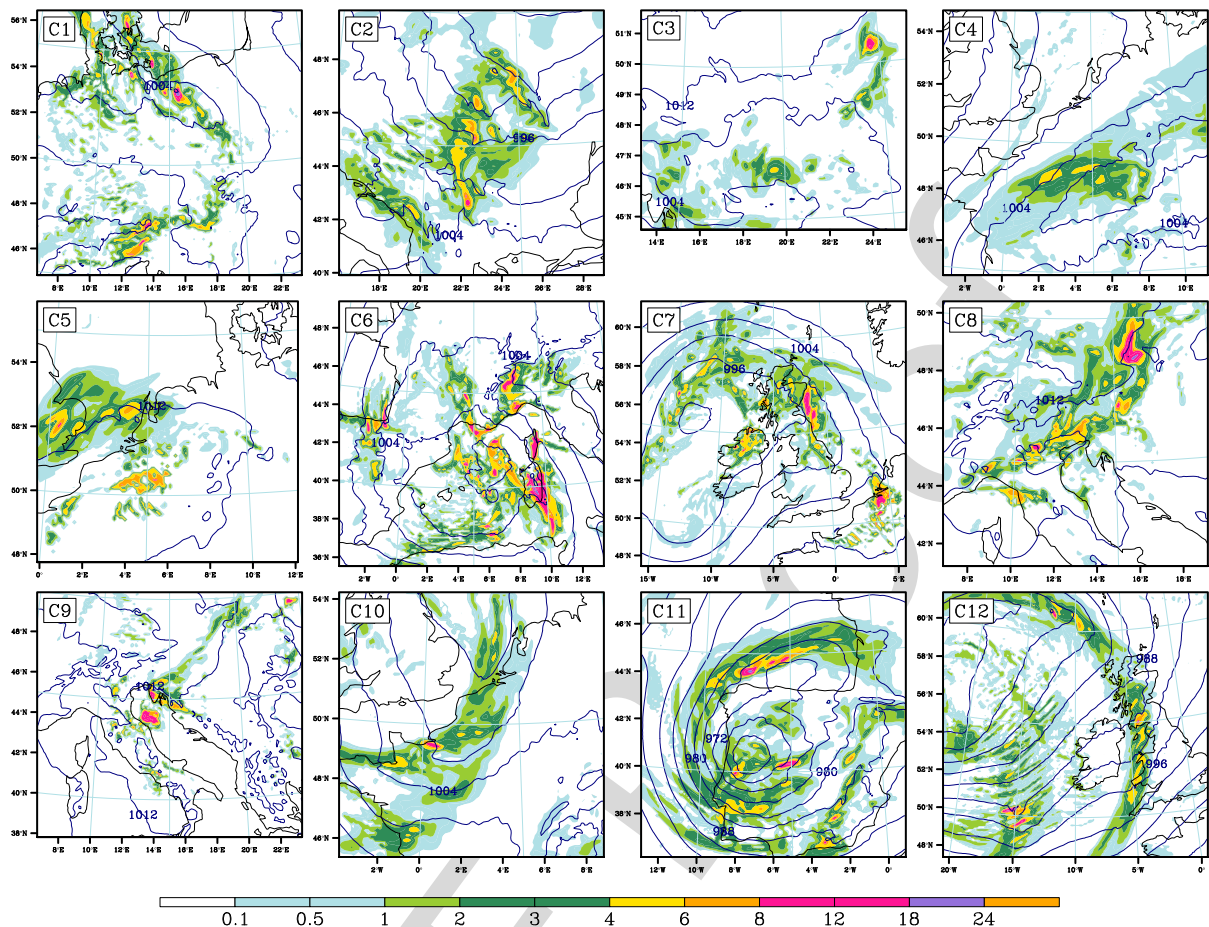


FIGURE 2. The surface rainfall rate (mm/h , shaded) and the surface pressure (hPa , contour) for all the 12 cases around the SSMIS overpass times. The SSMIS over-passed C1 at 18:13, July 02, 2007, C2 at 17:21, March 01, 2008, C3 at 04:52, May 20, 2008, C4 at 16:43, December 08, 2010, C5 at 17:00, August 18, 2011, C6 at 17:01, November 05, 2011, C7 at 17:15, June 28, 2012, C8 at 16:07, September 12, 2012, C9 at 16:22, August 26, 2012, C10 at 17:05 at November 20, 2013, C11 at 07:19 January 19, 2013, and C12 at 17:28 October 26, 2013. All times are in UTC. The WRF outputs are given at the closest full hour.

particles [42]. Lately, the Discrete Dipole Approximation method (DDA) [43] has been widely investigated to calculate the SSPs of frozen particles (e.g., [42], [44]–[47]), due to its flexibility regarding frozen particles with arbitrary and complex geometries. DDA calculations are very time consuming and several pre-computed DDA databases for frozen particles of different shapes are available [42], [45], [48]–[50], which can be incorporated directly into the radiative transfer models (e.g., ARTS). The [50] database will not be analyzed here as it does not provide the phase function. The [48] database contains 11 randomly oriented frozen particle habits (see Table 5), for frequencies from 13.4 to 340 GHz. The ice refractive indices are taken from [51] at temperatures between 273.15 K and 233.15 K. The [49] database is also tested, with its six randomly oriented non-spherical frozen particles at frequencies from 89 to 874 GHz. The ice refractive indices are from [52] at 243.15 K. These DDA datasets are calculated for a range of particle sizes, with specific assumptions on the par-

ticulate shape and density (see Table 5). Are the DDA hypotheses compatible with the cloud model parameterization? In order to choose a DDA database, we test the compatibility of the hypotheses adopted in the cloud model and in the DDA. The snow particle densities in the WSM6 scheme and in the DDA databases are compared in Figure 4, as a function of the particle maximum diameter (D_{max}). The snow density shows a considerable variability depending on the particle type and the database. The density of the [49] aggregates is closer to the one given in the WSM6 scheme, providing more consistency with the cloud model outputs. Therefore, the [49] DDA database for aggregates is used to provide the SSPs for snow particles between 89 and 664 GHz in this study. At lower MWI frequencies, the SSPs for snow are calculated with the Mie theory for spheres, with the scattering becoming negligible in this frequency range. This database have been also selected by [47] for its better performances as compared to other DDA databases. Up to now, note that modeling of

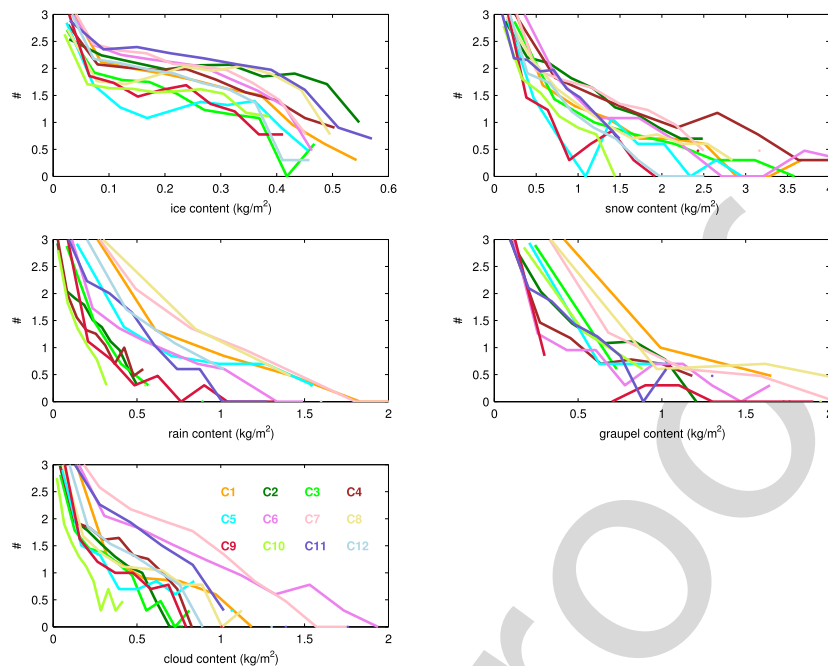


FIGURE 3. Histograms of ice water path (IWP), snow water path (SWP), rain water path (RWP), graupel water path (GWP), and cloud water path (CWP) from the WRF model for the 12 cases around SSMIS over-pass times. The y-axis is in log10.

the scattering properties with DDA methodology does not provide polarization information. Studies are underway to account for the orientation of particles in the DDA calculation, as the polarization information can provide additional information on the ice particle habits (shape and orientation), as discussed in [40], [53], and [54].

D. EVALUATION OF THE SIMULATION DATABASE BELOW 200 GHz

The WRF / ARTS simulations described above represent real meteorological cases and have been selected to correspond to SSMIS overpass times. The simulations are thus evaluated by comparisons with the SSMIS observations for the frequencies from 89 to 183 GHz.

Figure 5 shows the observed and the simulated brightness temperatures at 6 SSMIS channels, for two meteorological situations (cases 7 and 11). At all frequencies, the spatial structures of the observations are fairly well reproduced by the coupled WRF / ARTS simulations. At 89 GHz horizontal polarization, the emission from the cloud liquid phase is clearly observable over the cold oceanic background (the emissivity over ocean is significantly lower than over land). At this frequency, the good agreement between the simulations and the observations suggests that the liquid cloud characteristics have been correctly modeled by WRF and that TELSEM² and TESSEM² generate realistic surface emissivities. At 150 GHz, the observed brightness temperature depressions related to the scattering effect of the cloud frozen particles is also well reproduced by the simulations, implying that the parameterization of cloud frozen quantities

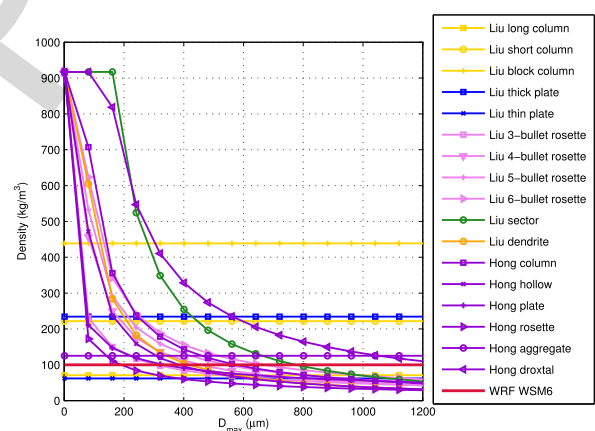


FIGURE 4. Particle densities derived from Liu and Hong DDA databases and the WRF WSM6 scheme as a function of particle D_{max} .

from WRF is realistic, as well as the selected scattering assumptions. In the three channels located in the water vapor absorption line at 183.3 GHz (183.3 ± 1 , ± 3 , and ± 7 GHz), the water vapor absorption tends to mask the cloud emission and scattering as well as the surface contribution, with the extent of the masking depending on the spectral distance from the center of the absorption line: the agreement between the simulations and the observations confirms the quality of the WRF simulations and their efficient coupling with ARTS. Similar conclusions can be drawn from other cases (not shown). However, note that the cloud and precipitation structures can be slightly misplaced by the cloud model compared

TABLE 5. For the frozen hydrometeor databases from Liu [48] and Hong [49] and for the snow in the WRF WSM6 microphysical scheme, the frozen particle habits, D_{max} , the range of equal-mass sphere radius, the coefficient a , the exponent b (SI units assumed), L is the particle length, and d is the hexagonal diameter (distance between opposite vertices).

Database	Frozen particle habits	D_{max} (μm)	Range of radius (μm)	a	b
Liu	Long column ($L/d = 4$)	121~4835	25~1000	37.09	3
	Short column ($L/d=2$)	83~3304	25~1000	116.12	3
	Block column ($L/d=1$)	66~ 2632	25~1000	229.66	3
	Thick plate ($L/d=0.2$)	81~3246	25~1000	122.66	3
	Thin plate ($L/d=0.05$)	127~5059	25~1000	32.36	3
	3-bullet rosette	50~10000	19~1086	0.32	2.37
	4-bullet rosette	50~10000	19~984	0.06	2.12
	5-bullet rosette	50~10000	21~1058	0.07	2.12
	6-bullet rosette	50~10000	21~1123	0.09	2.13
	Sector snowflakes	50~10000	25~672	0.002	1.58
	Dendrite snowflakes	75~12454	33~838	0.01	1.9
Hong	Hexagonal solid column	2~2000	0.74~283.39	0.03	2
	Hollow column	2~2000	0.85~310.88	0.02	2
	Hexagonal plate	2~2000	0.90~897.65	0.75	2.47
	6-branch bullet rosette	2~2000	0.84~307.98	0.18	2.34
	Aggregate	2~2000	1.07~344.21	65.45	3
	Droxtal	2~2000	0.51~514.72	347.31	3
WSM6 Snow	Sphere			$\pi 100/6$	3

to the observations, as already mentioned by several authors (e.g., [55], [56]). For case 11 for instance, the WRF simulates the extratropical cyclone over the North Atlantic closer to Portugal, compared to the satellite observations.

For a systematic comparison of the simulations and observations minimizing the effect of the observed mis-locations, the histograms of the observed and modeled brightness temperatures are compared, for some SSMIS frequencies and for the pixels in all the 12 scenes (Figure 6). The coastal pixels (up to ~ 15 km from the coast) have been excluded to avoid the large differences in brightness temperatures related to the high variability of the surface emissivity around the coast in addition to the difference in resolution between the surface emissivity estimation and the satellite footprints. The number of pixels has two peaks with the brightness temperatures around 200 K and 260 K at surface sensitive channel 89 GHz H, corresponding to the sea and land cases. At 89, 157 and 183 ± 7 GHz, the simulations produce lower brightness temperatures than the observations. This can be due to an overestimation of the cloud frozen quantities in WRF simulations, to deficiencies in the SSP of the frozen particles, or to a combination of these two effects. Overall, the WRF / ARTS model combination reproduces rather well the brightness temperature distributions for all the investigated channels at frequencies lower than 190 GHz. It gives us confidence in the possibility to simulate realistic brightness temperatures at higher frequencies up to 664 GHz.

Figure 7 shows the simulated brightness temperatures at all ICI and MWI channels for case 11. Note that this study focuses mostly on the ICI instrument, and we assume that all MWI channels have the same field-of-view as ICI, i.e.,

16 km. At low frequencies, strong contrasts are observed between ocean and land, with an increasing effect of the cloud structures over ocean as the frequency increases. In the window channels at 89 GHz and above, the presence of frozen particle is characterized by the scattering that increases with frequency. Above 325 GHz, the atmospheric opacity above the clouds tends to mask the scattering signal, at least for this case.

E. STATISTICAL ANALYSIS OF THE RETRIEVAL TRAINING DATABASE

Our retrieval database contains (1) the geophysical variables describing the 12 cases of Section II (atmospheric variables, especially the vertically-integrated contents and the vertical profiles of six hydrometeors), and (2) the corresponding simulated brightness temperatures at ICI and MWI channels. This retrieval dataset contains 57% pixels over land and 43% pixels over ocean. A question could arise: Are these cases enough for the training of a statistical retrieval? The 12 cases could be disjointed or describing only part of the possible hydrometeor cases. In order to verify this aspect, leave-one-out generalization tests have been performed (Section III) to ensure that these 12 cases sample well the complex space of hydrometeor profiles. The quality of a statistical retrieval database is essential for either a Bayesian [57] or a neural network [58] retrieval scheme. As a consequence, it is important to first analyse the quality of this database.

First, a preliminary information content analysis is performed in order to measure the degrees of freedom in the hydrometeor variables to retrieve and the information actually carried out by the satellite observations (i.e., ICI or MWI

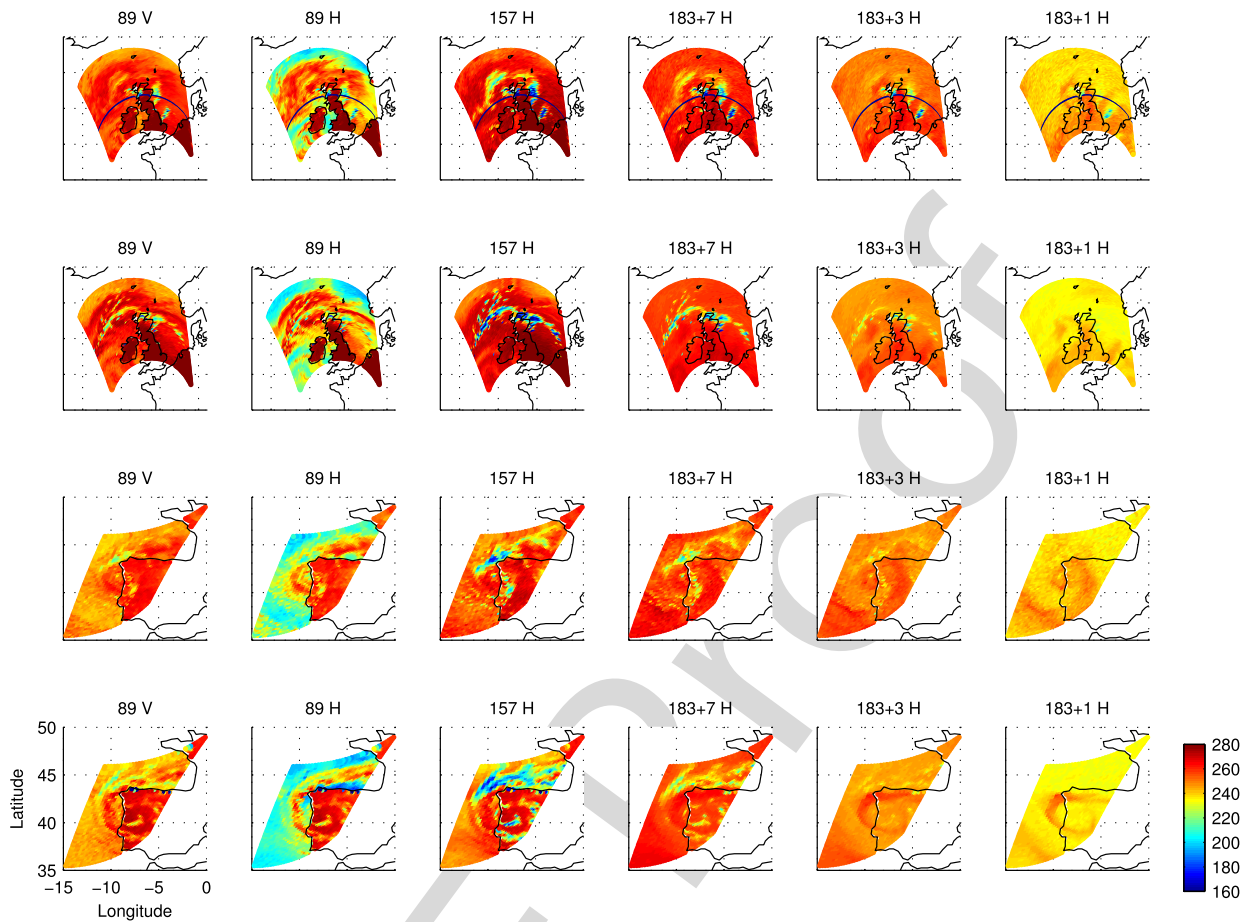


FIGURE 5. Observed (first and third rows) and simulated (second and fourth rows) brightness temperatures (K) at six SSMIS channels for case 7 (2 top rows) over UK at 17:00 UTC on June 28, 2012, and for case 11 (2 bottom rows) over Portugal at 07:00 UTC on January 19, 2013.

channels). Principal Component Analyses (PCA) is a statistical procedure that uses an orthogonal linear projection to transform correlated original vectors into a new uncorrelated coordinate system. PCA aims at explaining as much variance as possible in the first components, so it is a good technique to analyze the variability of a database, in particular by estimating the number of degrees of freedom.

Figure 8 represents the variance explained by the first PCA component for the hydrometeor information (integrated quantities and atmospheric profiles) and for the microwave brightness temperatures. Results show that the six integrated hydrometeor contents in the left panel (resp. $104 \times 6 = 624$ variables of the hydrometeor profiles in the middle panel) from WRF can be explained by 4 (resp. 36) components that represent more than 99% of the variance. Results are similar for land and ocean surfaces. These results mean that in order to retrieve the hydrometeor variables with 1% precision, at least 4 independent pieces of information would be required for the integrated quantities and 36 for the profiles. However, only 4 pieces of information can be derived from the 13 ICI channels (again for 99% variance),

shown in the right panel. This means that there are strong correlations between the ICI channels. This number increases to 6 pieces of information when using the 39 ICI+MWI channels (not shown). These results stress the difficulty of retrieving the integrated hydrometeor information with only ICI channels, and the hydrometeor profiles even when adding the MWI channels.

The number of degrees of freedom is a first assessment of the constraints for the retrieval. However, the retrieval really depends upon the relationship between the satellite observations and the variables to retrieve. Therefore, the correlation between the ICI brightness temperatures and the integrated hydrometeor quantities have been estimated over both land and sea (Figure 9). As mentioned in Section II-D, the ICI channels are more sensitive to the frozen phases (cloud ice, snow, and graupel) than to the liquid ones (rain and cloud water) in the clouds. Correlation with FWP reaches -0.85 (-0.83), -0.90 (-0.88), and -0.82 (-0.79) with respect to the 183 ± 7 , 243, and 325 ± 9.5 GHz window channels over land (sea), respectively. Note that negative correlations are as good as positive ones for the retrieval.

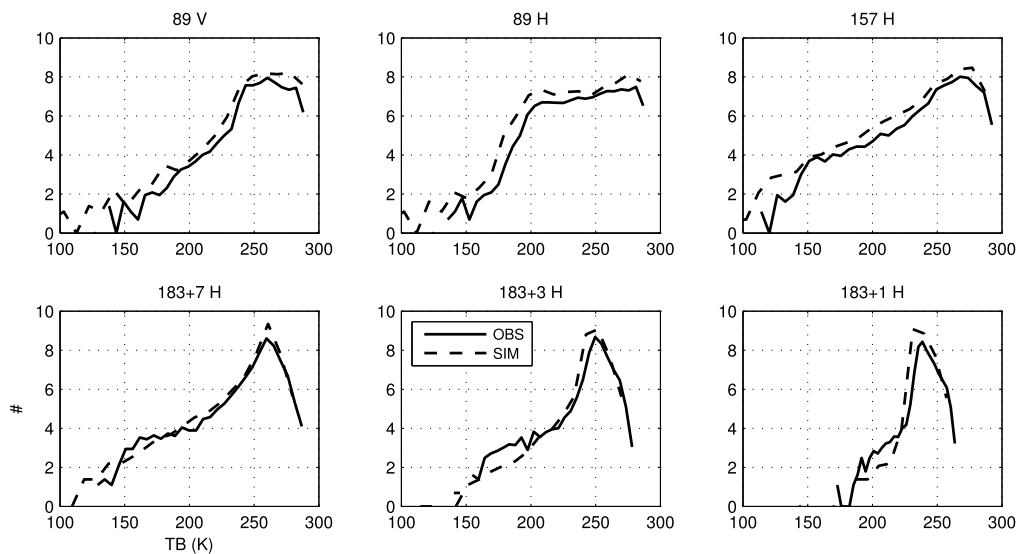


FIGURE 6. Histograms of observed and simulated brightness temperatures at six SSMIS channels for all the 12 cases at SSMIS over-pass times. The pixels on the coast are removed. The y-axis is in \log_{10} .

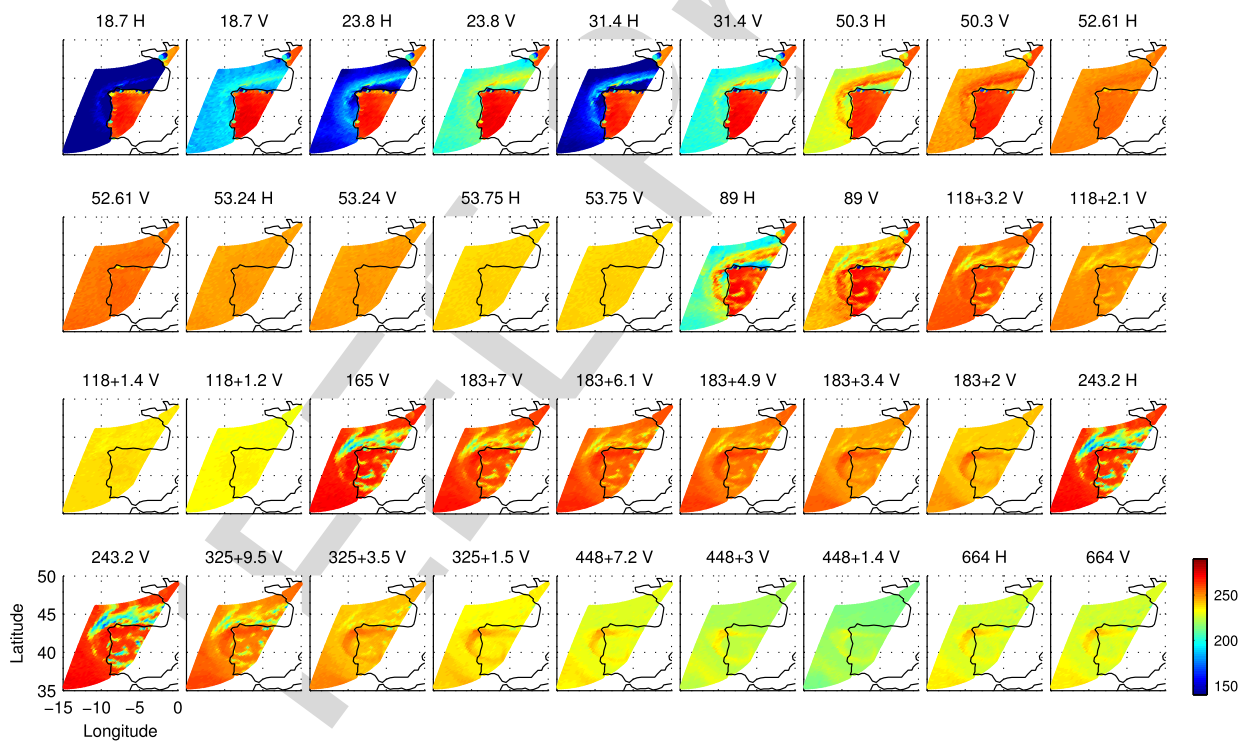


FIGURE 7. Simulated brightness temperatures (K) at MWI and ICI channels for case 11 over Portugal at 07:00 UTC on January 19, 2013.

Among the frozen particles, snow has the most significant signature at window channels (compared to cloud ice) due to its stronger scattering. This is opposite for higher frequencies ($> 448 \pm 7.2$ GHz). In addition, the correlation coefficients for the liquid phases are much lower, as expected, especially

for the cloud water (< 0.2 for all the channels). Therefore, Figure 9 shows the potential of ICI channels for frozen particle retrieval but also the difficulty for the liquid particle retrieval. However, ICI information can be complemented with MWI observations. The correlation between the MWI

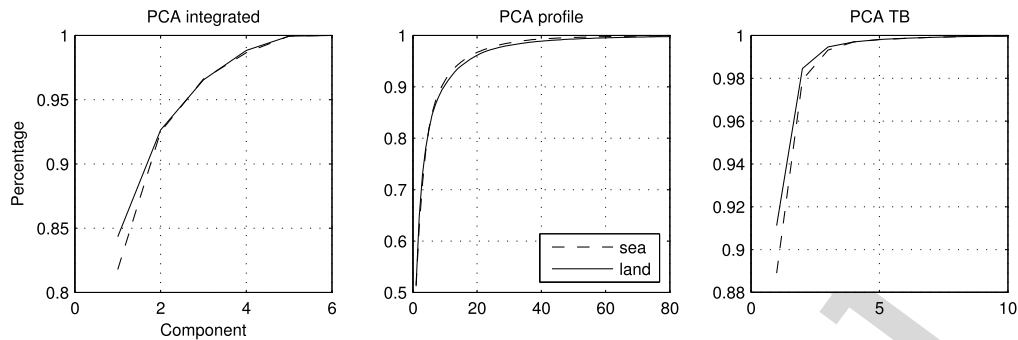


FIGURE 8. Percentage of total variance in Principal Component Analysis (PCA) for the vertically integrated hydrometeor contents, the hydrometeor profiles, and the simulated brightness temperatures for ICI channels over sea and land.

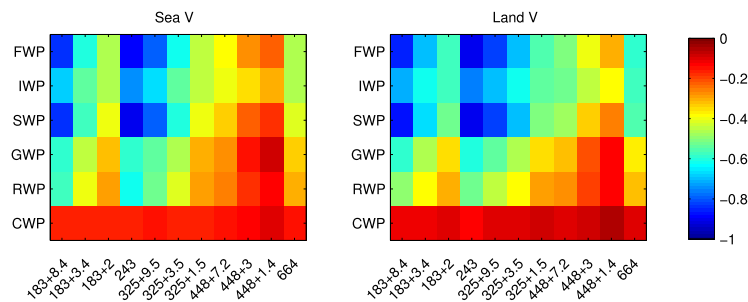


FIGURE 9. Correlation coefficients between the integrated hydrometeor contents (frozen water path (FWP), ice water path (IWP), snow water path (SWP), graupel water path (GWP), and cloud water path (CWP)) and the simulated brightness temperatures for the ICI channels in the vertical polarization over sea (left) and land (right).

brightness temperatures and the integrated hydrometeor contents has been calculated as well (not shown). Lower frequencies are typically the more sensitive channels to the integrated cloud liquid properties, especially over sea with a correlation of 0.72 / 0.74 at 31.4 GHz for cloud water/rain, which shows well the complementarity of both instruments.

III. STATISTICAL RETRIEVAL OF CLOUD HYDROMETEOR CONTENTS

In this section, a statistical retrieval scheme is developed to retrieve cloud hydrometeor contents (both frozen and liquid phases). A first step consists in the detection of clouds and the second one in the quantification of each hydrometeor integrated quantity and atmospheric profile. These two statistical steps are trained using the realistic database presented in Section II. Retrievals have been performed systematically using ICI-only and ICI+MWI channels.

A. CLOUD DETECTION AND CLASSIFICATION

The cloud detection (i.e., presence of cloud or not) and classification (i.e., specification of the cloud type) has two main applications. First, it is an interesting way to measure the information content of the satellite observations and study the sensitivity of each channel to the several types of hydrometeors (frozen and liquid). Second, it is a necessary preliminary step before the actual cloud retrieval that intends to quantify the hydrometeor quantities.

1) A NEURAL NETWORK (NN) CLASSIFIER

The NN is a nonlinear statistical model [59]. It can be used as a regression tool to estimate quantities, but it can also be used as a classifier, for instance for cloud classification [60]. A standard feedforward NN is used for each hydrometeor, in order to classify what type of cloud is present. The NNs have 13 or 39 inputs corresponding to the ICI or ICI+MWI channels, 10 neurons in the hidden layer and one output neuron. The NNs are trained with binary data (0 for no cloud, 1 for cloud pixel), but the NN outputs are continuous values between 0 and 1 and this output represents the *a posteriori* probability for the pixel to be cloudy [61]. Once trained, the NNs will provide, from the satellite observations only and for each pixel, a probability of being cloudy. A threshold on this probability will be needed to decide if the pixel is cloudy or not.

The training of the NNs uses the database containing the simulated (WRF+ARTS) brightness temperatures for ICI-only and ICI+MWI channels, for the twelve mid-latitude scenarios in Europe (Section II). The cloud flag for each hydrometeor is identified according to a threshold superior to 0.01 kg/m^2 on each hydrometeor vertically integrated content. A classification has also been defined for the total hydrometeor and total frozen hydrometeor (ice+snow+graupel) contents using the same threshold. The database is used to construct the learning (to train the NNs)

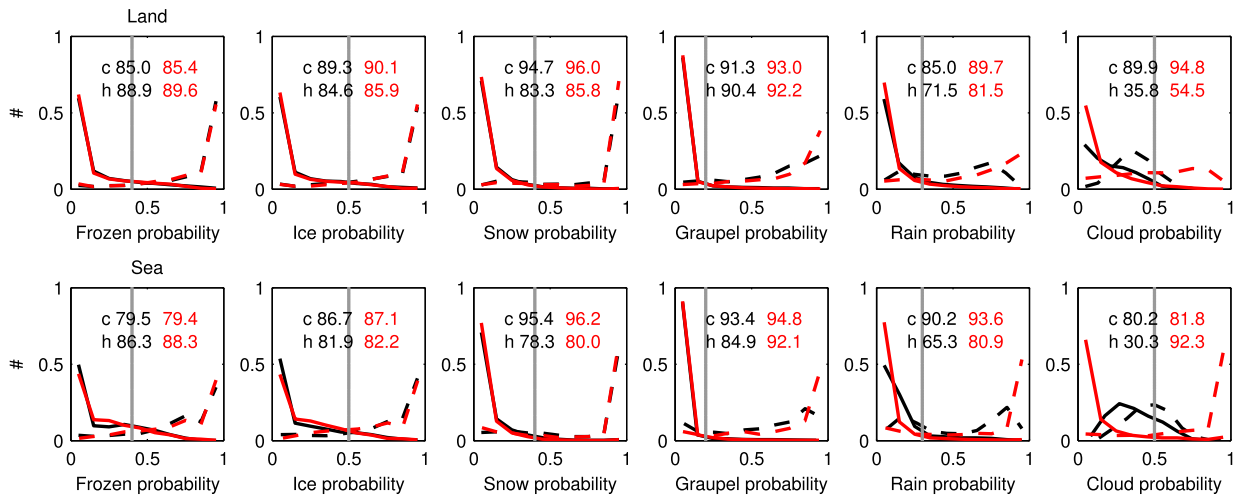


FIGURE 10. Probability histograms for each integrated hydrometeor content retrieved by a NN classification with ICI-only (black) and ICI+MWI (red) channels over sea and land. The classification accuracy for the non-hydrometeor (c) and hydrometeor pixels (h) are shown. The threshold value for each hydrometeor is shown by a grey line. The solid (resp. dashed) line represents the probability distribution of the non-hydrometeor (resp. hydrometeor) pixels.

and the testing (to test the NNs ability to classify) datasets.

The NNs are trained using a standard back-propagation algorithm [62]. A leave-one-out approach is used to minimize or prevent the over-fitting problem where NNs perform well on the training dataset, but are unable to work on new atmospheric situations. Each time, 11 out of the 12 cases are used for the training, and the remaining case is used to test the NN. This is performed 12 times, to obtain 12 testing cases. The results presented in the following section will be the synthesis of these 12 testing cases. Using a different approach would conduct to arbitrary obtain generalization results very dependent on the choice of the testing dataset (often with too optimistic results). The leave-one-out approach provides more confidence on the robustness of the results.

2) CLOUD CLASSIFICATION RESULTS

Figure 10 presents the histogram of the NN *a posteriori* probability of being cloudy, for each hydrometeor, over land and sea separately, for the 12 cases, from the ICI information only. The solid (resp. dashed) line represents the probability distribution of the non-hydrometeor (resp. hydrometeor) pixels. Ideally, the solid line would be a Dirac distribution over zero, and the dashed line would be a Dirac distribution over one. The wider the intersection of the distribution, the more ambiguous the classification is. Note that some distributions are more ambiguous for some hydrometeors (e.g., rain). Therefore, different thresholds for the classification need to be used for different hydrometeors. Threshold values of 0.4, 0.5, 0.4, 0.2, 0.3, and 0.5 have been chosen for total frozen, cloud ice, snow, graupel, rain, and cloud water hydrometeors, respectively. Resulting classification accuracies are satisfactory (up to 94.7% and 90.4% for the non-hydrometeor pixels and for the hydrometeor pixels, respec-

tively) over land. These rates are similar over sea since the surface contribution is very limited at frequencies higher than 183 GHz (ICI channels) due to large atmospheric opacity. The classification has also been performed for each hydrometeor when using ICI+MWI channels, the resulting accuracy for each hydrometeor has been specified in red in Figure 10. As expected, adding lower frequencies improves the detection of the cloud liquid phase, with an increase of the classification accuracies of 10.0% over land and 15.6% over sea for the rainy pixels, and 18.7% and 62.0% for the cloud water pixels. For the frozen particles, the classifier gives very similar results when using ICI-only or ICI+MWI channels, which suggests that the MWI channels do not provide more information for the frozen particles detection than ICI, as expected.

Figure 11 shows the spatial patterns of the integrated contents, the *a posteriori* cloud probabilities estimated by the NN classifier with ICI+MWI channels, the retrieved flags, and the initial flags, for all the six hydrometeors and the total hydrometeors, for case 11 (described in Table 2). The estimated spatial structure of each hydrometeor pixel by the NN classifier is globally similar to the initial one, which suggests that our classification has a good performance in detecting the location of each hydrometeor and total cloud. With ICI only (not shown), the frozen cloud structures (ice, graupel, and snow) are well detected, but there are difficulties to detect the liquid phase (cloud and rain) due to the lack of lower frequencies.

B. RETRIEVAL OF CLOUD INTEGRATED CONTENT

1) RETRIEVAL ALGORITHM

The relationships between the brightness temperatures at different frequencies and the hydrometeor column masses are complex, multivariate in nature, and non-linear. A multilayer feed-forward NN retrieval algorithm is again chosen to model

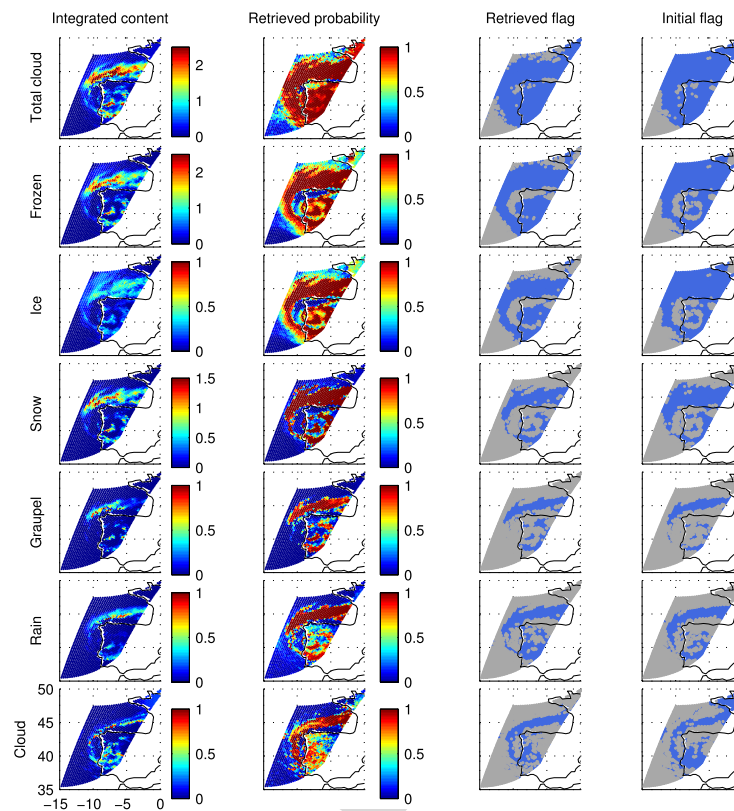


FIGURE 11. From left to right: the spatial patterns of six integrated contents (kg/m^2), the probabilities estimated by the NN classifier with ICI and MWI channels, the retrieved flags, and the initial flags for six hydrometeors and the total hydrometeors for case 11 over Portugal at 07:00 UTC, on January 19, 2013.

these complex physical links. The number of inputs are the same (13 channels for ICI-only and 39 channels for the ICI+MWI channels), 10 neurons in the hidden layer, and 6 neurons are used to code the FWP, IWP, SWP, RWP, GWP, and CWP retrieved vertically integrated quantities.

The training and testing datasets are the same as in Section III-A about cloud detection and classification, except that this time, the variables to retrieve are not binary (presence or not of the cloud) but real continuous variables (i.e., the cloud integrated quantities). The dataset contains only pixels classified as cloudy by our detection/classification process (Section III-A).

To reduce the effect of the classification uncertainty on the hydrometeor content retrieval, the individual hydrometeor classification is used, instead of using the total cloud classification (see Figure 11). This helps avoiding ambiguities in the cloud liquid phase detection when using only ICI channels. Again, the leave-one-out process (11 cases for training and one case for testing, repeated 12 times) was used to train and test the NNs, ensuring that no over-training is artificially increasing the confidence in the retrievals.

The leave-one-out scheme ensures that the 12 cases sample well the space of possible hydrometeor profile states. No

significant difference is measured on the 12 trials in the generalization tests. This means that there is no extreme departure of one case compared to the remaining 11 cases, and that the statistical NN retrieval is able to interpolate between the cases, despite the large variability of the cases. This also shows the statistical quality of the dataset built in Section II, for the retrieval purposes.

To determine the ability of the retrieval algorithm to accurately quantify the hydrometeor amounts, the differences between the retrieved and initial values are measured in terms of both the absolute and relative averaged errors, as a function of the hydrometeor amounts. Indeed, the relative error (resp. absolute error) is generally more relevant for evaluating the retrieval performances for the larger (resp. smaller) hydrometeor contents.

2) RESULTS

Figure 12 shows the scatter plots of the retrieved column contents of the six hydrometeors versus the initial ones, over land and sea, for ICI-only and ICI+MWI channels. No instrument noise is considered so far. Each color represents one of the 12 cases (each one is the testing dataset in the leave-one-out approach). When considering only ICI

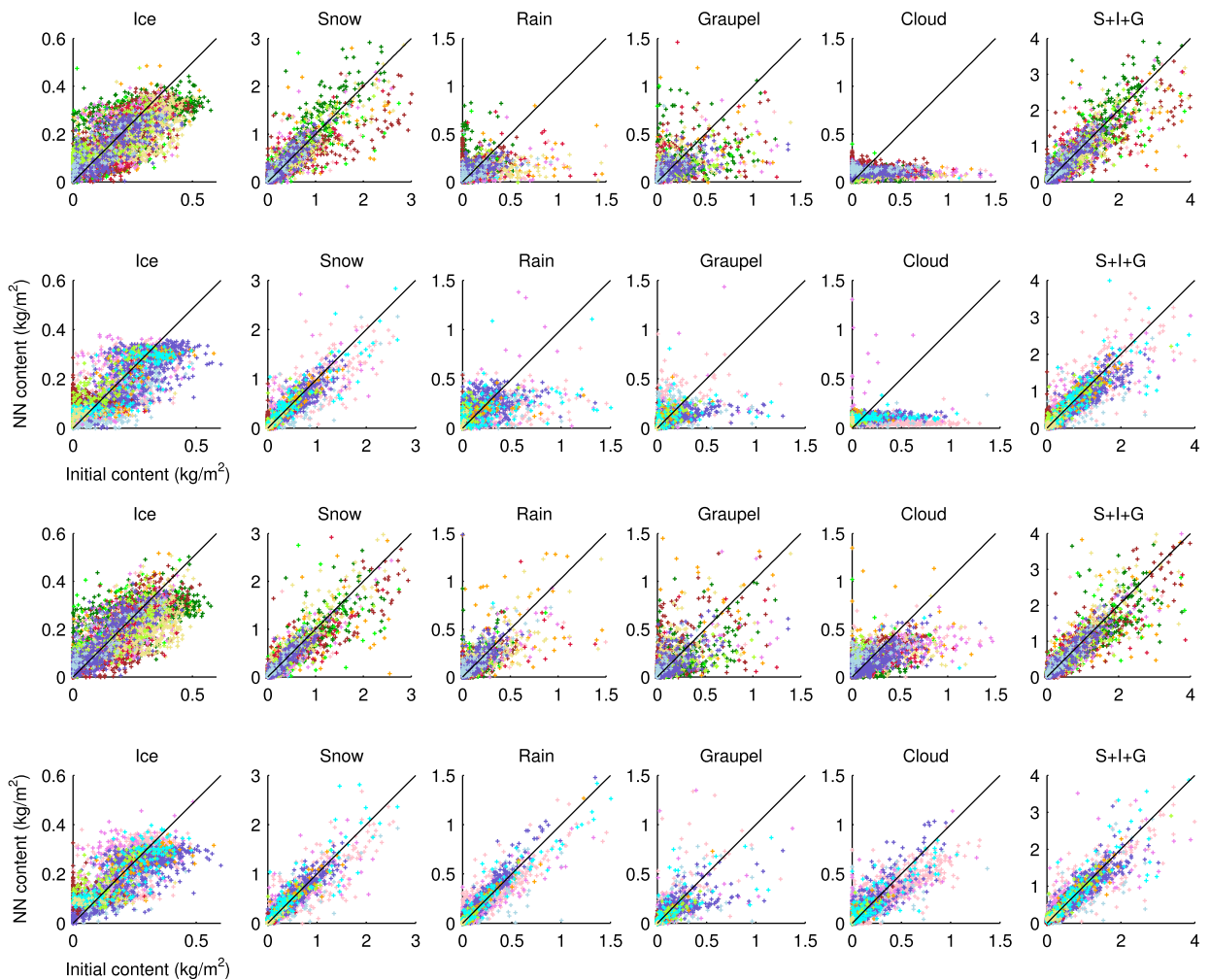


FIGURE 12. Scatter plots of vertically integrated contents of ice, snow, rain, graupel, cloud water, and total frozen quantities from the WRF outputs and the NN method with ICI-only channels (2 top rows) and ICI+MWI channels (2 bottom rows) over land (first and third rows) and sea (second and fourth rows). Each color represents the results for one case (same color as in Figure 3).

channels, the retrieved cloud liquid phases (RWP and CWP) saturate at their lower values (0.5 kg/m^2 and 0.3 kg/m^2), slightly underestimating the higher liquid phase contents, and overestimating the lower ones. This implies that the increasing opacity at higher frequencies and near the water vapor absorption line masks the signal from lower liquid clouds to a large extent. In contrast, the agreement between the retrieved and initial cloud frozen phase contents is very good, in particular for the SWP, due to the strong scattering signals at higher frequencies by frozen particles. Note that a saturation regime appears also in the IWP retrieval over both land and sea, around 0.4 kg/m^2 .

When adding the MWI channels, the retrieval performances are improved mainly for the cloud liquid phases, as expected. It illustrates well the sensitivity of the low microwave frequencies to the emission by the cloud liquid phase, and their limited sensitivity to the frozen phase above,

allowing the retrieval of the cloud liquid contents in a vertical column. Therefore, combining ICI and MWI instruments, by covering the frequency range from 18.7 to 664 GHz, allows overcoming the limitations of lower frequencies (i.e., not sensitive to the smaller frozen particles at higher altitudes) and of higher frequencies (i.e., lack of capacity to extract the information from lower altitudes). Over sea, the retrieval algorithm reproduces better the integrated hydrometeor contents, specially for the cloud liquid phases when using ICI+MWI channels. This is due to the fact that at surface-sensitive channels the surface contribution from the sea is rather limited (low surface emissivity) as compared to the land (high surface emissivity). As a consequence, these channels have a larger impact over sea than over land, as discussed by [63] or [64].

The ICI+MWI retrieved hydrometeor content patterns are shown in Figure 13 for case 11. The spatial distribution

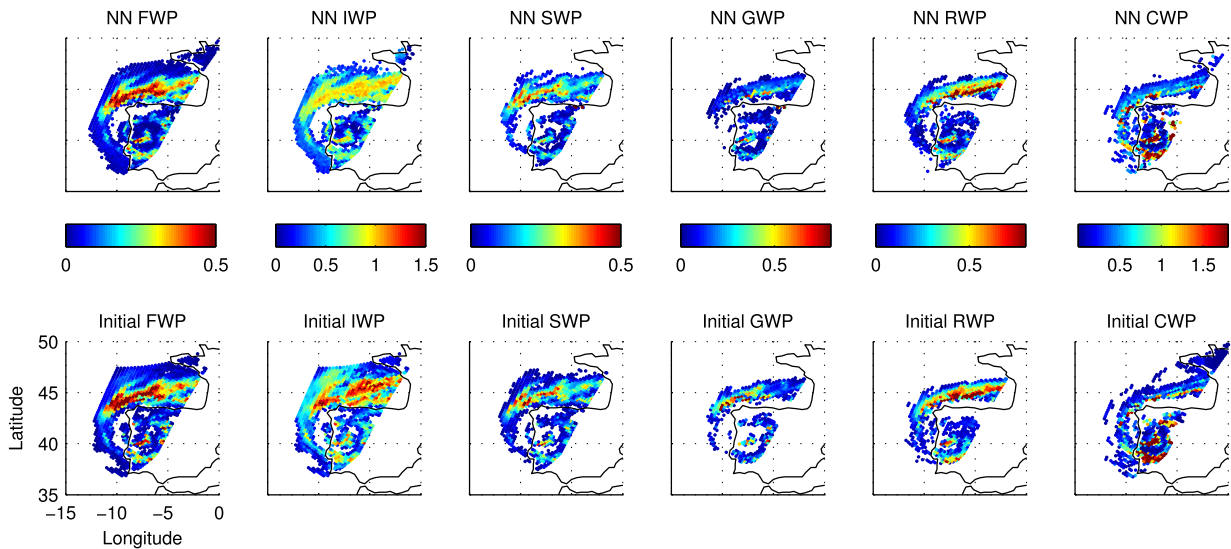


FIGURE 13. The retrieved (top row) and initial (bottom row) IWP, SWP, RWP, GWP, CWP, and FWP (kg/m^2) with ICI+MWI channels for case 11 over Portugal at 07:00 UTC on January 19, 2013.

of all the hydrometeors are well retrieved. The convective part of the eye wall is well retrieved. Note, however, an underestimation of the IWP north of the eye. Surprisingly, there is no evident discontinuity on the retrieved RWP and CWP over the coasts, although this is often observed in rainfall retrievals [65], [66]. This land / sea discontinuity however appears when only ICI channels are used in the CWP retrieval. This is due to the difficulty in distinguishing the emitted signals from cloud liquid particles from warmer land surface, losing the direct link between the brightness temperatures and the CWP.

Figure 14 shows the averaged absolute and relative retrieval errors, per bin of 0.01, 0.04, 0.04, 0.04, 0.02, and 0.06 kg/m^2 for, respectively, the six hydrometeor contents (IWP, SWP, RWP, GWP, CWP, and FWP), over land and sea, with ICI-only or ICI+MWI channels. The limited information from higher frequencies (ICI-only) induces large absolute and relative retrieval errors in RWP, CWP, and GWP (situated at relative lower altitudes), notably for larger contents. Therefore, the following discussion will focus on the retrieval results with ICI+MWI channels. As expected, in the light hydrometeor content ranges, the relative errors are higher, even exceeding 100% for very small contents. The relative retrieval errors for IWP, SWP, RWP, GWP, CWP, and FWP drop and remain below 20%, 20%, 20%, 40%, 30%, and 20% from 0.25, 0.5, 0.25, 0.2, 0.2, and 0.5 kg/m^2 , respectively. Note that the relative errors drop below 40% for 0.1-0.5 kg/m^2 . They increase again and start to fluctuate for larger hydrometeor contents, due to the limited number of these cases in our retrieval database. The absolute errors increase with hydrometeor contents, except for the IWP. The absolute errors are larger than 0.04 kg/m^2 for the IWP less than 0.05 kg/m^2 , showing the difficulty in

lower IWP retrieval. This high uncertainty associated with the low IWP is due to the lack of scattering, even at high sub-millimeter frequencies, over small ice particles in limited quantities. Note that both absolute and relative errors for the IWP retrieval are very similar in the two channel-configurations, demonstrating that the ICI channels can provide enough information for the IWP retrieval.

The impact of realistic instrumental noises on the accuracy of the retrieval algorithm was investigated. The instrumental noises go from 0.6 K to 1.2 K for the MWI channels and from 0.6 K to 1.9 K for the ICI channels (see Table 1). The noise value at each channel was added to the simulated brightness temperatures but their impact on the retrieval results was negligible (not shown) because the instrumental noise is negligible compared to the other sources of uncertainties such as, for instance, the low-information content of some channels for some hydrometeors, or the ambiguity of the signal in one channel.

C. HYDROMETEOR PROFILE RETRIEVAL

1) RETRIEVAL APPROACH BASED ON A PCA REPRESENTATION

In order to represent the ice water content (IWC), snow water content (SWC), rain water content (RWC), graupel water content (GWC), cloud water content (CWC), and frozen water content (FWC) vertical profiles, 6×10^4 variables are needed. It would be unrealistic to retrieve independently these 624 variables from the small number of microwave channels (and even lower number of independent pieces of information in the observations, see Section II-E). Therefore, a PCA technique was used to reduce the size of the outputs in the retrieval algorithm, by using the strong dependencies (correlations) that exist between the vertical layers in the profile, and among the hydrometeor types. In order to represent

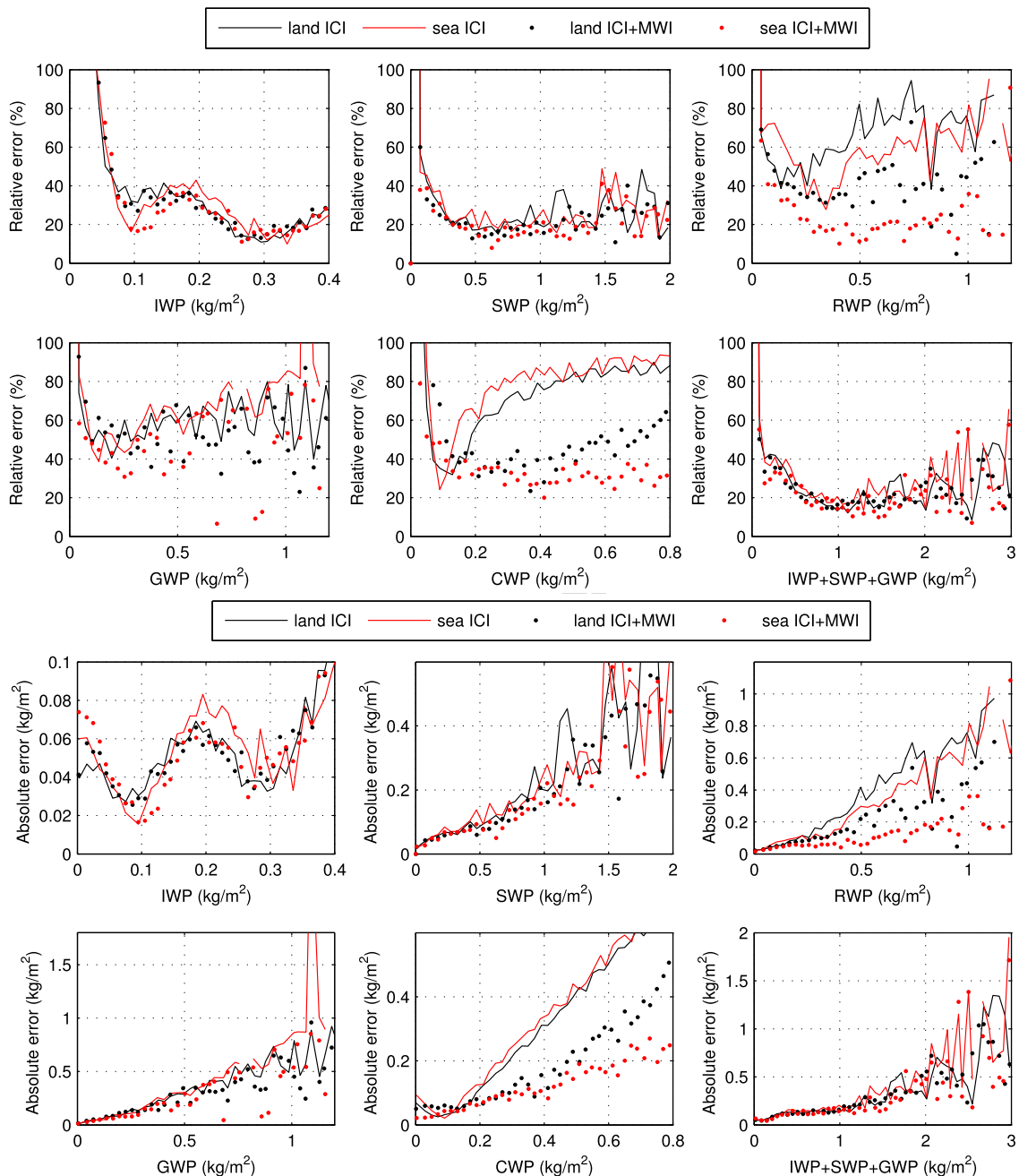


FIGURE 14. Retrieval relative (2 top rows) and absolute (2 bottom rows) errors per bin of 0.01, 0.04, 0.04, 0.04, 0.02, and 0.06 kg/m^2 for IWP, SWP, RWP, GWP, CWP, FWP, respectively, with ICI-only and ICI+MWI channels over sea and land.

99% of the 6 hydrometeor profiles variance, 35 components are necessary over sea and 42 components over land. Note that the PCA has been performed over all the hydrometeor profiles at once. A NN model is then used to retrieve, from the microwave channels, these 35 or 42 components that are then reversed into the original coordinates to obtain the hydrometeor profiles. It should be noted that only 4 (resp. 6) pieces of information were present in the ICI-only (resp. ICI+MWI)

channel-configuration (Section II-E) so obviously, only the dominant part of the profile variability can be retrieved, not the details (e.g., vertical inversions in the profiles or subtle structures in the atmospheric column).

2) RESULTS

Figure 15 shows the initial and retrieved IWC, SWC, RWC, GWC, CWC, and FWC profiles from the ICI+MWI channels

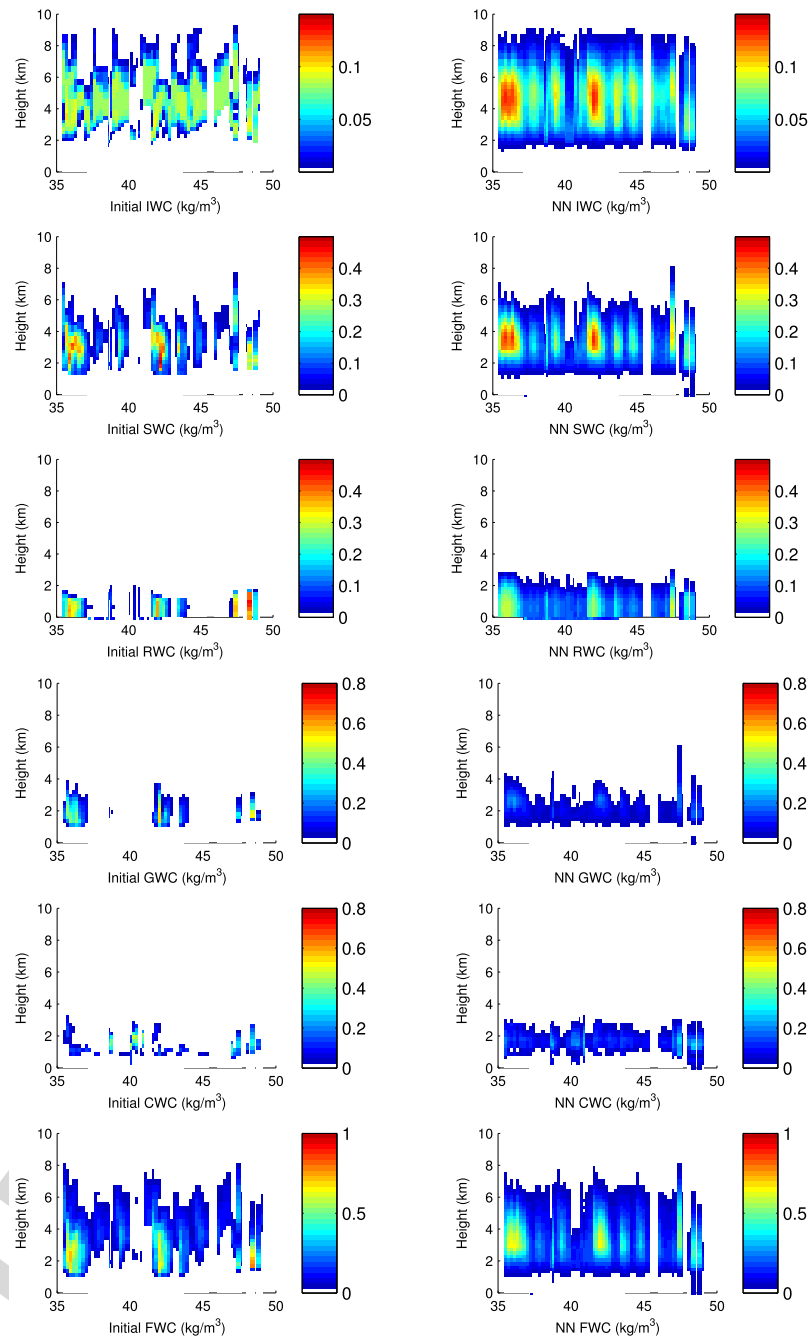


FIGURE 15. Initial (left) and retrieved (right) IWC, SWC, RWC, GWC, CWC, and FWC profiles from the ICI+MWI channels for case 11, along the transect between 8°W and 9°W.

(with no instrumental noises), for case 11, along the transect between 8°W and 9°W. The vertical structures of the cloud system, especially the convective core, are well reproduced, with a similar amount and location of the frozen particles than in the original WRF profiles. For the IWC profile retrieval, the results imply that the retrieved IWCs are much larger (up to 0.15 kg/m^3) than the initial ones (up to 0.08 kg/m^3).

This overestimation might be because the NN retrieval cannot separate the contribution of the ice from the other frozen hydrometeors in the brightness temperatures. For the liquid profile retrievals, the NN underestimates their contents, with limited vertical structures compared to the initial ones. Overall, the retrieval algorithm can capture the major structure of frozen phase profiles. Considering the number of

pieces of information required to fully represent the hydrometeor profiles, and the information content of the satellite observations, the retrieval of the six hydrometeor profiles remains a true challenge. Our retrieval gives one profile solution (i.e., the simplest and most regular profiles) among all the possible ambiguous ones. This is the only possible strategy, unless an independent source of information is added such as a model in the variational assimilation context.

IV. CONCLUSIONS AND PERSPECTIVES

The second generation of the EUMETSAT-EPS-SG will carry an instrument, ICI, with channels between 183 and 664 GHz. It will provide unprecedented measurements in the sub-millimeter spectral range above 200 GHz, contributing to an innovative characterization of the frozen phase in the clouds. This study is a contribution to the preparation of this upcoming satellite sub-millimeter imager, with the development of a statistical retrieval algorithm of the cloud frozen water content, based on NN methodologies. Combination of ICI and MWI observations has also been explored, with frequencies from 19 to 664 GHz.

The retrieval database is derived from ARTS radiative transfer simulations, fed with a detailed and realistic description of the atmospheric profiles from the WRF cloud resolving model, for twelve European mid-latitude cases. When coupling these two models, special attention has been paid to the selection of the microphysics scheme in WRF and the calculation of the SSPs in ARTS. The WRF WSM6 microphysical scheme has been selected: it predicts the mixing ratios of five hydrometeors (cloud ice, snow, graupel, rain, and cloud water). A DDA pre-calculated database from Hong provides realistic SSPs for snow particles. The performance of the coupling results has been evaluated by comparison with existing satellite observations up to 190 GHz with SSMIS. A good agreement has been obtained for the twelve cases at the investigated frequencies, giving us confidence in these WRF+ARTS simulations. The retrieval database prepared with the WRF+ARTS models includes the atmospheric variables of interest describing the 12 cases and the corresponding simulated brightness temperatures at ICI and MWI channels. The statistical quality of the database, as well as the information content of the simulated brightness temperatures have been investigated, with PCA and correlation analyses. A NN classifier and a NN retrieval algorithm are developed to detect and quantify each cloud hydrometeor quantity, trained on the WRF+ARTS database, for ICI-only and for ICI+MWI channels. The classifier gives very satisfactory accuracy in detecting the cloud frozen hydrometeors when using ICI-only channels, with an accuracy of $\sim 90\%$ of the cloud detection over land and ocean. For the cloud hydrometeor quantification, the retrieved cloud frozen phase contents is satisfactory with ICI-only channels for IWP above 0.05 kg/m^2 . The absolute error is larger than 0.04 kg/m^2 for IWP less than 0.05 kg/m^2 , showing the difficulty in lower IWP retrieval. The relative error for the retrieved integrated frozen water content (FWP) is below

$\sim 40\%$ for $0.1 \text{ kg/m}^2 < \text{FWP} < 0.5 \text{ kg/m}^2$ and below $\sim 20\%$ for $\text{FWP} > 0.5 \text{ kg/m}^2$. Adding the MWI channels improves the detection and quantification essentially for the cloud liquid phase, as expected. For the hydrometeor profiles, the retrieval algorithm can capture the major vertical structures of the cloud profile, but fails to detect the details.

This work is based on realistic simulations with the WRF+ARTS models, along with a carefully crafted retrieval methodology, to obtain a valid assessment of the retrieving capacity of the ICI and MWI instruments. The simulations (training and test databases) of 12 diverse and representative events have been compared and validated with existing satellite observations up to 200 GHz (which is rarely done in this field). This largely limits the sources of uncertainty. However, some sources of uncertainty have not yet been accounted for, which may affect the retrieval performance. The instrumental noises have been taken into account in the retrieval, but not the uncertainties in WRF modeling / parameterization and in the radiative transfer modeling with ARTS. This could have a major impact on the retrieval performance. We concentrated so far on European situations. With TRMM, studies focused on the Tropical regions and mid-latitude situations were deserving special attention. Tropical situations as well as polar cases will be added to the database. For that, it is advised again to simulate real scenes observed by the current satellites, for an evaluation of the radiative transfer simulations up to 200 GHz. An aircraft demonstrator of ICI, the International Sub Millimeter-wave Airborne Radiometer (ISMAR), has been flown during three campaigns on board the FAAM aircraft, with measurements from 118 to 664 GHz. Several flights were designed for the cloud and precipitation studies. Our retrieval could be adapted to aircraft situations and tested with ISMAR observations.

ACKNOWLEDGMENT

The ARTS community is appreciated for providing, developing, and maintaining such an open source software. The help of P. Eriksson and S. A. Buehler is specially acknowledged. The authors thank the G. Liu, G. Hong, and H. Nowell for providing the DDA databases.

REFERENCES

- [1] K.-N. Liou, "Influence of cirrus clouds on weather and climate processes: A global perspective," *Monthly Weather Rev.*, vol. 114, no. 6, pp. 1167–1199, 1986.
- [2] V. Ramaswamy and V. Ramanathan, "Solar absorption by cirrus clouds and the maintenance of the tropical upper troposphere thermal structure," *J. Atmos. Sci.*, vol. 46, no. 14, pp. 2293–2310, 1989.
- [3] U. Lohmann and E. Roeckner, "Influence of cirrus cloud radiative forcing on climate and climate sensitivity in a general circulation model," *J. Geophys. Res.*, vol. 100, no. D8, pp. 16305–16324, 1995.
- [4] S. Eliasson, S. A. Buehler, M. Milz, P. Eriksson, and V. O. John, "Assessing observed and modelled spatial distributions of ice water path using satellite data," *Atmos. Chem. Phys.*, vol. 11, no. 1, pp. 375–391, 2011.
- [5] D. E. Waliser, J.-L. F. Li, T. S. L'Ecuyer, and W.-T. Chen, "The impact of precipitating ice and snow on the radiation balance in global climate models," *Geophys. Res. Lett.*, vol. 38, no. 6, p. L06802, 2011, doi: 10.1029/2010GL046478.
- [6] A. J. Gasiewski, "Numerical sensitivity analysis of passive EHF and SMMW channels to tropospheric water vapor, clouds, and precipitation," *IEEE Trans. Geosci. Remote Sens.*, vol. 30, no. 5, pp. 859–870, Sep. 1992.

- [7] K. F. Evans and G. L. Stephens, "Microwave radiative transfer through clouds composed of realistically shaped ice crystals. Part II. Remote sensing of ice clouds," *J. Atmos. Sci.*, vol. 52, pp. 2058–2072, 1995, doi: 10.1175/1520-0469(1995)052<2058:MRTTCC>2.0.CO;2.
- [8] K. F. Evans, S. J. Walter, A. J. Heymsfield, and M. N. Deeter, "Modeling of submillimetre passive remote sensing of cirrus clouds," *J. Appl. Meteorol.*, vol. 37, no. 2, pp. 184–205, 1998.
- [9] W. B. Rossow and R. A. Schiffer, "Advances in understanding clouds from isccp," *Bull. Amer. Meteorol. Soc.*, vol. 80, no. 11, pp. 2261–2288, 1999.
- [10] S. A. Buehler et al., "Observing ice clouds in the submillimeter spectral range: The cloudice mission proposal for ESA's earth explorer 8," *Atmos. Meas. Techn.*, vol. 5, no. 7, pp. 1529–1549, 2012.
- [11] P. Schlüssel et al., "Eps-sg end user requirements document," EUMETSAT, Darmstadt, Germany, Tech. Rep. EUM/PEPS/REQ/09/0151, 2016.
- [12] C. Jiménez, S. A. Buehler, B. Rydberg, P. Eriksson, and K. F. Evans, "Performance simulations for a submillimetre-wave satellite instrument to measure cloud ice," *Quart. J. Roy. Meteorol. Soc.*, vol. 133, no. S2, pp. 129–149, 2007.
- [13] K. F. Evans, J. R. Wang, P. E. Racette, G. Heymsfield, and L. Li, "Ice cloud retrievals and analysis with the compact scanning submillimeter imaging radiometer and the cloud radar system during CRYSTAL FACE," *J. Appl. Meteorol.*, vol. 44, no. 6, pp. 839–859, 2005.
- [14] B. Rydberg, P. Eriksson, and S. A. Buehler, "Prediction of cloud ice signatures in submillimetre emission spectra by means of ground-based radar and in situ microphysical data," *Quart. J. Roy. Meteorol. Soc.*, vol. 133, no. S2, pp. 151–162, 2007.
- [15] W. C. Skamarock, and Coauthors, "A description of the advanced research WRF version 3," NCAR Tech. Note NCAR/TN-475+STR, Boulder, Colorado, Tech. Rep., 2008, doi: 10.5065/D68S4MVH.
- [16] F. Chen and J. Dudhia, "Free access coupling an advanced land surface hydrology model with the penn state UNCAR MM5 modeling system. Part II: Preliminary model validation," *Monthly Weather Rev.*, vol. 129, no. 4, pp. 587–604, 2001.
- [17] Z. I. Janjic, "Nonsingular implementation of the Mellor–Yamada level 2.5 scheme in the ncep mesomodel," *NCEP Office Note, Tech. Rep.*, vol. 437, pp. 1–61, Dec. 2002.
- [18] S.-Y. Hong, Y. Noh, and J. Dudhia, "A new vertical diffusion package with an explicit treatment of entrainment processes," *Monthly Weather Rev.*, vol. 134, no. 9, pp. 2318–2341, 2006.
- [19] E. J. Mlawer, S. J. Taubman, and P. D. Brown, "Radiative transfer for inhomogeneous atmosphere: Rrtm, a validated correlated-k model for the long-wave," *J. Geophys. Res. Atmos.*, vol. 102, no. D14, pp. 16663–16682, 1997.
- [20] J. Dudhia, "Numerical study of convection observed during the winter monsoon experiment using a mesoscale two-dimensional model," *J. Atmos. Sci.*, vol. 46, no. 20, pp. 3077–3107, 1989.
- [21] J. S. Kain, "The Kain–Fritsch convective parameterization: An update," *J. Appl. Meteorol.*, vol. 43, pp. 170–181, Jan. 2004.
- [22] K. N. Liou and S. C. Ou, "The role of cloud microphysical processes in climate: An assessment from a one-dimensional perspective," *J. Geophys. Res.*, vol. 94, no. D6, pp. 8599–8607, 1989.
- [23] M. Rajeevan, A. Kesarkar, S. B. Thampi, T. N. Rao, B. Radhakrishna, and M. Rajasekhar, "Sensitivity of wrf cloud microphysics to simulations of a severe thunderstorm event over southeast india," *Annals Geophys. Atmos. Hydrospheres Space Sci.*, vol. 28, no. 2, pp. 603–619, 2010.
- [24] A. P. Khain et al., "Representation of microphysical processes in cloud-resolving models: Spectral (bin) microphysics versus bulk parameterization," *Rev. Geophys.*, vol. 53, no. 2, pp. 247–322, 2015.
- [25] G. Thompson, P. R. Field, R. M. Rasmussen, and W. D. Hall, "Explicit forecasts of winter precipitation using an improved bulk microphysics scheme. part ii: Implementation of a new snow parameterization," *Monthly Weather Rev.*, vol. 136, no. 12, pp. 5095–5115, 2008.
- [26] K.-S. S. Lim and S.-Y. Hong, "Development of an effective double-moment cloud microphysics scheme with prognostic cloud condensation nuclei (ccn) for weather and climate models," *Monthly Weather Rev.*, vol. 138, pp. 1587–1612, May 2010.
- [27] S.-Y. Hong and J.-O. J. Lim, "The wrf single-moment microphysics scheme (wsm6)," *J. Korean Meteorol. Soc.*, vol. 42, no. 2, pp. 129–151, 2006.
- [28] Y.-L. Lin, R. D. Farley, and H. D. Orville, "Bulk parameterization of the snow field in a cloud model," *J. Climate Appl. Meteorol.*, vol. 22, no. 6, pp. 1065–1092, 1983.
- [29] S. A. Rutledge and P. V. Hobbs, "The mesoscale and microscale structure and organization of clouds and precipitation in midlatitude cyclones. VIII: A model for the 'Seeder-Feeder' process in warm-frontal rainbands," *J. Atmos. Sci.*, vol. 40, no. 5, pp. 1185–1206, 1983.
- [30] S.-Y. Hong, J. Dudhia, and S.-H. Chen, "A revised approach to ice microphysical processes for the bulk parameterization of clouds and precipitation," *Monthly Weather Rev.*, vol. 132, no. 1, pp. 103–120, 2004.
- [31] P. Eriksson, S. Buehler, C. Davis, C. Emde, and O. Lemke, "Arts, the atmospheric radiative transfer simulator, version 2," *J. Quant. Spectrosc. Radiat. Transf.*, vol. 112, no. 10, pp. 1551–1558, 2011.
- [32] C. Emde, S. Buehler, C. Davis, P. Eriksson, T. R. Sreerexha, and C. Teichmann, "A polarized discrete ordinate scattering model for simulations of limb and nadir long-wave measurements in 1-d/3-d spherical atmospheres," *J. Geophys. Res.*, vol. 109, no. 24, p. 24207, 2004.
- [33] C. Davis, C. Emde, and R. Harwood, "A 3-D polarized reversed Monte Carlo radiative transfer model for millimeter and submillimeter passive remote sensing in cloudy atmospheres," *IEEE Trans. Geosci. Remote Sens.*, vol. 43, no. 5, pp. 1096–1101, May 2005.
- [34] P. Rosenkranz, "Interference coefficients for overlapping oxygen lines in air," *J. Quant. Spectrosc. Radiat. Transf.*, vol. 39, no. 4, pp. 287–297, 1988.
- [35] D. Wang et al., "Surface emissivity at microwaves to millimeter waves over polar regions: Parameterization and evaluation with aircraft experiments," *J. Atmos. Ocean. Technol.*, 2016.
- [36] C. Prigent, F. Aires, D. Wang, S. Fox, and C. Harlow, "Sea surface emissivity parameterization from microwaves to millimeter waves," *Quart. J. Roy. Meteorol. Soc.*, 2016.
- [37] M. Wiedner et al., "Modeling of passive microwave responses in convective situations using output from mesoscale models: Comparison with TRMM/TMI satellite observations," *J. Geophys. Res. Atmos.*, vol. 109, no. D6, p. D06214, 2004.
- [38] I. Meirold-Mautner et al., "Radiative transfer simulations using mesoscale cloud model outputs: Comparisons with passive microwave and infrared satellite observations for mid-latitudes," *J. Atmos. Sci.*, vol. 64, no. 5, pp. 1550–1568, 2007.
- [39] M. S. Kulie, R. Bennartz, T. J. Greenwald, Y. Chen, and F. Weng, "Uncertainties in microwave properties of frozen precipitation: Implications for remote sensing and data assimilation," *J. Atmos. Sci.*, vol. 67, no. 11, pp. 3471–3487, 2010.
- [40] V. S. Galligani, C. Prigent, E. Defer, C. Jimenez, and P. Eriksson, "The impact of the melting layer on the passive microwave cloud scattering signal observed from satellites: A study using trmm microwave passive and active measurements," *J. Geophys. Res. Atmos.*, vol. 118, no. 11, pp. 5667–5678, 2013.
- [41] V. S. Galligani et al., "Meso-scale modelling and radiative transfer simulations of a snowfall event over france at microwaves for passive and active modes and evaluation with satellite observations," *Atmos. Meas. Techn.*, vol. 8, no. 3, pp. 1605–1616, 2015.
- [42] G. Liu, "Approximation of single scattering properties of ice and snow particles for high microwave frequencies," *J. Atmos. Sci.*, vol. 61, no. 20, pp. 2441–2456, 2004.
- [43] B. T. Draine and P. J. Flatau, "Discrete-dipole approximation for scattering calculations," *J. Opt. Soc. Amer.*, vol. 11, no. 4, pp. 1491–1499, 1994.
- [44] H. Okamoto, "Information content of the 95 ghz cloud radar signals: Theoretical assessment of effects of non-sphericity and error evaluations of the discrete dipole approximation," *J. Geophys. Res.*, vol. 107, no. D22, p. 4628, 2002.
- [45] G. Hong, "Parameterization of scattering and absorption properties of nonspherical ice crystals at microwave frequencies," *J. Geophys. Res. Atmos.*, vol. 112, no. D11, Jun. 2007.
- [46] M. J. Kim, "Single scattering parameters of randomly oriented snow particles at microwave frequencies," *J. Geophys. Res. Atmos.*, vol. 111, no. D14, pp. 1–8, 2006.
- [47] P. Eriksson, M. Jamali, J. Mendrok, and S. A. Buehler, "On the microwave optical properties of randomly oriented ice hydrometeors," *Atmos. Meas. Techn.*, vol. 8, pp. 1913–1933, May 2015.
- [48] G. Liu, "A database of microwave single-scattering properties for nonspherical ice particles," *Bull. Amer. Meteorol. Soc.*, vol. 89, no. 10, pp. 1563–1570, 2008.
- [49] G. Hong et al., "Scattering database in the millimeter and submillimeter wave range of 100–1000 GHz for nonspherical ice particles," *J. Geophys. Res. Atmos.*, vol. 114, no. D6, p. D06201, 2009, doi: 10.1029/2008JD010451.
- [50] H. Nowell, G. Liu, and R. Honeyager, "Modeling the microwave single-scattering properties of aggregate snowflakes," *J. Geophys. Res. Atmos.*, vol. 118, no. 14, pp. 7873–7885, 2013.

- [51] C. Matzler, *Thermal Microwave Radiation*. London, U.K.:The Institution of Engineering and Technology, 2006.
- [52] S. G. Warren, and R. E. Brandt, "Optical constants of ice from the ultraviolet to the microwave: A revised compilation," *J. Geophys. Res.*, vol. 113, p. D14220, 2008, doi:10.1029/2007JD009744.
- [53] C. Prigent, F. Chevallier, F. Karbou, P. Bauer, and G. Kelly, "AMSU-A land surface emissivity estimation for numerical weather prediction assimilation schemes," *J. Appl. Meteorol.*, vol. 44, no. 4, pp. 416–426, 2005.
- [54] E. Defier, V. S. Galligani, C. Prigent, and C. Jimenez, "First observations of polarized scattering over ice clouds at close-to-millimeter wavelengths (157 GHz) with MADRAS on board the megha-tropiques mission," *J. Geophys. Res. Atmos.*, vol. 119, no. 21, pp. 12301–12316, 2014, [Online]. Available: <http://dx.doi.org/10.1002/2014JD022353>
- [55] E. Wattrelot, "Implementation of the 1d+3d-var assimilation of radar reflectivities in the arome model at météo-france," in *Proc. Joint 19th ALADIN Workshop HIRLAM ASM*, Utrecht, The Netherlands, pp. 1852–1873, May 2009.
- [56] P. Bauer et al., "Satellite cloud and precipitation assimilation at operational nwp centres," *Quart. J. Roy. Meteorol. Soc.*, vol. 137, no. 661, pp. 1934–1951, 2011.
- [57] C. D. Kummerow et al., "The evolution of the goddard profiling algorithm to a fully parametric scheme," *J. Atmos. Ocean. Technol.*, vol. 32, no. 12, pp. 2265–2280, 2015.
- [58] E. Defier et al., "Development of precipitation retrievals at millimeter and sub-millimeter wavelengths for geostationary satellites," *J. Geophys. Res. Atmos.*, vol. 113, no. D8, p. D08111, 2008.
- [59] C. Bishop, *Neural Networks for Pattern Recognition*. Oxford, U.K.: Oxford Univ. Press, 1996, p. 482.
- [60] F. Aires, C. Prigent, F. Bernardo, and C. Jiménez, R. Saunders, and P. Brunel, "A tool to estimate land-surface emissivities at microwave frequencies (TELSEM) for use in numerical weather prediction," *Quart. J. Roy. Meteorol. Soc.*, vol. 137, no. 656, pp. 690–699, 2011.
- [61] M. D. Richard and R. P. Lippmann, "Neural network classifiers estimate bayesian a posteriori probabilities," *Neural Comput.*, vol. 3, no. 4, pp. 461–483, 1991.
- [62] D. Rumelhart, G. Hinton, and R. Williams, *Learning Internal Representations by Error Propagation*, vol. I. Cambridge, MA, USA, MIT Press, 1986, pp. 318–362.
- [63] C. Kummerow, W. S. Olson, and L. Giglio, "A simplified scheme for obtaining precipitation and vertical hydrometeor profiles from passive microwave sensors," *IEEE Trans. Geosci. Remote Sens.*, vol. 34, no. 5, pp. 1213–1232, Sep. 1996.
- [64] V. Marecal and J.-F. Mahfouf, "Four-dimensional variational assimilation of total column water vapor in rainy areas," *Monthly Weather Rev.*, vol. 130, no. 1, pp. 43–58, 2001.
- [65] J. R. McCollum and R. R. Ferraro, "Next generation of NOAA/NESDIS TMI, SSM/I, and AMSR-E microwave land rainfall algorithms," *J. Geophys. Res. Atmos.*, vol. 108, no. D8, p. 8382, 2003, doi:10.1029/2001JD001512.
- [66] S. Yuter et al., "Remaining challenges in satellite precipitation estimation using the tropical rainfall measuring mission," in *Proc. 4th Eur. Conf. Radar Meteorol. Hydrol.*, Barcelona, Spain, 2006, pp. 1–4.



DIE WANG received the M.S. degree in meteorology from the Nanjing University of Information Science and Technology, Nanjing, China, in 2013.

She is currently pursuing the Ph.D. degree with l'Université Pierre et Marie Curie, Paris, France, where he is involved in passive microwave and airborne remote sensing of clouds.



CATHERINE PRIGENT received the Ph.D. degree in physics from Paris University in 1988.

Since 1990, she has been a Researcher with the Centre National de la Recherche Scientifique, Laboratoire d'Etudes du Rayonnement et de la Matière en Astrophysique, Paris Observatory. From 1995 to 2000, she was with the NASA/Goddard Institute for Space Studies, Columbia University, New York. She is currently the Co-Founder of Estellus, a start-up specialized

in satellite Earth observations and also an Adjunct Research Scientist with the Water Center, Columbia University. She was involved in the modeling of the sea surface emissivities at microwave wavelengths and the estimation of atmospheric parameters over ocean from microwave measurements. She has authored over 120 papers in international journals, covering a large range of Earth remote sensing applications. Her current research interests include satellite microwave remote sensing of the Earth, for both surface and atmosphere characterization for global applications, the atmospheric and surface parameters over land from microwave observations using the synergy with satellite measurements at other wavelengths, key surface parameters include microwave land emissivities, all weather determination of land skin temperature, and the first estimates of the wetland extent and dynamics at global scale, and satellite remote sensing of clouds with the analysis of passive microwave and millimeter observations.



FILIPE AIRES received the Ph.D. degree in statistics from the University of Paris, Dauphine, France, in 1999, and the M.A. degree in mathematics of finance from Columbia University, New York, NY, USA, in 2002.

He was an Associate Research Scientist with the GISS/NASA, New York, USA, for five years. He joined the Laboratoire de Météorologie Dynamique as a Research Scientist with the Centre National de la Recherche Scientifique, Paris,

France. In 2009, he co-founded Estellus/Paris, a start-up working for space agencies, in the field of remote sensing. He has been an Adjunct Research Scientist with the Water Center, Columbia University, New York, NY, USA, since 2013. In 2015, he joined the Laboratoire d'Etudes du Rayonnement et de la Matière en Astrophysique, Observatoire de Paris, Paris, France, as a Senior Research Scientist. His research interests focus on satellite remote sensing of the earth and statistical analysis of the climate. In earlier works, he analyzed climatic variability using sophisticated mode decomposition, neural networks, or feedback analysis tools. He has developed multi-instrument and multi-parameter remote sensing algorithms to retrieve atmospheric variables such as temperature or water vapor profiles, and surface variables, such as surface skin temperature, wetland, soil moisture, or infrared/microwave emissivities. The instruments involved in these remote sensing studies include the AMSU, IASI, AIRS, SSM/I, TOVS, SWOT, SAPHIR, GPM. He was part of the Science and Algorithm Committee of the French/Indian mission Megha-Tropiques in charge of the atmospheric water vapor retrieval chain. He is currently a Principal Investigator for NASA, National Oceanic and Atmospheric Administration, European Space Agency, or Centre National d'Etudes Spatiales projects and also with the science committees of the Surface Water and Ocean Topography and the global precipitation measurement missions and involved in climate impacts in socioeconomic activities such as agriculture.



CARLOS JIMENEZ received the Ph.D. degree in environmental science from the Chalmers University of Technology, Gothenburg, Sweden, in 2003.

From 2007 to 2013, he was a Researcher with the Laboratoire d'Etudes du Rayonnement et de la Matière en Astrophysique, Observatoire de Paris, Paris, France. He is currently with Estellus, Paris. He was involved in the inversion of satellite limb sounding microwave observations to determine the chemical composition of the Earth's atmosphere.

His current research interests include the analysis of multisatellite observations to characterize different land surface components of the Earth water and energy cycles. He is also involved in satellite remote sensing of ice clouds from the analysis of passive microwave observations and is active in the development of submillimeter instruments for future cloud satellite missions.

...

References

- Ackerman, S. A., and G. L. Stephens, 1987: The absorption of solar radiation by cloud droplets: An application of anomalous diffraction theory. *J. Atmos. Sci.*, **44**, 1574–1588.
- Aires, F., O. Aznay, C. Prigent, M. Paul, and F. Bernardo, 2012: Synergistic multi-wavelength remote sensing versus a posteriori combination of retrieved products: Application for the retrieval of atmospheric profiles using metop-a. *Journal of Geophysical Research: Atmospheres*, **117** (17).
- Aires, F., C. Prigent, F. Bernardo, C. Jiménez, R. Saunders, and P. Brunel, 2011: A tool to estimate land-surface emissivities at microwave frequencies (telsem) for use in numerical weather prediction. *Quarterly Journal of the Royal Meteorological Society*, **137** (656), 690–699.
- Aires, F., C. Prigent, W. Rossow, and M. Rothstein, 2001: A new neural network approach including first-guess for retrieval of atmospheric water vapour, cloud liquid water path, surface temperature and emissivities over land from satellite microwave observations. *J. Geophys. Res.*, **106**, 14 887–14 907.
- Alberti, G., A. Memoli, G. Pica, M. R. Santovito, B. Buralli, S. Varchetta, S. d’Addio, and V. Kangas, 2012: Two microwave imaging radiometers for metop second generation. *Proc. of the 2012 CNIT Tyrrhenian Workshop*.
- Alishouse, J., S. Snyder, V. Jennifer, and R. Ferraro, 1990: Determination of oceanic total precipitable water from the ssm/i. *IEEE Trans. Geosci. Remote Sens.*, **28**, 811–816.
- Anderson, G. P., S. Clough, F. Kneizys, J. Chetwynd, and E. P. Shettle, 1986: Aflg atmospheric constituent profiles (0.120 km). *Tech. Rep., DTIC Document*.
- Arnott, W. P., Y. Dong, J. Hallett, and J. Poellot, 1994: Role of small ice crystals in radiative properties of cirrus: A case study, fire ii, november 22, 1991. *J. Geophys. Res.*, **99** (D1), 1371–1382.
- Baran, A. J., P. J. Connolly, A. J. Heymsfield, and A. Bansemmer, 2011: Using in situ estimates of ice water content, volume extinction coefficient, and the total solar optical depth obtained during the tropical active campaign to test an ensemble model of cirrus ice crystals. *Q. J. Roy. Meteor. Soc.*, **137**, 199–218.

- Barthazy, E., 1998: Microphysical properties of the melting layer. Ph.D. thesis, ETH, Zurich.
- Battaglia, A., C. Kummerow, D. B. Shin, and C. Williams, 2003: Constraining microwave brightness temperatures by radar brightband observations. *Journal of Atmospheric and Oceanic Technology*, **(6)**, 856–871, doi:10.1175/1520-0426(2003)020<0856:CMBTBR>2.0.CO;2.
- Bauer, P., 2001: Including a melting layer in microwave radiative transfer simulation for clouds. *Atmospheric Research*, **57 (1)**, 9–30, doi:10.1016/S0169-8095(00)00072-7.
- Bauer, P., and Coauthors, 2011: Satellite cloud and precipitation assimilation at operational nwp centres. *Q.J.R. Meteorol. Soc.*, **137**, 1934–1951, doi:10.1002/qj.905.
- Baum, B. A., A. J. Heymsfield, P. Yang, and S. T. Bedka, 2005: Bulk scattering properties for the remote sensing of ice clouds. part i: Microphysical data and models. *Journal of Applied Meteorology*, **44 (12)**, 1885–1895, doi:10.1175/JAM2308.1, URL <http://dx.doi.org/10.1175/JAM2308.1>, <http://dx.doi.org/10.1175/JAM2308.1>.
- Bernardo, F., F. Aires, and C. Prigent, 2013: Atmospheric water-vapour profiling from passive microwave sounders over ocean and land. Part II: Validation using existing instruments. *Quarterly Journal of the Royal Meteorological Society*, **139 (673)**, 865–878, doi:10.1002/qj.1946, URL <https://hal.archives-ouvertes.fr/hal-01091222>.
- Bishop, C., 1996: *Neural Networks for Pattern Recognition*, 482. Oxford University Press.
- Bohren, C. F., and L. J. Battan, 1982: Radar backscattering of microwaves by spongy ice spheres. *J. Atmos. Sci.*, **39**, 2623–2628.
- Bormann, N., A. Geer, and S. English, 2004: Evaluation and comparison of fastem version 2 to 5. Tech. rep., ECMWF, Reading, UK.
- Born, M., and E. Wolf, 1980: *Principles of Optics*. Oxford: Pergamon.
- Boukabara, S. A., L. Eymard, C. Guillou, D. Lemaire, P. Sobieski, and A. Guisard, 2002: Development of a modified two-scale electromagnetic model, simulating both active and passive microwave measurements. comparison to data remotely sensed over the ocean. *Radio Science*, **37 (4)**.
- Brandes, E. A., K. Ikeda, G. Zhand, M. Schonhuber, and R. M. Rasmussen, 2007: A statistical and physical description of hydrometeor distributions in colorado snowstorms using a video disdrometer. *J. Appl. Meteorol. Climatol.*, **46**, 634–650.

- Brogniez, H., P.-E. Kirstetter, and L. Eymard, 2011: Expected improvements in the atmospheric humidity profile retrieval using the megha-tropiques microwave payload. *Q. J. R. Meteorol. Soc.*, doi:10.1002/qj.1869.
- Bruggeman, V. D., 1935: Berechnung verschiedener physikalischer konstanten von heterogenen substanzen. i. dielektrizitetskonstanten und leitfehgkeiten der mischkerper aus isotropen substanzen. *Ann. Phys.*, **416**, 636–664.
- Brussaard, G., and P. A. Watson, 1995: *Atmospheric modelling and millimetre wave propagation*. New York : Chapman and Hall.
- Buehler, S. A., P. Eriksson, T. Kuhn, A. von Engeln, and C. Verdes, 2005: ARTS, the atmospheric radiative transfer simulator. *Journal of Quantitative Spectroscopy and Radiative Transfer*, **91** (1), 65–93, doi:10.1016/j.jqsrt.2004.05.051, URL <http://dx.doi.org/10.1016/j.jqsrt.2011.03.001>.
- Buehler, S. A., A. von Engeln, E. Brocard, V. O. John, T. Kuhn, and P. Eriksson, 2006: Recent developments in the line-by-line modeling of outgoing longwave radiation. *Journal of Quantitative Spectroscopy and Radiative Transfer*, **98** (3), 446–457, doi:<http://dx.doi.org/10.1016/j.jqsrt.2005.11.001>, URL <http://www.sciencedirect.com/science/article/pii/S0022407305003316>.
- Buehler, S. A., and Coauthors, 2007a: A concept for a satellite mission to measure cloud ice water path and ice particle size. *Q. J. R. Meteorol. Soc.*, **133** (S2), 109–128, doi:10.1002/qj.143.
- Buehler, S. A., and Coauthors, 2007b: A concept for a satellite mission to measure cloud ice water path, ice particle size, and cloud altitude. *Q. J. Roy. Meteorol. Soc.*, **133**, 109–128.
- Buehler, S. A., and Coauthors, 2012: Observing ice clouds in the submillimeter spectral range: The CloudIce mission proposal for ESA’s Earth Explorer 8. *Atmospheric Measurement Techniques*, **5** (7), 1529–1549, doi:10.5194/amt-5-1529-2012.
- Burns, B. A., 1997: Effects of precipitation and cloud ice on brightness temperatures in amsu moisture channels. *IEEE Transactions on Geoscience and Remote Sensing*, **35** (6), 1429–1437, doi:10.1109/36.649797.
- Cavan, N., M. E. Humphries, and S. D. Lewis, 2011: Preliminary development of a long-life contactless power and data transfer module for next generation radiometry devices. *Proceedings of the 14th European Space Mechanisms and Tribology Symposium ESMATS*, Constance, Germany.
- Chaboureau, J.-P., and Coauthors, 2008: A midlatitude precipitating cloud database validated with satellite observations. *Journal of Applied Meteorology and Climatology*, **47** (5), 1337–1353, doi:10.1175/2007JAMC1731.1, URL <http://dx.doi.org/10.1175/2007JAMC1731.1>, <http://dx.doi.org/10.1175/2007JAMC1731.1>.

- Charlton, J. E., S. Buehler, E. Defer, C. Prigent, B. Moyna, C. Lee, P. De Maagt, and V. Kangas, 2009: A sub-millimetre wave airborne demonstrator for the observation of precipitation and ice clouds. *International Geoscience and Remote Sensing Symposium (IGARSS)*, **3**, 1023–1026, doi:10.1109/IGARSS.2009.5417952.
- Chen, F., and J. Dudhia, 2001: Coupling an advanced land surface hydrology model with the penn state near mm5 modeling system. part ii: Preliminary model validation. *Mon. Wea. Rev.*, **129**, 587–604.
- Chylek, P., and J. D. Klett, 1991: Absorption and scattering of electromagnetic radiation by prismatic columns: anomalous diffraction approximation. *J. Opt. Soc. Am.*, **A8**, 1713–1720.
- Clark, M. R., and J. D. C. Webb, 2013: A severe hailstorm across the english midlands on 28 june 2012. *Weather*, **68**, 284–291, doi:10.1002/wea.2162.
- Colton, M. C., and G. A. Poe, 1999: Intersensor calibration of DMSP SSM/T's: F-8 to F-14, 1987-1997. *IEEE Transactions on Geoscience and Remote Sensing*, **37 (1 II)**, 418–439, doi:10.1109/36.739079.
- Czekala, H., S. Crewell, A. Hornbostel, A. Schroth, C. Simmer, and A. Thiele, 2001: Interpretation of polarization features in ground based microwave observations as caused by horizontally aligned oblate rain drops. *J. Appl. Meteorol.*, **40**, 1918–1932.
- Davis, C. P., C. Emde, and R. S. Harwood, 2005: A 3-d polarized reversed monte carlo radiative transfer model for millimeter and submillimeter passive remote sensing in cloudy atmospheres. *IEEE Trans. Geosci. Remote Sens.*, **43**, 1096–1101.
- Davis, C. P., K. F. Evans, S. A. Buehler, D. L. Wu, and H. C. Pumphrey, 2007: 3-d polarised simulations of space-borne passive mm/sub-mm midlatitude cirrus observations: a case study. *Atmospheric Chemistry and Physics, European Geosciences Union*, 1843–1853.
- Debye, P., 1929: *Polar molecules*. The Chemical Catalog Company Inc.
- Deeter, M., and K. F. Evans, 2000: A novel ice-cloud retrieval algorithm based on the millimeter-wave imaging radiometer (mir) 150-and 220-ghz channels. *J. Appl. Meteor.*, **39**, 623–633, doi:10.1175/1520-0450-39.5.623.
- Defer, E., V. S. Galligani, C. Prigent, and C. Jimenez, 2014: First observations of polarized scattering over ice clouds at close-to-millimeter wavelengths (157ghz) with madras on board the megha-tropiques mission. *J. Geophys. Res. Atmos.*, **119 (21)**, doi:10.1002/2014JD022353.
- Defer, E., C. Prigent, F. Aires, J. R. Pardo, C. J. Walden, O.-Z. Zanife, J.-P. Chaboureaud, and J.-P. Pinty, 2008: Development of precipitation retrievals at

- millimeter and sub-millimeter wavelengths for geostationary satellites. *J. Geophys. Res.*, **113**, doi:10.1029/2007JD008673.
- DeVoe, H., 1964: Optical properties of molecular aggregates. i. classical model of electronic absorption and refraction. *J. Chem. Phys.*, **41**, 393–400.
- DeVoe, H., 1965: Optical properties of molecular aggregates. ii. classical theory of the refraction, absorption, and optical activity of solutions and crystals. *J. Chem. Phys.*, **43**, 3199–3208.
- Draine, B. T., and P. J. Flatau, 1994: Discrete-dipole approximation for scattering calculations. *J. Opt. Soc. Amer.*, **11**, 1491–1499.
- Dudhia, J., 1989: Numerical study of convection observed during the winter monsoon experiment using a mesoscale two-dimensional model. *J. Atmos. Sci.*, **46** (20), 3077–3107.
- Eliasson, S., S. A. Buehler, M. Milz, P. Eriksson, and V. O. John, 2011: Assessing observed and modelled spatial distributions of ice water path using satellite data. *Atmospheric Chemistry and Physics*, **11** (1), 375–391, doi:10.5194/acp-11-375-2011.
- Emde, C., S. Buehler, C. Davis, P. Eriksson, T. R. Sreerekha, and C. Teichmann, 2004: A polarized discrete ordinate scattering model for simulations of limb and nadir long-wave measurements in 1-d/3-d spherical atmospheres. *Journal of Geophysical Research*, doi:10.1029/2004JD005140.
- English, S., 2006: Issues in ocean emissivity modelling. *1st Workshop on Remote Sensing and Modeling of Surface Properties*, Paris, France.
- English, S. J., and T. J. Hewison, 1998: Fast generic millimeter-wave emissivity model. *Proceedings SPIE Microwave Remote Sensing of the Atmosphere and Environment*, **3508**, 288–300.
- Eriksson, P., S. A. Buehler, C. P. Davis, C. Emde, and O. Lemke, 2011: Arts, the atmospheric radiative transfer simulator, version 2. *Journal of Quantitative Spectroscopy and Radiative Transfer*, **112** (10), 1551–1558.
- Eriksson, P., M. Jamali, J. Mendrok, and S. A. Buehler, 2015: On the microwave optical properties of randomly oriented ice hydrometeors. *Atmos. Meas. Tech.*, **8**, 1913–1933.
- Evans, K. F., and G. L. Stephens, 1995: Microwave radiative transfer through clouds composed of realistically shaped ice crystals. part i. single scattering properties. *Journal of the Atmospheric Sciences*, **52** (11), 2041–2057, doi:10.1175/1520-0469(1995)052<2041:MRTTCC>2.0.CO;2, URL [http://dx.doi.org/10.1175/1520-0469\(1995\)052<2041:MRTTCC>2.0.CO;2](http://dx.doi.org/10.1175/1520-0469(1995)052<2041:MRTTCC>2.0.CO;2), [http://dx.doi.org/10.1175/1520-0469\(1995\)052<2041:MRTTCC>2.0.CO;2](http://dx.doi.org/10.1175/1520-0469(1995)052<2041:MRTTCC>2.0.CO;2).

- Evans, K. F., S. J. Walter, A. J. Heymsfield, and G. M. McFarquhar, 2002: Submillimeter-Wave Cloud Ice Radiometer: Simulations of retrieval algorithm performance. *J. Geophys. Res.*, **107**, 4028, doi:10.1029/2001JD000709.
- Evans, K. F., J. R. Wang, P. E. Racette, G. Heymsfield, and L. Li, 2005: Ice Cloud Retrievals and Analysis with the Compact Scanning Submillimeter Imaging Radiometer and the Cloud Radar System during CRYSTAL FACE. *Journal of Applied Meteorology*, **44** (6), 839–859, doi:10.1175/JAM2250.1.
- Fabry, F., and W. Szyrmer, 1999: Modeling of the melting layer. part ii: Electromagnetics. *J. Atmos. Sci.*, **56**, 3593–3600.
- Ferraro, R., F. Weng, N. Grody, and A. Basist, 1996: An eight-year (1987-1994) time series of rainfall, clouds, water vapor, snow cover, and sea ice derived from ssm/i measurements. *Bull. Amer. Meteor. Soc.*, **77**, 891–905, doi:10.1029/2000JD000258.
- Field, P. R., and A. J. Heymsfield, 2003: Aggregation and scaling of ice crystal size distributions. *J. Atmos. Sci.*, **60**, 544–560.
- Field, P. R., A. J. Heymsfield, and A. Bansemer, 2007: Snow size distribution parameterization for midlatitude and tropical ice clouds. *J. Atmos. Sci.*, **64**, 4346–4365.
- Fox, S., 2015: Microwave radiometer polarization description. Tech. rep., UK Met Office.
- Fox, S., C. Lee, I. Rule, R. King, S. Rogers, C. Harlow, and A. Baran, 2014: ISMAR: A new submillimeter airborne radiometer. *13th Specialist Meeting on Microwave Radiometry and Remote Sensing of the Environment, MicroRad 2014 - Proceedings*, 128–132, doi:10.1109/MicroRad.2014.6878923.
- Fox, S., and Coauthors, 2016: Ismar: an airborne submillimetre radiometer. *Atmos. Meas. Tech. Discuss.*, doi:10.5194/amt-2016-310,2016.
- Franklin, C. N., G. J. Holland, and P. T. May, 2005: Sensitivity of tropical cyclone rainbands to ice-phase microphysics. *Mon. Wea. Rev.*, **133**, 2473–2493.
- Galligani, V. S., C. Prigent, E. Defer, C. Jimenez, and P. Eriksson, 2013: The impact of the melting layer on the passive microwave cloud scattering signal observed from satellites: A study using trmm microwave passive and active measurements. *J. Geophys. Res. Atmos.*, **118**, 5667–5678, doi:10.1002/jgrd.50431.
- Galligani, V. S., C. Prigent, E. Defer, C. Jimenez, P. Eriksson, J.-P. Pinty, and J.-P. Chaboureau, 2015: Meso-scale modelling and radiative transfer simulations of a snowfall event over france at microwaves for passive and active modes and evaluation with satellite observations. *Atmos. Meas. Tech.*, **8**, 1605–1616.
- Garnett, J. M., 1906: Colours in metal glasses, in metallic films, and in metallic solutions. *Philos. Tr. Roy. Soc. London*, 237–288.

- Geer, A. J., and F. Baordo, 2014: Improved scattering radiative transfer for frozen hydrometeors at microwave frequencies. *Atmospheric Measurement Techniques*, **7** (6), 1839–1860, doi:10.5194/amt-7-1839-2014.
- Gherboudj, I., M. Bernier, and R. Leconte, 2010: A backscatter modeling for river ice: Analysis and numerical results. *IEEE Trans. Geosci. Remote Sens.*, **48** (4), 1788–1798.
- Greenwald, T. J., 2002: Effect of cold clouds on satellite measurements near 183 GHz. *Journal of Geophysical Research*, **107** (D13), 1–9, doi:10.1029/2000JD000258.
- Guillou, C., S. J. English, C. Prigent, and D. C. Jones, 1996: Passive microwave airborne measurements of the sea surface response at 89 and 157 ghz. *Journal of Geophysical Research: Oceans*, **101** (C2), 3775–3788, doi:10.1029/95JC01720, URL <http://dx.doi.org/10.1029/95JC01720>.
- Guimaraes, L. G., and H. M. Nussenzveig, 1992: Theory of mie resonances and the ripple fluctuations. *Optics Commun.*, **89**, 363–369.
- Guissard, A., P. Sobieski, and C. Baufays, 1992: A unified approach to bistatic scattering for active and passive remote sensing of rough ocean surfaces. *Trends in Geoph.ys. Res.*, **1**, 43–68.
- Gunn, K. L. S., and J. S. Marshall, 1958: The distribution with size of aggregate snowflakes. *Journal of Meteorology*, **15**, 452–461.
- Harlow, R. C., 2009: Millimeter microwave emissivities and effective temperatures of snow-covered surfaces: evidence for Lambertian surface scattering. *Geoscience and Remote Sensing, IEEE Transactions on*, **47** (7), 1957–1970.
- Harlow, R. C., 2011: Sea ice emissivities and effective temperatures at MHS frequencies: An analysis of airborne microwave data measured during two arctic campaigns. *IEEE Transactions on Geoscience and Remote Sensing*, **49** (4), 1223–1237, doi:10.1109/TGRS.2010.2051555.
- Harlow, R. C., and R. Essery, 2012: Tundra snow emissivities at MHS frequencies: MEMLS validation using airborne microwave data measured during CLPX-II. *IEEE Transactions on Geoscience and Remote Sensing*, **50** (11 PART1), 4262–4278, doi:10.1109/TGRS.2012.2193132.
- Hewison, T. J., 2006: Aircraft validation of clear air absorption models at millimeter wavelengths (89-183 GHz). *Journal of Geophysical Research Atmospheres*, **111** (14), 1–11, doi:10.1029/2005JD006719.
- Hewison, T. J., and S. J. English, 1999: Airborne retrievals of snow and ice surface emissivity at millimeter wavelengths. *IEEE Transactions on Geoscience and Remote Sensing*, **37** (4), 1871–1879, doi:10.1109/36.774700.

- Hewison, T. J., N. Selbach, G. Heygster, J. P. Taylor, and A. J. McGrath, 2002: Airborne Measurements of Arctic Sea Ice, Glacier and Snow Emissivity at 24–183 GHz. *IEEE International Geoscience and Remote Sensing Symposium*, **5**, 2851–2855.
- Heymsfield, A. J., and J. Iaquinta, 2000: Cirrus crystals terminal velocities. *J. Atmos. Sci.*, **57**, 916–938.
- Heymsfield, A. J., S. Lewis, A. Bansemer, J. Iaquinta, L. M. Miloshevich, M. Kajikawa, C. Twohy, and M. R. Poellot, 2002: A general approach for deriving the properties of cirrus and stratiform ice cloud particles. *J. Atmos. Sci.*, **59** (1), 3–29.
- Heymsfield, A. J., Z. Wang, and S. Y. Matrosov, 2005: Improved radar ice water content retrieval algorithms using coincident microphysical and radar measurements. *J. Appl. Meteor.*, **44** (9), 1391–1412.
- Hocking, J., P. J. Rayer, D. Rundle, R. W. Saunders, M. Matricardi, A. Geer, P. Brunel, and J. Vidot, 2014: Rttov v11 users guide. 345.
- Hong, G., 2007: Parameterization of scattering and absorption properties of non-spherical ice crystals at microwave frequencies. *J. Geophys. Res.*, **112**, doi:10.1029/2006JD008364.
- Hong, G., G. Heygster, J. Miao, and K. Kunzi, 2005: Detection of tropical deep convective clouds from AMSU-B water vapor channels measurements. *Journal of Geophysical Research D: Atmospheres*, **110** (5), 1–15, doi:10.1029/2004JD004949.
- Hong, S., V. Lakshmi, E. E. Small, F. Chen, M. Tewari, and K. W. Manning, 2009: Effects of vegetation and soil moisture on the simulated land surface processes from the coupled WRF/Noah model. *Journal of Geophysical Research Atmospheres*, **114** (18), 1–13, doi:10.1029/2008JD011249.
- Hong, S.-Y., J. Dudhia, and S.-H. Chen, 2004: A revised approach to ice microphysical processes for the bulk parameterization of clouds and precipitation. *Mon. Wea. Rev.*, **132**, 103–120.
- Hong, S.-Y., and J.-O. J. Lim, 2006: The wrf single-moment microphysics scheme (wsm6). *J. Korean Meteor. Soc.*, **42**, 129–151.
- Hong, S. Y., Y. Noh, and J. Dudhia, 2006a: A new vertical diffusion package with an 557 explicit treatment of entrainment processes. *Mon. Wea. Rev.*, **134**, 2318–2341.
- Hong, S.-Y., Y. Noh, and J. Dudhia, 2006b: A new vertical diffusion package with an explicit treatment of entrainment processes. *Mon. Wea. Rev.*, **134**, 2318–2341.

- Huang, G. J., V. N. Bringi, R. Cifelli, D. Hudak, and W. A. Petersen, 2010: A methodology to derive radar reflectivity: liquid equivalent snow rate relations using c-band radar and a 2d video disdrometer. *J. Atmos. Ocean. Tech.*, **27**, 637–651.
- Janjic, Z. I., 2002: Nonsingular implementation of the Mellor–Yamada level 2.5 scheme in the NCEP meso model. Tech. Rep. 437, NCEP Office Note. 61.
- Jarret, M., and Coauthors, 2007: Establishment of mission and instrument requirements to observe cirrus clouds at sub-millimetre wavelengths. Final report, ESTEC Contract No. 19053/05/NL/AR.
- Jimenez, C., S. A. Buehler, B. Rydberg, P. Eriksson, and K. F. Evans, 2007: Performance simulations for a submillimetre-wave cloud ice satellite instrument. *Q. J. Roy. Meteorol. Soc.*, **133**, 129–149.
- John, V. O., and S. A. Buehler, 2004: The impact of ozone lines on AMSU-B radiances. *Geophysical Research Letters*, **31** (21), n/a–n/a, doi:10.1029/2004GL021214, URL <http://dx.doi.org/10.1029/2004GL021214>, l21108.
- John, V. O., and S. A. Buehler, 2005: Comparison of microwave satellite humidity data and radiosonde profiles: A survey of European stations. *Atmospheric Chemistry and Physics*, **5** (7), 1843–1853, doi:10.5194/acp-5-1843-2005, URL <http://www.atmos-chem-phys.net/5/1843/2005/>.
- John, V. O., S. A. Buehler, A. v. Engeln, P. Eriksson, T. Kuhn, E. Brocard, and G. Koenig-Langlo, 2006: Understanding the variability of clear-sky outgoing long-wave radiation based on ship-based temperature and water vapour measurements. *Quarterly Journal of the Royal Meteorological Society*, **132** (621), 2675–2691, doi:10.1256/qj.05.70, URL <http://dx.doi.org/10.1256/qj.05.70>.
- John, V. O., and B. J. Soden, 2006: Does convectively-detained cloud ice enhance water vapor feedback? *Geophysical Research Letters*, **33** (20), n/a–n/a, doi:10.1029/2006GL027260, URL <http://dx.doi.org/10.1029/2006GL027260>, l20701.
- Johnson, B. T., G. W. Petty, and G. Skofronick-Jackson, 2012: Microwave properties of ice-phase hydrometeors for radar and radiometers: Sensitivity to model assumptions. *J. Appl. Meteorol. Clim.*, **51**, 2152–2171.
- Kain, J. S., 2004: The Kain–Fritsch convective parameterization: An update. *J. Appl. Meteor.*, **43**, 170–181.
- Kangas, V., S. D’Addio, M. Betto, H. Barre, M. Loiselet, and G. Mason, 2012: Metop second generation microwave sounding and microwave imaging missions. *Proceedings of the 2012 EUMETSAT Meteorological Satellite Conference*, Sopot, Poland.
- Karbou, F., F. Aires, C. Prigent, and L. Eymard, 2005: Potential of advanced microwave sounding unit-A (AMSU-A) and AMSU-B measurements for atmospheric

- temperature and humidity profiling over land. *Journal of Geophysical Research: Atmospheres*, **110** (D7).
- Karbou, F., and C. Prigent, 2005a: Calculation of microwave land surface emissivity from satellite observations: Validity of the specular approximation over snow-free surfaces. *IEEE Geoscience and Remote Sensing Letters*, **2** (3), 311–314.
- Karbou, F., and C. Prigent, 2005b: Calculation of microwave land surface emissivity from satellite observations: Validity of the specular approximation over snow-free surfaces? *IEEE Geoscience and Remote Sensing Letters*, **2** (3), 311–314.
- Karbou, F., F. Rabier, and C. Prigent, 2014: The assimilation of observations from the advanced microwave sounding unit over sea ice in the french global numerical weather prediction system. *Monthly Weather Review*, **142** (1), 125–140.
- Kawanishi, T., T. Sezai, Y. Ito, and R. W. Spencer, 2003: The advanced microwave scanning radiometer for the earth observing system (amsr-e), nasda's contribution to the eos for global energy and water cycle studies. *IEEE Transactions on Geoscience and Remote Sensing*, **41** (2), 184–194.
- Kessler, E., 1969: On the distribution and continuity of water substance in atmospheric circulation. *Amer. Meteor. Soc.*, 84.
- Khain, A. P., and Coauthors, 2015: Representation of microphysical processes in cloud-resolving models: Spectral (bin) microphysics versus bulk parameterization. *Reviews of Geophysics*, **53** (2), 247–322, doi:10.1002/2014RG000468, URL <http://dx.doi.org/10.1002/2014RG000468>, 2014RG000468.
- Kim, M. J., 2006: Single scattering parameters of randomly oriented snow particles at microwave frequencies. *Journal of Geophysical Research Atmospheres*, **111** (14), 1–8, doi:10.1029/2005JD006892.
- Klaassen, W., 1988: Radar observations and simulation of the melting layer of precipitation. *J. Atmos. Sci.*, **45**, 3741–3753.
- Kneifel, S., U. Lehnert, A. Barraglia, S. Crewell, and D. Siebler, 2010: Snow scattering signals in ground-based passive microwave radiometer measurements. *J. Geophys. Res.*, **115** (D16214), 1–17.
- Knoll, G. F., 2010: *Radiation detection and measurement*. John Wiley Sons.
- Kulie, M. S., R. Bennartz, T. J. Greenwald, Y. Chen, and F. Weng, 2010: Uncertainties in Microwave Properties of Frozen Precipitation: Implications for Remote Sensing and Data Assimilation. *Journal of the Atmospheric Sciences*, **67** (11), 3471–3487, doi:10.1175/2010JAS3520.1.

- Kummerow, C., W. Barnes, T. Kozu, J. Shiue, and J. Simpson, 1998: The tropical rainfall measuring mission (trmm) sensor package. *Journal of Atmospheric and Oceanic Technology*, **15** (3), 809–817, doi:10.1175/1520-0426(1998)015<0809:TTRMMT>2.0.CO;2.
- Kummerow, C., and L. Giglio, 1994: A passive microwave technique for estimating rainfall and vertical structure information from space. part 1: Algorithm description. *J. Appl. Meteor.*, **33** (1), 3–18.
- Kummerow, C., W. S. Oison, and L. Giglio, 1996: A simplified scheme for obtaining precipitation and vertical hydrometeor profiles from passive microwave sensors. *IEEE Transactions on Geoscience and Remote Sensing*, **34** (5), 1213–1232, doi:10.1109/36.536538.
- Kummerow, C. D., D. L. Randel, M. Kulie, N.-Y. Wang, R. Ferraro, M. S. Joseph, and V. Petkovic, 2015: The evolution of the goddard profiling algorithm to a fully parametric scheme. *Journal of Atmospheric and Oceanic Technology*, **32** (12), 2265–2280, doi:10.1175/JTECH-D-15-0039.1.
- Liao, L., and R. Meneghini, 2005: On modeling air/spaceborne radar returns in the melting layer. *IEEE Trans. Geo. Remote Sens.*, **43**, 2799–2809.
- Liebe, H. J., G. A. Hufford, and M. G. Cotton, 1993: Propagation modeling of moist air and suspended water/ice particles at frequencies below 1000 ghz proc. *NATO/AGARD Wave Propagation Panel, 52nd meeting*, Mallorca, Spain, 1–10.
- Liebe, H. J., G. A. Hufford, and T. Manabe, 1991: A model for the complex permittivity of water at frequencies below 1 thz. *Internat. J. Infrared and mm Waves*, **12**, 659–675.
- Liebe, H. J., and D. H. Layton, 1987: Millimeter-wave properties of the atmosphere: Laboratory studies and propagation modeling. Report 87-224, National Telecommunications and Information Administration, Boulder, Colo.
- Liebe, H. J., P. Rosenkranz, and G. A. Hufford, 1992: Atmospheric 60 ghz oxygen spectrum: New laboratory measurements and line parameters. *J. Quant. Spectrosc. Radiat. Transfer*, **48**, 629–643.
- Lim, K.-S. S., and S.-Y. Hong, 2010: Development of an effective double-moment cloud microphysics scheme with prognostic cloud condensation nuclei (ccn) for weather and climate models. *Mon. Wea. Rev.*, **138**, 1587–1612, doi:http://dx.doi.org/10.1175/2009MWR2968.1.
- Lin, Y.-L., R. D. Farley, and H. D. Orville, 1983: Bulk parameterization of the snow field in a cloud model. *J. Appl. Meteor.*, **22**, 1065–1092.
- Liou, K.-N., 1986: Influence of cirrus clouds on weather and climate processes: A global perspective. *Mon. Wea. Rev.*, **114**, 1167–1199.

- Liou, K. N., and S. C. Ou, 1989: The role of cloud microphysical processes in climate: an assessment from a one-dimensional perspective. *J. Geophys. Res.*, **94**, 8599–8607.
- Liu, G., 2004: Approximation of single scattering properties of ice and snow particles for high microwave frequencies. *Journal of the Atmospheric Sciences*, **61**, 2441–2456, doi:10.1175/1520-0469(2004)061<2441:AOSSPO>2.0.CO;2.
- Liu, G., 2008: A database of microwave single-scattering properties for nonspherical ice particles. *Bull. Am. Met. Soc.*, **89**, 1563–1570.
- Liu, G., and J. A. Curry, 1998: An investigation of the relationship between emission and scattering signals in ssm/i data. *Journal of the Atmospheric Sciences*, **55** (9), 1628–1643, doi:10.1175/1520-0469(1998)055<1628:AIOTRB>2.0.CO;2, URL [http://dx.doi.org/10.1175/1520-0469\(1998\)055<1628:AIOTRB>2.0.CO;2](http://dx.doi.org/10.1175/1520-0469(1998)055<1628:AIOTRB>2.0.CO;2), [http://dx.doi.org/10.1175/1520-0469\(1998\)055<1628:AIOTRB>2.0.CO;2](http://dx.doi.org/10.1175/1520-0469(1998)055<1628:AIOTRB>2.0.CO;2).
- Liu, G., and J. A. Curry, 2000: Determination of ice water path and mass median particle size using multichannel microwave measurements. *J. Appl. Meteor.*, **38**, 1182–1194.
- Liu, Q., F. Weng, and S. J. English, 2011: An improved fast microwave water emissivity model. *IEEE Transactions on Geoscience and Remote Sensing*, **49** (4), 1238–1250, doi:10.1109/TGRS.2010.2064779.
- Liu, Y. Q., C. P. Weaver, and R. Avissar, 1999: Toward a parameterization of mesoscale fluxes and moist convection induced by landscape heterogeneity. *Journal of Geophysical Research-Atmospheres*, **104** (D1612354), 19 515–19 533, doi:10.1029/1999JD900361.
- Locatelli, J. D., and P. V. Hobbs, 1974: Fall speeds and masses of solid precipitation particles. *J. Geophys. Res.*, **79**, 2185–2197.
- Lohmann, U., and E. Roeckner, 1995: Influence of cirrus cloud radiative forcing on climate and climate sensitivity in a general circulation model. *J. Geophys. Res.*, **100**, 16 305–16 324.
- Magono, C., and T. Nakamura, 1965: Aerodynamic studies of falling snowflakes. *J. Meteor. Soc.*, **43**, 139–147.
- Manzato, A., 2012: Hail in northeast italy: climatology and bivariate analysis with the sounding-derived indices. *J. Appl. Meteorol. Climatol.*, **51** (3), 449–467.
- Marecal, V., and J.-F. Mahfouf, 2001: Four-dimensional variational assimilation of total column water vapor in rainy areas. *Mon. Wea. Rev.*, 43–58.
- Marshall, J. S., and W. M. K. Palmer, 1948: The distribution of raindrops with size. *J. Meteor.*, **5**, 165–166.

- Matricardi, M., F. Chevallier, and S. Tjemkes, 2001: An improved general fast radiative transfer model for the assimilation of radiance observations. *ECMWF Technical Memorandum*, 345.
- Matrosov, S. Y., A. J. Heymsfield, and Z. Wang, 2005: Dual-frequency radar ratio of nonspherical atmospheric hydrometeors. *Geophysical Research Letters*, **32** (13), 1–4, doi:10.1029/2005GL023210.
- Matzler, C., Ed., 2006: *Thermal Microwave Radiation*. The Institution of Engineering and Technology.
- McCollum, J. R., and R. R. Ferraro, 2003: Next generation of noaa/nesdis tmi, ssm/i, and amsr-e microwave land rainfall algorithms. *Journal of Geophysical Research*, doi:10.1029/2001JD001512.
- Meirolid-Mautner, I., C. Prigent, E. Defer, J.-R. Pardo, J.-P. Chaboureau, J.-P. Pinty, M. Mech, and S. Crewell, 2007: Radiative transfer simulations using mesoscale cloud model outputs: comparisons with passive microwave and infrared satellite observations for mid-latitudes. *J. Atmos. Sci.*, **64**, 1550–1568.
- Milbrandt, J. A., and M. K. Yau, 2005: A multimoment bulk microphysics parameterization. part ii: A proposed three-moment closure and scheme description. *J. Atmos. Sci.*, **62**, 3065–3081.
- Mishchenko, M. I., L. D. Travis, and A. A. Lacis, 2002: *Scattering, Absorption, and Emission of Light by Small Particles*. Cambridge Univ. Press, New York.
- Mitchell, D. L., R. Zhang, and R. L. Pitter, 1990: Mass dimensional relationships for ice particles and the influence of riming on snowfall rates. *J. Appl. Meteor.*, **29**, 153–163.
- Mlawer, E. J., S. J. Taubman, and P. D. Brown, 1997: Radiative transfer for inhomogeneous atmosphere: Rrtm, a validated correlated-k model for the longwave. *J. Geophys. Res.*, **102**, 16 663–16 682.
- Moncet, J. L., P. Liang, J. F. Galantowicz, A. E. Lipton, G. Uymin, C. Prigent, and C. Grassotti, 2011: Land surface microwave emissivities derived from AMSR-E and MODIS measurements with advanced quality control. *Journal of Geophysical Research Atmospheres*, **116** (16), 1–98, doi:10.1029/2010JD015429.
- Morrison, H., J. A. Curry, and V. I. Khvorostyanov, 2005: A new double-moment microphysics parameterization for application in cloud and climate models. part i: Description. *J. Atmos. Sci.*, **62**, 1665–1677.
- Morrison, H., G. Thompson, and V. Tatarskii, 2009: Impact of cloud microphysics on the development of trailing stratiform precipitation in a simulated squall line: Comparison of one- and two-moment schemes. *Mon. Wea. Rev.*, **137**, 991–1007.

- Noh, Y. J., G. Liu, E. K. Seo, J. R. Wang, and K. Aonashi, 2006: Development of a snowfall retrieval algorithm at high microwave frequencies. *Journal of Geophysical Research Atmospheres*, **111** (22), 1–16, doi:10.1029/2005JD006826.
- Nowell, H., G. Liu, and R. Honeyager, 2013: Modeling the microwave single-scattering properties of aggregate snowflakes. *Journal of Geophysical Research Atmospheres*, **118** (14), 7873–7885, doi:10.1002/jgrd.50620.
- ODell, C., J. Wentz, and R. Bennartz, 2008: Cloud liquid water path from satellite-based passive microwave observations: A new climatology over the global oceans. *J. Climate*, **21**, 1721–1739.
- Oguchi, T., 1983: Electromagnetic wave propagation and scattering in rain and other hydrometeors. *Proc. IEEE*, **71**, 1029–1078.
- Okamoto, H., 2002: Information content of the 95 ghz cloud radar signals: Theoretical assessment of effects of non-sphericity and error evaluations of the discrete dipole approximation. *J. Geophys. Res.*, **107** (D22), 4628.
- Olson, W. S., P. Bauer, C. D. Kummerow, Y. Hong, and W. K. Tao, 2001a: A melting-layer model for passive/active microwave remote sensing applications. part ii: Simulation of trmm observations. *J. Appl. Meteor.*, **40**, 1164–1179.
- Olson, W. S., P. Bauer, N. F. Viltard, D. E. Johnson, W.-K. Tao, R. Meneghini, and L. Liao, 2001b: A melting-layer model for passive/active microwave remote sensing applications. part i: Model formulation and comparison with observations. *J. Appl. Meteor.*, **40**, 1145–1163.
- Pardo, J. R., J. Cernicharo, and E. Serabyn, 2001: Atmospheric transmission at microwaves (atm): an improved model for millimeter/submillimeter applications. *IEEE Transactions on Antennas and Propagation*, **49** (12), 1683–1694, doi:10.1109/8.982447.
- Petty, G. W., and W. Huang, 2011: The modified gamma size distribution applied to inhomogeneous and nonspherical particles: Key relationships and conversions. *J. Atmos. Sci.*, **68**, 1460–1473.
- Picard, G., L. Brucker, A. Roy, F. Dupont, M. Fily, A. Royer, and C. Harlow, 2013: Simulation of the microwave emission of multi-layered snowpacks using the Dense Media Radiative transfer theory: the DMRT-ML model. *Geoscientific Model Development*, **6** (4), 1061–1078, doi:10.5194/gmd-6-1061-2013, URL <http://www.geosci-model-dev.net/6/1061/2013/>.
- Pinty, J. P., and P. Jabouille, 1998: A mixed-phase cloud parameterization for use in mesoscale non-hydrostatic model: simulations of a squall line and of orographic precipitations. *Proc. Conf. of Cloud Physics*, Everett, WA, USA, 217–220.

- Prabhakara, C., D. A. Short, W. Wiscombe, R. A. Fraser, and B. E. Vollmer, 1986: Rainfall over oceans inferred from nimbus 7 smmr: Application to 1982-83 el nifio. *J. Climate Appl. Meteor.*, **25**, 1464–1474.
- Prigent, C., and P. Abba, 1990: Sea surface equivalent brightness temperature at millimeter wavelength. *Annales Geophysicae*, **8**, 627–634.
- Prigent, C., F. Aires, W. Rossow, and E. Matthews, 2001: Joint characterization of vegetation by satellite observations from visible to microwave wavelengths: A sensitivity analysis. *Journal of Geophysical Research*, **106** (D18), 20 665.
- Prigent, C., F. Aires, and W. B. Rossow, 2006: Land Surface Microwave Emissivities over the Globe for a Decade. *Bulletin of the American Meteorological Society*, **87** (11), 1573–1584, URL <http://journals.ametsoc.org/doi/abs/10.1175/BAMS-87-11-1573>.
- Prigent, C., F. Aires, and D. Wang, 2016: Sea surface emissivity parameterization from microwaves to millimeter waves, quarterly Journal of the Royal Meteorological Society.
- Prigent, C., F. Chevallier, F. Karbou, P. Bauer, and K. G., 2005: Amsu-a surface emissivities for numerical weather prediction assimilation schemes. *Journal of Applied Meteorology*, **44**, 416–426.
- Prigent, C., E. Jaumouillé, F. Chevallier, and F. Aires, 2008: A parameterization of the microwave land surface emissivity between 19 and 100 GHz, anchored to satellite-derived estimates. *Geoscience and Remote Sensing, IEEE Transactions on*, **46** (2), 344–352.
- Prigent, C., P. Liang, Y. Tian, F. Aires, J.-L. Moncet, and S. A. Boukabara, 2015: Evaluation of modeled microwave land surface emissivities with satellite-based estimates. *Journal of Geophysical Research: Atmospheres*, **120** (7), 2706–2718.
- Prigent, C., W. B. Rossow, and E. Matthews, 1997: Microwave land surface emissivities estimated from SSM/I observations. *Journal of Geophysical Research: Atmospheres*, **102** (D18), 21 867–21 890.
- Pullianen, J. T., and J. Grandeil, 1999: HUT snow emission model and its applicability to snow water equivalent retrieval. *IEEE Transactions on Geoscience and Remote Sensing*, **37** (3 I), 1378–1390, doi:10.1109/36.763302.
- Putsay, M., A. Simon, I. Szenyan, J. Kerkmann, and G. Horvath, 2011: Case study of the 20 may 2008 tornadic storm in hungary - remote sensing features and nwp simulation. *Atmospheric Research*, **100**, 657–679, doi:10.1016/j.atmosres.2010.08.008.
- Racette, F., R. F. Adler, and J. R. Wang, 1996: An airborne millimeter-wave imaging radiometer for cloud, precipitation, and atmospheric water vapor studies. *Journal of atmospheric and oceanic technology*, **13**, 610–619.

- Rajeevan, M., A. Kesarkar, S. B. Thampi, T. N. Rao, B. Radhakrishna, and M. Rajasekhar, 2010: Sensitivity of wrf cloud microphysics to simulations of a severe thunderstorm event over southeast india. *Annales Geophysicae*, **28**, 603–619.
- Ramaswamy, V., and V. Ramanathan, 1989: Solar absorption by cirrus clouds and the maintenance of the tropical upper troposphere thermal structure. *J. Atmos. Sci.*, **46**, 2293–2310.
- Richard, M. D., and R. P. Lippmann, 1991: Neural network classifiers estimate bayesian a posteriori probabilities. *Neural Computation*, **3** (4), 461–483.
- Robert, A., and J. Houze, 1993: *Cloud dynamics*. ACADEMIC PRESS, California.
- Rosenkranz, P. W., 1998a: Interference coefficients for overlapping oxygen lines in air. *Journal of Quantitative Spectroscopy and Radiative Transfer*, **39** (4), 287–297.
- Rosenkranz, P. W., 1998b: Water vapor microwave continuum absorption: A comparison of measurements and models. *Radio Science*, **33** (4), 919–928, doi:10.1029/98RS01182.
- Rosenkranz, P. W., 2001: Retrieval of temperature and moisture profiles from AMSU-A and AMSU-B measurements. *IEEE Transactions on Geoscience and Remote Sensing*, **39** (11), 2429–2435, doi:10.1109/36.964979.
- Rossow, W. B., and R. A. Schiffer, 1999: Advances in understanding clouds from isccp. *Bull. Amer. Meteor. Soc.*, **80**, 2261–2288.
- Rumelhart, D., G. Hinton, and R. Williams, 1986: *Learning internal representations by error propagation*, Vol. I, 318–362. The MIT Press.
- Rutledge, S. A., and P. V. Hobbs, 1983: The mesoscale and microscale structure and organization of clouds and precipitation in mid- latitude cyclones. part viii: A model for the 'seeder-feeder' process in warm-frontal rainbands. *J. Atmos. Sci.*, **40**, 1185–1206.
- Rydberg, B., P. Eriksson, and S. A. Buehler, 2007: Prediction of cloud ice signatures in submillimetre emission spectra by means of ground-based radar and in situ microphysical data. *Q.J.R. Meteorol. Soc.*, **133**, 151–162, doi:10.1002/qj.151.
- Rydberg, B., P. Eriksson, S. A. Buehler, and D. P. Murtagh, 2009: Non-Gaussian Bayesian retrieval of tropical upper tropospheric cloud ice and water vapour from Odin-SMR measurements. *Atmospheric Measurement Techniques Discussions*, **2** (4), 1575–1624, doi:10.5194/amtd-2-1575-2009.
- Saunders, R. W., T. J. Hewison, S. J. Stringer, and N. C. Atkinson, 1995: The radiometric characterization of amsu-b. *IEEE Transaction on Microwave Theory and Techniques*, **43** (4), 760–771.

- Schlüssel, P., P. Snowden, C. Keegan, D. Antonelli, L. Lattanzi, G. Kayal, and M. Cohen, 2016: Eps-sg end user requirements document. Tech. rep., EUMETSAT.
- Selbach, N., T. J. Hewison, G. Heygster, J. Miao, A. J. McGrath, and J. P. Taylor, 2003: Validation of total water vapor retrieval with an airborne millimeter wave radiometer over arctic sea ice. *Radio Science*, **38** (4), 2477–2494, doi:10.1029/2002RS002669.
- Sihvola, A., 2000: Mixing rules with complex dielectric coefficients. *J. Subsurface Sensing Technologies and Applications*, **1393**.
- Skamarock, W. C., and Coauthors, 2008: A description of the advanced research wrf version 3. Tech. rep., NCAR Technical Note NCAR/TN-475+STR. doi:10.1175/JCLI-D-11-00300.1.
- Skofronick-Jackson, G., A. Gasiewski, and J. Wang, 2002: Influence of microphysical cloud parameterizations on microwave brightness temperatures. *IEEE Trans. Geosci. Rem. Sens.*, **40** (1), 187–196.
- Skofronick-Jackson, G., M. J. Kim, J. Weinman, and D. E. Chang, 2004: A physical model to determine snowfall over land by microwave radiometry. *Geoscience and Remote Sensing, IEEE Transactions*, **42** (5), 1047–1058.
- Sola, R. G., M. B. Pujades, M. Labriola, and M. A. P. Lazaro, 2014: The ice cloud imager for metop-sg: the development challenge has started, proceedings of the advanced rf sensors and remote sensing instruments and k-band earth observation radar missions, (arsi14 and keo14). *ESA/ESTEC*, The Netherlands.
- Spencer, R. W., H. M. Goodman, and R. E. Hood, 1989: Precipitation retrieval over land and ocean with ssm/i: Identification and characteristics of the scattering signal. *J. Atmos. Oceanic Technol.*, **6**, 254–273.
- Sreerekha, T. R., S. Buehler, and C. Emde, 2002: A simple new radiative transfer model for simulating the effect of cirrus clouds in the microwave spectral region. *Journal of Quantitative Spectroscopy and Radiative Transfer*, **75** (5), 611–624, doi:http://dx.doi.org/10.1016/S0022-4073(02)00034-1, URL <http://www.sciencedirect.com/science/article/pii/S0022407302000341>.
- Sreerekha, T. R., S. A. Buehler, U. O’Keeffe, A. Doherty, C. Emde, and V. O. John, 2008: A strong ice cloud event as seen by a microwave satellite sensor: Simulations and observations. *Journal of Quantitative Spectroscopy and Radiative Transfer*, **109** (9), 1705–1718, doi:http://dx.doi.org/10.1016/j.jqsrt.2007.12.023, URL <http://www.sciencedirect.com/science/article/pii/S0022407308000022>.
- Stahli, O., A. Murk, N. Kampfer, C. Matzler, and P. Eriksson, 2013: Microwave radiometer to retrieve temperature profiles from the surface to the stratopause. *Atmos. Meas. Tech.*, **6**, 2477–2494, doi:10.5194/amt-6-2477-2013.

- Stephens, G. L., and Coauthors, 2002: The cloudsat mission and the a-train. *Bulletin of the American Meteorological Society*, **83** (12), 1771–1790, doi:10.1175/BAMS-83-12-1771, URL <http://dx.doi.org/10.1175/BAMS-83-12-1771>, <http://dx.doi.org/10.1175/BAMS-83-12-1771>.
- Stogryn, A., 1967: Electromagnetic scattering from rough, finitely conducting surface. *Radio Sciences 2 (New Series)*, **4**, 415–428.
- Tao, W.-K., and J. Simpson, 1993: Goddard cumulus ensemble model. part i: Model description. *Terr. Atmos. Oceanic Sci.*, **4**, 35–72.
- Thompson, G., P. R. Field, R. M. Rasmussen, and W. D. Hall, 2008: Explicit forecasts of winter precipitation using an improved bulk microphysics scheme. part ii: Implementation of a new snow parameterization. *Mon. Wea. Rev.*, **136**, 5095–5115.
- Tonboe, R. T., 2010: The simulated sea ice thermal microwave emission at window and sounding frequencies. *Tellus, Series A: Dynamic Meteorology and Oceanography*, **62** (3), 333–344, doi:10.1111/j.1600-0870.2010.00434.x.
- Tsang, L., J. Pan, D. Liang, Z. Li, D. W. Cline, and Y. Tan, 2007: Modeling active microwave remote sensing of snow using dense media radiative transfer (dmrt) theory with multiple-scattering effects. *Geoscience and Remote Sensing, IEEE Transactions on*, **45** (4), 990–1004.
- Van, d. H. H. C., 1957: *Light scattering by small particles*. New York, Wiley.
- Vanek, M. D., and Coauthors, 2001: Far-infrared sensor for cirrus (fircs): an aircraft-based fourier-transform spectrometer to measure cloud radiance. *Appl. Opt.*, **40** (13), 2169–2176.
- Vivekanandan, J. T., and V. N. Bringi, 1991: Ice water path estimation and characterization using passive microwave radiometry. *J. Appl. Meteor.*, **30** (10), 1407–1421.
- Waliser, D. E., J.-L. F. Li, T. S. L'Ecuyer, and W.-T. Chen, 2011: The impact of precipitating ice and snow on the radiation balance in global climate models. *Geophys. Res. Lett.*, doi:10.1029/2010GL046478.
- Waliser, D. E., and Coauthors, 2009: Cloud ice: A climate model challenge with signs and expectations of progress. *Journal of Geophysical Research Atmospheres*, **114** (8), 1–27, doi:10.1029/2008JD010015.
- Wang, D., J. F. Miao, and Z. M. Tan, 2013: Impacts of topography and land cover change on thunderstorm over the huangshan (yellow mountain) area of china. *Natural Hazards*, **67** (2), 675–699.
- Wang, D., J. F. Miao, and D. L. Zhang, 2015: Numerical simulations of local circulation and its response to land cover changes over the yellow mountains of china. *J. Meteor. Res.*, **29** (4), 667–681.

- Wang, D., and Coauthors, 2016: Surface emissivity at microwaves to millimeter waves over polar regions: parameterization and evaluation with aircraft experiments, *J. AOT*.
- Wang, J. R., G. Liu, J. D. Spinhirne, P. Racette, and W. D. Hart, 2001: Observations and retrievals of cirrus cloud parameters using multichannel millimeter-wave radiometric measurements. *J. Geophys. Res.*, **106**, 15 251–15 263.
- Warren, S. G., 1984: Optical constants of ice from ultraviolet to the microwave. *Appl. Opt.*, **23**, 1206–1225.
- Wattrelot, E., O. Caumont, and J.-F. Mahfouf, 2014: Operational implementation of the 1d+3d var assimilation method of radar reflectivity data in the arome model. *Mon. Weather Rev.*, **142**, 1852–1873.
- Wendisch, M., and P. Yang, 2012: *Theory of Atmospheric Radiative Transfer*. Weinheim, Germany.
- Weng, F., and Q. Liu, 2003: Satellite Data Assimilation in Numerical Weather Prediction Models. Part I: Forward Radiative Transfer and Jacobian Modeling in Cloudy Atmospheres. *Journal of the Atmospheric Sciences*, **60**, 2633–2646, doi:10.1175/1520-0469(2003)060<2633:SDAINW>2.0.CO;2.
- Weng, F., B. Yan, and N. C. Grody, 2001: A microwave land emissivity model. *Journal of Geophysical Research*, **106 (D17)**, 20 115, doi:10.1029/2001JD900019.
- Weng, F. Z., and N. C. Grody, 2000: Retrieval of ice cloud parameters using a microwave imaging radiometer. *J. Atmos. Sci.*, **57**, 1069–1081.
- Wentz, F. J., 1983: Model function for ocean microwave brightness temperatures. *J. Geophys. Res.*, **88**, 1892–1908.
- Wiedner, M., C. Prigent, J. R. Pardo, O. Nuissier, J.-P. Chaboureau, J.-P. Pinty, and P. Mascart, 2004: Modeling of passive microwave responses in convective situations using output from mesoscale models: Comparison with trmm/tmi satellite observations. *J. Geophys. Res.*, **109**, doi:10.1029/2003JD004280.
- Wiesmann, A., and C. Matzler, 1999: Microwave emission model of layered snowpacks. *Remote Sensing of Environment*, **70 (3)**, 307–316, doi:10.1016/S0034-4257(99)00046-2.
- Wilheit, T. T., 1979: A model for the microwave emissivity of the ocean's surface as a function of wind speed. *IEEE Trans. Geosc. and Remote Sensing*, **17**, 244–249.
- Wilheit, T. T., A. T. C. Chang, M. S. V. Rao, E. B. Rodgers, and J. S. Theon, 1977: A satellite technique for quantitatively mapping rainfall rates over the oceans. *J. Appl. Meteor.*, **16**, 551–560.

- Wilson, S. H. S., N. Atkinson, and J. A. Smith, 1999: The development of an airborne infrared interferometer for meteorological sounding studies. *Journal of Atmospheric and Oceanic Technology*, **16** (12).
- Winker, D. M., and Coauthors, 2010: The calipso mission: A global 3d view of aerosols and clouds. *Bulletin of the American Meteorological Society*, **91** (9), 1211–1229, doi:10.1175/2010BAMS3009.1, URL <http://dx.doi.org/10.1175/2010BAMS3009.1>, <http://dx.doi.org/10.1175/2010BAMS3009.1>.
- Wu, D. L., and Coauthors, 2008: Validation of the aura mls cloud ice water content measurements. *J. Geophys. Res.*, **113**, 623–633, doi:10.1029/2007JD008931.
- Wu, R. Z., and J. A. Weinman, 1984: Microwave radiances from precipitating clouds containing aspherical ice, combined phase, and liquid hydrometeors. *Journal of Geophysical Research: Atmospheres*, **89** (D5), 7170–7178, doi:10.1029/JD089iD05p07170, URL <http://dx.doi.org/10.1029/JD089iD05p07170>.
- Xie, X., U. Lohmert, S. Kneifel, and S. Crewell, 2012: Snow particle orientation observed by ground-based microwave radiometry. *J. Geophys. Res.*, **117**, doi:10.1029/2011JD016369.
- Yang, P., Z. Zhang, A. B. Bryan, H. L. Huang, and Y. X. Hu, 2004: A new look at anomalous diffraction theory (adt): Algorithm in cumulative projected-area distribution domain and modified adt. *J. Quantitative Spectroscopy and Radiative Transfer*, **89**, 421–442.
- Yuter, S., M. Miller, J. Stout, R. Wood, J. Kwiatkowski, D. Horn, and C. Spooner, 2006: Remaining challenges in satellite precipitation estimation for the tropical rainfall measuring mission. *4th European Conference on Radar in Meteorology and Hydrology*, Barcelona.
- Zhao, L., and F. Weng, 2002: Retrieval of ice cloud parameters using the advanced microwave sounding unit. *Journal of Applied Meteorology*, 384–395, doi:10.1175/1520-0450(2002)041<0384:ROICPU>2.0.CO;2.